

2006

Magnetron sputtering of metallic coatings onto elastomeric substrates for a decrease in fuel permeation rate

Matthew F. Myntti
University of Dayton

Follow this and additional works at: https://ecommons.udayton.edu/graduate_theses

Recommended Citation

Myntti, Matthew F., "Magnetron sputtering of metallic coatings onto elastomeric substrates for a decrease in fuel permeation rate" (2006). *Graduate Theses and Dissertations*. 4613.
https://ecommons.udayton.edu/graduate_theses/4613

This Dissertation is brought to you for free and open access by the Theses and Dissertations at eCommons. It has been accepted for inclusion in Graduate Theses and Dissertations by an authorized administrator of eCommons. For more information, please contact mschlange1@udayton.edu, ecommons@udayton.edu.

**MAGNETRON SPUTTERING OF METALLIC COATINGS ONTO
ELASTOMERIC SUBSTRATES FOR
A DECREASE IN FUEL PERMEATION RATE**

A Dissertation

Submitted to

The School of Engineering

UNIVERSITY OF DAYTON

In Partial Fulfillment of the Requirements for

The Degree of

Doctor of Philosophy in Materials Engineering

by

Matthew F. Myntti

UNIVERSITY OF DAYTON

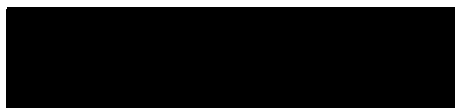
Dayton, Ohio

May 2006

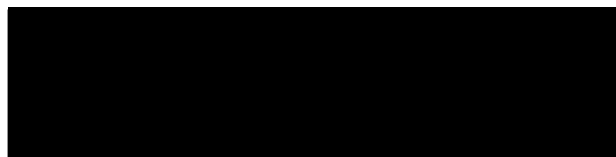
Heckman -
Please Do Not
Remove This Note!

MAGNETRON SPUTTERING OF METALLIC COATINGS ONTO ELASTOMERIC SUBSTRATES FOR A DECREASE IN FUEL PERMEATION RATE

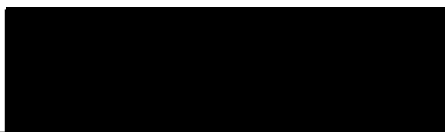
APPROVED BY:



Murray, P. Terrence, Ph.D.
Advisory Committee Chairman
Professor, Graduate Materials
Engineering Program



Eylon, Daniel, Ph.D.
Committee Member
Director, Graduate Materials
Engineering Program



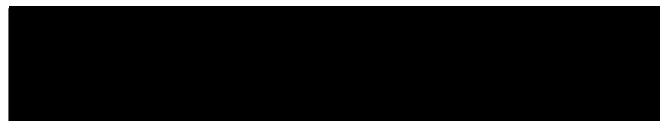
Meyendorf, Norbert G., Ph.D.
Committee Member
Professor, Graduate Materials
Engineering Program



Sheng, Qin, Ph.D.
Committee Member
Professor, Department of
Mathematics



Donald L. Moon, Ph.D.
Associate Dean
Graduate Engineering Programs and
Research, School of Engineering



Joseph E. Saliba, Ph.D., P.E.
Dean
School of Engineering

ABSTRACT

MAGNETRON SPUTTERING OF METALLIC COATINGS ONTO ELASTOMERIC SUBSTRATES FOR A DECREASE IN FUEL PERMEATION RATE

Myntti, Matthew, Franco
University of Dayton

Advisor: Dr. P. Terrence Murray

The purpose of this research was to investigate the application of a metallic coating by magnetron sputtering onto elastomeric substrates, as an inhibiting layer to permeation transport. The metallic coatings which were deposited were aluminum, titanium, and copper. The substrates used were NBR, FVMQ, and FKM elastomers. The permeating fluids were ASTM Fuel C, isooctane, and toluene.

The magnetron sputtering properties of these metallic elements were unique to each material, with the titanium sputtering rate being very low. The sputtering rates of these materials correlated well with their sublimation temperature. It was found that some of the metallic particles which were sputtered onto the substrates, implanted into the surface of the elastomeric membranes, with the total amount and distance of implantation being related to the density of the substrate material.

The permeation of these solvents through the composite materials was reduced by the presence of these coatings with the reduction in permeation rate ranging from 12 to 25% for Fuel C. The pervaporation properties of these substrates were also evaluated. It was found from this analysis that for the FVMQ and NBR substrates, the permeation rate of the permeating solute molecules was proportional to the size of the permeation molecule.

The substrate materials were not significantly stiffened by the addition of the thin metallic coatings. The coated materials were cohesive and well adhered, as determined by stretching of the substrate materials with the metallic layer in place. Upon stretching, there was no evidence of damage to the metallic coating.

ACKNOWLEDGEMENTS

This thesis work could not have been completed without the generous help of many fine people. Most notably, Dr. Terry Murray has provided an invaluable amount of guidance and support throughout the development of this work.

The author would also like to express his thanks to Vernay Laboratories for their support of this project. This project would not have been possible without their material support and their generosity is most appreciated.

Many thanks are also offered to Amanda Schrand of WPAFB for her help in obtaining the SEM pictures used in this analysis of microstructures of the metallic coatings.

TABLE OF CONTENTS

ABSTRACT	iii
ACKNOWLEDGEMENTS	v
TABLE OF CONTENTS	vi
LIST OF ILLUSTRATIONS	ix
LIST OF TABLES	xiv
LIST OF SYMBOLS/ABBREVIATIONS	xvi
CHAPTER 1. INTRODUCTION	1
1.1 Background	1
1.2 Research Objectives	3
1.3 Solvent Transport Mechanisms	4
1.3.1 Permeation and Diffusion	4
1.3.2 Swell Testing	7
1.3.3 Pervaporation	9
1.3.4 Gas Transport through a Porous Membrane	11
1.3.5 Estimating Solubility	12
1.4 Review of Related Research	17
CHAPTER 2. EXPERIMENTAL	23

2.1 Magnetron Sputtering	23
2.2 Deposition Chamber	24
2.3 Sample Preparation	30
2.4 Determination of Sputtering Rates	31
2.5 Test Sample Substrates	36
2.6 Coating Evaluation	38
2.6.1 Visual Observation of Samples	38
2.6.2 Mechanical Evaluation	39
2.6.3 Permeation Evaluation	39
CHAPTER 3. RESULTS AND DISCUSSION	44
3.1 Visual Observation of the Coatings	44
3.1.1 Microscopic Observation of the Coatings	44
3.1.2 SEM Observation of the Coatings	49
3.2 Mechanical Evaluation	58
3.2.1 Visual Observation of Strained Components	58
3.2.2 Tensile Testing of Components	66
3.3 Permeation Evaluation	72
3.3.1 Swell Testing	72
3.3.2 Permeation Testing	84
3.3.3 Pervaporation Testing	99
CHAPTER 4. SUMMARY, CONCLUSIONS AND RECOMMENDATIONS	112
4.1 Summary	112

4.1.1 Visual Observation	112
4.1.2 Mechanical Evaluation	116
4.1.3 Swell Testing	117
4.1.4 Weight Loss and Permeation	120
4.1.5 Pervaporation	123
4.2 Conclusions	124
4.3 Recommendations	126
BIBLIOGRAPHY	128
APPENDICES	135
A. SUPPORTING DATA	135
B. SUPPLEMENTARY DATA	172

LIST OF ILLUSTRATIONS

Illustration 1: Deposition Chamber Configuration	27
Illustration 2: Chamber Front View	28
Illustration 3: Chamber Rear View	28
Illustration 4: Deposition Rates	35
Illustration 5: Permeation Cup Assembly	43
Illustration 6: Permeation Cup Design	43
Illustration 7: FVMQ Uncoated	47
Illustration 8: FVMQ w/ Aluminum	47
Illustration 9: FVMQ w/ Copper	47
Illustration 10: NBR Uncoated	47
Illustration 11: NBR w/ Aluminum	47
Illustration 12: NBR w/ Copper	47
Illustration 13: FKM Uncoated	48
Illustration 14: FKM w/ Aluminum	48
Illustration 15: FKM w/ Copper	48
Illustration 16: FVMQ: 500X-PLANAR	52
Illustration 17: FVMQ: 2000X-PLANAR	52
Illustration 18: FVMQ: 5000X-PLANAR	52
Illustration 19: FVMQ: 500X-SIDE VIEW	53
Illustration 20: FVMQ: 1000X-SIDE VIEW	53
Illustration 21: NBR: 100X-PLANAR	54
Illustration 22: NBR: 500X-PLANAR	54
Illustration 23: NBR: 2000X-PLANAR	54
Illustration 24: NBR: 5000X-PLANAR	54
Illustration 25: NBR: 100X-SIDE VIEW	55

Illustration 26: NBR: 500X-SIDE VIEW	55
Illustration 27: NBR: 500X-3 CORNERS	55
Illustration 28: FKM: 200X-PLANAR	56
Illustration 29: FKM: 2000X-PLANAR	56
Illustration 30: FKM: 5000X-PLANAR	56
Illustration 31: FKM: 100X-SIDE VIEW	56
Illustration 32: FKM: 500X-SIDE VIEW	57
Illustration 33: FKM: 5000X-SIDE VIEW	57
Illustration 34: FKM: 2000X-SIDE VIEW	57
Illustration 35: NBR w/ Aluminum	60
Illustration 36: NBR w/ Aluminum: As Stretched 35%	60
Illustration 37: NBR w/ Copper	61
Illustration 38: NBR w/ Copper: As Stretched 35%	61
Illustration 39: FVMQ w/ Aluminum	62
Illustration 40: FVMQ w/ Aluminum: As Stretched 35%	62
Illustration 41: FVMQ w/ Copper	63
Illustration 42: FVMQ w/ Copper: As Stretched 35%	63
Illustration 43: FKM w/ Aluminum	64
Illustration 44: FKM w/ Aluminum: As Stretched 35%	64
Illustration 45: FKM w/ Copper	65
Illustration 46: FKM w/ Copper: As Stretched 35%	65
Illustration 47: NBR Tensile Curves	69
Illustration 48: NBR Modulus from Origin	69
Illustration 49: FVMQ Tensile Curves	70
Illustration 50: FVMQ Modulus from Origin	70
Illustration 51: FKM Tensile Curves	71
Illustration 52: FKM Modulus from Origin	71
Illustration 53: Polymer Only Swell Testing (648 Hours in ASTM Fuel C)	74
Illustration 54: NBR Swell Testing – Average of Coated Samples	77
Illustration 55: NBR Aluminum Swell Testing	77
Illustration 56: NBR Copper Swell Testing	78
Illustration 57: NBR Swell Vs. Film Thickness	78

Illustration 58: FVMQ Swell Testing – Average of Coated Samples	80
Illustration 59: FVMQ Aluminum Swell Testing	80
Illustration 60: FVMQ Copper Swell Testing	81
Illustration 61: FVMQ Swell Vs. Film Thickness	81
Illustration 62: FKM Swell Testing – Average of Coated Samples	83
Illustration 63: FKM Aluminum Swell Testing	83
Illustration 64: FKM Copper Swell Testing	83
Illustration 65: NBR Average of Coated Samples (ASTM Fuel C)	91
Illustration 66: NBR - Average Perm. Rates from Start of Test (ASTM Fuel C) ...	91
Illustration 67: NBR – Averages: Permeation Rate Between Data Points	91
Illustration 68: FVMQ Average of Coated Samples (ASTM Fuel C)	94
Illustration 69: FVMQ - Average Perm. Rates from Start of Test (ASTM Fuel C)..	94
Illustration 70: FVMQ – Averages: Permeation Rate Between Data Points	94
Illustration 71: FKM Average of Coated Samples (ASTM Fuel C)	96
Illustration 72: FKM - Average Perm. Rates from Start of Test (ASTM Fuel C) ...	96
Illustration 73: FKM – Averages: Permeation Rate Between Data Points	96
Illustration 74: Toluene IR Spectra	101
Illustration 75: Isooctane IR Spectra	102
Illustration 76: Fuel C IR Spectra	103
Illustration 77: Fuel C After Permeation Spectra	104
Illustration 78: NBR Weight Loss Over Time	107
Illustration 79: NBR-Isooctane Weight Loss Over Time	107
Illustration 80: NBR-Toluene Weight Loss Over Time	107
Illustration 81: FVMQ Weight Loss Over Time	108
Illustration 82: FVMQ-Isooctane Weight Loss Over Time	108
Illustration 83: FVMQ-Toluene Weight Loss Over Time	108
Illustration 84: NBR Permeation – Between Data Points	109
Illustration 85: NBR - Isooctane Permeation – Between Data Points	109
Illustration 86: NBR – Toluene Permeation – Between Data Points	109
Illustration 87: FVMQ Permeation – Between Data Points	110
Illustration 88: FVMQ - Isooctane Permeation – Between Data Points	110
Illustration 89: FVMQ – Toluene Permeation – Between Data Points	110

Illustration 90: Substrate Density Vs. Area Coverage	114
Illustration 91: Substrate Density Vs. Permeation Reduction	115
Illustration 92: Hansen Solubility Parameters Vs. Swell.....	119
Illustration 93: Hansen Solubility Parameters Vs. Permeation	122
Illustration 94: Nitrile Swell Diagrams	136
Illustration 95: Fluorosilicone Swell Diagrams	138
Illustration 96: Fluorocarbon Swell Diagrams	140
Illustration 97: Nitrile Weight Changes	143
Illustration 98: Fluorosilicone Weight Change Parts	146
Illustration 99: Fluorocarbon Weight Change Charts	149
Illustration 100: Nitrile Permeation Charts	152
Illustration 101: Fluorosilicone Permeation Charts	155
Illustration 102: Fluorocarbon Permeation Charts	158
Illustration 103: Nitrile Permeation Charts (Between Points)	161
Illustration 104: Fluorosilicone Permeation Charts (Between Points)	164
Illustration 105: Fluorocarbon Permeation Charts (Between Points)	167
Illustration 106: NBR Tensile Curves (All Samples)	168
Illustration 107: NBR Modulus Curves (All Samples)	168
Illustration 108: FVMQ Tensile Curves (All Samples)	169
Illustration 109: FVMQ Modulus Curves (All Samples)	169
Illustration 110: FKM Tensile Curves (All Samples)	170
Illustration 111: FKM Modulus Curves (All Samples)	170
Illustration 112: Permeation Cup Design	178
Illustration 113: Deposition Chamber	186
Illustration 114: Main Chamber	186
Illustration 115: Secondary Chamber	187
Illustration 116: Interior End View – Sample Shutter Closed	187
Illustration 117: 10 mTorr Copper Deposition – Side View	188
Illustration 118: 10 mTorr Copper Deposition – Rear View	188
Illustration 119: NBR Uncoated	189
Illustration 120: NBR-Al 10 mTorr	189
Illustration 121: NBR-Al 20 mTorr	189

Illustration 122: NBR-Al 30 mTorr	189
Illustration 123: NBR-Cu 10 mTorr	190
Illustration 124: NBR-Cu 20 mTorr	190
Illustration 125: NBR-Cu 30 mTorr	190
Illustration 126: FVMQ Uncoated	190
Illustration 127: FVMQ-Al 10 mTorr	191
Illustration 128: FVMQ-Al 20 mTorr	191
Illustration 129: FVMQ-Al 30 mTorr	191
Illustration 130: FVMQ-Cu 10 mTorr	191
Illustration 131: FVMQ-Cu 20 mTorr	192
Illustration 132: FVMQ-Cu 30 mTorr	192
Illustration 133: FKM Uncoated	192
Illustration 134: FKM-Al 10 mTorr	192
Illustration 135: FKM-Al 20 mTorr	193
Illustration 136: FKM-Al 30 mTorr	193
Illustration 137: FKM-Cu 10 mTorr	193
Illustration 138: FKM-Cu 20 mTorr	193
Illustration 139: FKM-Cu 30 mTorr	194

LIST OF TABLES

Table 1: Hansen Solubility Parameters for Applicable Solvents	16
Table 2: Hansen Solubility Parameters for Applicable Polymers	17
Table 3: Interaction Parameter Values	17
Table 4: Deposition Chamber Components	29
Table 5: Test Sample Production Values	31
Table 6: Sputtering Target Information	34
Table 7: Predicted Film Thickness	34
Table 8: Target Deposition Rates	35
Table 9: Test Sample Substrates	37
Table 10: ANOVA for Swell Testing	74
Table 11: ANOVA for Weight Loss at 528 Hours	86
Table 12: ANOVA for Weight Loss at 648 Hours	86
Table 13: ANOVA for Permeation from Start of Test at 528 Hours	87
Table 14: ANOVA for Permeation from Start of Test at 648 Hours	87
Table 15: ANOVA for Permeation Between Data Points at 528 Hours	88
Table 16: ANOVA for Permeation Between Data Points at 648 Hours	88
Table 17: Permeation Coefficients	98
Table 18: Membrane Coverage	98
Table 19: Toluene – IR Absorption	101
Table 20: Isooctane – IR Absorption	102
Table 21: Fuel C – IR Absorption	103
Table 22: Post Permeation Fuel C – IR Absorption	104
Table 23: Permeation Coefficients – Toluene Permeation	111

Table 24: Permeation Coefficients – Isooctane Permeation	111
Table 25: Nitrile Swell Data	135
Table 26: Fluorosilicone Swell Data	137
Table 27: Fluorocarbon Swell Data	139
Table 28: Aluminum Coated Nitrile Weight Change Data	141
Table 29: Copper Coated Nitrile Weight Change Data	142
Table 30: Aluminum Coated Fluorosilicone Weight Change Data	144
Table 31: Copper Coated Fluorosilicone Weight Change Data	145
Table 32: Aluminum Coated Fluorocarbon Weight Change Data	147
Table 33: Copper Coated Fluorocarbon Weight Change Data	148
Table 34: Aluminum Coated Nitrile Permeation Data	150
Table 35: Copper Coated Nitrile Permeation Data	151
Table 36: Aluminum Coated Fluorosilicone Permeation Data	153
Table 37: Copper Coated Fluorosilicone Permeation Data	154
Table 38: Aluminum Coated Fluorocarbon Permeation Data	156
Table 39: Copper Coated Fluorocarbon Permeation Data	157
Table 40: Aluminum Coated NBR Permeation Data (Between Points)	159
Table 41: Copper Coated NBR Permeation Data (Between Points)	160
Table 42: Aluminum Coated FVMQ Permeation Data (Between Points)	162
Table 43: Copper Coated FVMQ Permeation Data (Between Points)	163
Table 44: Aluminum Coated FKM Permeation Data (Between Points)	165
Table 45: Copper Coated FKM Permeation Data (Between Points)	166
Table 46: Sample Testing Records (Samples 1 through 22)	171
Table 47: Sample Testing Records (Samples 23 through 55)	172

LIST OF SYMBOLS, ABBREVIATIONS AND NOMENCLATURE

A:	Cross-sectional area of permeation membrane (m^2)
A_{12} :	Relative energy difference of molecular interaction
D:	Steady state diffusion rate
D_A :	Diffusion rate of species A
D_B :	Diffusion rate of species B
d_f :	Density of a grown film
d_g :	Density of single crystal quartz (2.649 gm/cm^3)
DH:	Heat of solution of a polymer and solvent
D_o :	Diffusion coefficient of a polymer and solvent
d_p :	Number of pores/ m^2 in a porous membrane
E:	Total cohesion energy
E_d :	Activation energy of diffusion
E_D :	Dispersion forces
E_H :	Hydrogen bonding forces
E_o :	Initial energy of impinging atom in sputtering
E_p :	Permanent dipole forces
E_r :	Recoil energy of target atom in sputtering
F_c :	Frequency of coated quartz crystal
FKM:	Fluorocarbon rubber
F_q :	Frequency of uncoated quartz crystal
FVMQ:	Fluorosilicone tubber
h:	Initial sample thickness
H:	Cohesive energy density
ΔH_{sorp} :	Molar heat of sorption

HSP:	Hansen solubility parameter
k:	$4/3(2\pi/(RT))^{1/2}$
K:	Constant of polymer solvent interaction
M:	Molar mass of a gas
m_1 :	Mass of target atom in sputtering
m_2 :	Mass of impinging atom in sputtering
M_c :	Molecular mass between cross-links
M_f :	Mass of solvent uptake at equilibrium
M_o :	Initial mass of polymer
m_s :	Molar mass of solvent absorbed
M_s :	Mass of solvent absorbed
M_t :	Mass of solvent uptake at time t.
n:	Exponent related to diffusion transport mechanism
N:	Gas concentration (number/cm ³)
N_{at} :	Frequency constant of AT-cut quartz (1661000 Hz)
NBR:	Nitrile Butadiene Rubber
P:	Permeability of a porous membrane
Q:	Steady state permeation through a barrier
Q_{bp} :	Permeation rate between data points (mg/(m ² *sec))
Q_{st} :	Permeation rate from start of test (mg/(m ² *sec))
Qt:	Molar absorption time
Q_{∞} :	Molar absorption at equilibrium
r:	Mean pore radius of a porous membrane
"r":	Ratio of polymer size to solvent size
R:	Universal gas constant (1.987 cal/mol K)
R_a :	Difference in HSP for a solvent and parameter
RED:	Relative energy difference of R_a and R_o
R_o :	Radius of interaction for a HSP solubility sphere
S:	Solubility of a solvent in a polymer
S_A :	Solubility of species A
S_B :	Solubility of species B

SF:	Actual separation factor of pervaporation
S_o :	Solubility constant of a polymer and solvent
SW:	Swell (%)
T:	Absolute temperature (K)
t:	Time (sec)
T_f :	Thickness of coating on Si crystal
ΔU :	Change in internal energy of an atom
u_f :	Shear modulus of coating material
u_g :	Shear modulus of quartz crystal
v:	Average velocity of permeates through a porous membrane $(8RT/\pi M)^{1/2}$
V:	Molar volume of a solvent
v_1 :	Velocity of impacting atoms in sputtering
v_2 :	Velocity of sputtered atoms
$w_{(t+1)}$:	Weight of permeation cup at time (t-1)
w_f :	Final weight of sample after permeation (g)
w_o :	Weight of permeation cup at time t_o (g)
w_t :	Weight of permeation cup at time t (g)
x:	Polymer penetrant interaction parameter
X_{12} :	Flory interaction parameter
x_{A1}/x_{A2} :	Upstream molar ratios of species A:B
x_{B1}/x_{B2} :	Downstream molar ratios of species A:B
X_c :	Critical (χ) parameter for solubility
$\alpha_{A/B}$:	Idealized interaction parameter of pervaporation
β :	Lattice constant ≈ 0
ε :	Porosity of a porous membrane ($n\pi r^2$)
κ :	Boltzmann constant
λ :	Mean free path
σ_c :	Collision cross-section
δ :	Thickness of a porous membrane
δ :	Hildebrand solubility parameter
δ_D :	Hansen dispersion parameter

δ_H :	Hansen hydrogen bonding parameter
δ_P :	Hansen permanent dipole parameter
μ_K :	Shape factor of pores in a porous membrane
ρ :	Density
\varnothing :	Volume fraction of swollen rubber
γ :	Cross-link density

CHAPTER 1

INTRODUCTION

1.1 Background

It is possible to deposit a thin metallic layer onto an elastomeric membrane by magnetron sputtering with good adhesion and flexibility as a barrier for the reduction of the permeation rate of fuels through the substrate material.

Permeation is the flow of a fluid through material. The permeation of solvents through elastomers can significantly affect their performance and functional life. The rate of permeation of solvents through polymers is a key aspect of the suitability of a given elastomer for usage conditions. In the case of fuels, permeation is of great concern to the automotive industry. The EPA's standard on evaporative emissions for unburned hydrocarbons was lowered from 10 grams per vehicle per 24 hours to 2 grams in 1998. In 2004, the Federal Evaporative Emission Standards for Light Vehicles and Light-Duty Trucks reduced this emission to allow a loss 0.67 grams per 24 hours for the entire vehicle (2 grams in three days) [EPA]. The evaporative emissions value reflects the loss of gasoline in a vehicle to the atmosphere without being used in combustion. These emission levels must be maintained for ten years, even if

fuel formulations change, as they have to higher percentages of methanol, which is more aggressive to elastomers than standard gasoline.

The importance of these emission standards to elastomers is due to their usage throughout light passenger vehicles in a fuel containing mode. The major elastomeric usage in fuel systems is in the fuel lines, through which fuel is delivered to the engine from the tank, and in the sealing components that are used to in the fuel system and fuel tank itself. Because these emission standards are so stringent, for the vehicle to meet these standards, there can be little allowable permeation through these elastomeric components.

Because of these permeation restrictions, more exotic materials must be used to limit this permeation. There are several materials with acceptable resistance to degradation by exposure to fuels, including; nitrile butadiene rubber (NBR), epichlorohydrin (ECO), fluorosilicone (FVMQ), and fluorocarbon (FKM). Of these materials, only FKM is widely used, because its permeation rate is at least one order of magnitude lower than the other materials. The drawback of FKM is its high cost, being at least five times more expensive than NBR or ECO, and double the cost of FVMQ for high-fluorine content FKM, as used in fuel systems.

There are many factors which impact the permeation rate of chemicals through elastomeric materials. These factors include the respective size of the solvent molecules as compared to the polymer network spacing, the interaction of the permeating species with the polymer functional groups, the viscosity of the permeating species, and the molecular weight of the permeating species. In

addition, it has been found that the use of fillers in the polymeric material can decrease the permeation rate of polymer systems by both forcing the permeating species to take a more tortuous path through the material and by the interaction of the filler material with the polymer.

1.2 Research Objectives

This research was undertaken to determine if the permeation rate of fuels through fuel resistant, permeable materials could be reduced by the application of flexible metallic coating onto the surface of the polymer. There is an obvious benefit to doing this, as the permeation rate of solvents through metals is orders of magnitude lower than that any elastomeric material. There are many problems that need to be addressed with the coating of an elastomer with a metallic coating. The most important of these is providing adequate adhesion of a metallic layer on an elastomeric substrate. In addition, the coating material must be flexible enough that the component retains sufficient flexibility to fulfill its original design intent. Porosity in the coating must be limited to ensure good permeation resistance and damage to the surface layer by the coating process must be minimized. Some implantation of the metallic particles beyond the surface of the elastomeric substrate is favorable to ensure adhesion, but too much may be an issue if it causes substrate damage.

To address these issues, magnetron sputtering was used to apply the metallic surface coating with the process optimized to produce micro-scale particles. These particles agglomerate on the surface, providing larger surface

coverage than individual molecules, while still providing for flexibility between the agglomerates. The micro-scale particles will have some gap between them, which allows for some permeation. As such, the size of the gaps between the particles affects the permeation rates of solvents through the coating. These gaps do have some benefit in that they will alleviate stresses in the coating layer due to stretching or bending of the substrate, by allowing the agglomerates to separate.

The properties of the coated components investigated were; the permeation rate of solvents through the coated and uncoated materials, damage to the coating due to solvent transport through the material and swelling of the substrate material, and adhesion effects on the coating material due to swelling of the substrate material.

1.3 Solvent Transport Mechanisms

1.3.1 Permeation and Diffusion

Molecular transport of organic liquids is dependent upon the density of the chain entanglements and chain ends, cross-link density of the elastomer, compatibility of the polymer and liquid, and the type and amount of filler [37]. In the absence of relaxation and irreversible processes, the steady-state permeation of a solvent through a barrier (Q) is determined by the product of the diffusion rate (D) and solubility (S) [3]. Diffusion is the general transport of matter

through the thermal agitation. Solubility is the extent to which one substance will dissolve in another.

Diffusion is primarily a function of the size and concentration of diffusing molecules [3]. The rate of diffusion of small molecules dissolved in rubber is dependent upon the rate of formation of interchange gaps (increase in the free volume) [1].

There are two basic types of diffusion through polymers, Fickian and type II diffusion. In Fickian diffusion, the rate of change of the concentration of the diffusing species is proportional to the change in the concentration gradient with distance in a given direction. For Fickian transport, the rate of diffusion of the penetrant molecules is much less than the relaxation rate of the polymer chains [21]. In type II diffusion, there are strong interactions between the polymer and the diffusing species. In this case, the diffusion is occurring so fast that there is no time for the polymer to relax.

For gases and for the most solvent-polymer systems, the rate of diffusion can be determined by Fick's second law of diffusion [1], as shown in equation 1. In this equation, D_0 is the diffusion coefficient, which is a constant for the given polymer and diffusing species. The activation energy (E_d) is the energy needed to form a hole in the polymeric lattice network plus the energy required to enable the diffusing molecule to jump into the hole [3]. As the size of solvent molecules increase, it takes more energy for them to transport through the material. As such, for any given polymer, the activation energy of diffusion increases proportionately with the 2nd power of the collision diameter of the permeating gas

molecules [43]. As the cohesive energy density of the polymer is increased, the system has to have high energy for diffusion to occur. This additional energy increases the mean free path through a tightly bound system, allowing for diffusion to occur. As such, these activation energies of diffusion are directly proportional to the cohesive energy density of the different polymers [43].

$$D = D_0 e^{(-E_d/RT)} \quad (1)$$

One method of determining the transport mechanism of a solvent through a polymer network is by examination of the molar absorption rate. This is described by the empirical relationship, expressed in equation 2 [21]. If the transfer mechanism exponent (n) is found to be equal to 0.5, the mechanism is Fickian. If it is 1, it is case II type transport [21]. In this equation, Q_t is the molar absorption time at time t, Q_∞ is the molar absorption at equilibrium, and K is a constant of the polymer-solvent interaction.

$$\text{Log} \left(\frac{Q_t}{Q_\infty} \right) = \log K + n \log t \quad (2)$$

Solubility is a function of the chemical interaction between dissolved molecules and the polymer matrix [3]. Solubility can be determined from the properties of the solvent and polymer [9], as shown in equation 3. For a given polymer and solvent pair, S_0 is the solubility constant and ΔH_{sorp} is the molar heat of sorption. The molar heat of sorption itself is due to two factors; the molar heat of condensation, and mixing of the penetrant into the polymer phase [9]. It has been found that there is a linear correlation between the Arrhenius, E_d and $\log D_0$ of elastomers, being a straight-line which is equal to 0.10 [13].

$$S = S_0 e^{(-\Delta H_{\text{sorp}}/RT)} \quad (3)$$

1.3.2 Swell Testing

Swell testing is another method of examining polymer-solvent interactions. There are two main factors that affect swelling; the fraction of the amorphous phase, and the chemical compatibility of the polymer and solvent. As the crystal fraction decreases, there is a subsequent increase in the volume of the amorphous region and the chain lengths between the crystal sections also increase. Because sorption occurs much more readily into the amorphous regions of polymeric material, larger volumes of amorphous regions, yields larger material volumes which are accessible for liquid sorption to occur and higher swelling [10].

Swell testing can also be used to determine diffusion and solubility parameters. Diffusivity can be calculated from solubility testing using equation 4 [12]. Solubility can be calculated using equation 5 [12]. In these equations, θ is the initial slope of the sorption curve, and h is the initial sample thickness. Q_∞ is the equilibrium solvent uptake, which can be calculated as follows ($Q_\infty = ((M_S/m_S)/M_0) \times 100$), where M_S is the mass of solvent absorbed, m_S is the molar mass of the solvent, and M_0 is the initial mass of the polymer.

$$D = \pi \left[\frac{h\theta}{4Q_\infty} \right] \quad (4)$$

$$S = \frac{M_f}{M_0} \quad (5)$$

From swell-testing data, the method of diffusion can be also be determined by analyzing the mass uptake rate, as expressed in the empirical equation 6 [13]. In this equation, M_t is the mass uptake at time t , M_f is the mass uptake at equilibrium, K is a constant of the polymer and solvent, and n again is an exponent related to the transfer mechanism. If the transfer mechanism exponent is found to be equal to 0.5, the mechanism is Fickian. If it is 1, it is case II type transport [13].

$$\frac{M_t}{M_f} = Kt^n \quad (6)$$

Another use of swell testing is for the determination of the cross-link density (γ) of elastomers and the molecular weight between cross-links (M_c). Because cross-links prevent the polymer chains in an elastomer from spreading apart from each other, as the cross-link density of an elastomer increases its swelling rate and total amount of solvent uptake is decreased. The cross-link density is equal to $\frac{1}{2}$ of the molecular weight between cross-links. The method for relating the molecular weight between cross-links and swelling is described in equations 7 through 9 [12]:

$$M_c = \frac{\rho_p V \phi^{1/3}}{\ln(1-\phi) + \phi + x\phi^2} \quad (7)$$

Where: ρ_p = Polymer density

V = Molar volume of solvent

ϕ = Volume fraction of swollen rubber

x = Polymer penetrant interaction parameter

$$x = \beta + v_s \frac{(\delta_s - \delta_p)}{RT} \quad (8)$$

Where: β = Lattice constant ≈ 0

R = Universal gas constant

T = Temperature (K)

δ = Hildebrand solubility parameters

$$\phi = \frac{w_1/\rho_1}{(w_1/\rho_1) + (w_2/\rho_2)} \quad (9)$$

Where: w_1 = Weight of rubber sample

ρ_1 = Density of rubber sample

w_2 = Weight of solvent in rubber samples

ρ_2 = Density of solvent

A further relationship has also been found between the elastic modulus (E) of elastomeric materials and their molecular weight [13]. As the molecular weight of a given elastomer is increased, the elastic modulus decreases. This is due to a reduction in the ability of the polymeric chains to re-orient themselves in the direction of the stress applied, reducing the number of polymer chains aligned to resist the force applied.

$$E = \frac{3\rho_p RT}{Mc} \quad (10)$$

1.3.3 Pervaporation

Due to their varying sizes and affinities for the functional groups in the polymer chains, it is reasonable to assume that in a combined mixture of solvents

exposed to one side of a permeation barrier, each solvent will permeate through the membrane at different rate. Pervaporation is the process by which two chemicals are separated due to the difference in affinity of a polymer for each solvent [17]. In an ideal sense, the membrane acts as a molecular scale filter separating a feed mixture of A and B into a permeate of pure A and a nonpermeant or retinate of pure B.

The idealized interaction parameter ($\alpha_{A/B}$) can be determined from the ratio of the solvent diffusion rates (D_A/D_B) and the ratio of their solubilities (S_A/S_B) in the polymeric membrane, as shown in equation 11. Practically, the actual separation parameter can be calculated by comparing the upstream and downstream molar ratios of the two solvents before and after passing through the polymeric separation membrane. This relationship is shown in equation 12. These equations neglect the effects of the complicating factor of coupling. Coupling is the phenomenon, when the permeation rate of one component is modified by physical and chemical interactions, which can occur with the other component. These interactions can be positive or negative, and are dependent upon the particular solvents and polymer combinations [50].

$$\alpha_{A/B} = \frac{\begin{bmatrix} D_A \\ D_B \end{bmatrix}}{\begin{bmatrix} S_A \\ S_B \end{bmatrix}} \quad (11)$$

$$SF = \frac{(X_{A1}/X_{B1})}{(X_{A2}/X_{B2})} \quad (12)$$

1.3.4 Gas Transport through a Porous Membrane

All of the permeation, diffusion, and solubility information shown in section 1.3.1 through 1.3.3 relate to a solid, homogeneous polymeric membrane. However, in this research we are applying a porous metallic coating to these materials. The transport of a liquid through a porous non-reacting membrane, such as a metallic layer is not based on chemical absorption and diffusion, but on the physical flow of the solvent through the pores in the membrane. As such, the permeability of a metallic coating layer can be modeled by Knudsen diffusion [20], as shown in equation 13. The important factors in Knudsen diffusion are: the pore size, shape and density in the membrane, the thickness of the membrane, and the temperature, velocity, and molar mass of the permeant. As would be expected, as the size of the permeating species increases, the permeability of that species decreases. In general, for membranes, permeation is inversely proportional to the square root of the molecular weight of the gas.

$$P = \frac{2 \varepsilon \mu_K v r}{3 RT \delta} = \frac{K d_p r^3}{\delta M^{1/2}} \quad (13)$$

Where: P = permeability ($\text{mol}/(\text{cm}^2\text{Pa})$)

ε = Porosity ($n \pi r^2$)

d_p = Number of pores/ m^2

r = Mean pore radius

μ_K = Shape factor

δ = Thickness (μm)

R = Gas constant ($8.314 \text{ J}/(\text{mol K})$)

T = Temperature (K)

v = Average velocity (m/s) = $(8RT/\pi M)^{1/2}$

k = $4/3(2\pi/(RT))^{1/2}$

M = molar mass of gas (kg/mol)

Assuming a 90% coating coverage area on the membranes and nominal permeation rates of NBR and FVMQ to be 4.3 and 2.9 mg/(m²*sec), the estimated permeation rate of the coated samples has been calculated. The expected permeation reduction was calculated to be 77% for the NBR at this coverage area, yielding a predicted permeation rate of 0.97 mg/(m²*sec). For the FVMQ, the expected permeation reduction was calculated to be 72% at this coverage area, yielding a predicted permeation rate of 0.93 mg/(m²*sec).

1.3.5 Estimating Solubility

One possible method for estimating the solubility of a solvent and polymer is the Hansen Solubility Parameter (HSP). This solubility parameter can be related to the Flory Interaction Coefficient (χ_{12}), which has been used for describing polymer-solvent interaction effects. This method has been used successfully in the past to determine the solubility of solvents in polymers. The Hansen Solubility Parameter theory states that the total energy of vaporization of a liquid consists of several parts: dispersion (atomic) forces, permanent dipole-permanent dipole forces (molecular), and hydrogen bonding (electron exchange). Adding these forces together yields the total cohesive energy (E), which can be measured by the evaporation rate of a liquid [37].

Of the three major types of interaction for organic materials, the most general are the dispersion forces (E_D). These are composed of non-polar interactions due to atomic forces. The permanent dipole-permanent dipole forces (E_P) is a measure of the polarity of the material. Hydrogen bonding (E_H) is an electron exchange parameter, which is due to attraction among molecules because of hydrogen bonding [37]. Solubility and swell testing have been used to confirm the solubility parameter assignments of many liquids. These have been used to derive group contribution methods and suitable equations based on molecular properties to arrive at estimates of the three parameters for additional liquids.

The Total Cohesion Energy (E) is the sum of the individual energies.

$$E = E_D + E_P + E_H \quad (14)$$

Dividing these values by the Molar Volume (V) and squaring yields the Hansen D, P, and H components.

$$\frac{E}{V} = \frac{E_D}{V} + \frac{E_P}{V} + \frac{E_H}{V} \quad (15)$$

$$\delta^2 = \delta_D^2 + \delta_P^2 + \delta_H^2 \quad (16)$$

Summing these values yields the Hildebrand Solubility Parameter (δ), which quantitatively accounts for the cohesion energy density.

The usual equation used in HSP correlations is:

$$(Ra)^2 = 4(\delta_{D2} - \delta_{D1})^2 + (\delta_{P2} - \delta_{P1})^2 + (\delta_{H2} - \delta_{H1})^2 \quad (17)$$

Ra is a modified difference between the HSP values for a solvent (1) and polymer (2). Ra must not exceed Ro , which is the radius of interaction of an HSP

solubility sphere, for solubility to be maintained. This solubility sphere is a measured area of correlation factors, inside of which solubility is maintained for a solvent and polymer interaction. One way of determining solubility is by the Relative Energy Difference (RED) [37].

$$RED = Ra/Ro \quad (18)$$

If the RED = 0, there is no energy difference between the solvent and polymer, indicating that the solvent will dissolve the polymer. If the RED is 1, the solvent is on the boundary of the sphere for the polymer, and is the limit at which complete swelling can occur. If this number is less than 1, there will be higher affinity and high swelling. If this number is greater than 1, there is less affinity between the polymer and solvent and there will be less swelling of the polymer.

For Ra to be consistent with the Flory Interaction Parameter (X_{12}), as a means of comparing calculated values with published values of X_{12} , it must be normalized by $4R_M^2$ to yield the Hansen Solubility Parameter (HSP). R_M is the maximum solubility parameter difference which still allows for the polymer to be dissolved [37].

$$HSP = \frac{RA^2}{R_M^2} = \left(\frac{(\delta D_2 - \delta D_1)^2 + (\delta P_2 - \delta P_1)^2/4 + (\delta H_2 - \delta H_1)^2/4}{R_M^2} \right) \quad (19)$$

Where: $RA = Ra/2$ and $R_M = Ro/2$

RA/R_M is a ratio of solubility parameters. H is a ratio of cohesive energy densities. It has a value of 0 when the solubility parameters for the solvent and polymer match and increases as the difference increases. RA/R_M and $H =$

$(RA/R_M)^2$ will be 1.0 on the boundary surface of a sphere describing the solubility parameter.

The Flory interaction parameter can also be calculated from these values by the following method [37].

$$A_{12} = [(\delta D_2 - \delta D_1)^2 + 0.25(\delta P_2 - \delta P_1)^2 + 0.25(\delta H_2 - \delta H_1)^2] \quad (20)$$

$$X_{12} = (V^*A_{12})/(RT) \quad (21)$$

Where: A_{12} = relative energy difference

R = gas constant (1.987 cal/mol K)

T = absolute temperature (K)

For polymers having a high molecular weight, X_{12} must be close to 0.5 at the point of solvation/ precipitation. This boundary is the critical (χ) parameter X_C . As such, for high molecular weight polymers:

$$X_{12} = X_C(RED)^2 = H/2 \quad (22)$$

Taking the molar volume (V) into account:

$$R_M^2 = (R_0/2)^2 = \{0.5(1 + 1/r^{1/2})RT/V\} \quad (23)$$

Where: " r " = ratio of polymer size to solvent size

In general, if a solvent is being dissolved into a polymer, the Flory interaction parameter (X_{12}) needs to be 0.5 for full swelling to occur. For two low molecular weight materials (such as two solvents), this value needs to be less than 2. As polymers are mostly immiscible, If both materials are high molecular weight polymers, this value is equal to 0 [37].

The Hansen solubility parameters for the polymers and solvents used in this research are given in the tables 1 and 2. The calculated interactions

parameters are given in table 3. As can be seen, it would be expected that the solvents would be much more likely to swell into the NBR material. In the case of toluene, having an H value of less than 1, swelling it completely. The isooctane will still swell the NBR, but not completely. The FKM will have some swell from both solvents, but neither preferentially. The FVMQ will have minimal swell from the isooctane, and larger swell from the toluene material.

These swelling values are important, as they indicate the affinity for the solvent in the polymer. As the swell increases, the permeation increases. From these calculations it has been predicted that for the permeation of toluene, NBR will have the highest permeation followed by FVMQ and FKM. The permeation of isooctane will follow the same trend, with the permeation rates being lower across the board for all of the polymers as compared to that of toluene.

Table 1: Hansen Solubility Parameters for Applicable Solvents

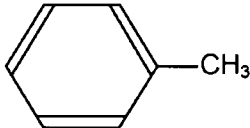
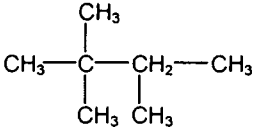
Solvent	Dispersion (δ_D)	Polar (δ_P)	Hydrogen Bonding (δ_H)	Molar Volume (V)
Toluene 	18.0	1.4	2.0	106.8
IsoOctane (2,2,4-Trimethylpentane) 	14.1	0.0	0.0	166.1

Table 2: Hansen Solubility Parameters for Applicable Polymers

Polymer	Dispersion (δ_D)	Polar (δ_P)	Hydrogen Bonding (δ_H)	Interaction Radius R_o
FKM (R FKM (Viton) 0.76)	11.6	23.0	5.0	21.6
NBR (R NBR)	19.8	17.8	3.2	19.0
FVMQ (R FQ FL/SI)	15.9	20.1	6.9	16.8

Table 3: Interaction Parameter Values

Polymer	Solvent	Ra	RED	H	X ₁₂	HSP
FKM	Toluene	25.3	1.17	1.37	0.69	14.80
FKM	IsoOctane	24.1	1.11	1.24	0.62	13.40
NBR	Toluene	16.8	0.78	0.78	0.39	7.54
NBR	IsoOctane	21.4	0.99	1.27	0.63	8.99
FVMQ	Toluene	19.8	1.18	1.39	0.69	8.57
FVMQ	IsoOctane	21.6	1.28	1.65	0.82	10.12

1.4 Review of Related Research

Polymers have been coated from many reasons. Hybrid components and composites use the favorable properties of materials and diminish the disadvantages. Polymeric parts are used to make low weight parts that are easily processed, but they have low scratch and wear resistance, solubility and UV instability. These properties can be improved by coating the polymers with hard coatings. Lugscheider has coated titanium nitride and alumina onto a variety of rigid thermoplastics, including polyamide (PA), polycarbonate (PC), poly-butadiene-terephthalate (PBT), and poly-ether-ether-ketone(PEEK) by reactive sputtering. These coatings had good peel results and adhesion [3]. Fukuda has coated gold and gold-alloy films on poly-ethylene-terephthalate (PET) by DC magnetron sputtering. Aluminum, silicon, and manganese have all been

coated over a titanium interlayer. It was found in this study that the gold grain growth is faster with the titanium interlayer than over the bare PET. The Ti layer also improved the grain size and crystal orientation [14].

Nakahigashi has attempted to create a flexible diamond like carbon (DLC) on rubbers and plastics by radio frequency pulsed laser deposition. There were several problems encountered coating the rubber articles, including the low heat resistance of the polymer surfaces, pollution of the film surfaces due to the presence of process aids, and transformation of the base material. These issues were addressed by using an amplitude modulated radio frequency cathodic vapor deposition coating while controlling the temperature of the process. They also cleaned the surface by plasma to make the film flexible. This coating provided some measure of permeation reduction of oxygen through polyethylene [11].

Kupfer has investigated the deposition of metallic coatings onto polymers by ion beam assisted magnetron sputtering, followed by electroplating. In this case, an argon ion beam was used to alter the surface chemistry of the deposited film. Copper was then applied by magnetron sputtering onto poly-phenylene sulfide (PPS) and poly-ether-imide (PEI) substrates, using Argon as a sputtering gas. This coating was then reinforced by electroplating in a copper sulfate/sulfuric acid solution. A problem with this approach was that the ion-beam pre-treatment graphitized (burned) the surface, yielding a decrease in the adhesion strength. However, by using the ion beam assisted deposition, good adhesion could be obtained for copper on PPS. The adhesion strength was

dependent upon the ion/atom ratio and energies, with low ratios and energies yielding low adhesion strengths. If the ion ratio and energy was too high, the adhesion was also poor, due to destruction of the interface. The addition of a titanium layer beneath the copper coating increased the bond substantially. Plasma etching of the surface with oxygen and nitrogen yielded a columnar structure with increased surface area and increased mechanical anchor sites, also increasing adhesion [34].

Metallic coatings have also been applied to polymers to prevent chemical contamination of sterile fields by mechanical straining of the polymer. In this work by Lugscheider, PBT and PA were coated with titanium nitride by magnetron sputtering in a nitrogen atmosphere. The crystal structure of the coatings could be controlled to be a fine columnar crystalline structure by increasing controlling the target power and radio frequency voltage [47].

Film adhesion and stress in deposited films are especially important for non-rigid substrates, such as elastomeric rubber. Tashlykov has deposited films onto rubber plates by self sputtering. In this case a resonance vacuum ion source was used to coat rubber plates with titanium, chrome, zirconium, molybdenum, and tungsten [42]. It was found that in the first stage of coating, metal atoms penetrate deeply into the elastomer. It was found in this study that chrome, zirconium, and molybdenum had good adhesion, while titanium and tungsten exhibited poor adhesion. The adhesion performance was related to the presence of chemical or physical bonds across the interface, which indicates that the chemical nature of the metal in the interface region is an important factor in

adhesion. It was also found, in this study, that the metal coating formed a semi-periodic structure due to wrinkling of the deposited layer induced by the non-rigid surface [42].

Tashlykov performed a second study on the coating of rubber, this time using ion-beam assisted deposition to increase adhesion. Self-sputtering was again used to prevent the accumulation of atomic gas at the film interface. Chrome, zirconium, and molybdenum targets were used to coat rubber sheets which had a negative potential applied to them to accelerate the ions. In this case oxygen, carbon, hydrogen, and other trace elements diffused from the rubber and appeared in the film. The metal ions were found to penetrate deeply into the rubber surface. It was found in this study that metal atoms that formed complexes with oxygen at the interface yielded an increase in adhesion. These films were found to slightly increase the modulus of the rubber sheets and caused changes in the contact angle of water at the coated surface [25].

Rau has coated cross-linked polydimethylsiloxane (PDMS) by pulsed laser ablation deposition (PLAD). This method is a solvent-less process offering fast deposition rates and the capability to produce multi-layer composites. It also allows control of the etch-depth, lack of thermal damage adjacent to the site, and low energy densities. It was found that at high energy densities, there was large scale degradation of the polymers. At lower energy densities, the film was similar to the target. The deposition rate increased with the energy density, as would be expected. The deposition rate was greater at low pressures than high, possibly due to decreased scattering [23].

Calcium phosphate has also been coated onto flexible substrates of polyethylene (PE) and PDMS by radio frequency magnetron sputtering in argon by Feddes. Oxygen plasma pre-treatment was applied, followed by a soak in the oxygen atmosphere. In the case of PE, there is carbon-oxygen bonding that takes place, while the PDMS has an increase in silicon-oxygen bonding. These coatings were found to have good adhesion due to the formation of oxygen compounds at the surface [8].

Magnetron sputtering has been used to produce micro-scale particles of aluminum and copper in the range of 7 to 50 nm by Hahn, by sputtering at low pressures [67]. Farhat investigated the properties of nanocrystalline particles. As the diameter of particles of nickel and copper decrease in the nanometer range, the hardness is found to increase. In addition, the wear resistance of nanocrystalline aluminum was found to increase dramatically as the diameter was decreased in the nanometer range [60].

Schulte has investigated the magnetron sputtering of aluminum in argon and found that the sputtering rate is dependant upon the argon pressure only [54]. Aluminum has been coated onto copper, aluminum, austenitic stainless steel, and high strength steels with Argon as a sputtering gas by Muller to study the adhesion strength of the coating. It was found that the copper yields, a coating is very strong, with excellent adhesion [63].

An interesting application of aluminum sputtering was the coating of porous paper for use as a permeation barrier to oxygen by Chung. In this case, magnetron sputtering was used in argon to sputter aluminum onto untreated

porous paper. As the power density of deposition increases, the deposition rate increased linearly up to a limit, where if the power was increased, the paper was damaged. The permeation of oxygen was reduced some, but there was large-scale permeation through crevices, cracks, and pinholes in the coatings [18].

High rate deposition of copper has been achieved with high rate magnetron sputtering sources that used an unbalanced magnetron source with high current and low voltage by Boo. A field ion exchange grid with a negative potential between the copper and substrate increased the deposition rate by two to three times. This grid increased the density of the electrons and therefore the collision probability of electrons with neutral atoms, further ionizing the argon and copper, leading to higher flux [7].

CHAPTER 2

EXPERIMENTAL

2.1 Magnetron Sputtering

Magnetron sputtering is the most widely used variant of DC sputtering. DC sputtering is a physical vapor deposition process, meaning that the depositing atoms are liberated from the surface of the target material by physical means, rather than chemical processes or due to thermal effects. In the basic process of DC sputtering, atoms can be ejected or sputtered from solid materials at room temperature by bombardment of the target with energetic, positively charged ions. These sputtered atoms can then traverse a reduced pressure ambient and deposit on the substrate that is to be coated. The impinging atoms are generated in a gas plasma in the deposition chamber. A plasma is a quasineutral gas, composed of weakly ionized gases consisting of electrons, ions, neutral atoms and molecular species.

In magnetron sputtering, the sputtering gas plasma is magnetically confined such that secondary electrons emitted from the target are trapped in small spaces and yield higher local ionization. This leads to higher ion bombardment upon the target and a subsequently increased sputter rate at lower pressures than normal DC sputtering [69]. Since magnetron sputtering occurs at

low pressures (typically a few millitorr), the sputtered atoms fly-off in ballistic fashion to impinge on the substrate to be coated. This is accomplished, as the sputtered atoms avoid gas phase collisions and scattering. As such, this is a line of sight process, with high compressive stresses. Because the gas pressure is low in magnetron sputtering, the sputtered atoms are not scattered by the background gas. Appendix B contains a more extensive description of the process of magnetron sputtering.

For this research, the metallic coatings applied to the elastomeric substrates were applied by magnetron sputtering in a high-vacuum Argon atmosphere. By varying the sputtering source power and the pressure within the chamber, the sputtered particle size can be varied, as can the deposition rate. It was intended that some of the particles produced in the sputtering process implant some distance into the samples to improve the adhesion of the metallic coating.

2.2 Deposition Chamber

The basic configuration of the deposition chamber is shown in Illustration 1. The sample to be coated is mounted centrally in the deposition chamber facing the target, which is mounted to the magnetron sputtering unit. A vacuum pump is used to evacuate the chamber of contaminating gases and to reduce the pressure in the deposition chamber to the desired sputtering conditions. A deposition rate monitor was mounted in the chamber to allow for the measurement of the sputtering rate prior to deposition onto the test samples.

Illustrations 2 and 3 along with Table 4 schematically represent the deposition chamber configuration used in this research. The notable components within this system for this sputtering research are; the deposition chamber, secondary (sample-introduction) chamber, magnetron sputtering gun, sample linear-introducer, deposition rate monitor, pressure monitor, gas valves, shutter valves, and the turbo-pump.

The main chamber is a spherical stainless-steel vacuum chamber. The secondary chamber, magnetron sputtering gun, deposition rate monitor, pressure monitor, and gas valve were all attached to this chamber, as were several windows which allowed for observation of the deposition process. The distance from the magnetron to the sample was 12 cm. The secondary chamber is a spherical stainless-steel chamber attached to the main chamber by a shutter-valve. The linear introducer was attached to this chamber, with the ability to pass into the main chamber. The samples were attached to the linear introducer which could be accessed through the sample door. This configuration allowed for the main chamber to be sealed-off from the secondary chamber for sample changes, so that the entire chamber did not need to be reduced to a vacuum between every sample, but only the smaller secondary chamber.

The magnetron sputtering gun is an AJA International model A320-1035. This is an ultra-high vacuum sputtering source with internal-cooling, with a 2 inch target diameter. For this research, we used an RFPP RF55 radio-frequency power supply to control the wattage of the sputtering process. The deposition rate monitor is a Leybold Inficon XTM/2 deposition rate monitor. This system

utilizes the sensitivity of a piezoelectric quartz monitor crystal to the addition of mass. The Varian gas valve is a low-flow valve used to control the flow of Argon into the main chamber. Several pressure monitors were used on this chamber; a Granville Phillips 275 convectron pressure gauge, a MKS 627 baratron pressure gauge, and an Ion pressure gauge. The use of these three gauges allowed for monitoring of the pressure in the chamber from ambient down to 10^{-7} Torr. The vacuum pump used on this chamber is a Leybold Turbovac 361 with a Turbotronik NT-20. This pump allowed the chamber to be evacuated in approximately five minutes.

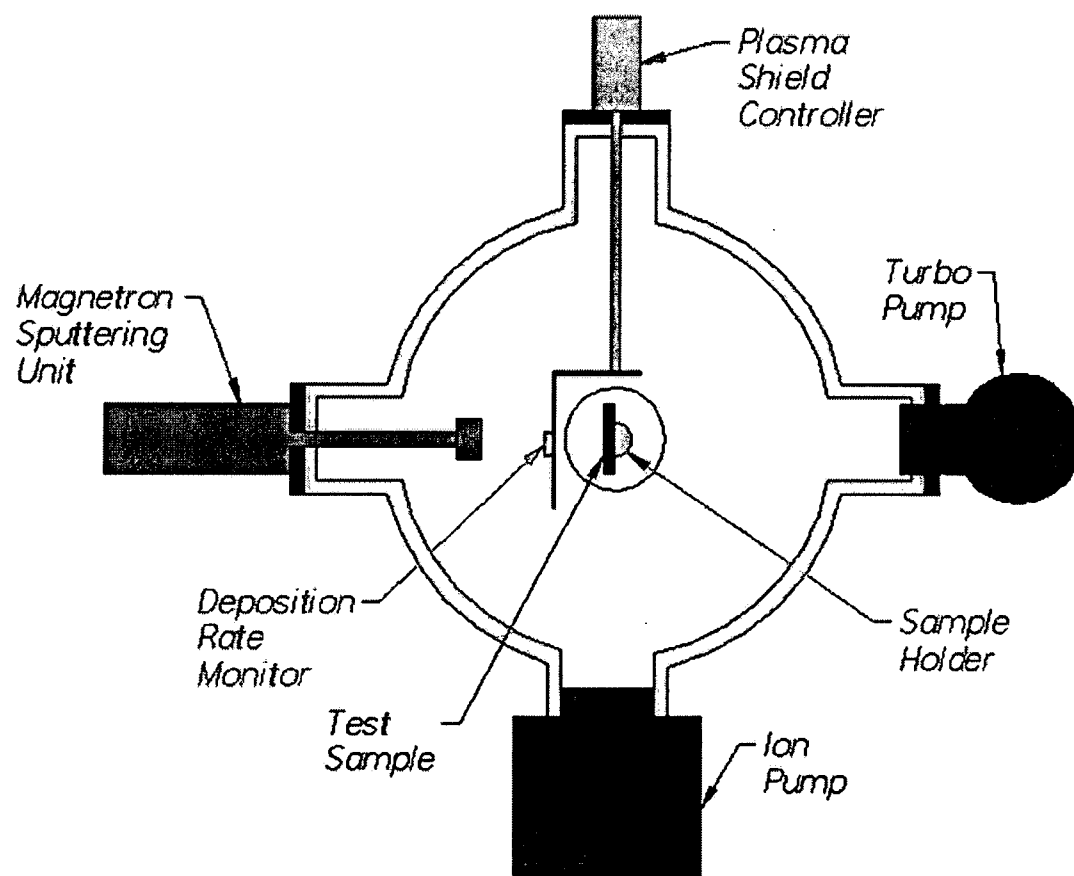


Illustration 1: Deposition Chamber Configuration

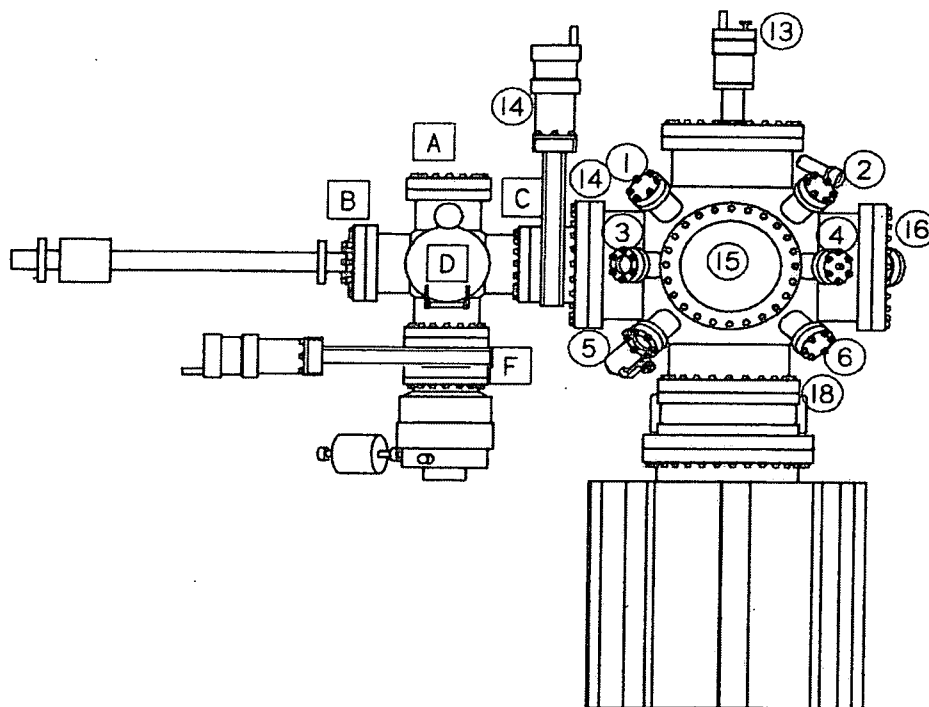


Illustration 2: Chamber Front View

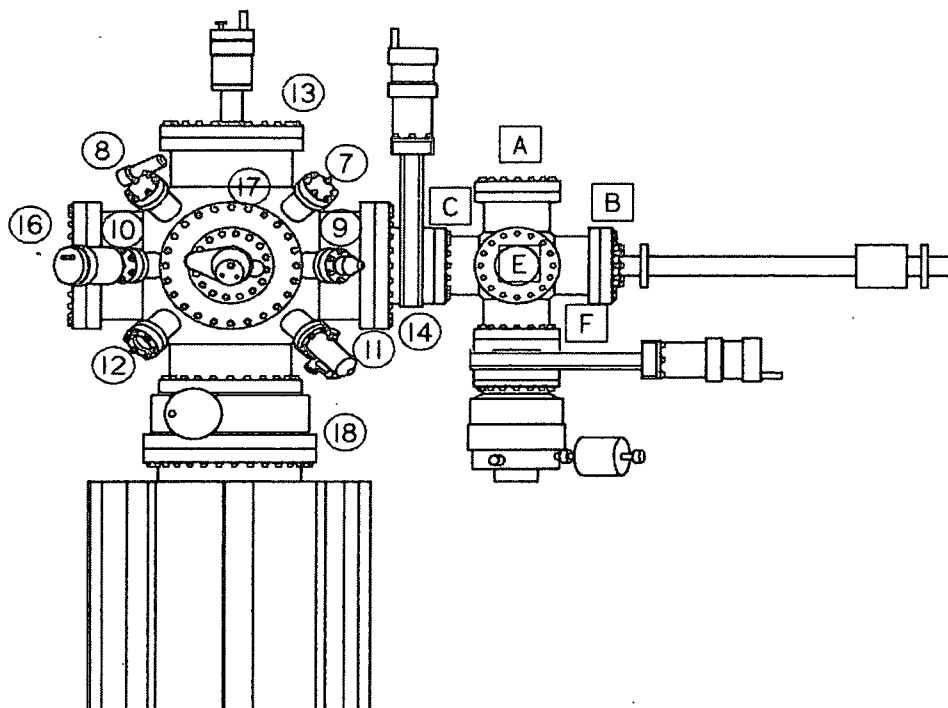


Illustration 3: Chamber Rear View

Table 4: Deposition Chamber Components

Main Chamber Components								
Loc.	Inch Size	Item Size	Description	Manufact.	Model No.	Instrument	Manufact	Model No.
1	3.5	3.5	Cap					
2	3.5	3.5	Cap					
3	3.5	3.5	Window					
4	3.5	3.5	BNC: Dep Rate Monitor	Inficon	NA	Dep. Rate Monitor	Inficon	XTM/2
5	3.5	3.5	Window					
6	3.5	3.5	Cap					
7	3.5	3.5	Cap					
8	3.5	3.5	Convectron Pressure Gauge	Granville Phillips	NA	Pressure Gauge	Granville Phillips	275
9	3.5	3.5	Ion Pressure Gauge	NA	NA			
10	3.5	3.5	Baritron Pressure Gauge	MKS	627	Pressure Gauge	MKS	PDR-C-2C
11	3.5	3.5	Gas Valve	Varian	NA	Argon		
12	3.5	3.5	Window					
13	10	3.5	Rotary Shutter	Huntington	VF-166			
14	10	8	Shutter – Sec. Chmbr	MDC	GV4000-M			
15	10	10	Window					
16	10	10	Window					
17	10	6	Magnetron Gun	AJA Intern.	A320-1035	RF Power Supply	RFPP	RF55
18	10	10	Shutter – Ion Pump	MDC	GV8000-M			
Secondary Chamber Components								
Loc.	Inch Size	Item Size	Description	Manufact.	Model No.	Instrument	Manufact	Model No.
A	6	6	Cap					
B	6	3.5	Linear Introducer	MDC				
C	6	6	Shutter - Main Chamber	MDC	GV4000-M			
D	6	6	Sample Door	MDC				
E	6	6	Window					
F	6	6	Shutter - Pump	MDC	GV4000-M			
			Turbo Pump	Leybold	Turbovac 361	Vacuum Pump	Turbo-tronik	NT-20

2.3 Sample Preparation

The basic deposition process of the production of these test samples was followed for each of these materials. Prior to being coated, the elastomeric samples were trimmed to fit the linear introducer fixture and then were wiped with toluene and isopropyl alcohol to ensure that they were no contaminants on the surface of them. After loading the sample into the chamber, the vacuum chamber was evacuated to 10^{-7} Torr using the Turbopump. The chamber was then filled with Argon through the gas valve to the chosen deposition pressure (10 to 30 mTorr). Next, the sample was sputter-coated at 200W. Internal water cooling was used in the magnetron gun. No external sample heating was applied. Deposition was carried out for five to ten minutes, depending upon the deposition rate of the sputtering material, as determined by testing of the deposition rate performed with the deposition rate monitor. The particular deposition time used was designed to yield a coating thickness of 100nm.

A full factorial design was chosen for the production of the test samples. As such, aluminum and copper were applied at 10, 20, and 30 mTorr on each of the three substrate materials. Titanium was not used to coat any of the substrate materials, as the deposition rate of this material was too low as to be practical, as described in the next section. Table 5 is a summary of the experimental variables for the production of these test samples. The energy of the sputtered atoms produced by this deposition process at 200 watts was approximately five to ten electron volts.

Table 5: Test Sample Production Variables

Target Material	Substrate Material	Deposition Time	Deposition Pressure
Aluminum	FKM	10min	10mTorr
			20mTorr
			30mTorr
Aluminum	FVMQ	10min	10mTorr
			20mTorr
			30mTorr
Aluminum	NBR	10min	10mTorr
			20mTorr
			30mTorr
Copper	FKM	7min	10mTorr
			20mTorr
			30mTorr
Copper	FVMQ	7min	10mTorr
			20mTorr
			30mTorr
Copper	NBR	7min	10mTorr
			20mTorr
			30mTorr

2.4 Determination of Sputtering Rates

High purity metallic samples were used for all of the sputtering targets. The specific targets used for this research are listed in Table 6. The sputtering rate is different for each of these materials, due to differences in the binding energy of each of the target materials and due to differences in the energy transfer ratio for each target material. The energy transfer efficiency can be calculated from the masses of the impinging and target atoms as described in equation 24. When the ions are impinging directly (0°), the cosine term goes to one. Under this condition of perpendicular impingement, the sputtering ratios for

these targets were calculated to be 96%, 98%, and 99% for aluminum, copper, and titanium respectively.

$$\frac{E_r}{E_o} = \frac{4 \cdot m_1 \cdot m_2}{(m_1 + m_2)^2} \cdot \cos^2 \theta \quad (24)$$

The threshold energy, E_{th} , is the minimum energy that is required to be transferred into a target atom for it to overcome the forces that are binding it in place and allow it to sputter from the surface. This energy is dependent upon the incident ion, and the mass and atomic number of the target atoms. However, the most important factor in sputtering energy requirements is the binding energy of the atoms to the surface (U_s). The binding energy of a material may be measured by its heat of vaporization. The heat of vaporization for these materials are 293.4, 300.3, and 421.0 kJ/mol for aluminum, copper, and titanium. A simple approximation for the threshold energy of sputtering (E_{th}) is to multiply the heat of vaporization by four, yielding threshold energies of 12.2, 12.4, and 17.5eV for aluminum, copper, and titanium respectively. This correlates well with measured values for the Argon threshold for sputtering of these materials: 13eV for aluminum, 17eV for copper, and 20eV for titanium [26]. This indicates titanium will require much higher energies for sputtering to occur with Argon.

The sputtering rate for each of the metals was determined by the use of a Leybold inficon XTM/2 deposition rate monitor. This system utilizes the sensitivity of a piezoelectric quartz monitor crystal to the addition of mass to its surface. At the proper frequency, an applied voltage will induce a resonance in the crystal. As mass is added to the crystal face, this resonance frequency

decreases. If the mass and density of the coating material is known, the deposition rate can then be calculated using equation 25.

$$T_f = \left(\frac{N_{at} d_q}{\pi d_f F_c (d_q u_q / d_f u_f)} \right) \arctan \left(\left(\frac{d_q u_q}{d_f u_f} \right) \left[\frac{1}{2} \tan \left(\frac{\pi (F_q - F_c)}{F_q} \right) \right] \right) \quad (25)$$

Where: T_f = thickness of the coating

N_{at} = 166100Hz cm (the frequency constant of AT cut quartz)

d_q = 2.649 gm/cm³ (density of single crystal quartz)

d_f = density of the film

F_c = frequency of the coated quartz crystal

F_q = frequency of the uncoated quartz crystal

u_q = shear modulus of the quartz crystal

u_f = shear modulus of the coating material

Table 8 along with Illustration 4 summarizes the deposition rate information for each of the coating materials. The general trend of all of the materials is that deposition rate increases with decreasing pressures. Obviously, the pressure can not be decreased to the point where the plasma can not be sustained. As such, 10 mTorr was chosen as the practical lower limit for sputtering. As can be seen, the average deposition rates for the aluminum and copper samples were measured to be 10.73 and 16.78 nm/min. The titanium only had a deposition rate of 0.75 nm/min. These values correlate well with the published data for sputtering yields of these materials with Argon. At 0.5keV, Argon has been shown to have sputtering ratios of; 1.05 for aluminum, 2.35 for copper, and 0.51 for titanium. Because the deposition rate of titanium was so

low, the decision was made to produce samples only with aluminum and copper. Based on this information, the aluminum targets were used to deposit films for ten minutes, and the copper deposition was performed for seven minutes. The predicted film thicknesses for these conditions are summarized in Table 7.

Table 6: Sputtering Target Information

Material	Supplier	Stock Number	Lot Number	Target Size	Purity
Aluminum	Electronic Space Products	knc6552	X3204	2" dia x .205" thk	5N
Copper	Electronic Space Products	knc5892	Q2781	2" dia x .250" thk	4N
Titanium	AJA International	N/A	93-6067/01	2" dia x .250" thk	99.995

Table 7: Predicted Film Thickness

Pressure	Aluminum	Copper
10 mTorr	90 nm	134 nm
20 mTorr	120 nm	101 nm
30 mTorr	94 nm	72 nm

Table 8: Target Deposition Rates

Measured Deposition Rates					
Aluminum					
Pressure (mTorr)	Thickness (Å)	Time (sec)	Rate (A/sec)	Rate (A/min)	Rate (nm/min)
10	449.2	300	1.497	89.84	8.98
20	601.0	300	2.003	120.20	12.02
30	472.3	300	1.574	94.46	9.45
Average:					10.73
minutes for 100 nm					9.32
Copper					
Pressure (mTorr)	Thickness (Å)	Time (sec)	Rate (A/sec)	Rate (A/min)	Rate (nm/min)
10	955.8	300	3.186	191.16	19.12
20	722.0	300	2.407	144.40	14.44
30	514.4	300	1.715	102.88	10.29
Average:					16.78
minutes for 100 nm					5.96
Titanium					
Pressure (mTorr)	Thickness (Å)	Time (sec)	Rate (A/sec)	Rate (A/min)	Rate (nm/min)
5	53.5	300	0.178	10.70	1.07
10	33.8	300	0.113	6.75	0.68
20	25.9	300	0.086	5.18	0.52
30	19.4	300	0.065	3.88	0.39
Average:					0.75
minutes for 100 nm					132.57

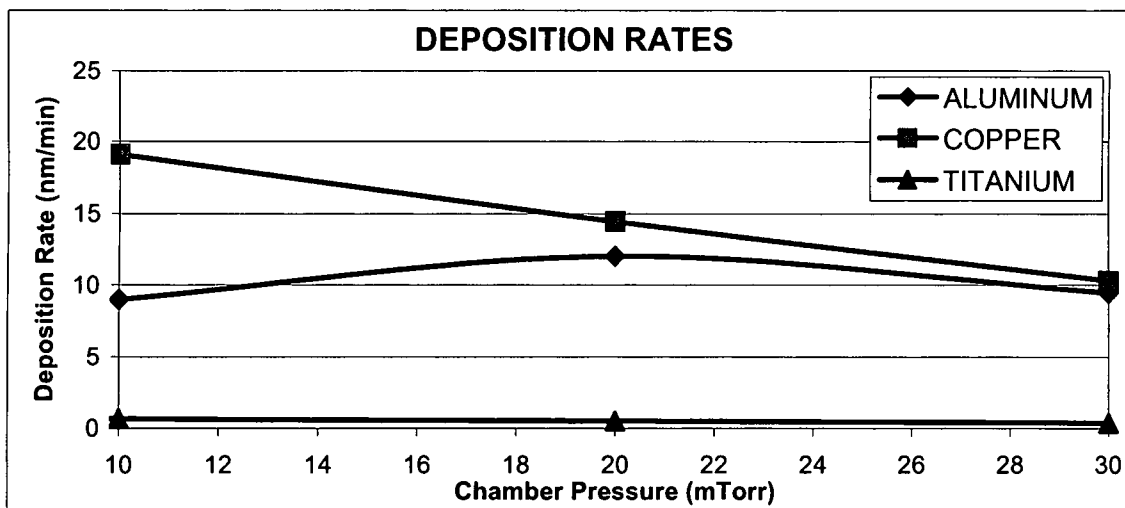


Illustration 4: Deposition Rates

2.5 Test Sample Substrates

The substrates chosen for this experiment were fluorocarbon rubber (FKM), fluorosilicone rubber (FVMQ), and nitrile butadiene rubber (NBR). All three of these materials are currently used for various fuel-system applications and all are inherently resistant to degradation by exposure to the fuels currently being used. These materials are summarized in Table 9. FKM is currently the best material available for fuel-system applications, and possesses excellent fuel-permeation resistance. It was chosen for this research as the control material against which to measure the other candidate materials. Both FVMQ and NBR have good resistance to chemical degradation from fuels, but both have poor swelling characteristics and fuel permeation resistance as compared to FKM.

Chemically, NBR and FKM are both hydrocarbon materials with traditional carbon backbones. NBR is a copolymer composed of acrylonitrile and butadiene monomers. The butadiene sections have a high degree of unsaturation, which allows for cross-linking of the elastomer and provide flexibility to the polymer backbone. The acrylonitrile units with their nitrogen atoms repel hydrocarbon liquids and thusly impart solvent resistance at the expense of elasticity, while the butadiene component attracts chemically similar hydrocarbons. The material used in this research has approximately 38% acrylonitrile content. In the case of FKM, fluorine atoms replace many of the hydrocarbon atoms of a traditional hydrocarbon. In general, the higher the fluorine content of these materials, the better the fuel permeation resistance of the polymer. The particular material

used in this research is a GF-type material, composed of a terpolymer of vinylidene fluoride (VF2), hexafluoropropene (HFP), and TFE (trifluoroethylene). This material has approximately 70% fluorine replacement of hydrogen in the polymer structure. FVMQ is a polymer with a silicon-oxygen backbone. This type of polymer has much higher flexibility than traditional carbon-carbon type elastomers. In the case of FVMQ, fluorine-containing trifluoropropyl side-groups are used to replace some of the methyl groups in the polymer to increase the solvent resistance of these materials.

Table 9: Test Sample Substrates

TYPE	LAB #	PROD #	LAB CODE	HARDNESS	S.G.
FKM	VL1502T39	8-15-370	28245	84	1.898
	$\left[\left(\text{CH}_2 - \text{CF}_2 \right)_x \left(\text{C} \begin{array}{c} \text{F} \\ \\ \text{CF}_3 \end{array} - \text{CF}_2 \right)_y \right]_n$				
FVMQ	VL1401M247	8-14-134	27937	57	1.540
	$\left[\left(\text{Si} \begin{array}{c} \text{CF}_3\text{CH}_2\text{CH}_2 \\ \end{array} - \text{O} \right)_x \left(\text{Si} \begin{array}{c} \text{CH}_3 \\ \\ \text{CH}_3 \end{array} - \text{O} \right)_y \right]_n$				
NBR	VL104Z6	8-01-394	25309	70	1.197
	$\left[\left(\text{CH}_2 - \text{CH} = \text{CH} - \text{CH}_2 \right)_x \left(\text{CH}_2 - \text{CH} \begin{array}{c} \text{CN} \\ \end{array} \right)_y \right]_n$				

2.6 Coating Evaluation

The effectiveness of these coatings was evaluated for a number of properties. To evaluate the adhesion and flexibility of the coating, they were evaluated by visual observation of the coating and mechanical evaluation of the coated and uncoated samples. To evaluate the effectiveness of this coating for permeation reduction, they were evaluated in by permeation and swell-testing. Permeation testing followed by IR analysis of the solvents before and after permeation was used to evaluate these coated membranes for their viability as pervaporation barriers.

2.6.1 Visual Observation of the Coatings

The coated and uncoated samples were evaluated by visual inspection. These evaluations were performed using both microscopic methods and with SEM. Visual observation was used to determine the bulk coating properties and the uniformity of the coverage of the samples. The SEM was used for determining the micro-scale grain size, shape and uniformity and for measurement the grain size of the coated metallic layers. SEM was also used for measurement of the grain boundary size separating the agglomerates, measurement of the coating thickness, and for observation of any implantation of metallic molecules into the sample substrate.

2.6.2 Mechanical Evaluation

To evaluate the adhesion of the coating to the substrate, the coating coated samples were stretched 35%, by wrapping the samples around a 10.8mm mandrel and evaluating the coatings for delamination and coating failure. Visual observation of the samples under magnification before, during, and after testing was used to evaluate the adhesive properties of the coatings. To determine if the metallic coating increased the stiffness of the composite material, mechanical testing of the samples was performed by tensile-testing of the coated and uncoated samples. All of the samples were stretched to 50% elongation in an Instron tensile tester, using an ASTM D638-5 tensile bar. From this testing, the elastic modulus was calculated. The change in stiffness caused by the addition of the metallic layer was calculated to determine if the elastic properties of the composite material were still acceptable to be used in sealing and flexible hose applications.

2.6.3 Permeation Evaluation

The standard ASTM test fluid for the testing of elastomers for use in exposure to gasoline and for permeation is ASTM test fuel C. Test fuel C is composed of a 50/50 volumetric blend of toluene and isooctane. To evaluate the improvement of the fuel permeation resistance of the coated samples versus the uncoated samples, a modified version of ASTM D814, which is the measurement method of the permeation of volatile liquids through elastomeric materials. In this method, the mass of fuel permeating through a membrane of known exposed

diameter and thickness is measured over time. Illustration 5 depicts the design of the permeation cup design, with full dimensions for the permeation cup in Appendix B. For this testing, a metallic screen is incorporated into the lid to keep the material from ballooning when it swelled, thus increasing the surface area. The exposed diameter of the membrane used in this testing was 5.1 cm, yielding an exposed surface area of 20.27 cm². The samples were tested with the metallic coating surface facing the test fuel in the chamber, so that the fuel must pass through the coating prior to entering the substrate elastomeric material.

To measure the permeation rate through the test samples, the permeation test cup was weighed with the liquid and the membrane in place prior to the start of the permeation period and the periodically as permeation occurred. From the change in weight as compared to the original weight of the permeation cup over time, the permeation rate (Q) was calculated using equation 26. This yields the permeation rate from the start of the test, which is the normally reported permeation rate. Another means of evaluating the permeation rate is the permeation rate between data points, as shown in equation 27. This method calculates the permeation rate over time between subsequent data points. The value of this testing is that it provides information on how the permeation rate changes as the testing progresses. These test samples were also weighed before and after exposure to the permeating fuel for calculation of the amount of swelling (S) that occurred in the test samples, as shown in equation 28.

$$Q_{st} = \frac{w_t - w_0}{t * A} \quad (26)$$

Where: Q = Permeation rate (mg/(m²*sec))

w_t = Weight of the permeation cup at time t (g)

w₀ = Weight of cup assembly prior to permeation (g)

t = Permeation time (sec)

A = Cross-sectional area of the membrane (m²)

$$Q_{bp} = \frac{w_t - w_{(t-1)}}{t * A} \quad (27)$$

Where: Q_{bp} = Permeation rate (mg/(m²*sec))

w_(t-1) = Weight of permeation cup at time t-1 (g)

$$S = \frac{w_f - w_0}{w_0} \quad (28)$$

Where: S = Swelling (%)

w_f = Final weight of test sample after permeation (g)

w₀ = Original weight of the test sample (g)

To determine if pervaporation is occurring in these samples, infra-red analysis was performed on test fuel C, which is composed of a 50/50 blend of toluene and isooctane before permeation and on the remaining test fluid after permeation through an NBR membrane with copper coating. By comparing these spectra to neat toluene and isooctane spectra, the change in the fuel composition was determined and from this the separation factor for the composite membrane was determined. Additionally to evaluate the pervaporation properties of these coated membranes, permeation testing was

performed on NBR and FVMQ samples coated with copper in toluene and isooctane separately. From this, the separate permeation rate for these solvents was calculated and this information was used to calculate the idealized separation parameters, for these membranes, was determined.

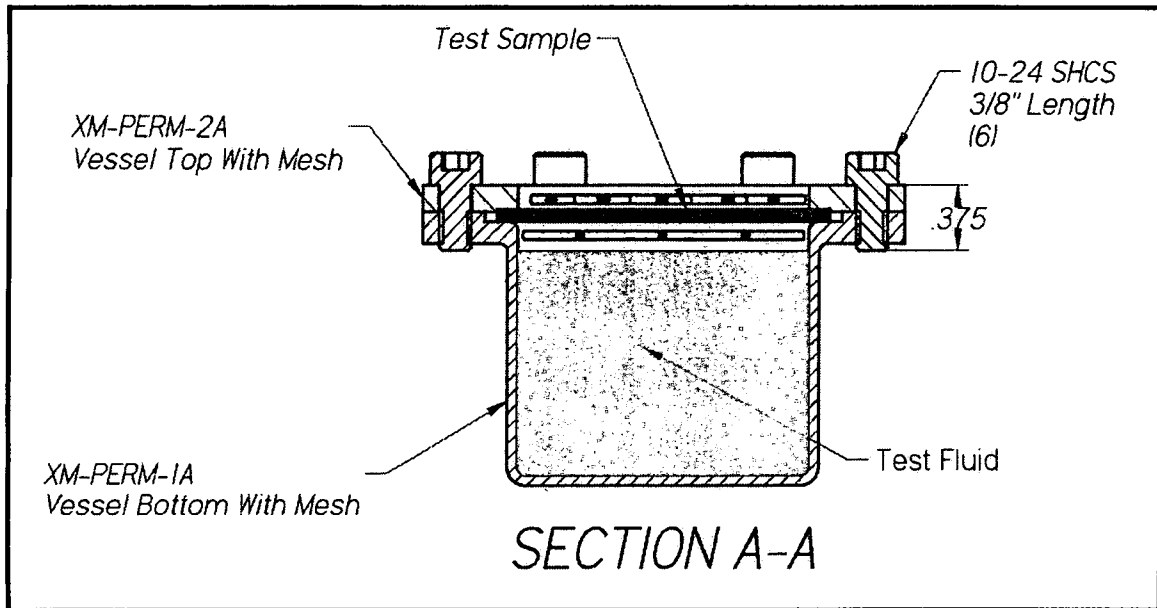


Illustration 5: Permeation Cup Assembly

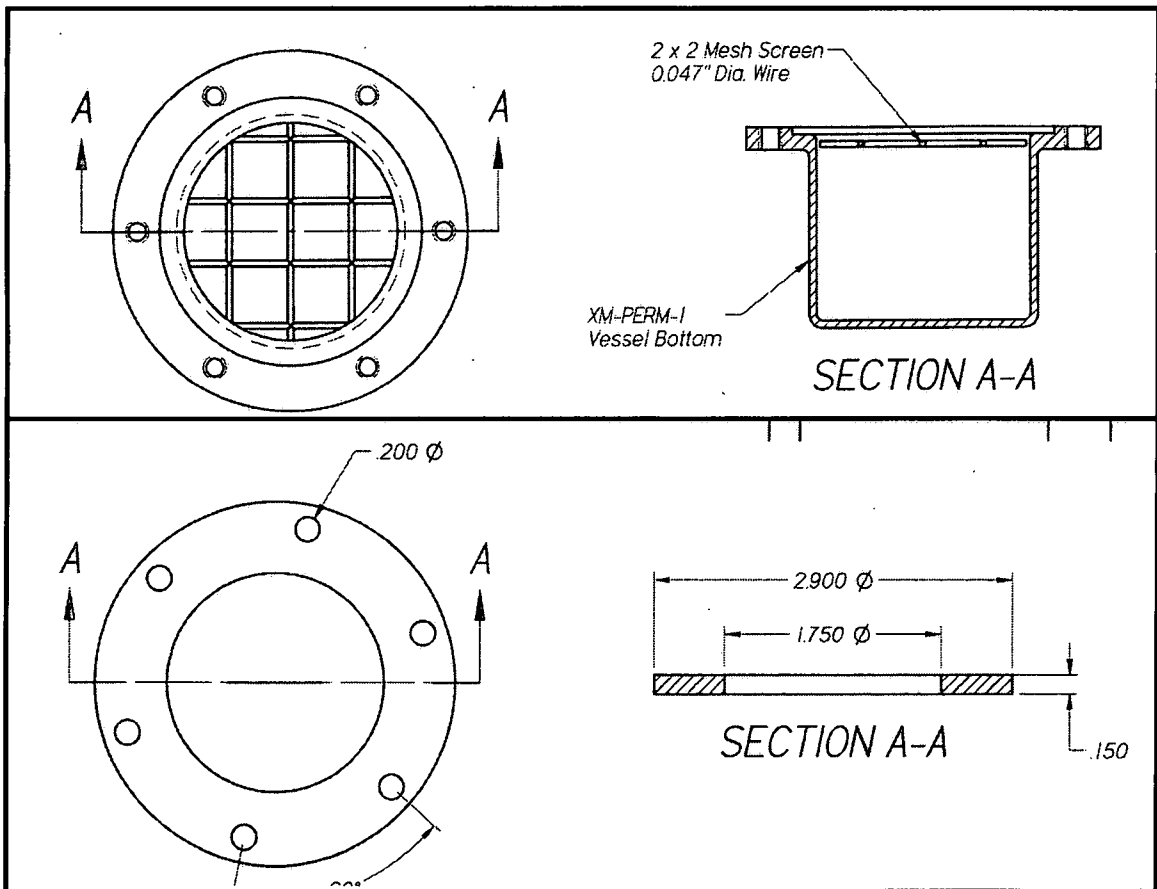


Illustration 6: Permeation Cup Design

CHAPTER 3

RESULTS AND DISCUSSION

3.1 Visual Observation of the Coatings

3.1.1 Microscopic Observation of the Coatings

The samples as observed under 30X magnification had notable differences in their physical appearance depending upon the sample substrate and sputtered materials. Most noticeable were the changes due to the substrate. The fluorosilicone samples appeared to have a very thin, porous coating as compared to the nitrile coatings, which appeared to have significantly more coverage, and the fluorocarbon samples looked to have complete coverage.

Illustrations 7 through 9 are 30X photographs of the FVMQ samples. As can be seen for these samples, there was some porosity present in both the aluminum and copper coated samples. The copper coating looked to be much thicker than the aluminum coating with much fuller coverage, having long-range order. This coating seems to be a cohesive coating with a large percentage of area covered. There are large grains in this coating with thin grain boundaries surrounding these large grains. The aluminum did not provide uniform and complete coverage, as the orange pigment of the FVMQ material showed

through the coating and there was no metallic reflection as in the copper samples. In general, it looked like a light inhomogeneous powder of coating has been applied to the samples in the aluminum coating with no long-range structure. Again, these appear to be separate particles that have been deposited. On a macro scale, visibly the copper coating was a dense black color. Microscopically, the copper coating had distinct grains with large grain boundaries with these grains being much larger than the aluminum grains. The copper grains appeared to be approximately 0.15 mm in diameter, versus 0.01 mm for the aluminum.

As can be seen in illustrations 10 through 12, both the aluminum and copper coatings on the NBR form a distinct, cohesive layer on the polymer surface. In this case (as with the FVMQ) the copper coating looked as though it had a much larger grain structure (approximately 0.1 mm), than the aluminum, which was composed of very small, distinct grains (approximately 0.01 mm). The copper coating again appeared to be a dense sheet of coating with large grains surrounded by thin grain boundaries. As with the FVMQ sample, the aluminum coating appeared to be composed of a thin inhomogeneous powder coat with no long-range structure.

For the FKM (illustrations 13 through 15), there was full coverage with both the aluminum and the copper. Again, the grains appeared larger in the copper coating (up to 0.3 mm) than the aluminum (approximately 0.05 mm). The coating appeared thicker and more complete in the FKM samples than in the case of either the nitrile or the copper. For the FKM, the aluminum coating did

not appear to be a powdery coating, but instead appeared to be a homogeneous film. However, it appears that this was a very thin coating, as the underlying structure of the FKM was still visible in these photographs. There was no visible porosity in the FKM coatings for either the aluminum or copper coatings.

For the aluminum coatings on all of the substrates, the coating is thin, with very small particles on the surfaces. These particles do not appear to have any interaction with each other, indicating that the permeation through these coating would be inferior to the copper coatings. The copper coatings were complete for all of the materials, with large grains. There were some grains in the FKM that were so large, that they appeared to be metallic inclusions. These particles were so large as to no longer be considered nanoparticles. As such, the copper coating would be expected to have much better fuel permeation resistance, but would be more likely to have some mechanical effects on the elastomeric substrate which could compromise the functional attributes of elastomeric parts with this coating.

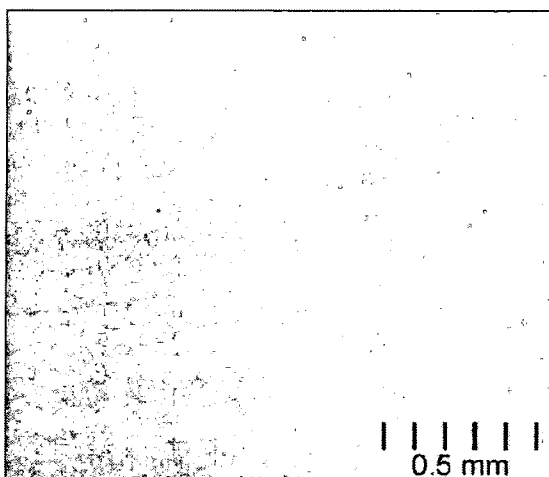


Illustration 7: FVMQ Uncoated

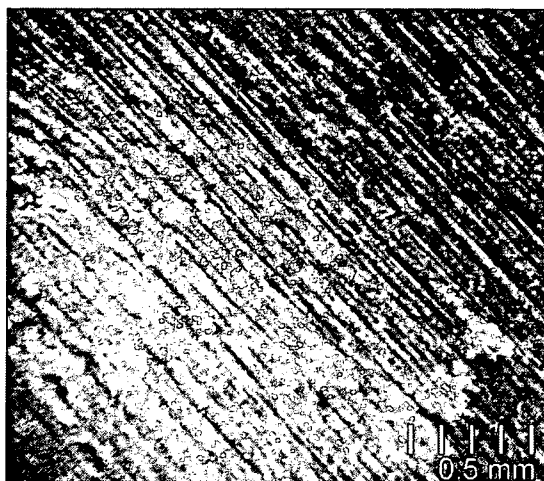


Illustration 10: NBR Uncoated

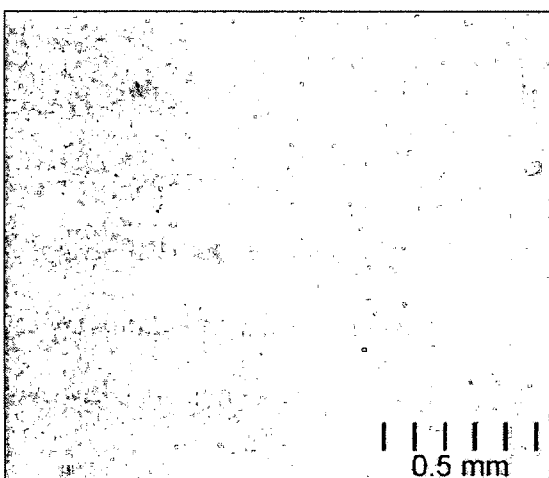


Illustration 8: FVMQ w/ Aluminum

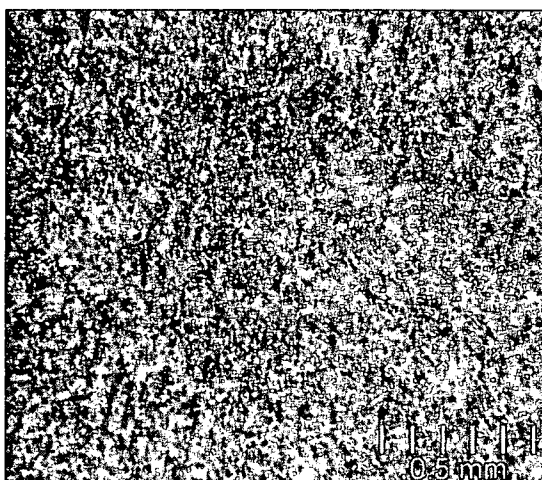


Illustration 11: NBR w/ Aluminum

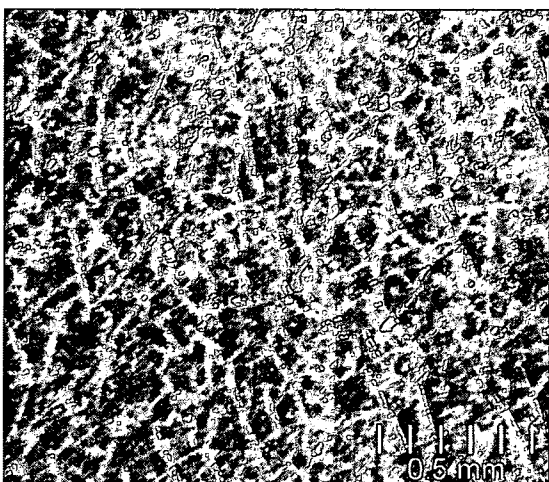


Illustration 9: FVMQ w/ Copper

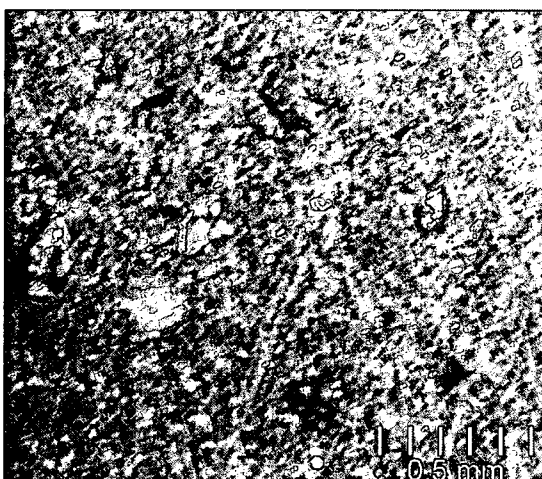


Illustration 12: NBR w/ Copper

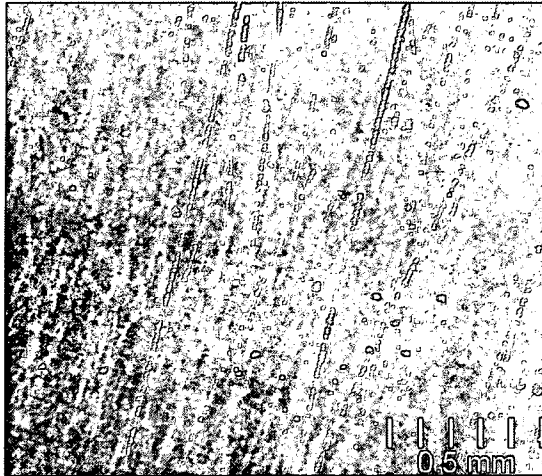


Illustration 13: FKM Uncoated

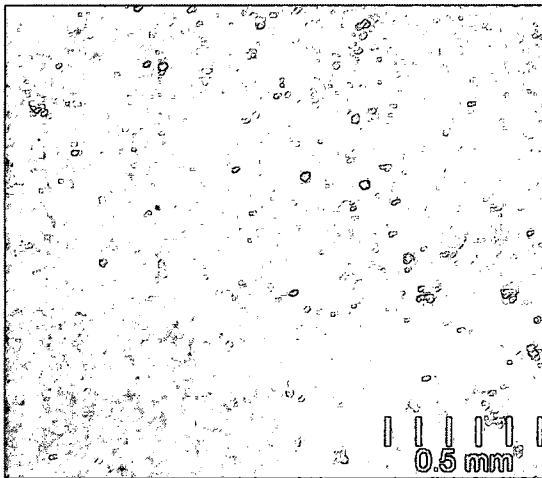


Illustration 14: FKM w/ Aluminum

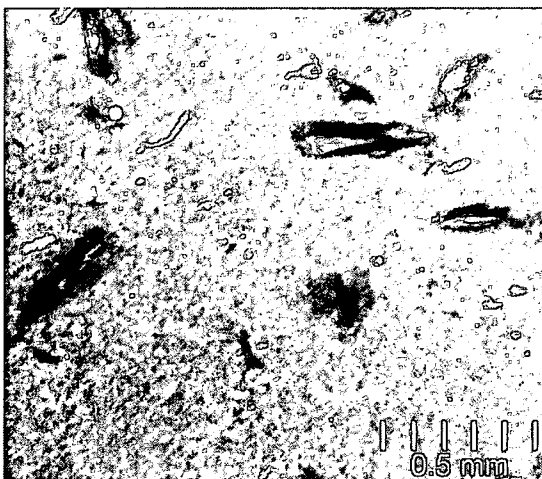


Illustration 15: FKM w/ Copper

3.1.2 SEM Observation of the Coatings

Illustrations 16 through 34 are SEM pictures of the aluminum coated samples. All of the materials exhibited some level of porosity and cracking at the surface. In addition, there was a lot of implantation of the metallic atoms into the substrate material, with the penetration in some cases nearing 100 μm .

For the planar FVMQ samples (illustrations 16 through 17), there were a great deal of small grains in the material with regions devoid of the aluminum coating where potentially permeation can occur unhindered. The grains in this case appear to be in the 1 to 3 μm range. The boundary gaps between the grains are up to 1 μm wide and extend throughout the coating. The estimated coverage for this coating is approximately 70% at the sample surface. The FVMQ side view pictures (illustrations 18 and 19) show the interpenetration of the aluminum atoms into the surface of the FVMQ, indicating that aluminum atoms were implanted into the substrate. Obviously, the aluminum particles could not form a cohesive boundary layer to prevent diffusion in this condition as the permeating species can merely travel around the aluminum atoms to get through the material. This layer of interpenetration is approximately 35 to 50 μm .

In the case of the NBR samples forward view (illustrations 21 through 24), the aluminum coating has a grainy structure with large areas lacking in coverage. However, the coating grains are much larger in the NBR samples than in the FVMQ samples and the regions between the grains are much smaller. The individual grains are in the 30 to 80 μm range with the boundaries being less than

10 μm wide. The coverage area on the surface of the NBR is approximately 40%. As can be seen from the NBR side-view pictures (illustrations 25 through 27), there is no evidence that the aluminum atoms penetrated into the NBR surface, and the samples have the appearance that the aluminum has formed a very thin layer on the surface of the material. In fact, the aluminum coating on the surface was so thin that it could not be measured. It seems most likely that most of the aluminum atoms have passed into the NBR surface, but this was not visible in these pictures. It is theorized that this lack of visualization is due to these atoms being so widely dispersed in the substrate that they are not visible here.

The aluminum coating on the FKM, as shown in illustrations 28 through 31, is a very consistent, cohesive coating that does not appear to be grainy or disperse. There are some small pores (less than 2 μm) in what appears to be a single uniform layer, but even with these pores, the coating area for the aluminum on FKM is greater than 95%. In the FKM side view pictures (illustrations 32 through 34), the distinct aluminum layer on the FKM substrate can be seen. The thickness of this layer is between 3 and 8 μm . There is very little visible penetration of aluminum particles into the substrate of the FKM material. Without any implantation, the coating produced on the FKM samples would be expected to be the least adhered. If it is well adhered, this cohesive coating on the surface would also be expected to induce more stiffening than the dispersed particles present on the FVMQ and NBR samples.

From these SEM pictures, it can be seen that the coatings applied to these substrates are quite different, even though the same sputtering techniques and target materials were used to create all of the coatings. Obviously, the nature of the substrate is dramatically affecting the coatings applied to them. This seems to be due to the implantation of the metallic particles into the FVMQ and NBR substrates, which prevent the formation of a homogeneous coating upon the surface of these materials.

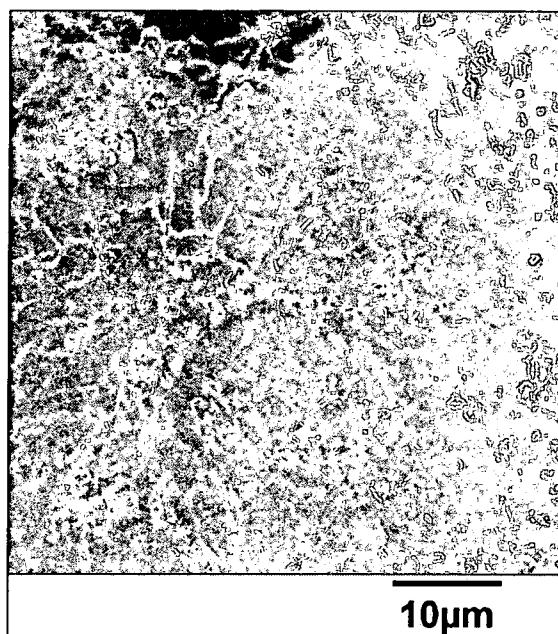
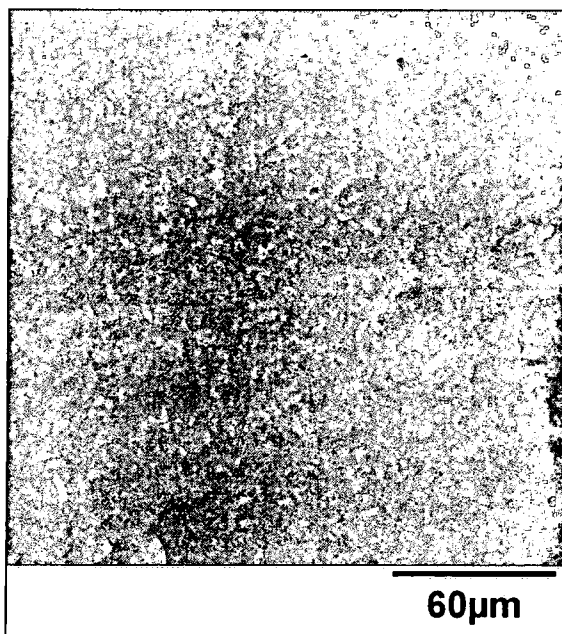


Illustration 16: FVMQ: 500X-PLANAR Illustration 17: FVMQ: 2000X-PLANAR

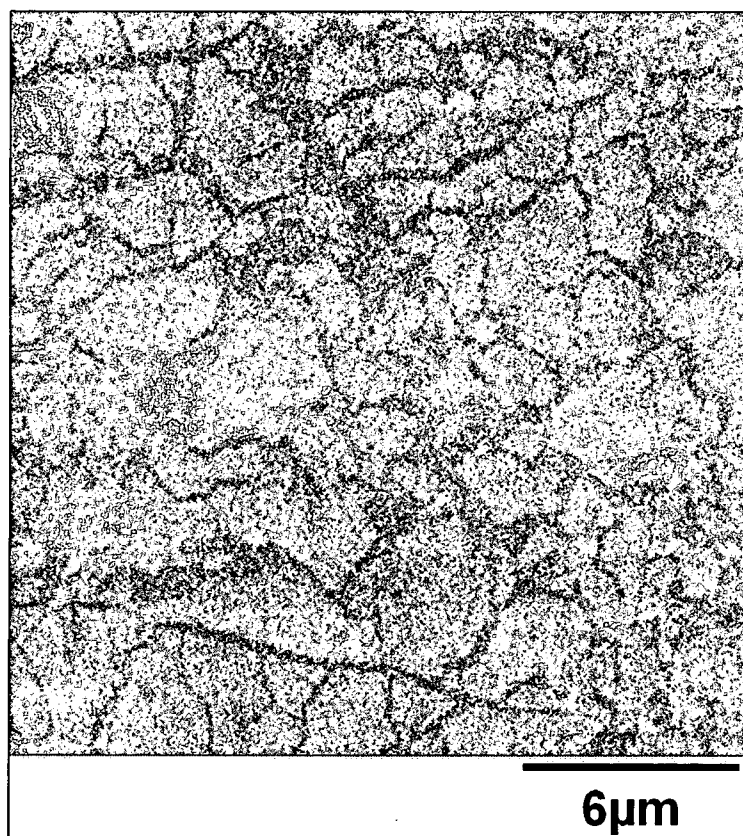


Illustration 18: FVMQ: 5000X – PLANAR VIEW

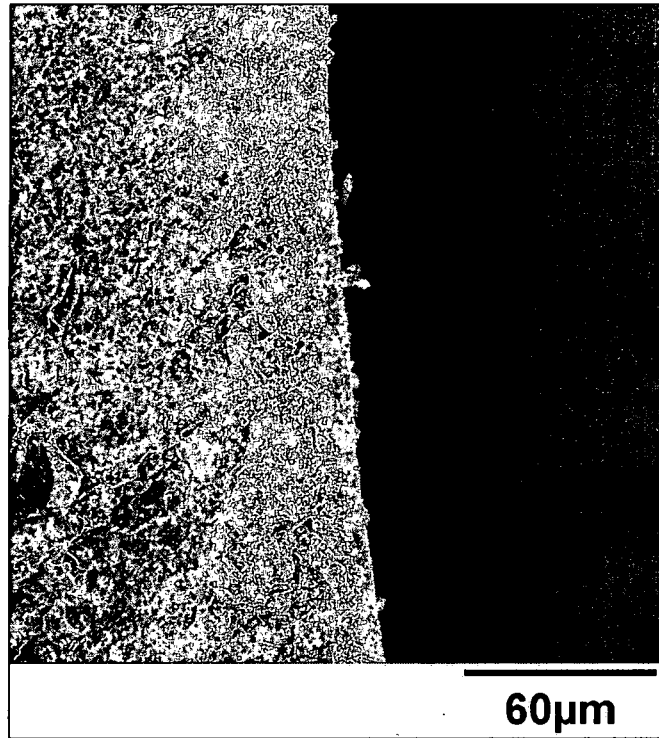


Illustration 19: FVMQ: 500X – SIDE VIEW

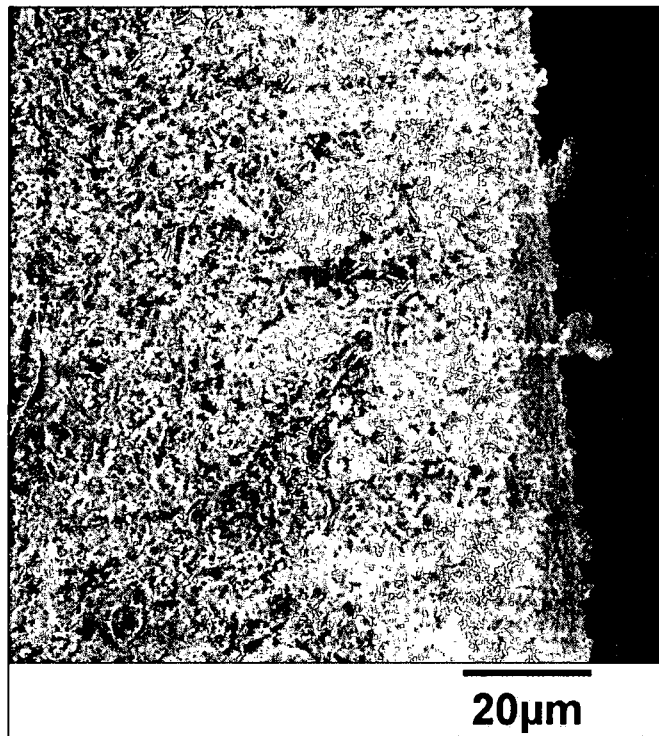


Illustration 20: FVMQ: 1000X – SIDE VIEW

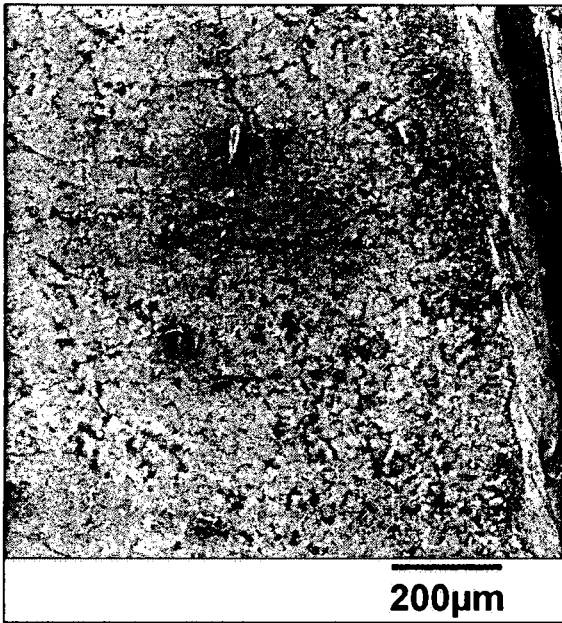


Illustration 21: NBR: 100X-PLANAR

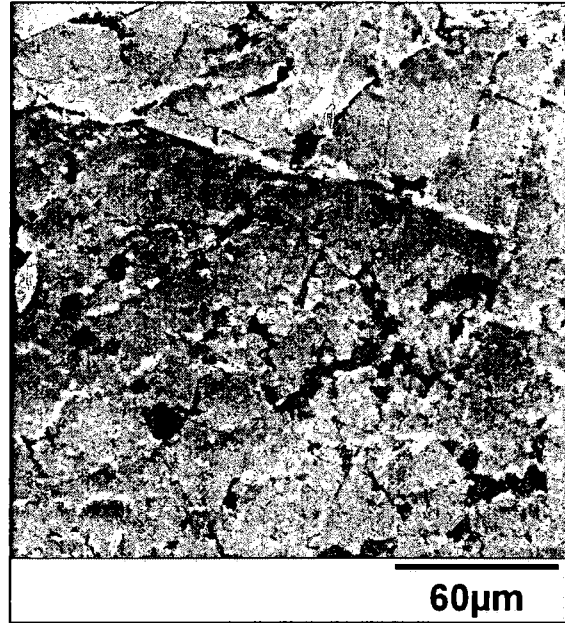


Illustration 22: NBR: 500X-PLANAR



Illustration 23: NBR: 2000X-PLANAR



Illustration 24: NBR: 5000X-PLANAR



Illustration 25: NBR: 100X-SIDE VIEW Illustration 26: NBR: 500X-SIDE VIEW

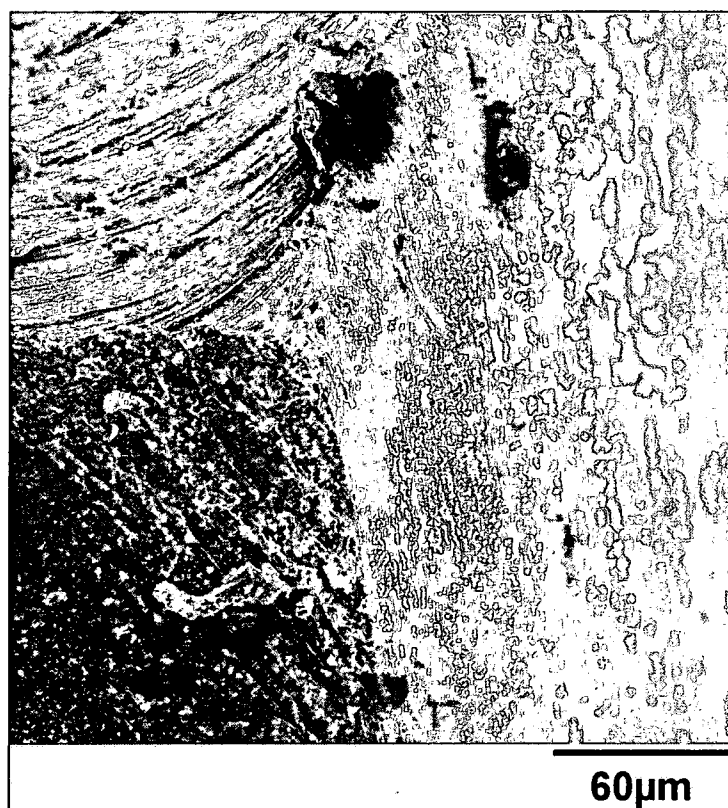


Illustration 27: NBR: 500X – 3 CORNERS

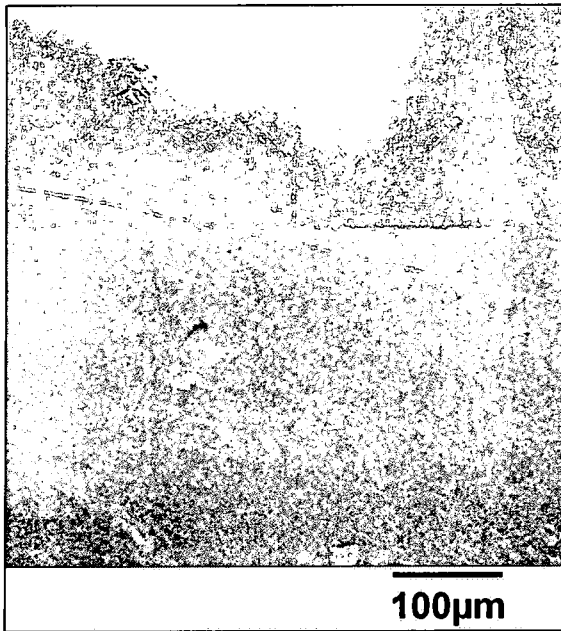


Illustration 28: FKM: 200X-PLANAR

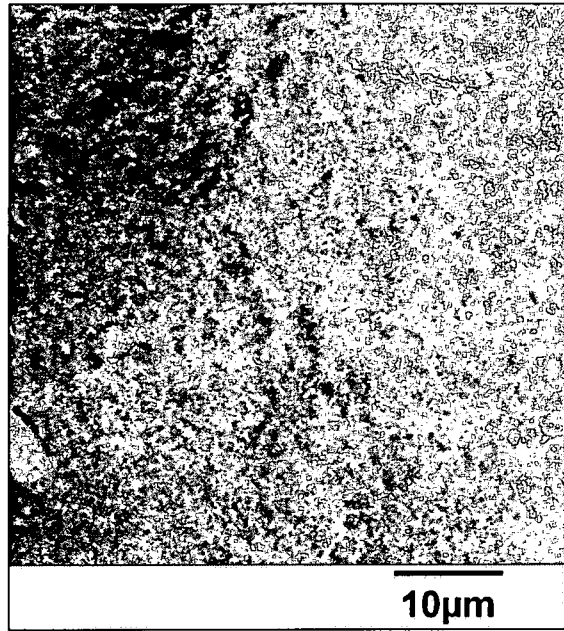


Illustration 29: FKM: 2000X-PLANAR

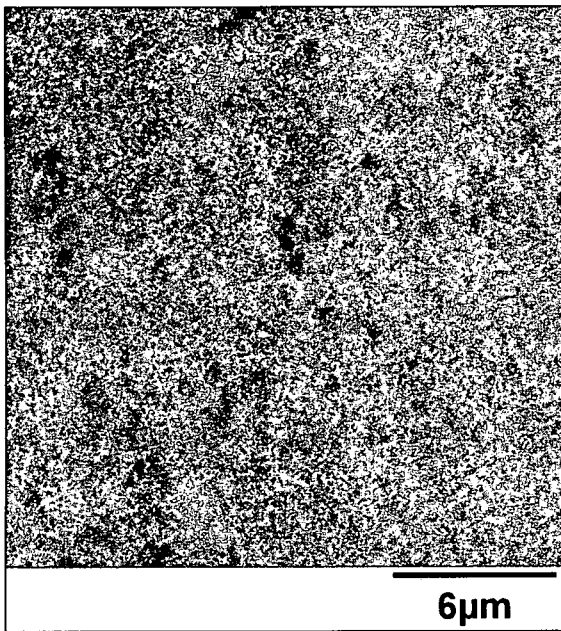


Illustration 30: FKM: 5000X-PLANAR



Illustration 31: FKM: 100X-SIDE VIEW

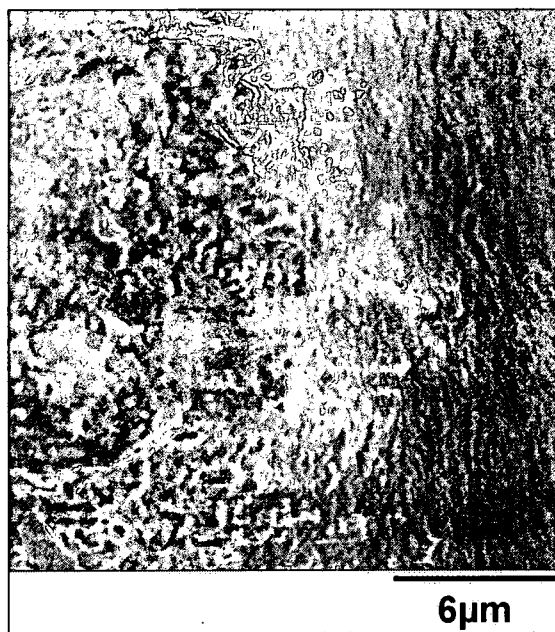
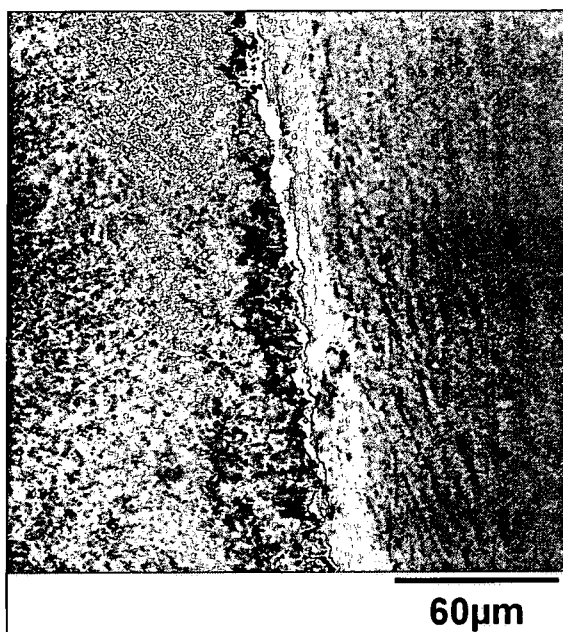


Illustration 32: FKM: 500X-SIDE VIEW Illustration 33: FKM 5000X-SIDE VIEW

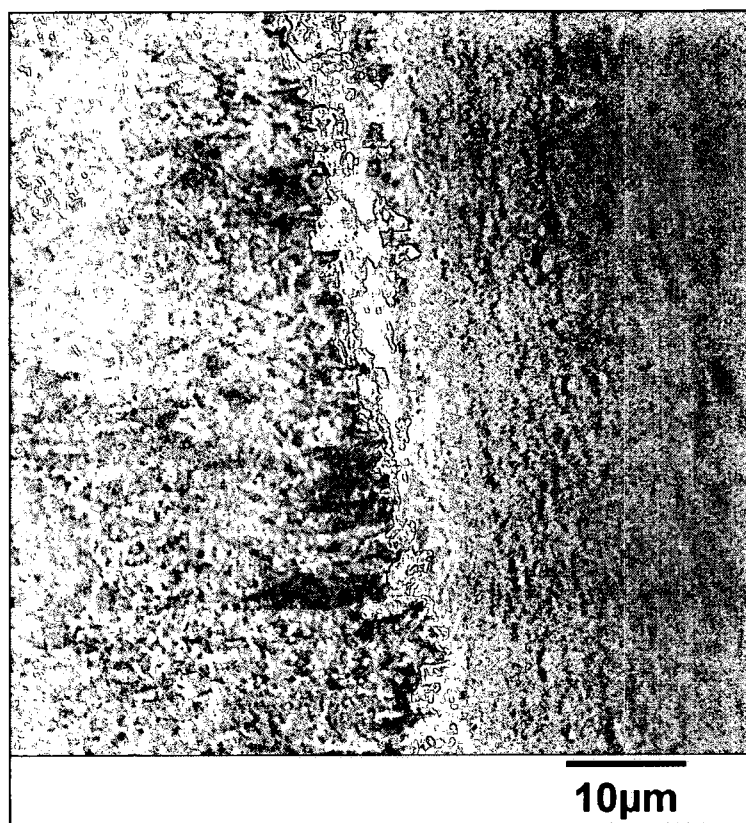


Illustration 34: FKM: 2000X – SIDE

3.2 Mechanical Evaluation

3.2.1 Visual Observation of Strained Components

To examine the mechanical adhesion of the coatings to the substrate, the coated samples were stretched 35% and observed at 40X magnification. In the following series of images, the first picture is of the sample on a flat surface in the relaxed condition. For the second picture, the part was wrapped around a 10.8mm mandrel which induced a 35% strain on the surface of the sample.

For the NBR samples coated with aluminum (illustrations 35 and 36), the grainy coating was again visible. As the part was stretched, the grains elongated, but the coverage was maintained, with no pores becoming evident that could be seen at this magnification level. As such, as can be seen at this level of magnification, a uniform coverage is maintained and it can be inferred that the adhesion of this coating is acceptable at this level of straining. For the copper coated NBR samples (illustrations 37 and 38), the same effect was noted. There were small pores visible in both the stretched and flat samples. As the part was stretched, the grains elongated and the grain boundaries became more pronounced, but no additional substrate material was exposed. Again, uniform coverage was maintained for these materials and the adherence can be considered acceptable at this level of straining.

The aluminum coated FVMQ samples (illustrations 39 and 40) exhibited a definite grain structure with many visible pores interrupting the coating coverage. The stretched picture shows no reduction in the coverage area due to stretching

of the samples. The copper coating was definitely more uniform on the FVMQ samples (illustrations 41 and 42) than the aluminum coating with much less visible substrate material. However, the stretching did not expose any additional substrate material, and a cohesive layer was maintained. As such, both the aluminum and copper coatings on the FVMQ have sufficient adherence to the substrates to be acceptable at these levels of strain.

The aluminum coating of the FKM samples (illustrations 43 and 44) was very uniform with no visible substrate. Stretching the material revealed the grain structure of the coating, but did not induce a breach in the coating. The copper coating on the FKM samples (illustrations 45 and 46) had a definite grain structure with some small amount of substrate visible. Stretching does not appear to have adversely affected this coating and did not appear to open up any pores in the surface. The opening of grain boundaries in the coating shows that these particles, although being tightly packed on the substrate surface, can still move independently on the substrate surface.

These results indicate that these coatings were well adhered to all of the substrates even at high strain levels. The sample area covered with the coating was not adversely affected by the stretching of the samples, indicating that the base level of permeation resistance from these coatings can be maintained in use. Since the metallic coating did not delaminate and flexed with the substrate, it can be inferred that the coating was well adhered to the substrate. This also indicates that the metallic coating was very compliant as it flexed with the substrate material.

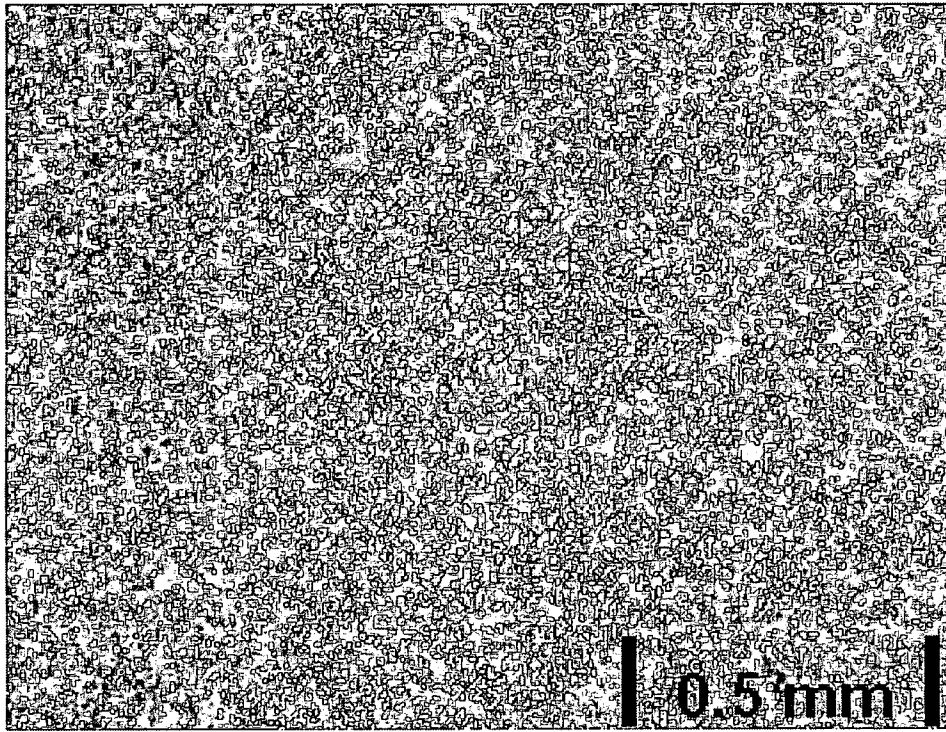


Illustration 35: NBR w/ Aluminum

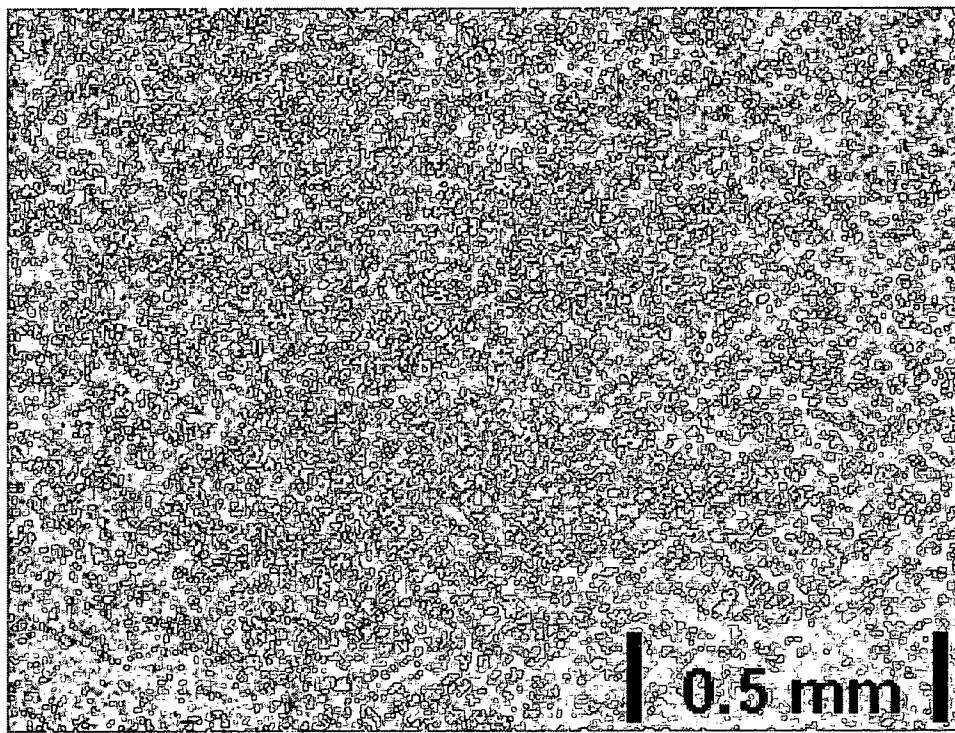


Illustration 36: NBR w/ Aluminum: As stretched 35%

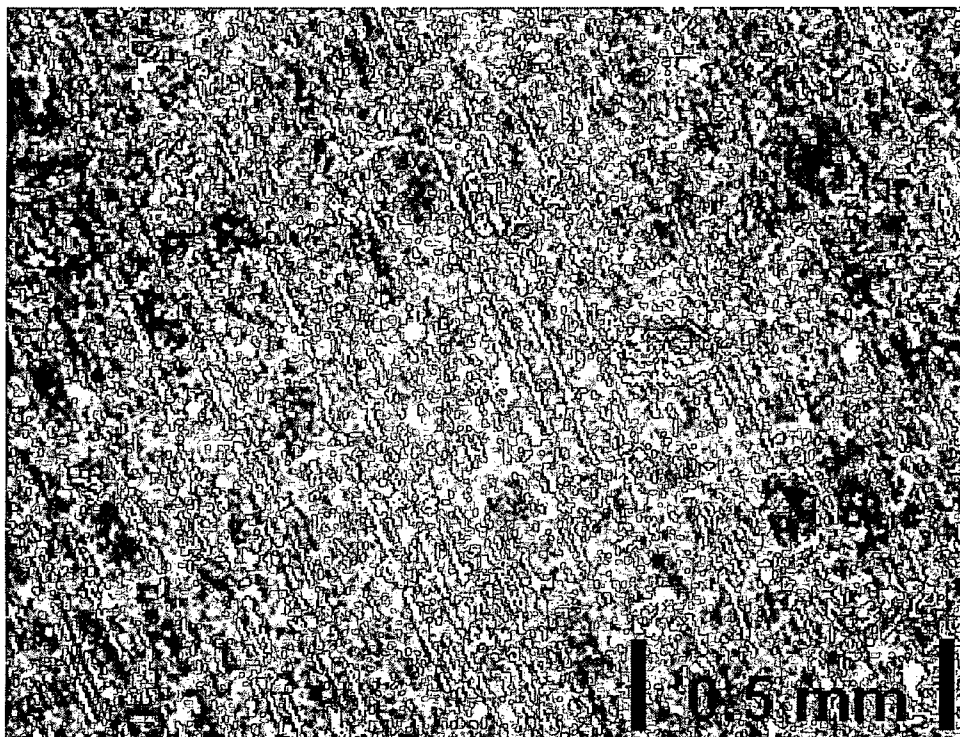


Illustration 37: NBR w/ Copper

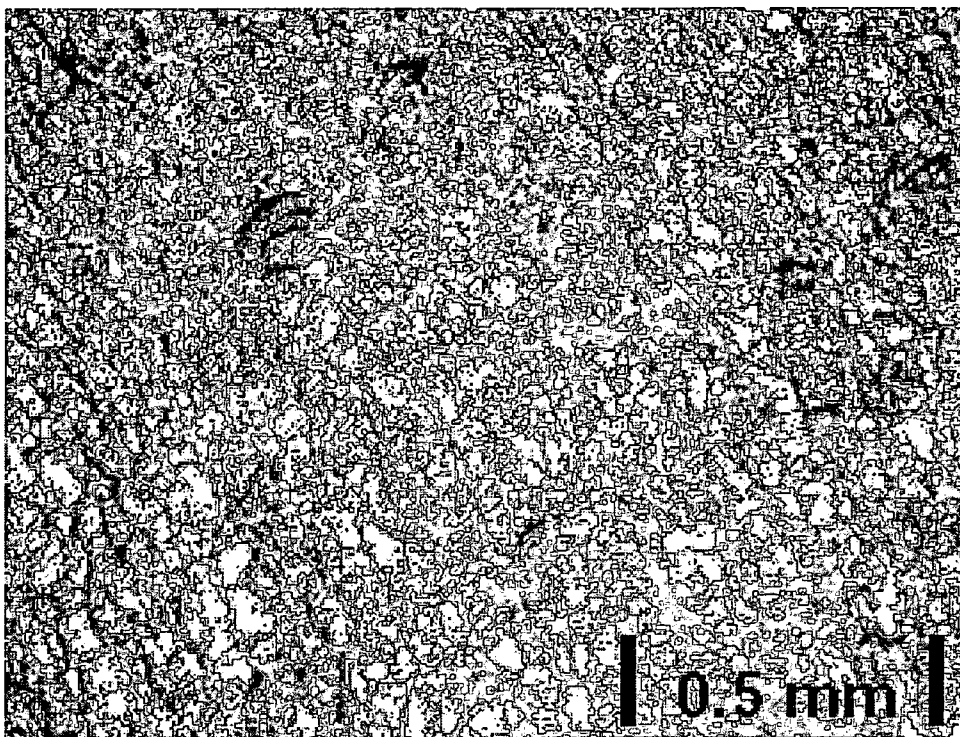


Illustration 38: NBR w/ Copper: As stretched 35%

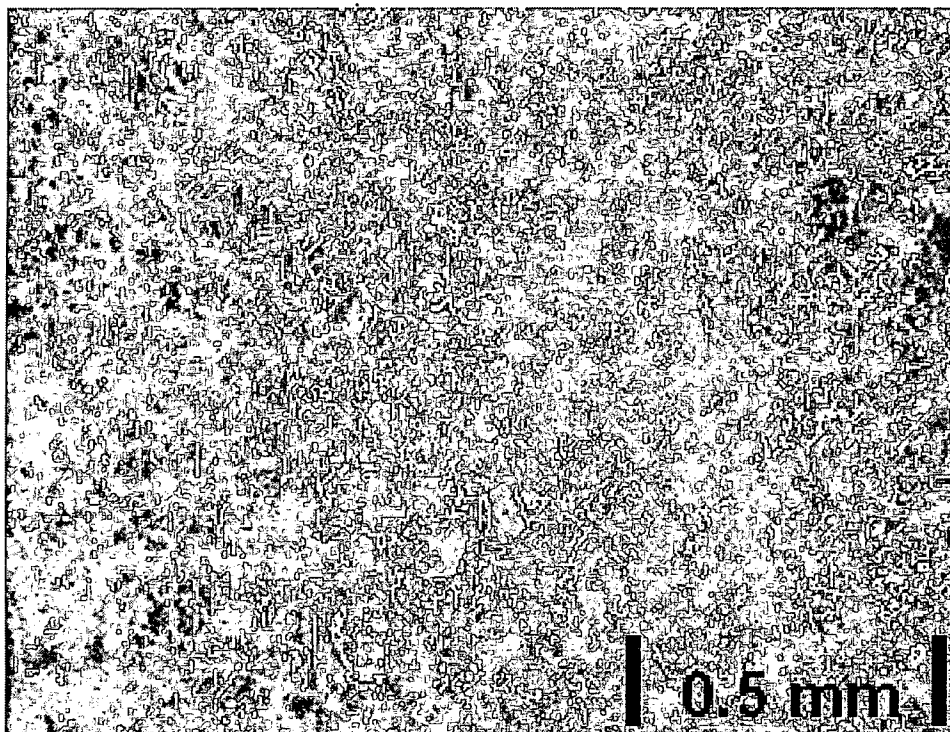


Illustration 39: FVMQ w/ Aluminum

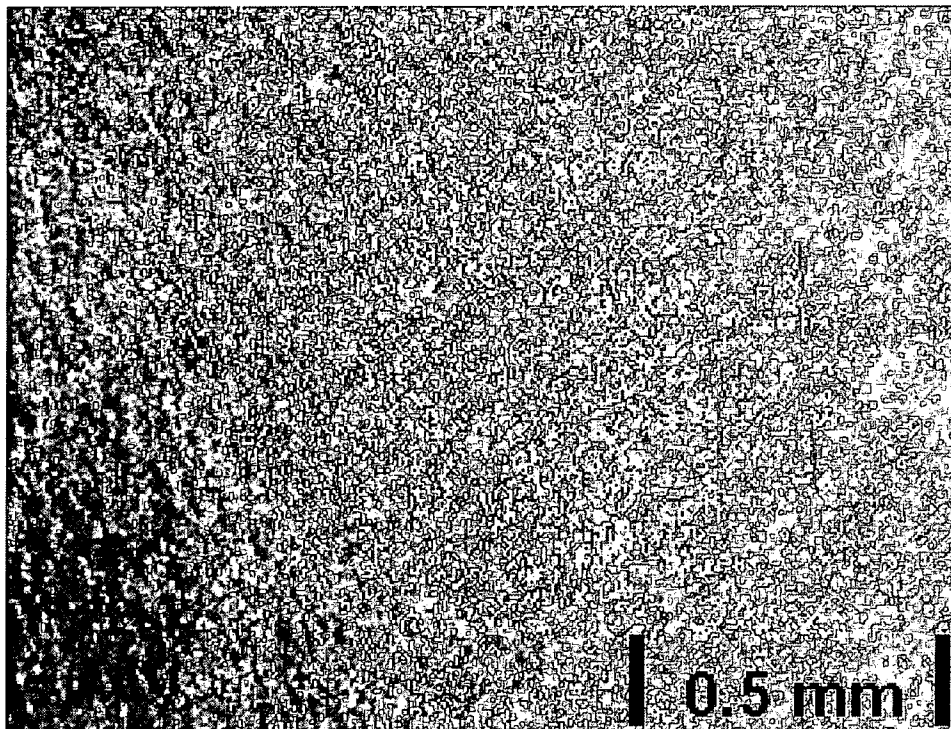


Illustration 40: FVMQ w/ Aluminum: As stretched 35%

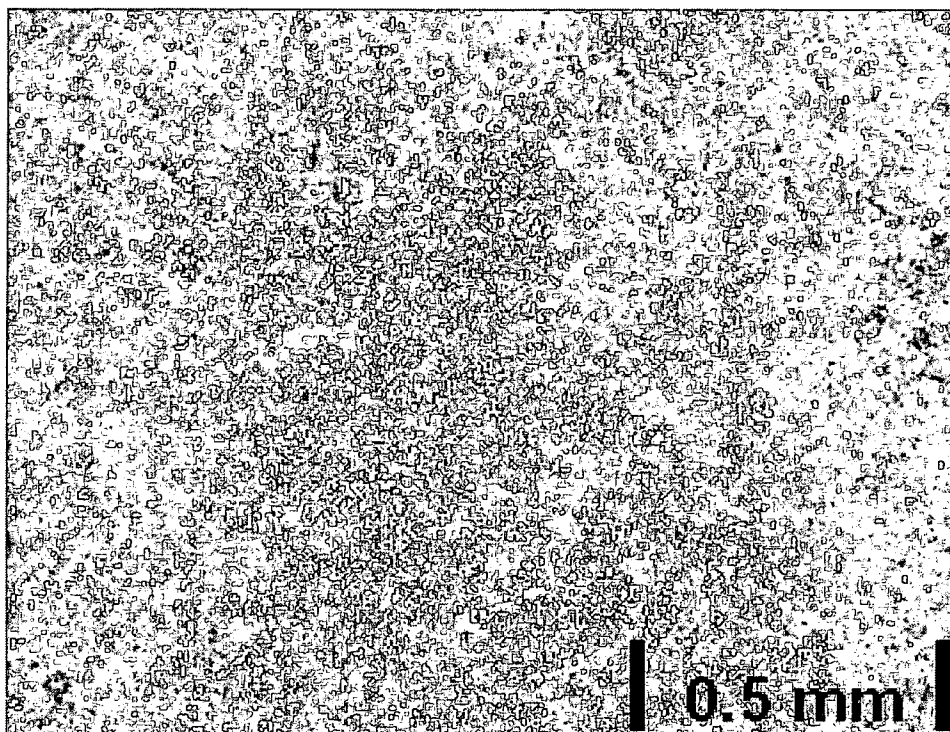


Illustration 41: FVMQ w/ Copper

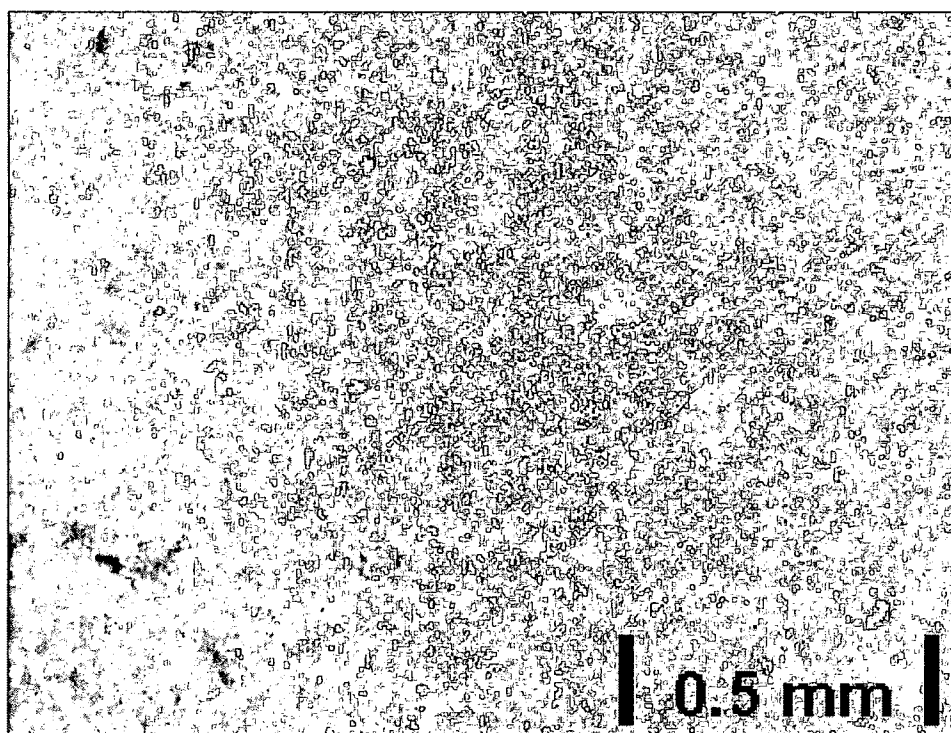


Illustration 42: FVMQ w/ Copper: As stretched 35%

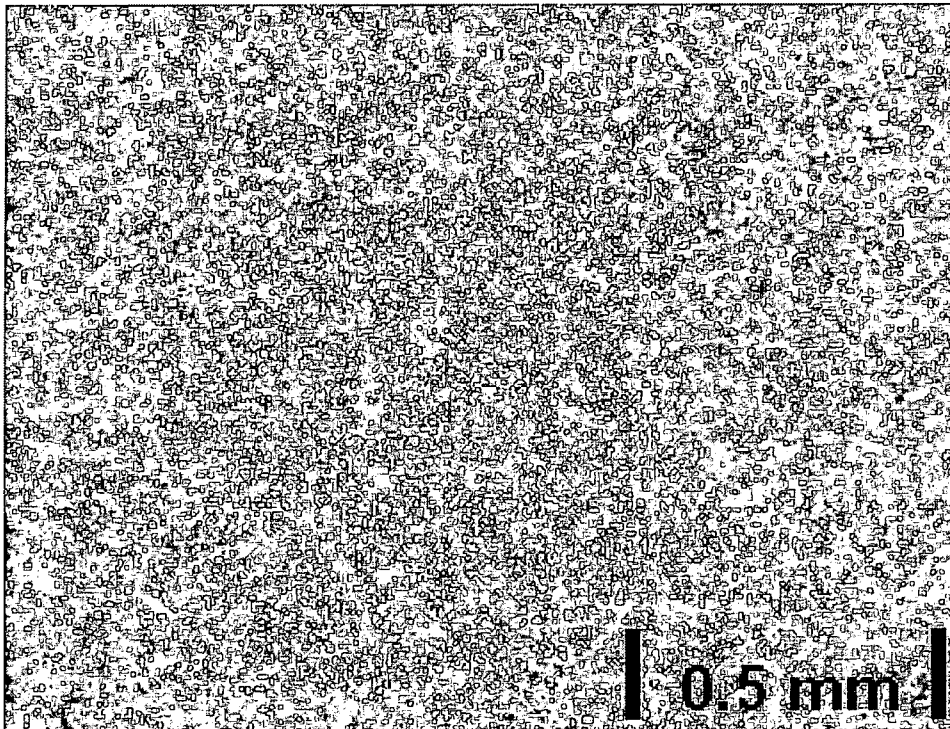


Illustration 43: FKM w/ Aluminum

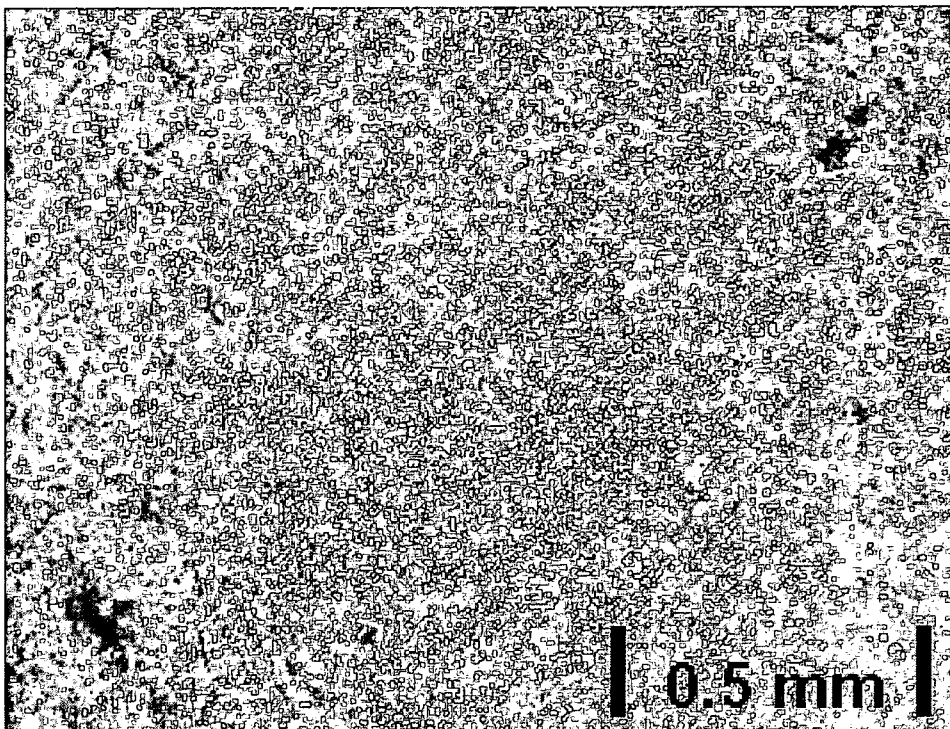


Illustration 44: FKM w/ Aluminum: As stretched 35%

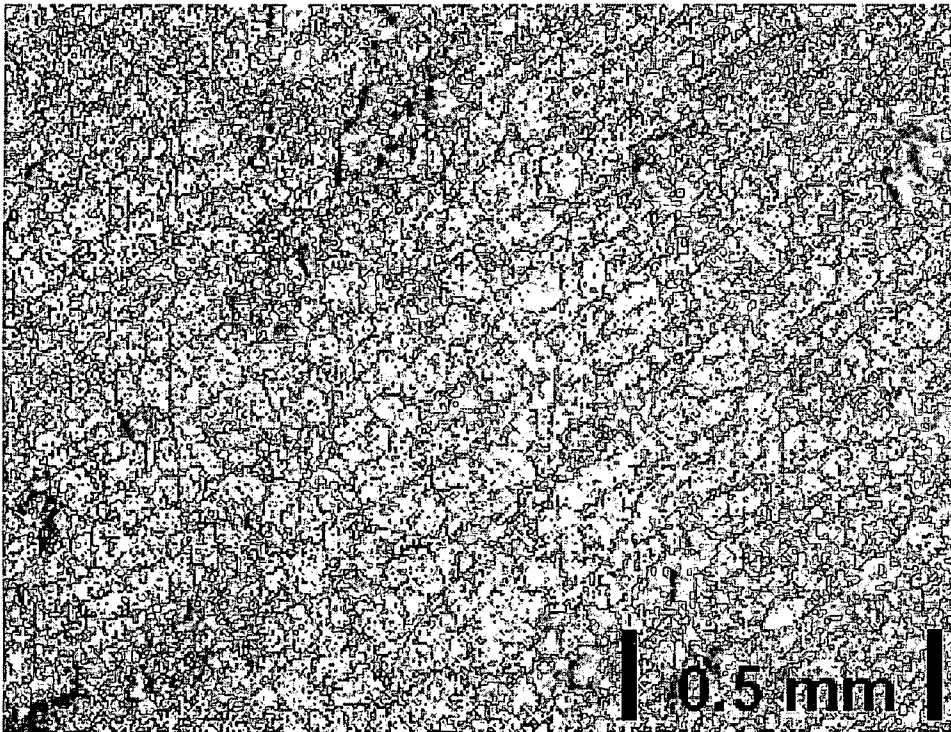


Illustration 45: FKM w/ Copper

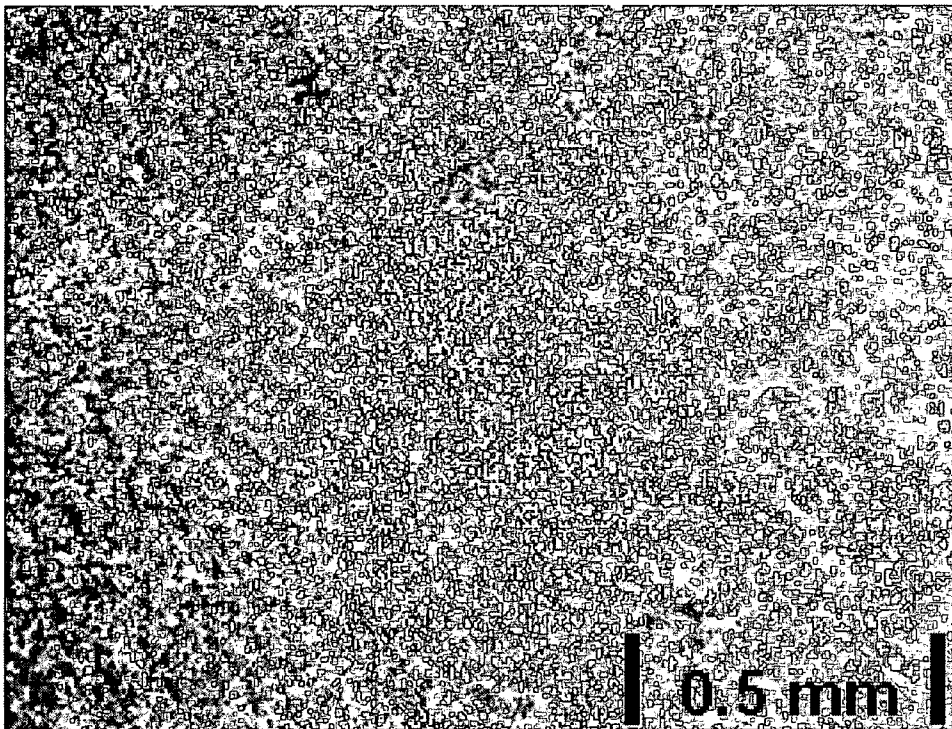


Illustration 46: FKM w/ Copper: As stretched 35%

3.2.2 Tensile Testing of the Components

To examine the affects of the coating on the substrate surface compliance, tensile testing was performed on the coated and uncoated materials as described in the experimental section. As is described in the following discussion, the tensile and modulus curves of the coated and uncoated samples were very similar. In general there was not an appreciable change in the properties of these materials due to the presence of these coatings. This indicates that a thin, metallic layer deposited by the magnetron sputtering process does not appreciably change the elastic properties of the coated component. The illustrations that follow are of the median curves for each type.

As can be seen, the tensile response of the NBR material (illustration 47) was slightly affected by the presence of either the aluminum or copper coatings. The low strain values exhibited a small change in the tensile stress. The average stress at 50% elongation for these samples is 1.65MPa. The maximum change in the stress at 50% elongation was a 3% decrease for the copper coated samples and a 9% decrease for the aluminum coated samples. As would be expected from the tensile curves, the modulus did not change drastically with the addition of the coatings (illustration 48). The average change in the elastic modulus at 10% elongation was a 14% decrease for the aluminum coated samples and a 6% decrease for the copper coated samples. The average modulus values at 10% elongation for the uncoated, aluminum coated, and copper coated samples were 6.68, 5.75, and 6.31Mpa respectively. From this data, it appears that the presence of the coating is not adding stiffness to the

elastomeric material. However, due to the reduction in the modulus and tensile stress, it is possible that the implantation of the aluminum and copper samples could be degrading the substrate slightly.

For the FVMQ samples, there appears to be more of a difference between the coated and uncoated samples (illustration 49). It should be noted that due to the low friction of the metallic-coated FVMQ parts, there was a great deal of slippage at the tensiometer grips, which led to a lot of variation in the data. The percentage decrease for the stresses at 50% elongation in the aluminum and copper coated samples was 17% for the aluminum coating and 28% for the copper coating. The modulus curve trends closely match the tensile curve changes (illustration 50). The average change in the modulus for the aluminum coated samples was a 3% decrease for the aluminum samples and 14% increase for the copper coated samples. The average modulus for the uncoated, aluminum coated, and copper coated samples were 2.88, 2.88, and 3.28MPa respectively. As with the NBR samples, this indicates that the coating is not increasing the stress of the substrate material, but that implantation of the metal particles could be slightly degrading the substrate material.

The FKM data (illustration 51) followed the same trends as the NBR and FVMQ materials. The average decrease in the tensile stress at 40% elongation for the FKM material was 7% for the aluminum coating and 10% for the copper coating. The average modulus at 10% elongation for these samples for the uncoated, aluminum coated, and copper coated samples were 9.79, 7.87, and 8.66MPa respectively. This reflects a 20% decrease for the aluminum coated

samples and a 12% decrease for the copper coated samples. Again, this is indicative of slight substrate damage due to the coating process, with no increase in the stiffness of the samples due to the presence of the coating.

In summary, the tensile data for these samples indicates that the implantation of the metallic particles and possible substrate damage to the coating process is affecting the substrate material. The aluminum coating has induced a greater decrease in the modulus of these samples as compared to the copper coatings, which seems to correlate well with the visual data which also indicates that there is greater implantation of the aluminum particles as compared to the copper particles. However, the reduction of the modulus of these materials is slight, indicating that the performance of these materials would not be compromised in application by the addition of these coatings. As the modulus of all of the samples was reduced, there is no indication that the metallic coating layer is increasing the stiffness of the samples. This is also correlates well with the visual data, which indicates that the coating is flexible and not prone to increasing the stiffness of these materials.

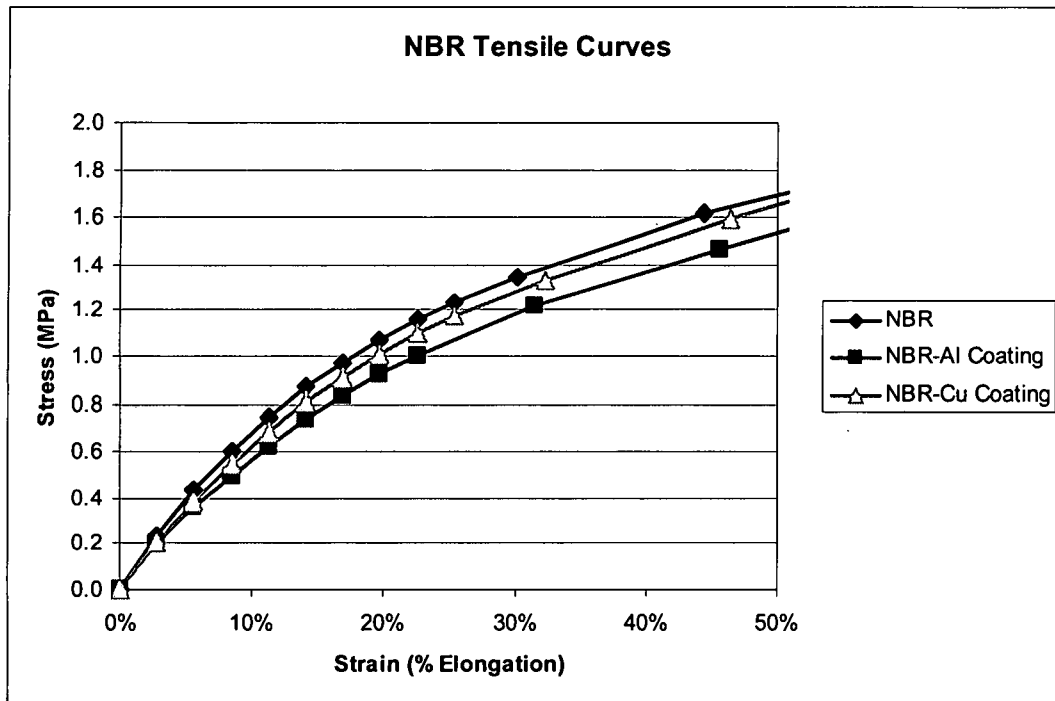


Illustration 47: NBR Tensile Curves

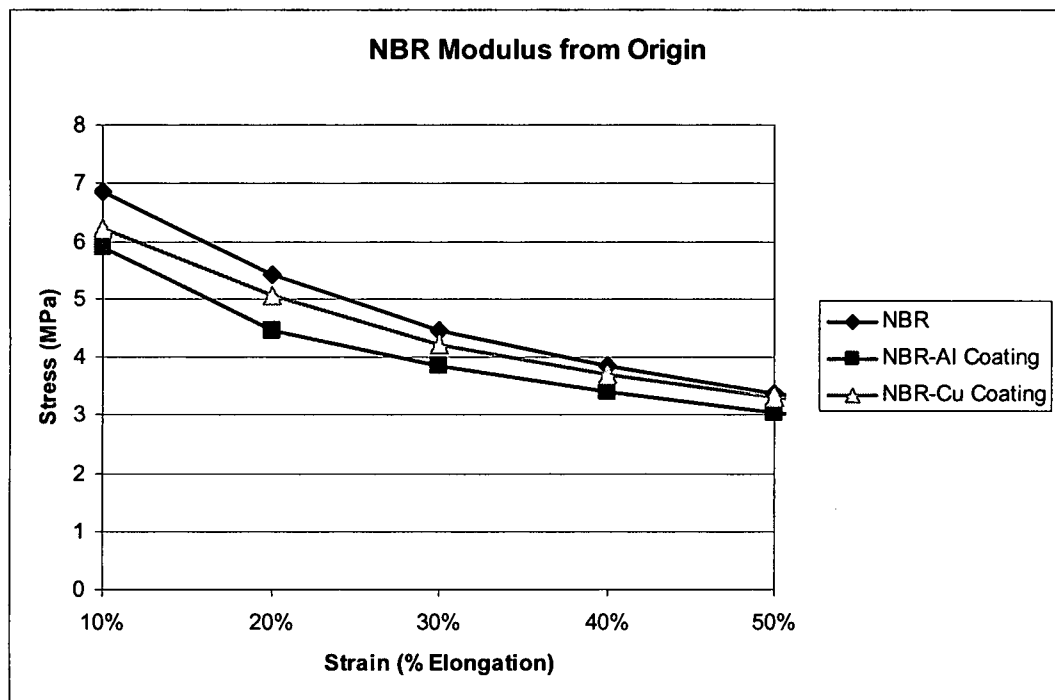


Illustration 48: NBR Modulus from Origin

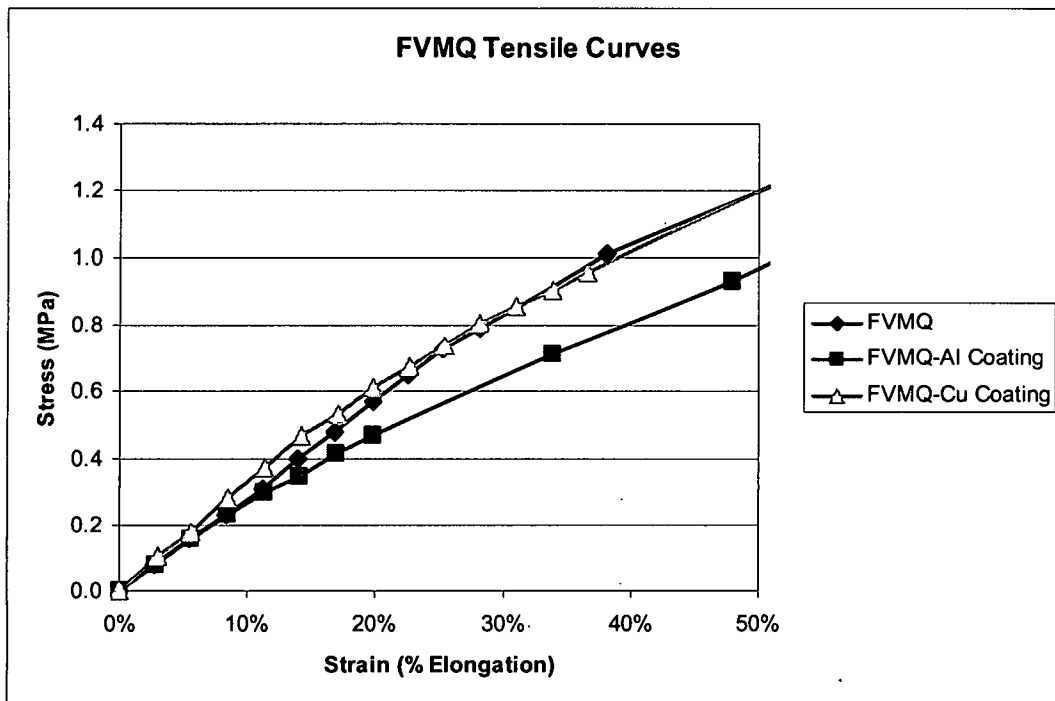


Illustration 49: FVMQ Tensile Curves

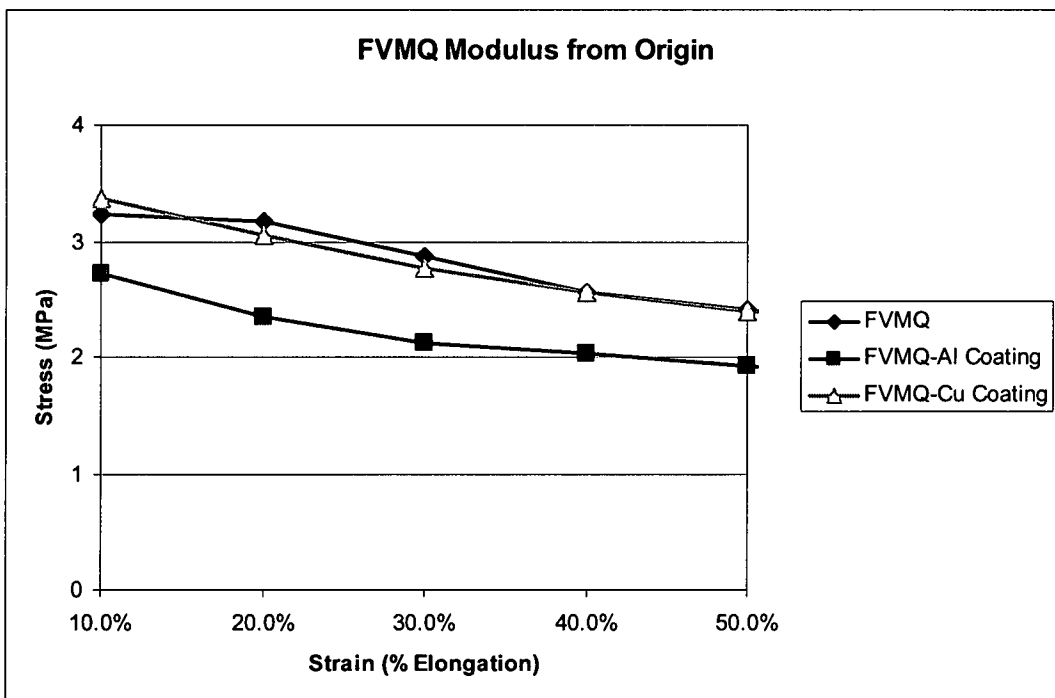


Illustration 50: FVMQ Modulus from Origin

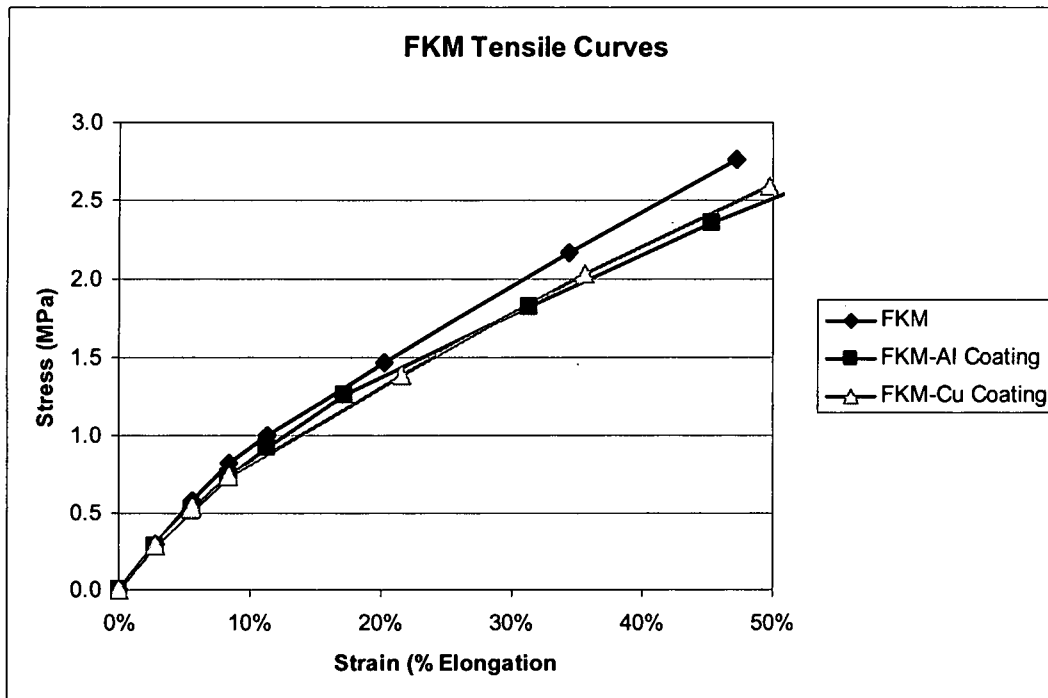


Illustration 51: FKM Tensile Curves

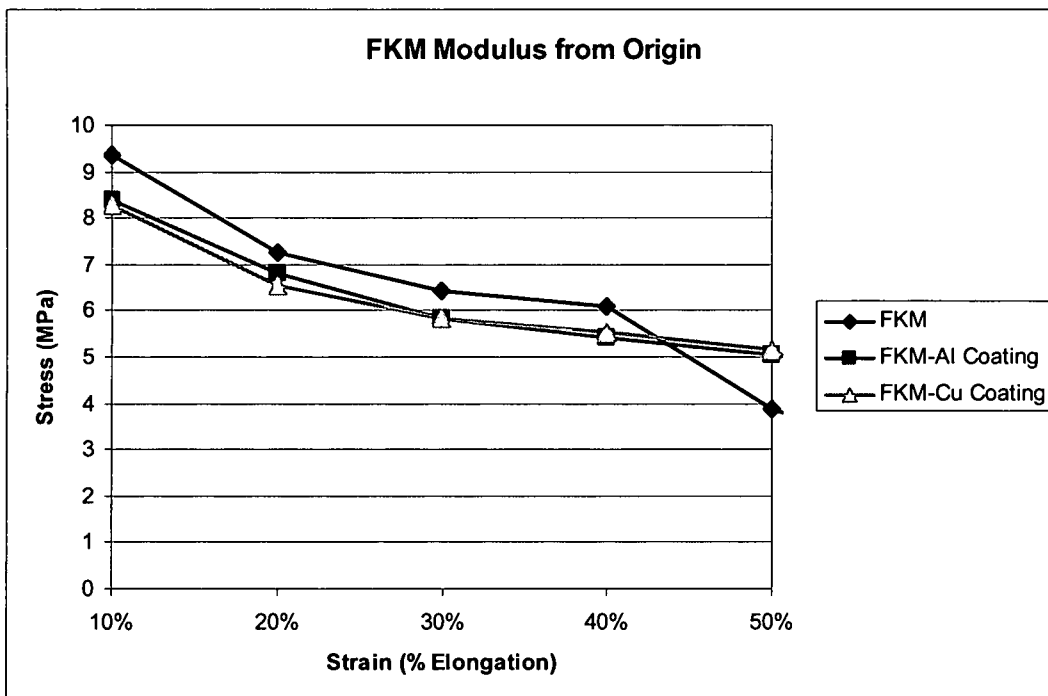


Illustration 52: FKM Modulus from Origin

3.3 Permeation Evaluation

3.3.1 Swell Testing

The swell rate for each sample was calculated by using equation 28 to determine the solubility of Fuel C in each of these materials. As can be seen in illustration 53, the swell of the NBR material was much higher than the FVMQ and FKM, with the NBR swelling three times as much as the FVMQ and twelve times more than the FKM. These results are in good agreement with the Hansen Solubility Parameters, as shown in Table 3, which indicates that NBR will have higher swell in Fuel C than FVMQ, with FKM having the lowest swell.

From the swell data, the cross-link density was calculated for each of these materials using equation 29.

$$Mc = \frac{\rho_p * V * \phi^{1/3}}{\ln(1 - \phi) + \phi + x * \phi^2} \quad (29)$$

Where: ρ_p = Polymer density

V = Molar volume of the solvent

ϕ = Volume fraction of swollen rubber

x = Polymer penetrant interaction parameter

The cross-link density for NBR was calculated to be $14.73 \times 10^4 \text{ g}^* \text{mol} / \text{cm}^3$. For the FVMQ material, the cross-link density was calculated to be $10.49 \times 10^4 \text{ g}^* \text{mol} / \text{cm}^3$. The cross-link density for the FKM material was determined to be $13.33 \times 10^4 \text{ g}^* \text{mol} / \text{cm}^3$.

An Analysis of Variance on the totality of swell data for all points, as shown in table 10, indicates that only the polymer type (variable A) is truly a

significant factor, with a confidence interval of greater than 99%. The confounding factor of polymer with coating type (variable AB) is approximately significant, with a 90% confidence interval. The coating type is, however, statistically significant within the individual polymer groups. Because we know that these are porous coatings and the length of exposure time is quite high, it is reasonable to expect that the swelling properties will not be affected by their presence. These coatings will not change the swelling properties of the bulk substrate material to such an extent as to significantly affect the bulk polymer properties, but can only affect the flux rate of the solvating fluid entering into the material. This would have the affect of reducing the rate of swelling, but not the equilibrium solvent uptake, which has been measured for this research.

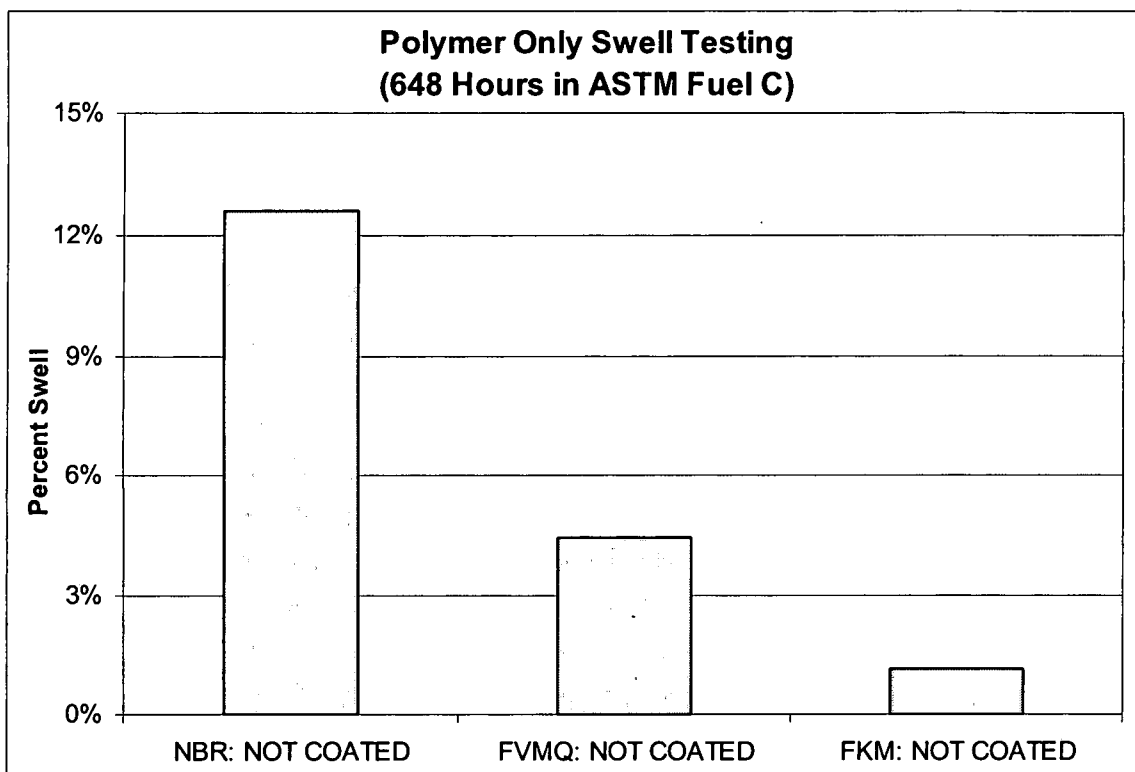


Illustration 53: Polymer Only Swell Testing

Table 10: ANOVA for Swell Testing

Source	Sum of Squares	DF	Mean Square	F Value	Prob > F	
Model	0.108399	23	0.004713	78.44105	< 0.0001	significant
A (Polymer)	0.107508	2	0.053754	894.6605	< 0.0001	
B (Coating)	3.01E-05	1	3.01E-05	0.500693	0.486	
C (Pressure)	0.000156	3	5.21E-05	0.866389	0.4721	
AB	0.000295	2	0.000148	2.45527	0.1071	
AC	0.000133	6	2.22E-05	0.370203	0.8906	
BC	0.000132	3	4.41E-05	0.734628	0.5416	
ABC	0.000143	6	2.39E-05	0.397943	0.873	
Pure Error	0.001442	24	6.01E-05			
Cor Total	0.109841	47				

The NBR material exhibited a varied response to the amount of swelling with the coatings in place. As can be seen in illustration 54, the copper coated samples had a definite decrease in the swelling of fuel C into the nitrile membranes. In the case of these coatings on NBR, the specific coating material is a statistically significant variable. The aluminum samples did not produce a statistical decrease in the swelling of the material. Any change in the amount of swelling that occurs was due to the coating material limiting the flux rate of the solvent into the substrate. The decrease in swelling from this is actually due to a decrease in the flux density, as the fuel permeates out of the substrate at a different rate than it goes into solution on the coating side. This is most likely to occur in the NBR material, as this substrate has an inherently high flow rate of solvent through the material. As such, the decrease in swell with the copper-coated samples indicates that the copper coating was limiting the amount of test fuel entering the substrate polymer. This seems reasonable, as the visual data shows that there is more coverage area with the copper coating than the aluminum coating. This indicates that the copper-coated samples will have less permeation results than the base material or the aluminum coated material.

As shown in illustration 55, the aluminum coated NBR samples had a great deal of variation in the swell data. This swell data closely matched the predicted film thickness, as calculated from the deposition rate experiments as shown in section 2.4. The 20mTorr samples have the lowest swell and highest predicted film thickness, and the 10mTorr has the highest swell and lowest predicted film thickness. The results of the individual copper film swell data

(illustration 56) in relation to the predicted film thickness also indicated a correlation. The 10mTorr samples had the lowest swell and the highest predicted film thickness and the 30mTorr samples had the highest swell and the lowest predicted film thickness. Illustration 57 is a graph depicting the relationship between the percentage swell in these samples versus the predicted film thickness.

As can be seen, the copper material was better than the aluminum material at preventing swell in the substrate material. The mechanism for this decreased must be a reduction in the rate of the solvent flux into the substrate. As the thickness of the coating correlates well with the swelling data, it can be surmised that there is an increase in the coverage ratio of the coating with increasing thickness, further limiting the allowable permeation area. As such, it is likely that the permeation rate of NBR will be reduced by the addition of these coatings, with the copper coating having the greatest affect.

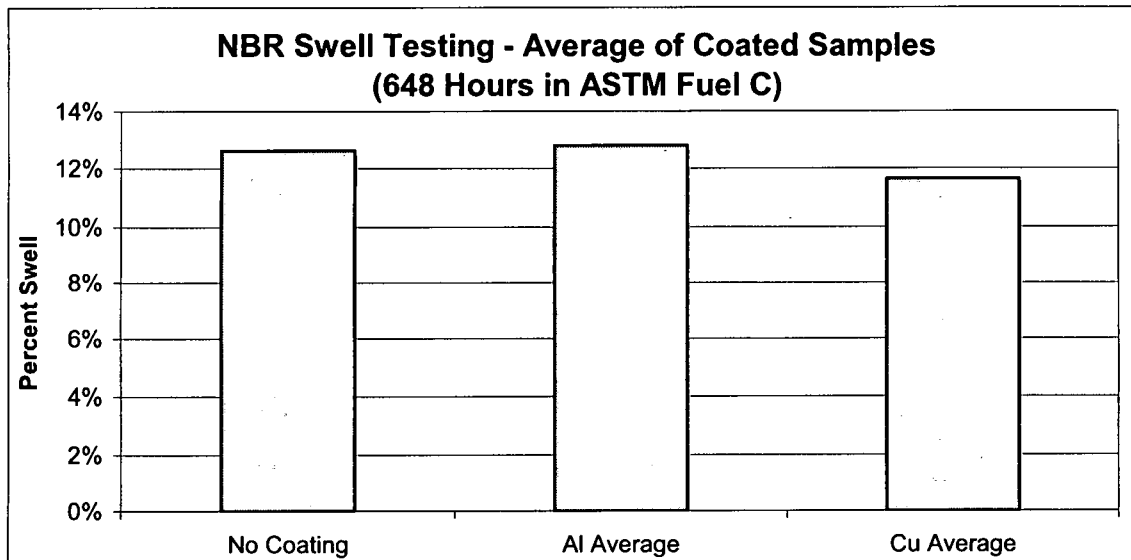


Illustration 54: NBR Swell Testing - Average of Coated Samples

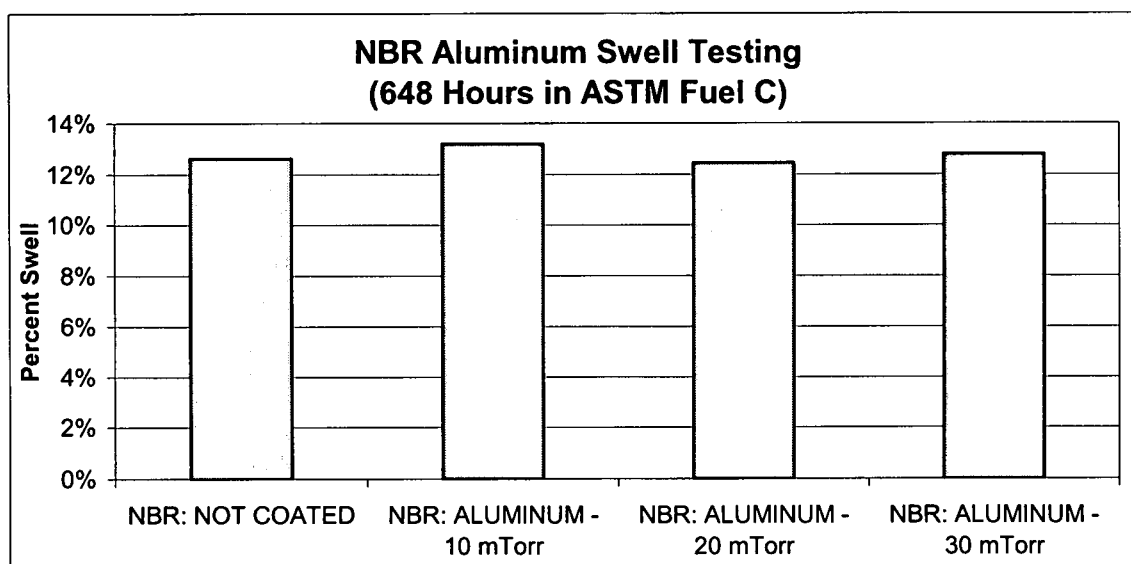


Illustration 55: NBR Aluminum Swell Testing

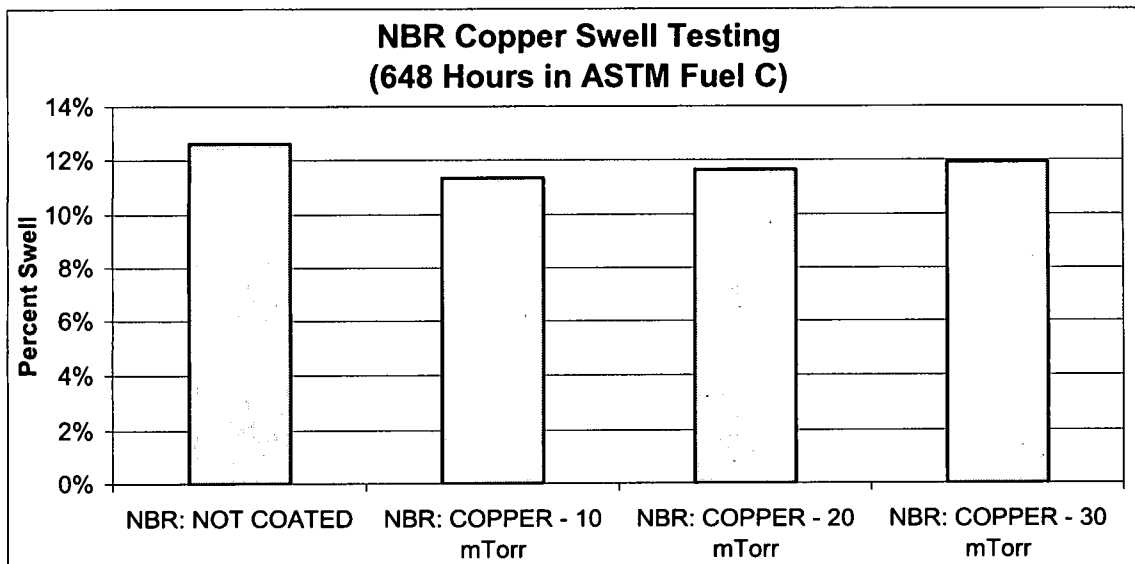


Illustration 56: NBR Copper Swell Testing

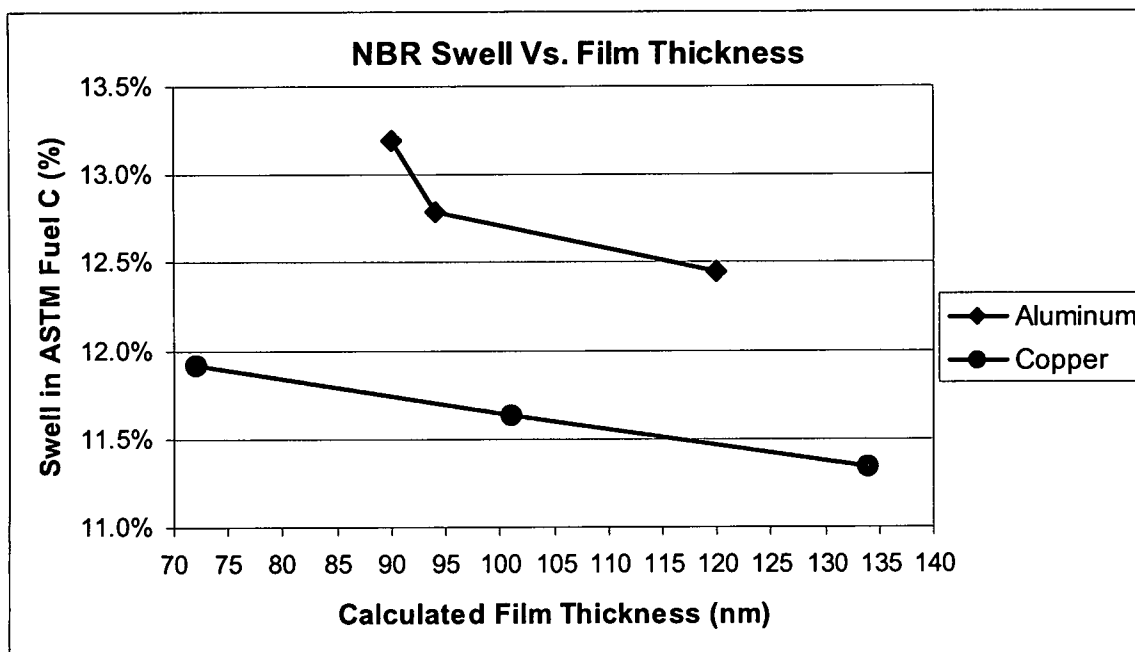


Illustration 57: NBR Swell Vs. Film Thickness

The FVMQ material exhibited a varied response to the amount of swelling with the application of these coatings, as shown in illustration 58. As with the NBR samples, both the copper and aluminum coatings produced a decrease in the percentage swell. The decrease in swell with these coatings indicates that these coatings were limiting the amount of test fuel entering the substrate polymer. As the aluminum coated samples had superior swell results, this would seem to indicate that the aluminum coated samples will have a lower permeation rate than the base material or the copper coated material.

As shown in illustration 59, the aluminum coated FVMQ samples had a minimal variation in the swell data. Again, the trends for the swell data closely match the predicted film thickness. The 20mTorr samples had the lowest swell and highest calculated film thickness, and the 10mTorr had the highest swell and lowest calculated film thickness. The results of the individual copper film swell data (illustration 60) in relation to the calculated film thickness indicated an inverse relationship. However, these results are so close to each other that there is no statistical difference between them and the trend of the change versus thickness is essentially flat. The 10mTorr samples had the highest swell and the highest calculated film thickness and the 30mTorr samples had the lowest swell and the lowest calculated film thickness. Illustration 61 graphs the relationship between the percentage swell in these samples versus the calculated film thickness. As can be seen, the aluminum coating was better than the copper coating at preventing swell into the substrate.

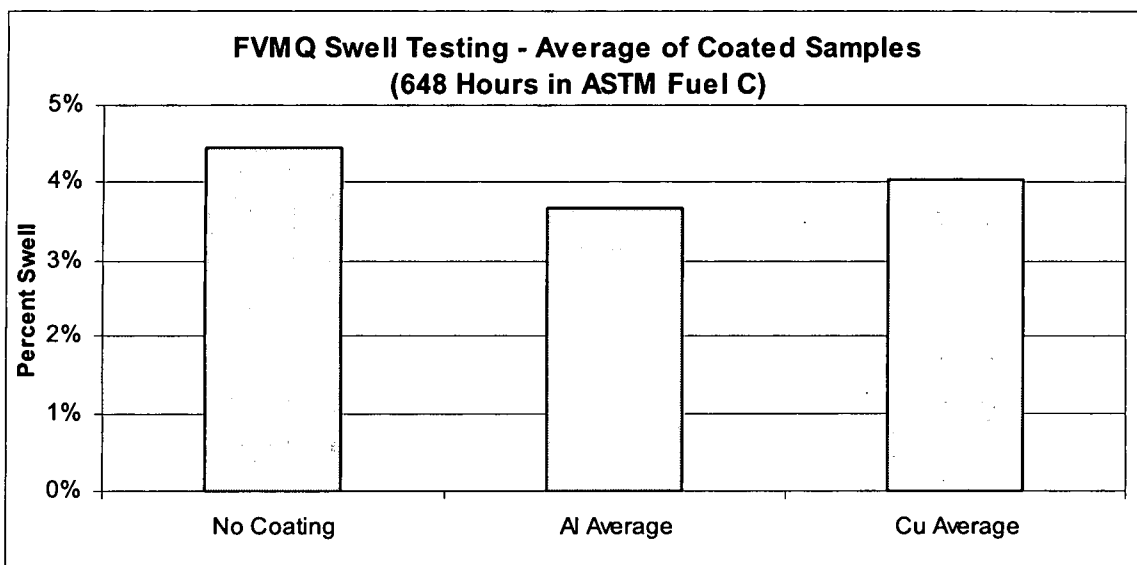


Illustration 58: FVMQ Swell Testing - Average of Coated Samples

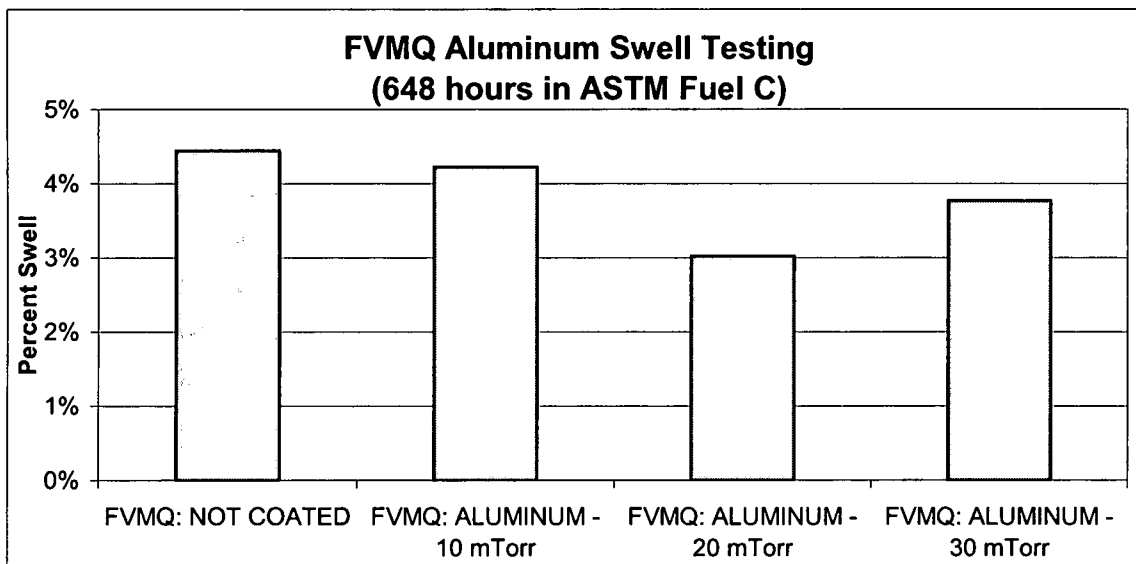


Illustration 59: FVMQ Aluminum Swell Testing

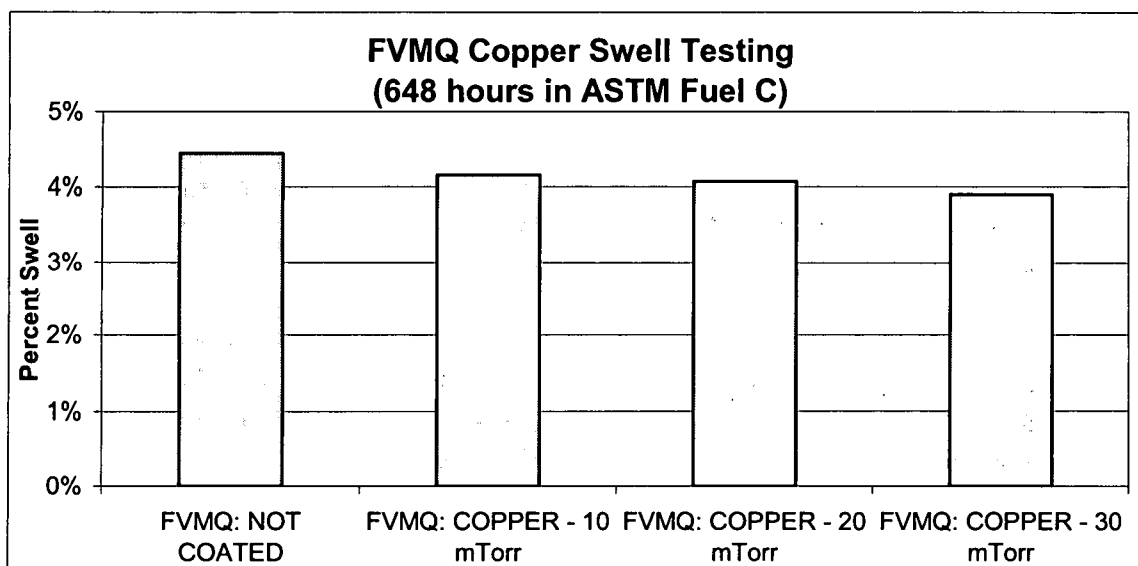


Illustration 60: FVMQ Copper Swell Testing

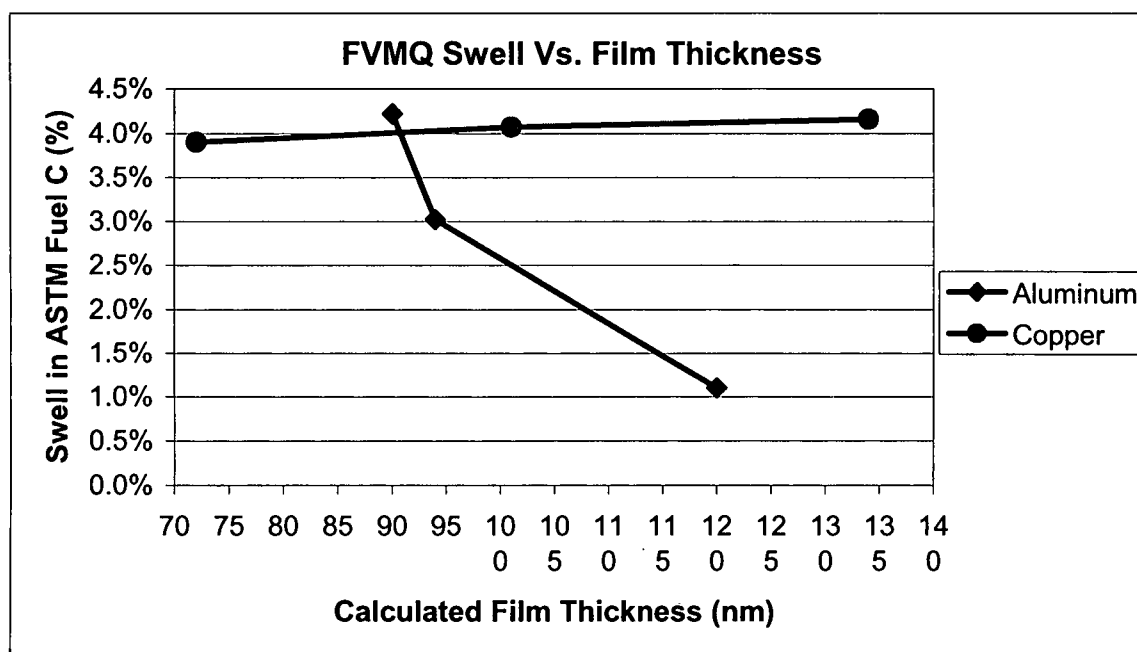


Illustration 61: FVMQ Swell Vs. Film Thickness

The FKM material also exhibited some variation in the amount of swelling with the coatings in place as well. In this case the base swelling of FKM is so low and both the aluminum and copper coatings induced such small changes in the swelling properties that the difference is insignificant. In this case these coatings do not seem to be limiting the amount of test fuel entering the substrate polymer, as shown in illustration 62. This is most likely because, unlike the NBR and FVMQ materials, the permeation rate through the FKM is so slow that the permeation through the coating is not significantly reduced, so as to affect the swelling of this material.

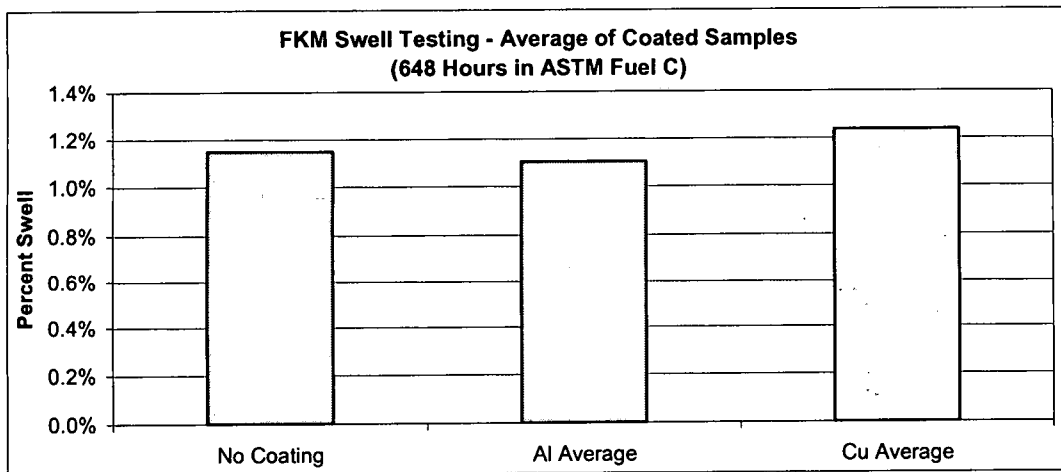


Illustration 62: FKM Swell Testing - Average of Coated Samples

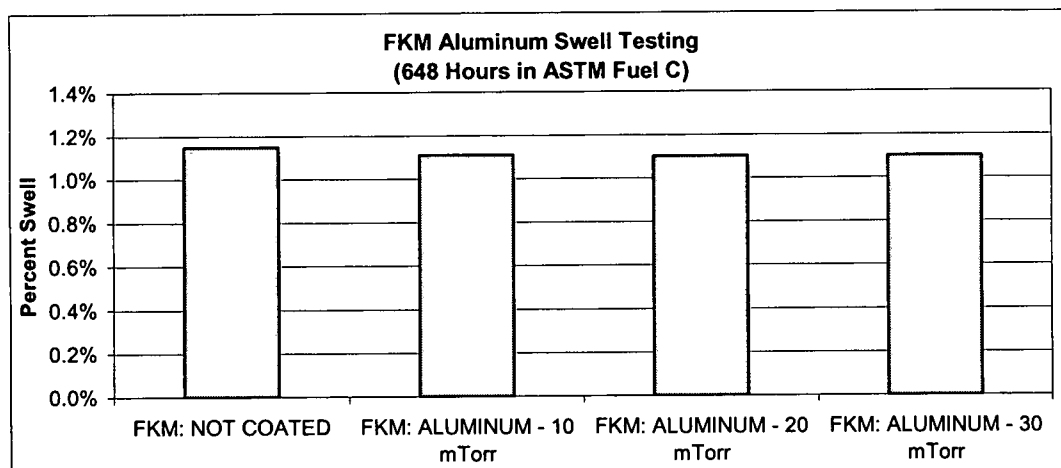


Illustration 63: FKM Aluminum Swell Testing

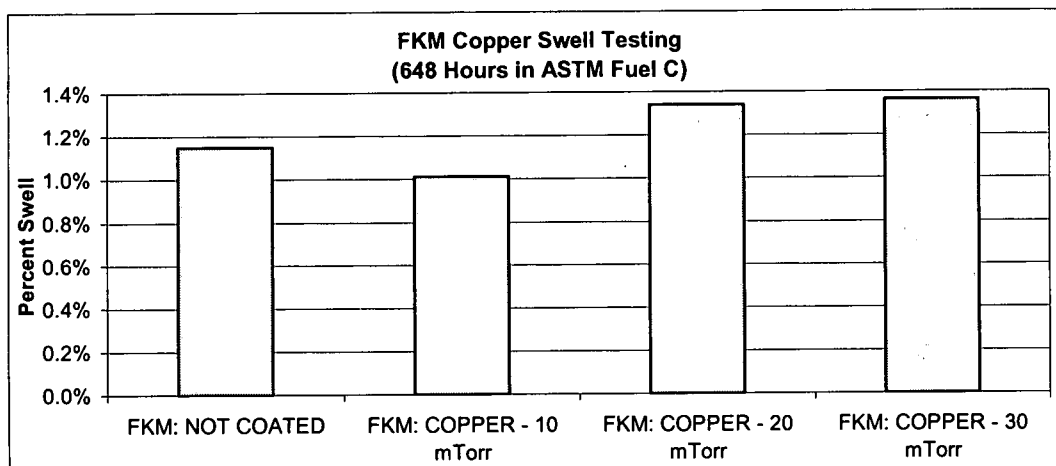


Illustration 64: FKM Copper Swell Testing

3.3.2 Permeation Testing

An analysis of variance for weight loss at 528 hours and at 648 hours was performed for all data points. These ANOVA are shown in tables 11 and 12. The analysis for the 528 hour data indicates that the polymer type and coating type were the main effects that were significant with a probability of occurrence of less than 0.01% and 1.76%. The confounded source of the polymer and deposition pressure was also significant with a probability of occurrence of 2.81%. For the 648 hour data, the polymer type and coating were again important, with probabilities of less than 0.01% and 2.06% respectively. The confounded source of the polymer and deposition pressure was also significant with a probability of occurrence of 1.80%

This indicates that the deposition pressure was only important as it pertained to the particular polymer type. As such the thickness, which was controlled by the coating pressure was important within each polymer group itself, but was not significant in comparison to the large differences imposed by the polymer types and coating type. An analysis of variance for the permeation from the start of the test at 528 hours and at 648 hours was performed for all data points (tables 13 and 14). The analysis of the data at 528 hours indicates that the polymer type and coating type were the main variable that were significant with a probability of occurrence of less than 0.01% and 1.39%. The confounded source of the polymer and deposition pressure was also significant with a probability of occurrence of 4.10%.

For the 648 hour data, the polymer type and coating type were significant, with probabilities of <0.01% and 1.16% respectively. The confounded source of polymer and deposition pressure was again significant with a probability of less than 2.70%. This is in agreement with the weight change ANOVA results indicating that the deposition pressure and therefore the thickness was only important as it pertained to the particular polymer type. As such the thickness, which is controlled by the coating pressure, was important only as it applied to each polymer type individually. Again, the effects on the permeation rate due to the coating thickness are small in comparison to the effects due to the polymer and coating types.

An analysis of variance for the permeation from between data points at 528 hours and at 648 hours was performed for all data points (tables 15 and 16). This analysis indicates that the polymer type was the only effect that was significant with a probability of occurrence of less than 0.01%. For the 648 hour data, the polymer and coating type were both significant, with probabilities of less than 0.01% and 1.16%.

Table 11: ANOVA for Weight Loss at 528 hours

Source	Sum of Squares	DF	Mean Square	F Value	Prob > F	
Model	479.1285	17	28.18403	134.9645	< 0.0001	significant
A (polymer)	465.4533	2	232.7267	1114.455	< 0.0001	
B (coating)	2.200145	1	2.200145	10.53581	0.0176	
C (pressure)	1.524648	3	0.508216	2.433689	0.163	
AB	1.323878	2	0.661939	3.169819	0.115	
AC	6.933859	6	1.155643	5.534015	0.0281	
BC	1.692586	3	0.564195	2.701755	0.1387	
Residual	1.252953	6	0.208825			
Cor Total	480.3814	23				

Table 12: ANOVA for Weight Loss at 648 Hours

Source	Sum of Squares	DF	Mean Square	F Value	Prob > F	
Model	597.2845	17	35.13438	137.893	< 0.0001	significant
A (polymer)	580.8238	2	290.4119	1139.789	< 0.0001	
B (coating)	2.479601	1	2.479601	9.731769	0.0206	
C (pressure)	0.646556	3	0.215519	0.845853	0.5171	
AB	1.517642	2	0.758821	2.97817	0.1264	
AC	10.20774	6	1.70129	6.677106	0.018	
BC	1.60921	3	0.536403	2.105239	0.201	
Residual	1.528767	6	0.254794			
Cor Total	598.8133	23				

Table 13: ANOVA for Permeation from Start of Test at 528 hours

Source	Sum of Squares	DF	Mean Square	F Value	Prob > F	
Model	32.8475	17	1.932206	127.9544	< 0.0001	significant
A (polymer)	31.95248	2	15.97624	1057.977	< 0.0001	
B (coating)	0.178262	1	0.178262	11.80483	0.0139	
C (pressure)	0.101581	3	0.03386	2.242306	0.1838	
AB	0.091872	2	0.045936	3.041977	0.1224	
AC	0.426131	6	0.071022	4.703201	0.0407	
BC	0.097179	3	0.032393	2.14512	0.1958	
Residual	0.090604	6	0.015101			
Cor Total	32.9381	23				

Table 14: ANOVA for Permeation from Start of Test at 648 hours

Source	Sum of Squares	DF	Mean Square	F Value	Prob > F	
Model	26.24074	17	1.543573	31.20698	0.0002	significant
A (polymer)	20.81226	2	10.40613	210.3846	< 0.0001	
B (coating)	0.01115	1	0.01115	0.225423	0.6517	
C (pressure)	0.998065	3	0.332688	6.726084	0.024	
AB	0.119019	2	0.05951	1.203128	0.3636	
AC	4.14851	6	0.691418	13.97866	0.0027	
BC	0.151726	3	0.050575	1.022499	0.4464	
Residual	0.296775	6	0.049462			
Cor Total	26.53751	23				

Table 15: ANOVA for Permeation Between Points at 528 hours

Source	Sum of Squares	DF	Mean Square	F Value	Prob > F	
Model	20.80676	17	1.223927	39.07589	< 0.0001	significant
A (polymer)	20.06369	2	10.03185	320.2833	< 0.0001	
B (coating)	0.119371	1	0.119371	3.811104	0.0988	
C (pressure)	0.060113	3	0.020038	0.639736	0.6167	
AB	0.128043	2	0.064021	2.043988	0.2104	
AC	0.299528	6	0.049921	1.593819	0.2928	
BC	0.136009	3	0.045336	1.447439	0.3195	
Residual	0.187931	6	0.031322			
Cor Total	20.99469	23				

Table 16: ANOVA for Permeation Between Points at 648 hours

Source	Sum of Squares	DF	Mean Square	F Value	Prob > F	
Model	14.87949	17	0.875264	35.76162	0.0001	significant
A (polymer)	13.79485	2	6.897427	281.8157	< 0.0001	
B (coating)	0.314051	1	0.314051	12.83152	0.0116	
C (pressure)	0.127539	3	0.042513	1.736995	0.2585	
AB	0.212778	2	0.106389	4.346847	0.0681	
AC	0.276438	6	0.046073	1.882457	0.2304	
BC	0.153828	3	0.051276	2.095038	0.2023	
Residual	0.14685	6	0.024475			
Cor Total	15.02634	23				

As can be seen in illustration 65, the weight change over time for the NBR samples was reduced with the application of both the aluminum and copper. The copper coating produced a much larger reduction in the weight change over time. The average decrease in weight change as compared to the uncoated sample for the aluminum material was 12%. For the copper coated samples, the average weight change decrease was 33%.

The curves of the permeation rates from the start of the test (illustration 66) closely followed the weight change curves. This is to be expected as the permeation rate from the start of the test is directly related to the weight change over time. This graph indicates that the permeation rate increased to a maximum value at approximately 192 hours and then decreased for the rest of the test. The maximum rate of permeation as calculated from this method was 4.04 mg/(m²*sec) for the uncoated material, 3.56 mg/(m²*sec) for the aluminum coated material, and 2.94 mg/(m²*sec) for the copper coated material.

The final permeation rates at 648 hours as calculated by this method were 2.49 for the uncoated material, 2.19 for the aluminum coated, and 1.88 for the copper coated material. As such, the reduction in permeation for the aluminum coating was 12% for the aluminum coating at both 192 and 648 hours. For the copper, the reduction was 27% at 192 hours and 24% at 648 hours. The permeation rate between data points was more interesting. As can be seen in illustration 67, the permeation rate increased to a maximum for all of the samples and then slowly decreased, approaching a level rate. The aluminum and copper coatings still provided for a reduction in the permeation rate at 192 hours. The

permeation rates at 192 hours were 4.29, 3.80, and 3.04 mg/(m²*sec) for the uncoated material, aluminum, and copper coated samples respectively. At 648 hours, these rates were 1.09, 1.05, and 1.68 mg/(m²*sec) for the uncoated, aluminum and copper coated materials. The aluminum coating provided for a reduction in the permeation rate of 11% at 192 hours and 3% at 648 hours. The copper coating provided a coating reduction of 29% at 192 hours and an increase of 5% at 648 hours.

In summary, the weight change and permeation of Fuel C through NBR was reduced by the addition of both aluminum and copper. Since the reduction in permeation by the addition of these coatings is expected to be by limiting the exposed surface area of the substrate to the permeating fluid, it is expected that the coating with a higher coverage area will have lower permeation. As expected from the visual testing which indicates a higher percentage of sample coverage with copper, the copper-coated samples had lower permeation than the aluminum coated samples. This data is also in good agreement with the swelling data, in which the copper-coated samples had lower swell than the aluminum-coated samples. The decrease in the swelling rate after some time at higher permeation levels is most likely due to pervaporation, which will we discussed later in that section.

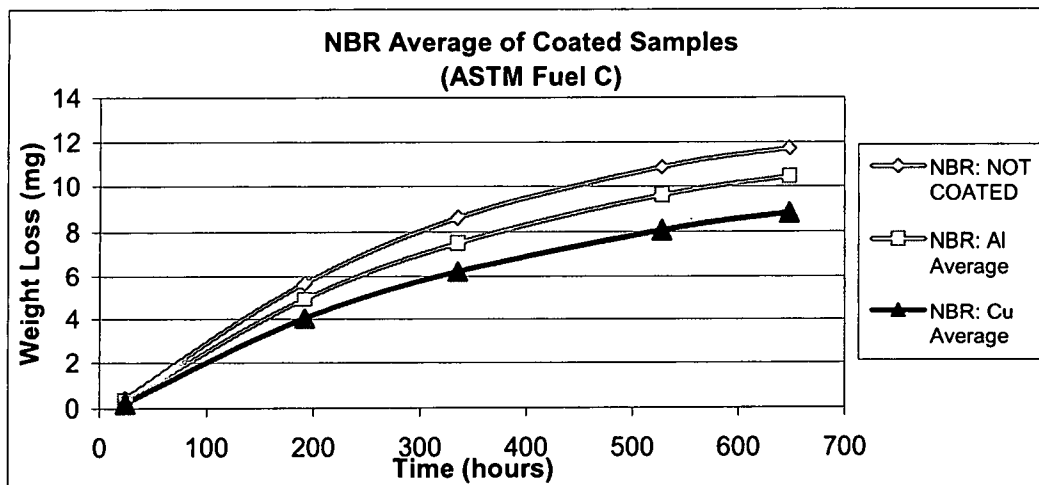


Illustration 65: NBR Average of Coated Samples

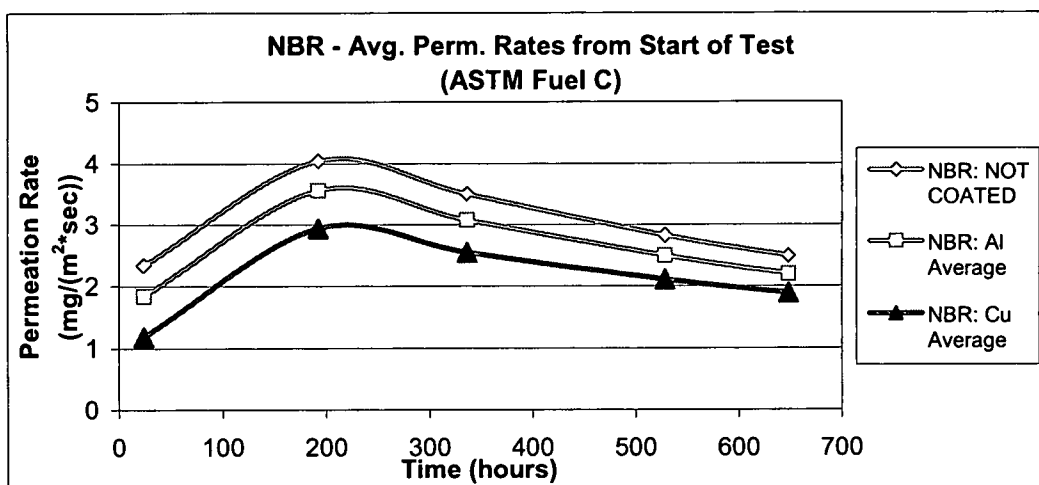


Illustration 66: NBR - Avg. Perm. Rates from Start of Test

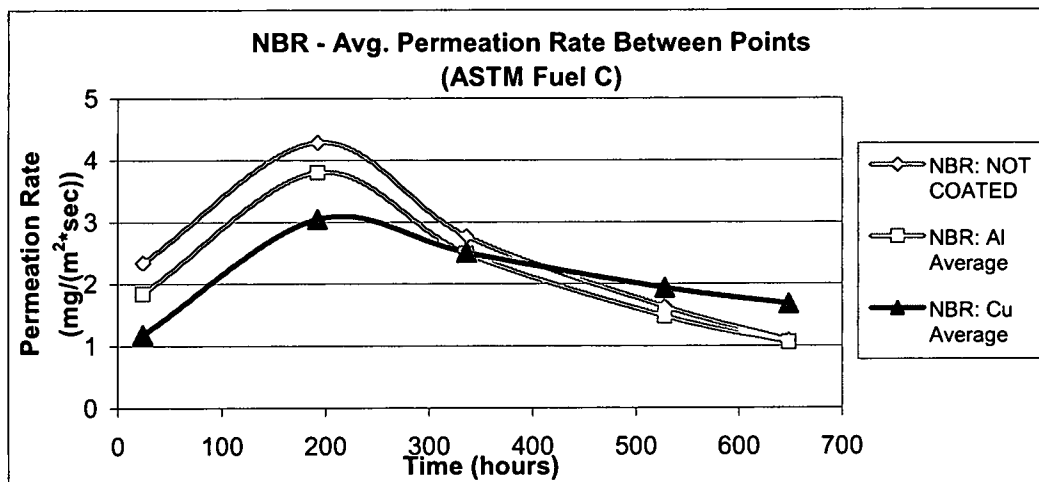


Illustration 67: NBR - Avg. Permeation Rate Between Points

As can be seen in illustration 68, the weight change over time for the FVMQ samples was not significantly affected by the application of either the aluminum or the copper. The aluminum coated samples actually had greater weight loss than the uncoated material. The copper coated samples had no measurable difference in their weight loss as compared to the uncoated material. All of the changes in this case were not statistically significant. As with the NBR data, the plots of the permeation rate from the start of the test (illustration 69) closely followed the weight change plots. As can be seen, the copper coating produced a very small reduction in the permeation rate, while the aluminum coating produced a small increase. Again, this was not statistically significant.

The permeation rate from the start of the test increased slightly to a maximum value at approximately 192 hours and then slightly decreased for the rest of the test. The maximum rate of permeation as calculated from this method was $2.88 \text{ mg}/(\text{m}^2 \cdot \text{sec})$ for the uncoated material, $2.99 \text{ mg}/(\text{m}^2 \cdot \text{sec})$ for the aluminum coated material, and $2.58 \text{ mg}/(\text{m}^2 \cdot \text{sec})$ for the copper coated material. The final permeation rates in $\text{mg}/(\text{m}^2 \cdot \text{sec})$ at 648 hours as calculated by this method were 2.04 for the uncoated material, 2.09 for the aluminum coated, and 2.33 for the copper coated material. The permeation rate between data points was again more telling. As can be seen in illustration 70, the permeation rate increased to a maximum for all of the samples and then slowly decreased, approaching a level rate. The aluminum coating provided for no reduction in the permeation rate.

The copper coating did provide for a reduction in the permeation rate between points with an eventual cross-over, where the permeation rate of the coated material is greater than the uncoated material. Again, this is most likely due to pervaporation of the solvents in the Fuel C blend, which will be discussed in that section. The permeation rates were 2.92, 2.91, and 2.54 mg/(m²*sec) for the uncoated material, aluminum, and copper coated samples respectively. At 648 hours, these rates were 1.74, 1.67, and 1.97 mg/(m²*sec) for the uncoated, aluminum and copper coated materials. In summary, the aluminum coating provides for a reduction in the permeation rate of 1% at 192 hours and 4% at 648 hours. The copper coating provided a permeation reduction of 13% at 192 hours and an increase of 13% at 648 hours.

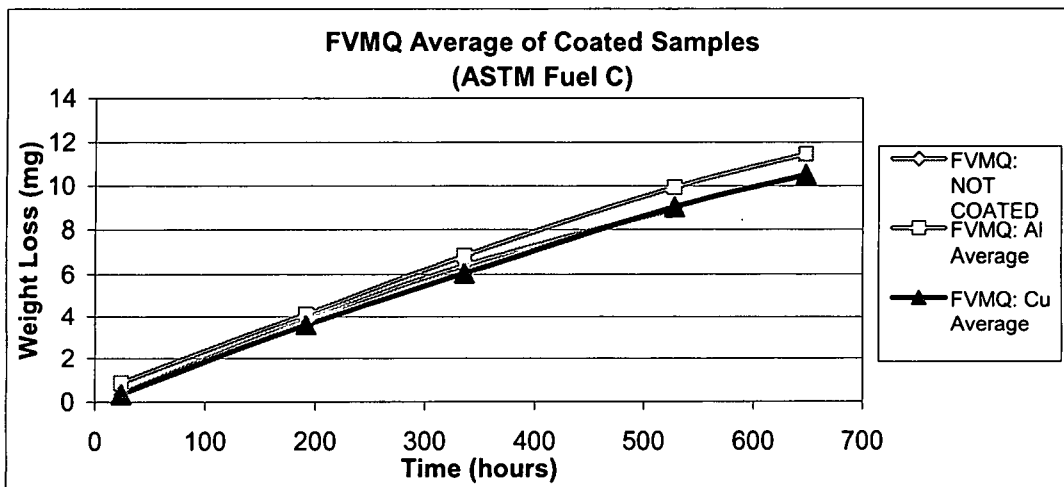


Illustration 68: FVMQ Average of Coated Samples

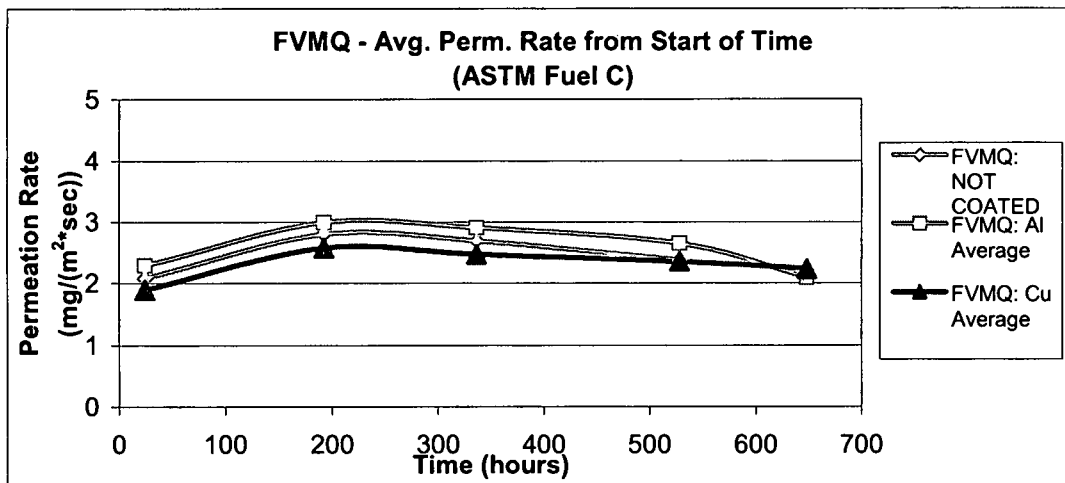


Illustration 69: FVMQ - Avg. Perm. Rate from Start of Time

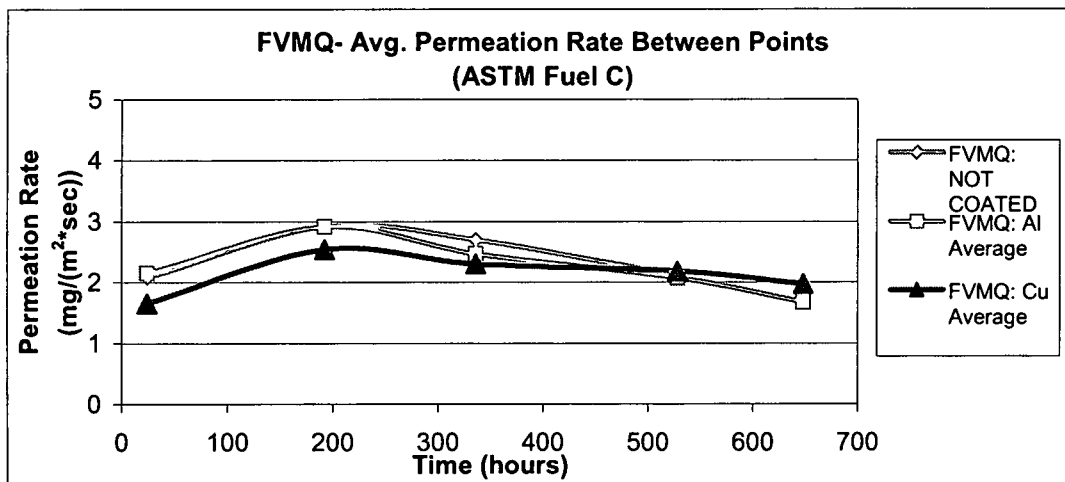


Illustration 70: FVMQ- Avg. Permeation Rate Between Points

As can be seen in illustration 71, the weight change over time for the FKM samples was so low that there is no statistical difference between them. In fact, the actual weight change is so close to zero, that the actual readings are within the experimental error of the test equipment. As with the NBR and FVMQ, the graph of the permeation rate from the start of the test closely followed the weight change data. Illustration 72 indicates that the permeation rate was so low that it was almost impossible to measure. The rate was basically zero through the whole test. The permeation rate between data points also indicates that the permeation rate was approximately zero for all of the samples (illustration 73). Again, any variation is not significant. Since the permeation levels are so low, no changes due to the presence of the coatings can be measured.

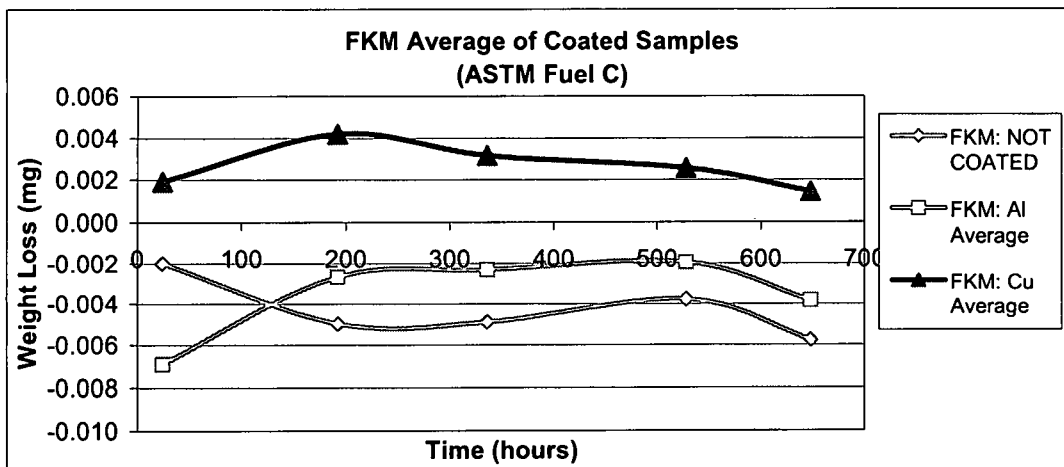


Illustration 71: FKM Average of Coated Samples

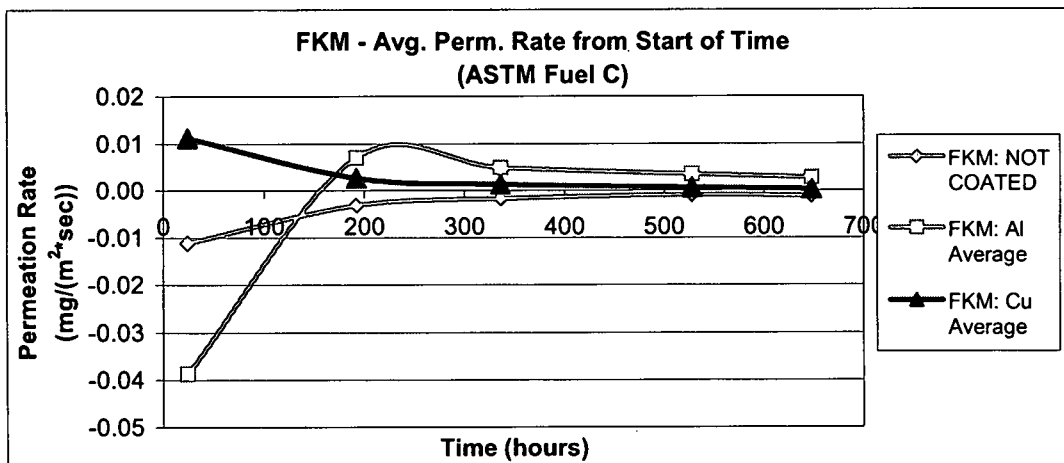


Illustration 72: FKM - Avg. Perm. Rate from Start of Time

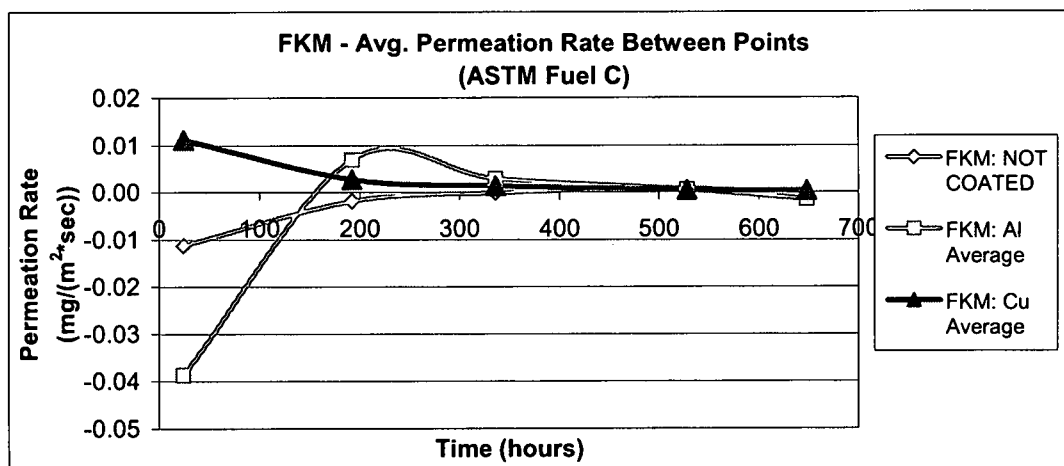


Illustration 73: FKM - Avg. Permeation Rate Between Points

The permeation rates for these materials were taken from the between points permeation values at 192 hours. The solubility parameter for these materials can be calculated from the total swell data as described in Chapter 2, using equation 26. Since the permeation rate is the product of the solubility and the rate of diffusion, the diffusion parameter was determined by dividing the solubility into the permeation rate. Table 17 summarizes the permeation coefficient values of the base polymers. As can be seen, the NBR had a permeation rate quite a bit higher than that of the FVMQ, 4.29 versus 2.92 mg/(m²*sec). The FKM had an extremely low permeation rate, as would be expected.

Using the porous membrane permeation equation (equation 13), the metallic coating substrate coverage was also calculated. Table 18 summarizes the results of these calculations. On average, the metallic coverage area for the NBR samples was approximately 40%. For the FVMQ samples, the coverage area was approximately 68%. The FKM had excellent coverage, near 100%. It is interesting to note that both the copper and aluminum coatings had such similar coverage areas. This indicates that the coatings were very similar in their deposition thickness, as were the characteristics of the cracks and pores in the coating.

As can be seen from these results, the actual reductions in the permeation rate of the coated materials was much less than the predicted reductions. The actual percentage reductions for the NBR was 11% for aluminum coating and 29% for copper coating as apposed to the predicted value of 77%. For the

FVMQ, the actual percentage reductions were 4% for the aluminum coating and 13% for the copper coating as apposed to the predicted value of 72%.

The majority of this lack of permeation reduction can be attributed to the actual coating area coverage, as the NBR had only 40% cohesive coating area coverage and the FVMQ had only a 70% cohesive coating area coverage, as a good portion of the sputtered particles passed into the substrate material. Additionally, swelling of the substrate material, although constrained somewhat by the mesh in the testing apparatus also adds to the permeation rate, as the swelling of the substrate material will increase the area of the substrate not covered by the coating.

Table 17: Permeation Coefficients

Fuel C Permeation			
	P (mg/(m ² *sec))	D (mg/(m ² *sec))	S (g/g)
NBR	4.29	34.05	0.126
FVMQ	2.92	66.36	0.044
FKM	0	0.07	0.011

Table 18: Membrane Coverage

Fuel C Permeation				
	Coating Material	Open Area (cm ²)	Covered Area (cm ²)	Percentage Covered
NBR	Al	12.60	7.67	38%
	Cu	12.22	8.05	40%
FVMQ	Al	6.66	13.61	67%
	Cu	6.29	13.98	69%
FKM	Al	0.03	20.24	100%
	Cu	0.02	20.25	100%

3.3.3 Pervaporation Testing

One possible characteristic of these membranes is that they may be operating as pervaporation membranes, allowing one of the fuel species to permeate through, while blocking the package of the other. To investigate this, IR spectra were taken of untested test fuel C and post-permeation NBR test fuel with copper coating (test sample number 29). This fuel was yellow in color, whereas the test fuel C is clear. These IR results for are shown in illustrations 74 through 76. The first two IR spectra (Illustrations 74 and 75) are for toluene and isooctane, with their peak labels assigned. The charts following list the correlating vibrational modes associated with these peaks (Tables 19 and 20). As can be seen, these solvents have completely different IR spectra, which are related to the nature of the chemical bonds within their structures. These differences in IR spectra make it possible to detect the change in solvent make-up in the Fuel C as it permeates through the sample membranes. The next two IR spectra (illustrations 76 and 77) and composition tables (tables 21 and 22) are of the Fuel C prior to usage in the permeation test and after permeation in sample number 29 (copper coated NBR).

As can be seen, the nature of the Fuel C changed dramatically over the time period of 648 hours in the permeation cup. The toluene peaks have all decreased dramatically, with some of them being totally absent. The isooctane peaks remain present and show an increase in their concentration. This indicates that toluene permeated through the samples at a much faster rate than the isooctane, leaving an isooctane rich solution behind. An inference from this

data can be made to calculate the separation factor of the membrane for this fuel composition, using equation 15. The relative molar ratio of toluene to isooctane for Fuel C is 1.55. The relative molar ratio of toluene to isooctane for the remaining fuel in the permeation cup after permeation is 0.44. These values yield an actual separation factor of 3.5, indicating that these membranes are indeed acting as pervaporation membranes, allowing the toluene to permeate through the samples, while retaining the isooctane due to its lower permeation rate.

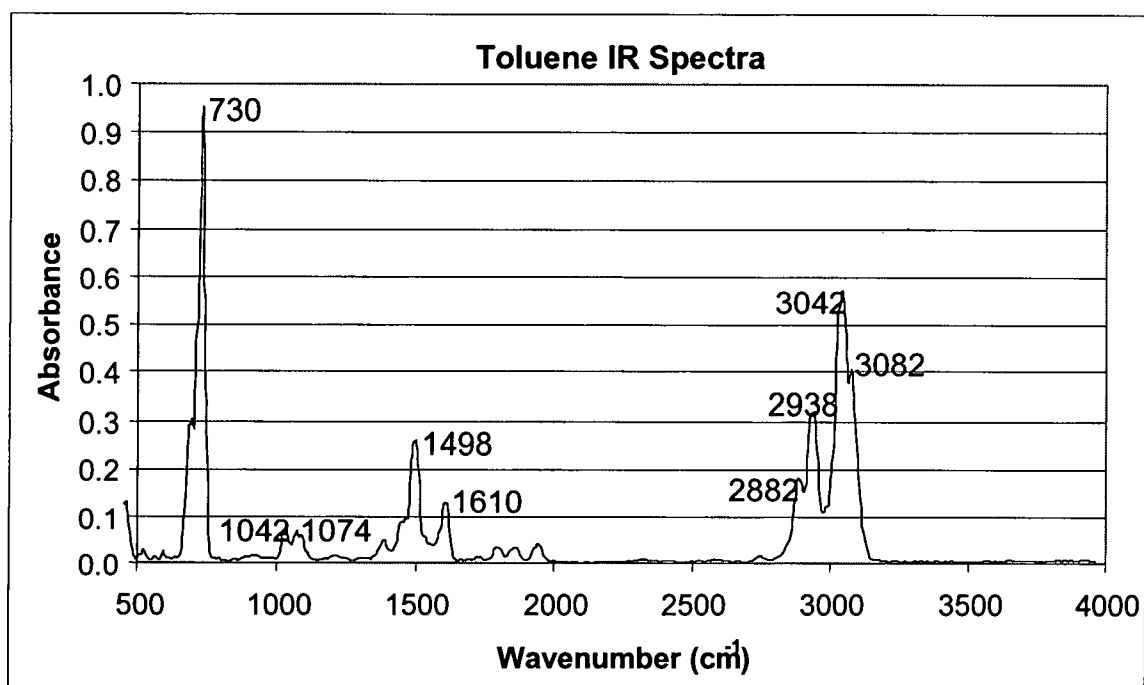


Illustration 74: Toluene IR Spectra

Table 19: Toluene - IR Absorption

Peak	Bond Type	Compound	Frequency (cm ⁻¹)	Absorbance
730	C-H out-of-plane	Aromatic	900-675	0.950
1042	C-H in-plane	Aromatic	1150-1000	0.070
1074	C-H in-plane	Aromatic	1150-1000	0.070
1498	C=C in-ring	Aromatic	1500-1400	0.262
1610	C=C in-ring	Aromatic	1600-1585	0.131
2882	C-H stretching	Alkane	3000-2850	0.183
2938	C-H stretching	Alkane	3000-2850	0.319
3042	C-H stretching	Aromatic	3100-3000	0.575
3082	C-H stretching	Aromatic	3100-3000	0.396

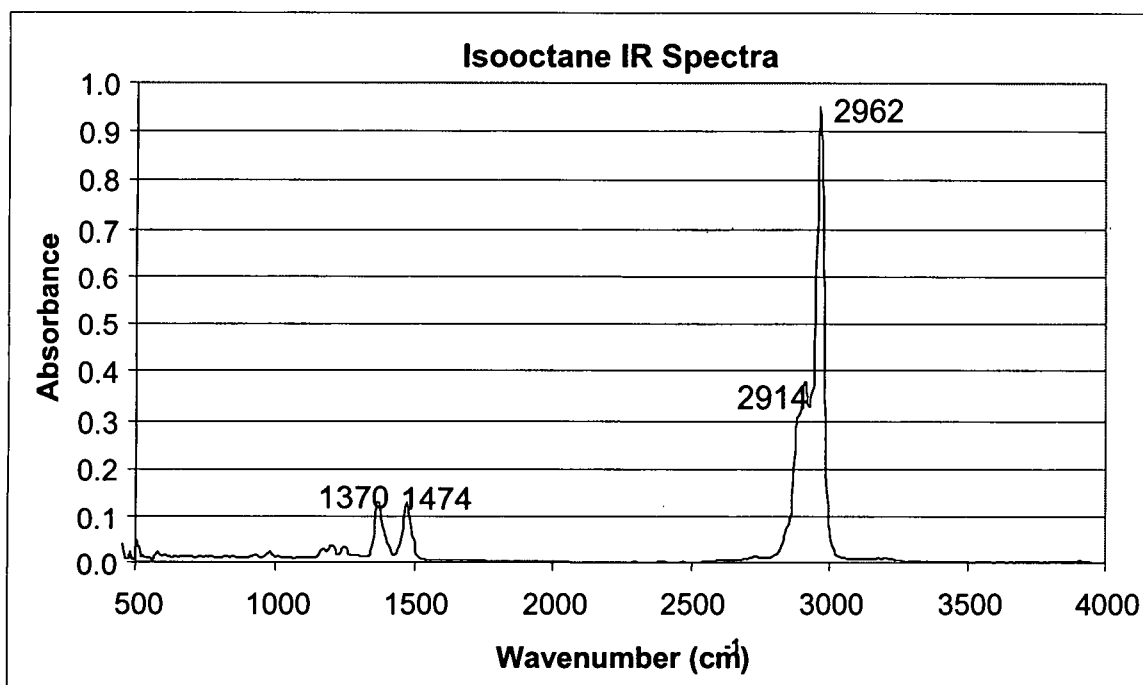


Illustration 75: Isooctane IR Spectra

Table 20: Isooctane - IR Absorption

Peak	Bond Type	Compound	Frequency (cm ⁻¹)	Absorbance
1370	C-H rocking	Alkane	1370-1350	0.130
1474	C-H	Alkane	1470-1450	0.129
2914	C-H stretching	Alkane	3000-2850	0.378
2962	C-H stretching	Alkane	3000-2850	0.950

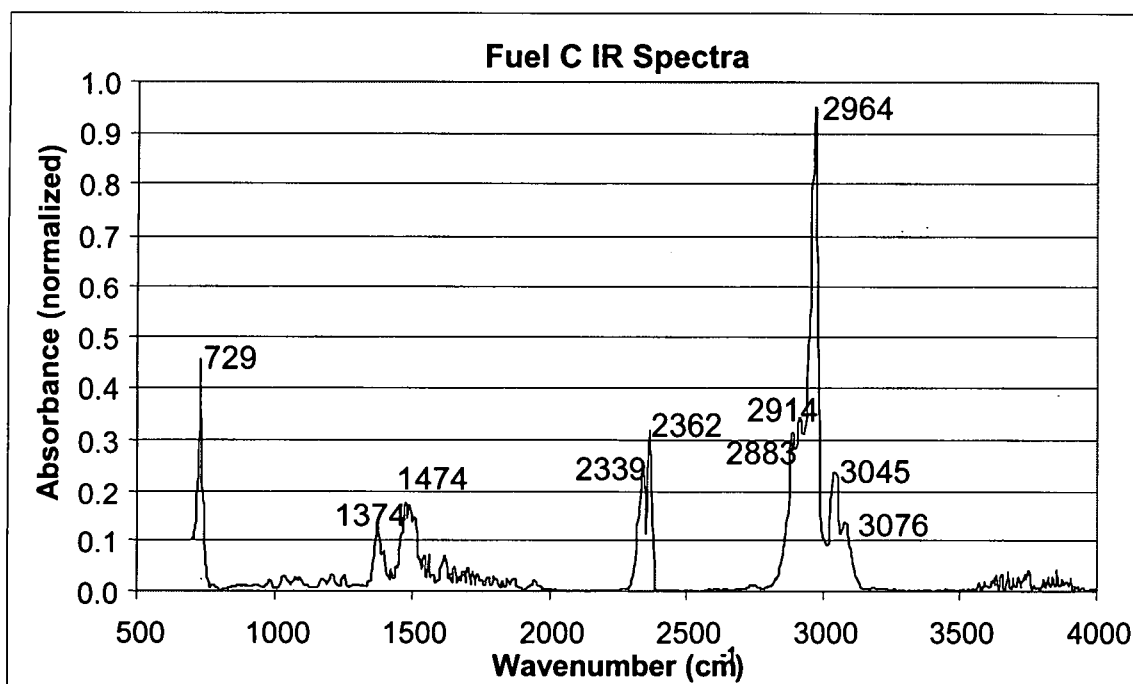


Illustration 76: Fuel C IR Spectra

Table 21: Fuel C - IR Absorption

Peak	Bond Type	Compound	Frequency (cm ⁻¹)	Source	Absorb.
729	C-H out-of-plane	Aromatic	900-675	Toluene	0.450
1374	C-H rocking	Alkane	1370-1350	Isooctane	0.127
1474	C=C in-ring	Aromatic	1500-1400	Toluene	0.177
2339	C≡C stretch	Alkyne	2260-2100	Contam.	0.237
2362	C≡C stretch	Alkyne	2260-2100	Contam.	0.318
2883	C-H stretching	Alkane	3000-2850	Isooctane	0.317
2914	C-H stretching	Alkane	3000-2850	Isooctane	0.344
2964	C-H stretching	Alkane	3000-2850	Isooctane	0.950
3045	C-H stretching	Aromatic	3100-3000	Toluene	0.238
3076	C-H stretching	Aromatic	3100-3000	Toluene	0.140

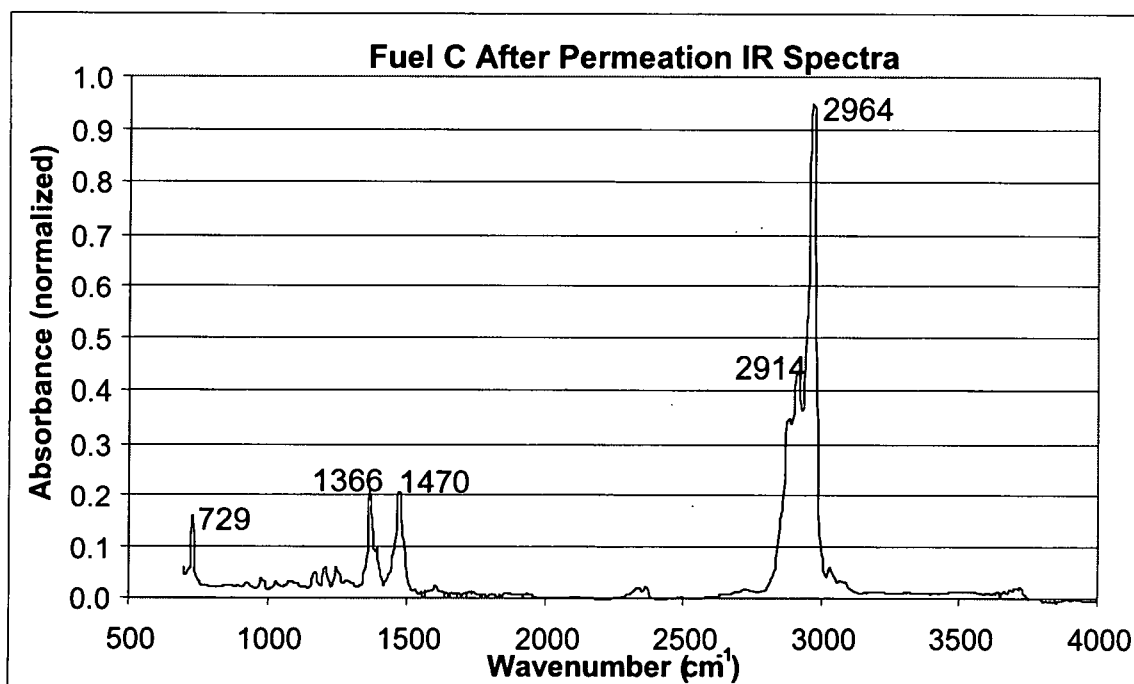


Illustration 77: Fuel C After Permeation IR Spectra

Table 22: Post-Permeation Fuel C – IR Absorption

Peak (cm ⁻¹)	Bond Type	Compound Type	Frequency (cm ⁻¹)	Source	Absorb	% Chg
729	C-H out-of-plane bending	Aromatic	900-675	Toluene	0.16	-64%
1366	C-H rocking	Alkane	1370-1350	Isooctane	0.207	63%
1470	C-H scissor/bending	Alkane	1470-1450	Isooctane	0.205	16%
2914	C-H stretching	Alkane	3000-2850	Isooctane	0.436	27%
2964	C-H stretching	Alkane	3000-2850	Isooctane	0.95	0%
Toluene Average Change						-64%
Isooctane Average Change						26%

To further evaluate the pervaporation properties of these membranes, permeation testing was performed with only toluene and only isooctane with both the NBR and FVMQ samples. For this testing, permeation test fixtures were prepared with only toluene or isooctane. For the NBR, the toluene weight change was much greater than the isooctane weight change as shown in illustration 78. This is in good agreement with the Hansen Solubility Parameters, where the NBR/toluene mix has an interaction radius parameter of 0.78 as compared to the NBR/isooctane with an interaction parameter radius of 1.27. As the interaction parameter is less than 1 for toluene, toluene falls within the radius of interaction for NBR, indicating it would completely solvate the NBR without the presence of cross-links in the NBR material. For the NBR/isooctane, this value is greater than 1, indicating a limited amount of swelling and permeation is to be expected.

There was no discernable change in the weight loss of isooctane or toluene through the NBR material due to the addition of the copper coating as shown in illustrations 79 and 80. For the FVMQ, the weight loss of toluene through the samples was also much higher than the isooctane (illustration 81). This is also to be expected, as the interaction parameter radius for the FVMQ/toluene is 1.39 and for the FVMQ/isooctane is 1.65. As such, the permeation would be expected to be greater for the toluene than for the isooctane. There was no reduction in the weight loss of either toluene or isooctane from the addition of the copper coating to the surface of FVMQ, as shown in illustrations 82 and 83.

For the NBR material, the permeation data shows that the toluene permeation was greatest at the beginning of the test and then decreased towards some level rate over time (illustration 84). This would seem to indicate that as the toluene permeates through the material, there was a decrease in the difference in partial pressure of toluene across the membrane and therefore a reduction in the driving force for permeation to occur. The permeation rate for toluene was much higher than for isooctane (13.15 versus 0.001 mg/(m²*sec)).

For the isooctane, the permeation appeared to slowly ramp up and then the rate decreased to some level rate (illustrations 84 through 86). This form is consistent, but the accuracy is questionable, as the permeation rate was extremely low in both cases. The toluene permeation was the same for the coated and uncoated NBR samples, decreasing from the start of the test. This is consistent with the weight loss data. This can be seen in illustrations 85 and 86.

The permeation rate of the toluene and isooctane was flat through the FVMQ, as seen in illustration 87. This would indicate that the partial pressure of these solvents did not decrease significantly over the test period. Again the permeation rate of toluene was much higher than isooctane (4.0 versus 0.4 mg/(m²*sec)). There was no improvement in the permeation rate of toluene or isooctane through the FVMQ due to the copper coating, as seen in illustrations 88 and 89.

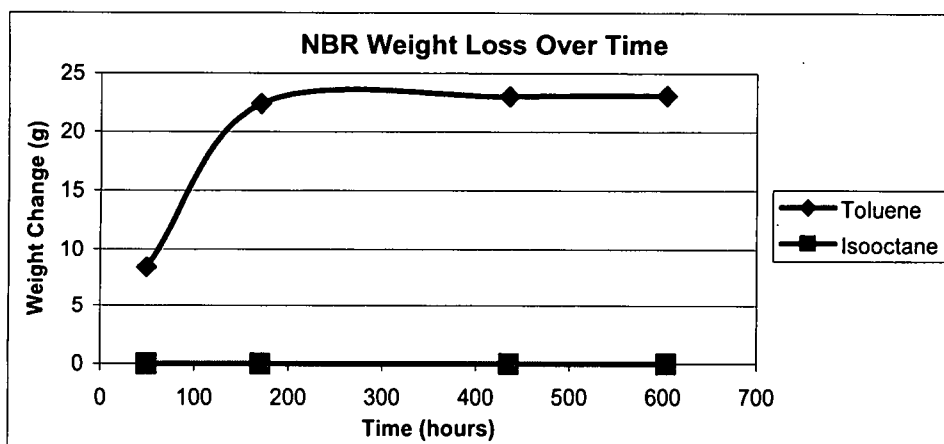


Illustration 78: NBR Weight Loss Over Time

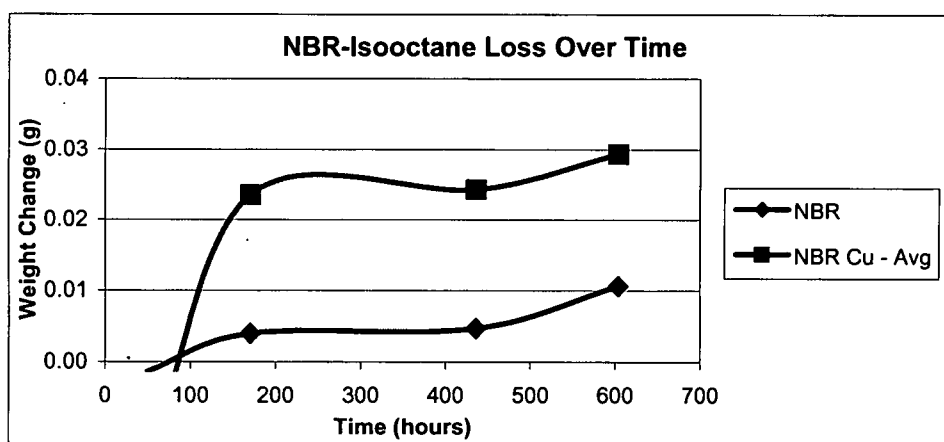


Illustration 79: NBR-Isooctane Loss Over Time

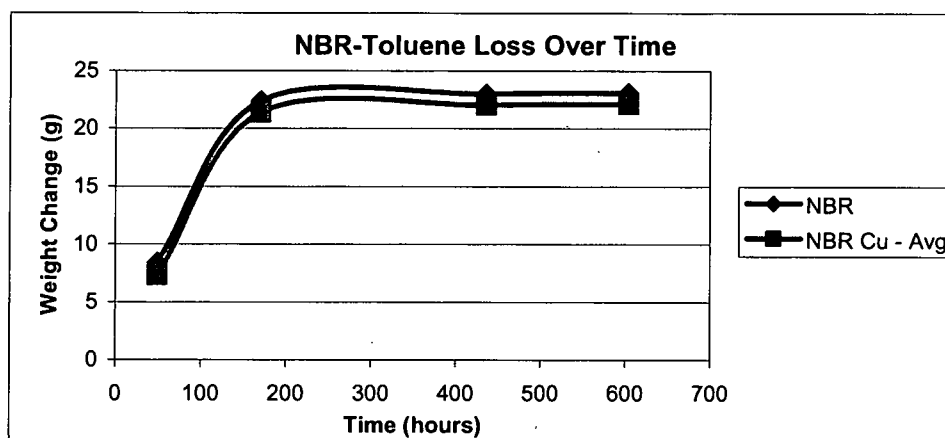


Illustration 80: NBR-Toluene Loss Over Time

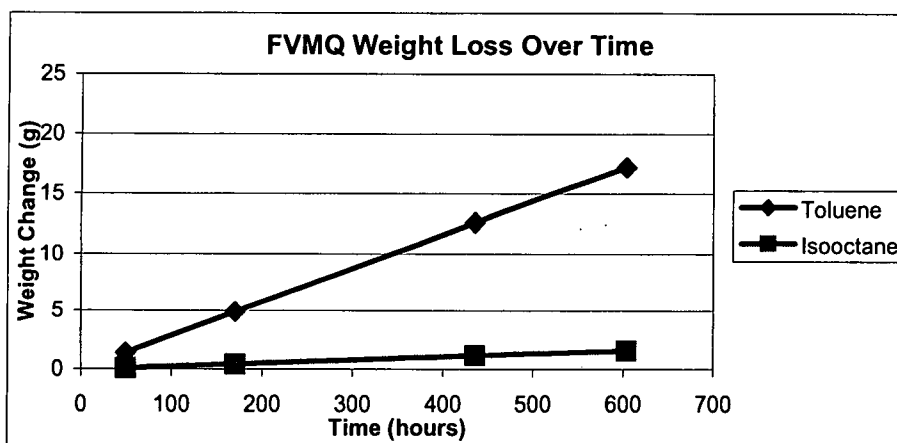


Illustration 81: FVMQ Weight Loss Over Time

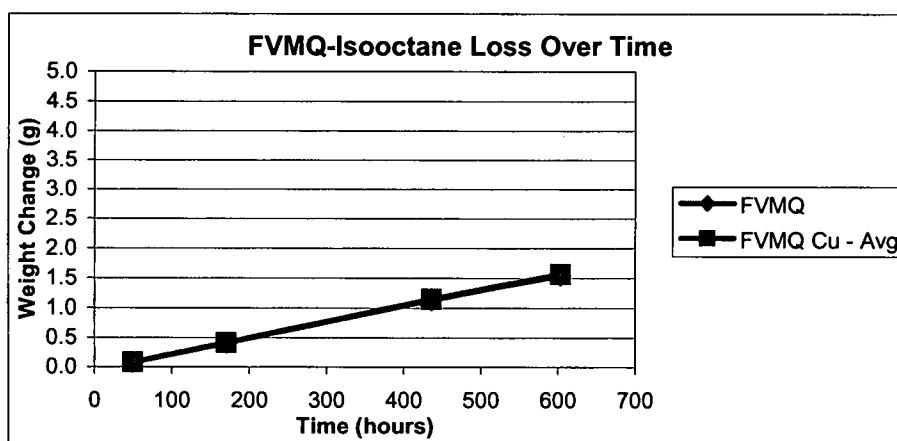


Illustration 82: FVMQ-Isooctane Loss Over Time

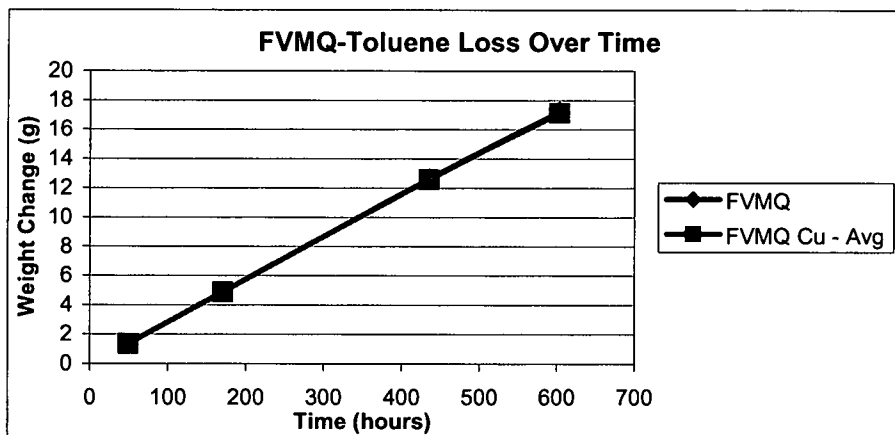


Illustration 83: FVMQ-Toluene Loss Over Time

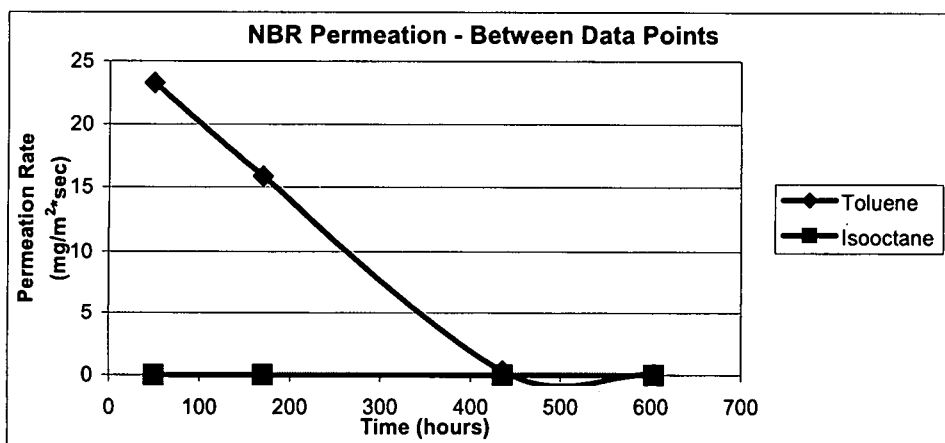


Illustration 84: NBR Permeation - Between Data Points

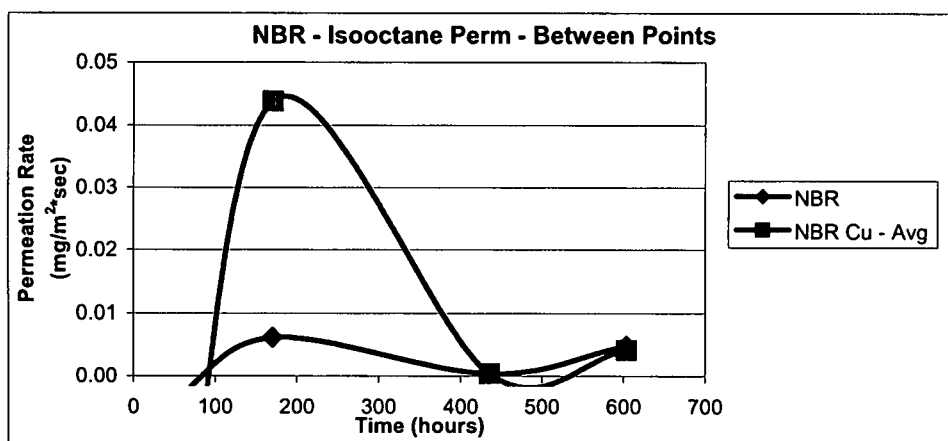


Illustration 85: NBR - Isooctane Permeation - Between Points

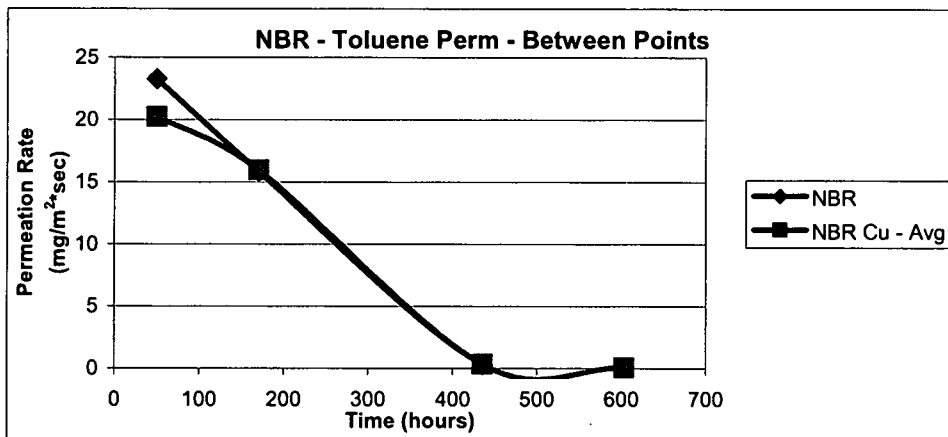


Illustration 86: NBR - Toluene Permeation - Between Points

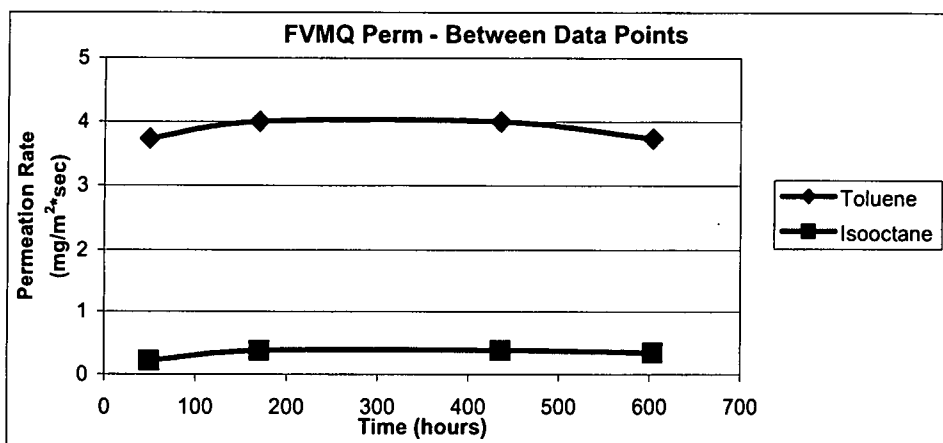


Illustration 87: FVMQ Perm - Between Data Points

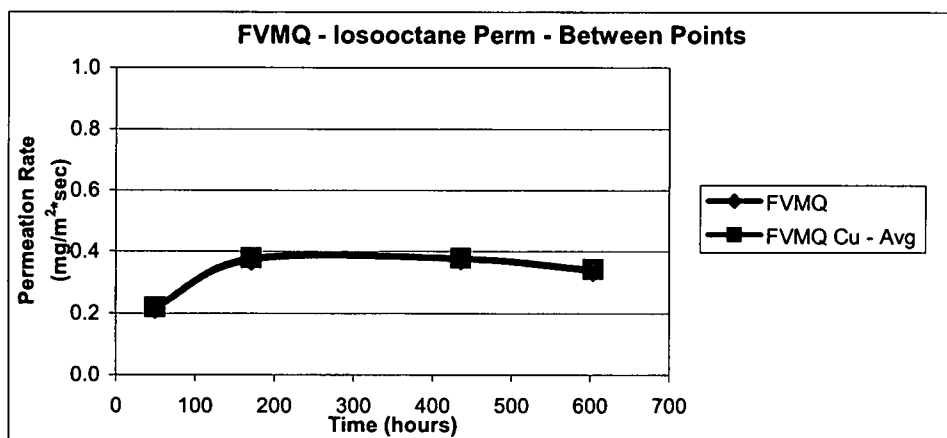


Illustration 88: FVMQ - Isooctane Perm - Between Points

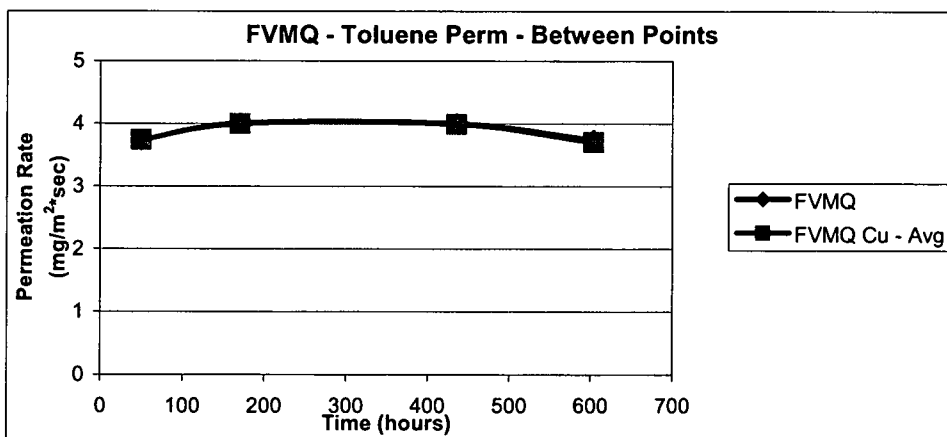


Illustration 89: FVMQ - Toluene Perm - Between Points

Tables 23 and 24 show the permeation coefficients for toluene and isooctane in NBR and FVMQ. These calculations were performed in the same manner as for Fuel C. As can be seen, the permeation rate for toluene in NBR was a great deal higher than for isooctane (13.15 versus 0.006 mg/(m²*sec)). This is due to both a higher diffusion coefficient and higher solubility. In the case of FVMQ, the permeation rate was also higher for toluene than for isooctane (3.91 versus 0.33 mg/(m²*sec)), but the difference was not nearly as great as for NBR. Again, this was due to an increase in both the solubility and diffusion coefficient. From this data, the idealized interaction parameter has been calculated using equation 14. For NBR, this factor was 2378, which is an extremely high factor. The actual separation factor, as determined by the IR analysis was 3.5. For the FVMQ, this factor was 11.84. This indicates that, although both copper coated FVMQ and NBR could be used to separate toluene and isooctane, NBR would be much more efficient.

Table 23: Permeation Coefficients: Toluene Permeation

	P (mg/(m ² *sec))	D (mg/(m ² *sec))	S (g/g)
NBR	13.15	32.49	0.41
VMQ	3.91	36.07	0.11

Table 24: Permeation Coefficients: Isooctane Permeation

	P (mg/(m ² *sec))	D (mg/(m ² *sec))	S (g/g)
NBR	0.006	0.14	0.04
FVMQ	0.33	18.12	0.02

CHAPTER 4

SUMMARY, CONCLUSIONS, AND RECOMMENDATIONS

4.1 Summary

4.1.1 Visual Observation

In the 30X views, the NBR and FVMQ samples exhibited porosity which was not evident in the FKM samples. In the SEM pictures, this porosity became more pronounced, with large cracks and pores visible in the NBR and FVMQ samples with the aluminum coating. There was some minor porosity visible in the FKM coating, but the percentage of area covered was much higher than for the NBR and FVMQ samples. The calculated sample coverage percentages for these samples were 40%, 70%, and 95% for the NBR, FVMQ, and FKM respectively.

In the side-views from SEM, it can be seen that the aluminum particles penetrated deeply into the surfaces of the FVMQ and NBR. There was no discernable coating on the fluorosilicone samples, but there is a wide mixed region of combined metallic and insulating materials, indicating that the aluminum atoms have penetrated the surface. The NBR also had a mixed region, but did show some evidence of a pure metallic region on the surface. In contrast to

these, the FKM material had a well-defined boundary between the metallic coating and the substrate with no measurable penetration into the substrate material.

Since it seems likely the amount of particles implanted into a material and the depth of implantation is related to the density of the substrate material it was assumed that there is a relationship between the implantation of ions in sputtering and the density of the coated materials. One can see evidence of this by examining illustration 90, which compares the percentage of area coated to the interaction radius of the polymers themselves and the density of the specific material formulations used for the substrates. It is apparent that many of the metallic coating particles have passed into the low density NBR material, whereas the majority of the sputtered atoms have been stopped at the surface of the FKM material. The FVMQ material, being of a density between the two has a corresponding coating area coverage.

This decrease in implantation of the substrate particles can also be correlated to the reduction in permeation through these materials. As the amount of implantation occurs and the coating area decreases, the lower-density materials should see less of a reduction in their permeation rates as compared to the higher density materials. As can be seen in Illustration 91, there is good correlation between the decrease in permeation rate from the coating and the density of the substrate material. As such, this also supports the conclusion that the higher density materials prevent ion implantation leading to the production of a cohesive coating at the surface.

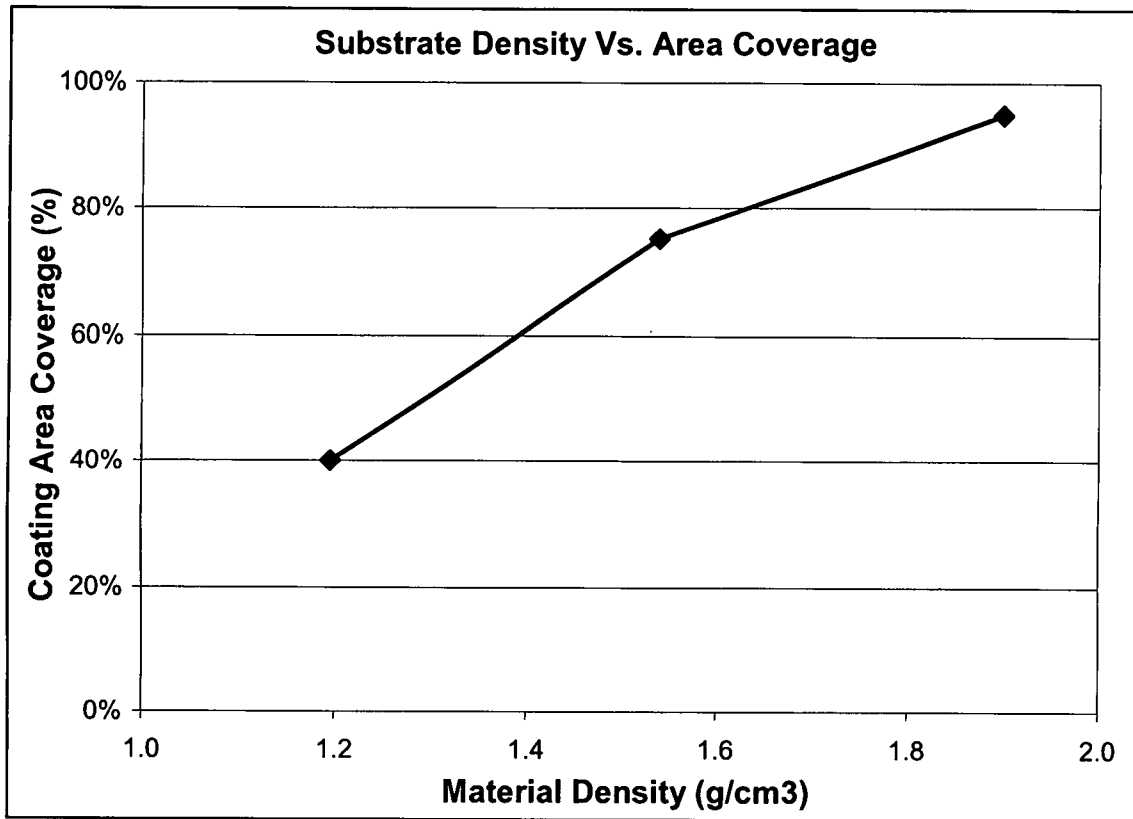


Illustration 90: Substrate Density Vs. Area Coverage

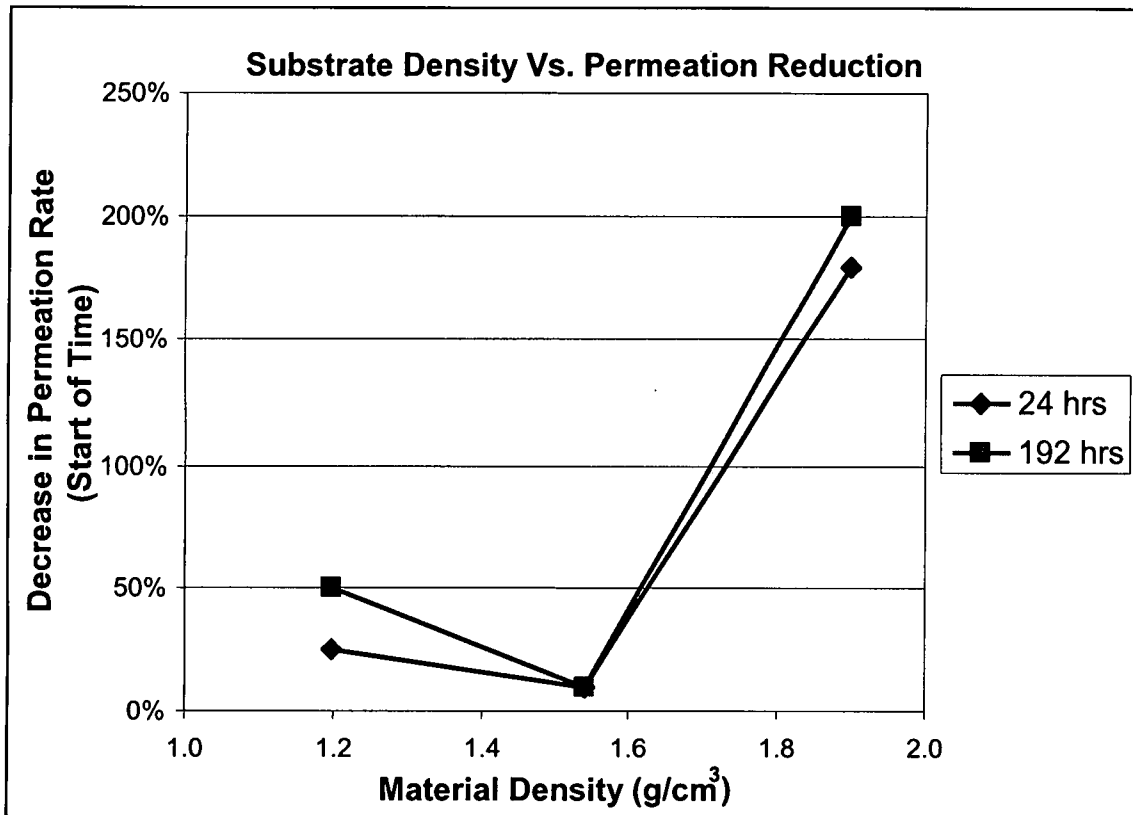


Illustration 91: Substrate Density Vs. Permeation Reduction

4.1.2 Mechanical Evaluation

The results of the adherence testing indicate that both the aluminum and copper coatings were very well adhered to the substrate materials. The flexure and elongation of the surface of the parts imparted a large degree of strain into this coating. As there was no flaking of the coating material or breakage in the coated sections from the surface, the coating must have been sufficiently well adhered and flexible enough to withstand these mechanical insults. This indicates that sputtering of these micro-scale particles has produced a flexible membrane with minor gaps on the surface of the substrates, with good adhesion, possibly due to implantation of some of the coating particles.

The tensile testing of these parts has provided evidence that the metallic coatings on these parts were sufficiently thin and flexible enough to prevent causing an undesired increase in the stiffness of these elastomeric substrates, as measured by the elastic modulus. However, it does appear that the implantation of these metallic atoms has degraded the substrate material. All of the modulus and tensile strengths decreased with the application of the coatings. The average decrease in tensile modulus at 10% elongation for the aluminum coated materials was 11%. The average decrease for the copper coated materials was 14%. There is good correlation between these results and the visual observation of the area coverage, as the aluminum coatings induced a greater decrease in the substrate modulus of these samples than the copper coatings, and the visual data indicates that there is greater implantation of aluminum particles than copper particles. These decreases are most likely due to polymer

chains scission and cleavage at the surface from the thermal insult induced by the deposition process and the implantation of the metallic atoms. However, the reduction in the modulus of these substrate materials is slight, indicating that the mechanical properties of these materials would not be significantly compromised by the addition of these metallic coatings.

4.1.3 Swell Testing

As expected from the Hansen solubility parameters, the NBR had the highest swell in fuel C (13%) followed by the FVMQ (4.4%) and the FKM (1.1%). There was a relationship between the average Hansen solubility parameter for Fuel C (average of toluene and isooctane) and the percentage swell in Fuel C as shown in illustration 94. As would be expected, as the Hansen Solubility Parameter for a polymer/solvent pair increases, the amount of swelling from that solvent and polymer pair decreases. This indicates that these parameters can be used to predict the comparative swelling phenomenon of elastomers in these test fuels and verifies that the swelling of these materials follows a reasonable trend.

There was a small decrease in the swelling rate of NBR and FVMQ with the aluminum and copper coatings. In general, the copper material was better than the aluminum material at preventing swell in the substrate material. The mechanism for this decreased must be a reduction in the rate of the solvent flux into the substrate. In addition, the general trend is that increased coating thickness yields a decreased swelling rate. As the thickness of the coating

correlates well with the swelling data, it can be surmised that there is an increase in the coverage ratio of the coating with increasing thickness, further limiting the allowable permeation area. For the FKM, there was no significant change in the swelling rate. For the NBR and FVMQ, the change in swelling is most likely due to a change in the flux of the material into the samples. In this testing, the test fuel was in contact only with one side of the membrane. As such, full swelling was not possible as the fuel could permeate away from the outside surface. Therefore, the decrease in swell with the application of these materials was due to the coating limiting the flux rate of the solvent into the sample. The coating was not expected to affect the solubility parameter of the substrate materials. As such, these results are not surprising as the permeation reduction from the coating was expected to be the result of limiting the diffusion rate through the material. In this case these coatings do not seem to be limiting the amount of test fuel entering the substrate polymer, as shown in illustration 62. This is most likely because, unlike the NBR and FVMQ materials, the permeation rate through the FKM is so slow that the permeation through the coating is not significantly reduced, so as to affect the swelling of this material.

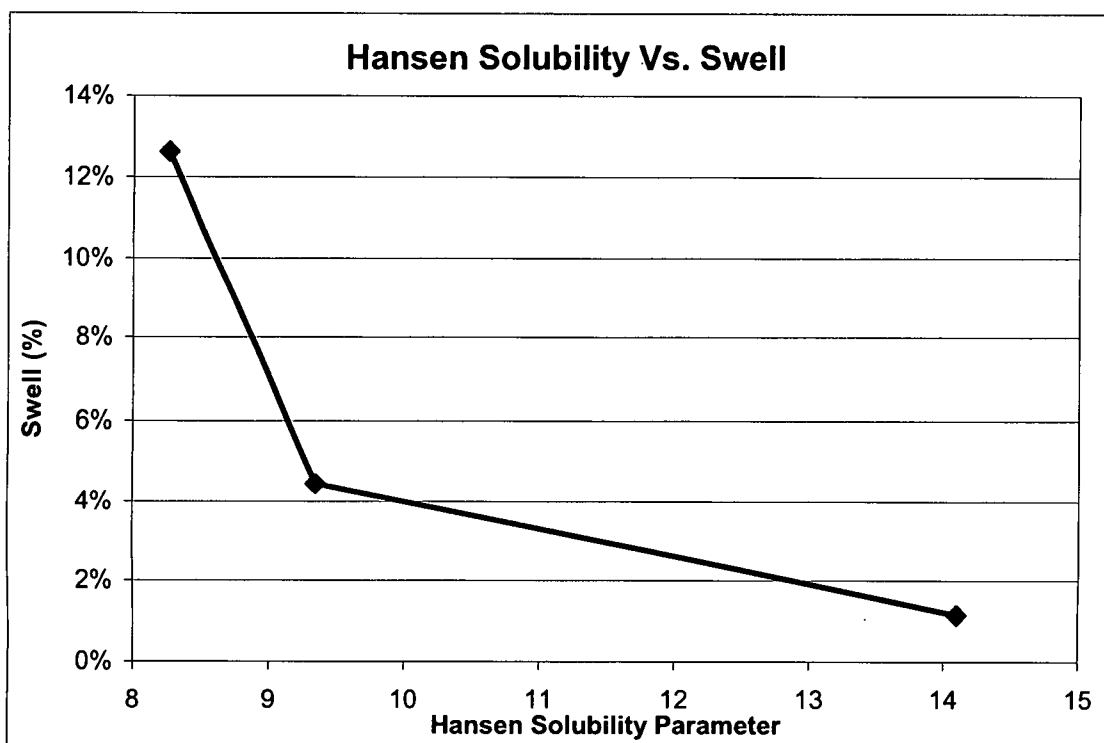


Illustration 92: Hansen Solubility Vs. Swell

4.1.4 Weight Loss and Permeation

The weight change and permeation rate from the start of time correlated with each other quite well as expected as the permeation rate is calculated directly from the weight loss information. The permeation rate between points was also reflective of the same condition, but provides the most telling information about the permeation process. As such, these permeation values are used for the discussion that follows on the permeation phenomenon. The permeation results for the base polymeric materials and solvents were also in agreement with the Hansen Solubility Parameter as would be expected since the permeation rate is a product of the solubility and diffusion. Illustration 95 is a chart, which displays the linear relationship between the Hansen Solubility Parameter and the permeation rate. These parameters can be used to predict the permeation trends of Fuel C in these polymer and solvent pairs.

The application of the aluminum and copper coatings to these materials did provide for a decrease in the permeation rate for the NBR and FVMQ substrates. The permeation of the FKM was so low that no difference could be detected. The copper and aluminum coatings provided similar levels of permeation reduction for both materials. The average reduction at 192 hours was 13%. This was followed by an average increase of 15% at 648 hours. This could indicate that the permeation rate was reduced early in the permeation process, delaying the permeation of the Fuel C. Eventually the permeation of this fuel occurs, leading to higher permeation rates later in the test cycle.

Using the permeation rate at 192 hours the amount of coverage by the aluminum and copper coatings has been determined. This coverage was approximately 40% for the NBR, 68% for the FVMQ substrates and 100% for the FKM samples. Again, the results for the copper and aluminum were very similar and correlate well with the visual observation of the sample coverage area under SEM. As such, it is reasonable to assume that the permeation of fuel through these membranes was slowed as a result of the decrease in the surface area of the elastomeric material that was exposed to the test fuel as expected. All of this evidence suggests that the fuel permeation reduction for any of these polymers is primarily dependent upon the coverage area of the coating. The improved response of copper as compared to aluminum appears to be related more to the increased coverage obtained with the copper coating, than to the nature of the metal itself. Again, this indicates that the substrate density is important, as the coverage area is dependent upon the amount of implantation into the substrate materials, which reduces the coating area coverage. However, the results of the statistical evaluation of the permeation rate data indicates that the coating thickness is not important. This supports the validity of the porous membrane model for the permeation method through the coating, as the permeation rate is dependent upon the coating area coverage and not the thickness of the coating.

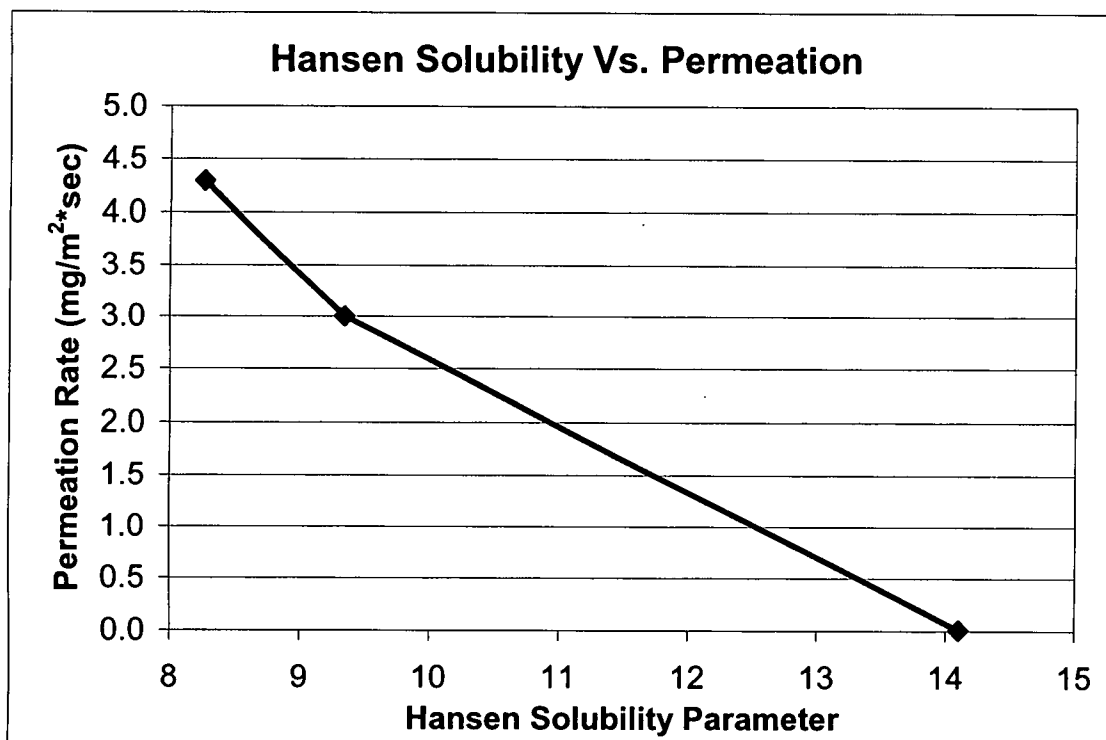


Illustration 93: Hansen Solubility Vs. Permeation

4.1.5 Pervaporation

The infrared spectroscopy performed on the Fuel C material before and after permeation provides definitive proof that the NBR membrane was operating as a pervaporation membrane. As expected by the Hansen Solubility Parameters, the toluene material permeates through the substrate membrane much more quickly than the isooctane. In the case of NBR, this actual separation factor has been inferred to be 3.5. The individual fuel permeation of toluene and isooctane also support the supposition that pervaporation was occurring. The toluene permeation rate through NBR was several orders of magnitude greater than isooctane. The permeation rate of toluene through FVMQ was one order of magnitude greater than isooctane. As such, both of these materials would be expected to work as pervaporation membranes.

The fact that pervaporation was occurring can be used to explain the odd shapes of the diffusion curves of Fuel C through these materials, whereby the permeation increased to some high level and then decreased to some slower level rate. In this case, the toluene permeated out quickly and preferentially through these materials, to the point where the concentration of toluene in the test fuel began to decrease quickly, leading to lower permeation rates of the isooctane rich fuel. The addition of the metallic coatings to these substrates did provide for some reduction in the permeation of toluene, in the range of 4%. There was some evidence that the copper coatings on NBR provided for a reduction in the permeation of isooctane. With the rate of permeation of isooctane being so low, a decrease in the permeation rate of isooctane should

yield an even more pronounced pervaporation effect in the NBR membranes. However, in the bulk Fuel C, the reduction in the permeation of Fuel C provided by these substrates was due to the reduction in the permeation rate of the toluene species in the fuel C blend.

4.2 Conclusions

Both aluminum and copper can be applied by magnetron sputtering to these elastomers to form a cohesive well-adhered coating that does not break or flake-off due to flexing of the underlying substrate. Physically, these coatings are well adhered and maintain their structure, without void formation and coating cracking when it was stretched. By producing a thin coating of distinct micro-scale particles and implanting some number of particles into the surface, a coating can be produced that is quite flexible and resilient with a large coverage area. These coatings have a minimal effect on the physical properties of the coating substrates by reducing the modulus of the substrate material due to effects of sputtering and implantation of the metallic particles into the substrate. These thin flexible coatings are compliant enough to be coated onto the elastomeric substrates without decreasing the flexibility of the materials. In summary, these coatings can be applied to elastomeric substrates without negatively affecting the substrates flexibility, ability to seal, or its ability to conform to a shape.

The sample coverage area of the sputtered coatings is dependent upon the substrate density due to increased implantation of the sputtered metallic particles into the lower density substrates. The permeation rate reduction itself is also related to the substrate density as those coatings with higher coverage areas have better permeation resistance. The permeation reduction dependent upon the coating area coverage and is thickness independent.

As a means of reducing the permeation rate of fuels through these substrates, these metallic coatings applied at these thickness levels are of minimal value. They did provide for some reduction (approximately 15%) due to limiting the surface area of the substrate elastomer in contact with the fuel, but do not form a hermetic seal of the substrate, which could eliminate permeation completely. Even though these coatings did provide for a reduction in the permeation rate of fuel C by limiting the area of the substrate in contact with the test fuel, the permeation reduction was relatively modest and did not produce a composite with equivalent properties to the FKM material.

It was found that the toluene permeates through this material much more rapidly than the isooctane. The addition of these coatings reduced the permeation of toluene approximately 4% in the case of coating NBR. There was no apparent reduction in the permeation of isooctane, but the permeation of isooctane was at such a low level, a reduction may not have been noticeable. This testing did reveal that the permeation of Fuel C through these membranes leads to a reduction in the toluene content of the solvent blend, especially as evident in the NBR with the copper coating, as the toluene permeated through

the membrane. This led to an isooctane-rich solvent being left behind in the permeation cup. As such, the NBR with a copper coating can be used to produce a separation cell for toluene and isooctane.

4.3 Recommendations

The coatings applied in this study were very thin, in the range of 100 nm. The sputtered metal coatings penetrated quite deeply into the substrate material, and did not produce a cohesive hermetic layer on the surface. As such, it is recommended that additional work be done in sputtering the metal particles onto the surface to achieve higher thickness levels. It would also be advised to investigate lower sputtering energies, which may produce a better coating with less penetration and therefore a more homogeneous surface coating.

Although the adherence of these coatings was found to be quite good, it would be important to evaluate the adherence of these coatings after repeated stretching and flexing. This would be a very important property of the metallic coating for any elastomeric application that requires the component to be used dynamically.

These substrate materials were inherently poor for permeation resistance. As such, other elastomers with more inherent permeation resistance should be evaluated with these coatings applied to them. Ideally these elastomers would have higher densities, thus decreasing the level of implantation that occurs in the sputtering process. This will again help to form a cohesive layer on the surface.

These materials should be evaluated for their ability to prevent permeation of other solvents and chemicals. The pore size produced by permeation in this case may be sufficient to prevent the permeation of larger molecules, such as proteins in dialysis applications. Additional substrate materials should also be investigated for the evaluation of their pervaporation properties. These materials could have some functional use as separation membranes for other solvents or fluids.

There are many other possible uses for the unique properties of these metallic-coated elastomers. Due to the pervaporative properties of these coated materials, they could find use as filters. The metallic coating layer could also be used as a novel technique for the joining of elastomers by soldering. This metallic coating could also be used for the prevention of UV-degradation of elastomers. In addition, by masking the substrate prior to sputtering, it would be possible to produce flexible circuit boards.

For the application of this technology, the production process would need to be scaled-up beyond this laboratory method. This would require the use of a large-scale sputtering unit. For this manufacturing method to be financially feasible, this chamber would integrate reel-to-reel transfer mechanism within the chamber for coating continuous strips of material without needing to pump out the vacuum chamber between components. By utilizing this method, the sputtering process can continue unhindered, thus increasing the throughput rates. It would also be possible with this type of method, using multiple targets, to produce multi-layer coatings on the elastomeric substrates.

BIBLIOGRAPHY

- 1) N. von Solms, N. Zecchin, A. Rubin, S. I. Andersen, E. H. Stenby, European Polymer Journal 41 (2005) p. 341-348, Direct measurement of gas solubility and diffusivity in poly(vinylidene fluoride) with a high pressure microbalance.
- 2) S. D. Epke, L. W. Bezuidenhout, S. K. Dew, Thin Solid Films 474 (2005) p. 330-336, Deposition Rate model of magnetron sputtered particles.
- 3) E. Lugscheider, K. Bobzin, M. Maes, A. Kramer, Thin Solid Films 459 (2004) p. 313-317, On the coating of polymers – basic investigations.
- 4) D. Rivin, R. S. Lindsay, W. J. Shuely, A. Rodriguez, Journal of Membrane Science 246 (2005) p. 39-47, Liquid permeation through nonporous barrier materials.
- 5) D. Rivin, R. S. Lindsay, W. J. Shuely, A. Rodriguez, Journal of Membrane Science 246 (2005) p. 39-47, Liquid permeation through nonporous barrier materials.
- 6) J. Scholz, G. Nocke, F. Hollstein, A. Weissbach, Surface and Coatings Technology 192 (2005) p. 252-256, Investigations on fabrics coated with precious metals using the magnetron sputter technique with regard to their anti-microbial properties.
- 7) J.-H. Boo, M. J. Jung, H. K. Park, K. H. Nam, J. G. Han, Surface and Coatings Technology 188-189 (2004) p. 721-727, High-rate deposition of copper thin films using newly designed high-power magnetron sputtering source.
- 8) B. Feddes, J. G. C. Wolke, A. M. Bredenberg, J. A. Jansen, Biomaterials 25 (2004) p. 633-639, Initial deposition of calcium phosphate ceramic on polyethylene and polydimethylsiloxane by rf magnetron sputter deposition: the interface chemistry.

- 9) M. G. De Angelis, G. C. Sarti, A. Sanguineti, P. Maccone, Journal of Polymer Science: Part B: Polymer Physics, Vol. 42 (2004) p. 1987-2006, Permeation, Diffusion, and Sorption of Dimethyl Ether in Fluoroelastomers.
- 10) G. Gozzelino, G. Malucelli, Colloids and Surfaces A: Physiochemical Engineering Aspects 235 (2004) p. 35-44, Permeation of methanol/methyl-t-butyl ether mixtures through poly(ethylene-co-vinyl acetate) films.
- 11) T. Nakahigashi, Y. Tanaka, K. Miyake, H. Oohara, Tribology International 37 (2004) p. 907-912, Properties of flexible DLC film deposited by amplitude-modulated RF P-CVD.
- 12) A. Joseph, A. E. Mathai, S. Thomas, Journal of Membrane Science 220 (2003) p. 13-30, Sorption and diffusion of methyl substituted benzenes through cross-linked nitrile rubber/poly(ethylene co-vinyl acetate) blend membranes.
- 13) K. S. Kwan, C. N. P. Subramaniam, T. C. Ward, Polymer 44 (2003) p. 3071-3083, Effect of penetrant size, shape, and chemical nature on its transport through a thermoset adhesive. II. Esters.
- 14) S. Fukuda, S. Kawamoto, Y. Gotoh, Thin Solid Films 442 (2003) p. 117-120, Degradation of Ag and Ag-alloy mirrors sputtered on poly(ethylene terephthalate) substrates under visible light irradiation.
- 15) A-C Dubreuil, F. Doumeric, B. Guerrier, D. Johannsmann, C. Allain, Polymer 44 (2003) p. 377-387, Analysis of the solvent diffusion in glassy polymer films using a set inversion method.
- 16) B. Barriere, L. Leibler, Journal of Polymer Science: Part B: Polymer Physics, Vol. 41 (2003) p. 166-182, Kinetics of Solvent Absorption and Permeation through a Highly Swellable Elastomeric Network.
- 17) B. Barriere, L. Leibler, Journal of Polymer Science: Part B: Polymer Physics, Vol. 41 (2003) p. 183-193, Permeation of a Solvent Mixture through an Elastomeric Membrane – The Case of Pervaporation.
- 18) Y. M. Chung, M. J. Jung, K. H. Nam, J. G. Han, S. H. Baeg, S. H. Yang, Surface and Coatings Technology 171 (2003) p. 65-70, A study on formation of Al and Al₂O₃ on the porous paper by DC magnetron sputtering.
- 19) E. Ho, K. Edmund, D. Peacock, Sealing Technology October (2002) p. 6-10, Effect of temperature and pressure on permeation, ageing and emissions of elastomers.

- 20) H. L. Lira, R. Paterson, Journal of Membrane Science 206 (2002) p. 375-387, New and modified anodic alumina membranes Part III. Preparation and characterization by gas diffusion of 5 nm pore size anodic alumina membranes.
- 21) A. E. Mathai, R. P. Singh, S. Thomas, Journal of Membrane Science 202 (2002) p. 35-54, Transport of substituted benzenes through nitrile rubber/natural rubber blend membranes.
- 22) S. Han, L. Puech, R. V. Law, J. H. G. Steinke, A. Livingston, Journal of Membrane Science 199 (2002) p. 1-11, Selection of elastomeric membranes for the separation of organic compounds in acidic media.
- 23) K. Rau, R. Singh, E. Goldberg, Material Research Innovations (2002) 5 p. 162-169, Synthesis and characterization of cross-linked silicone thin films by pulsed laser ablation deposition (PLAD).
- 24) S. Matsui, D. R. Paul, Journal of Membrane Science 195 (2002) p. 229-245, Pervaporation separation of aromatic/ aliphatic hydrocarbons by crosslinked poly(methyl acrylate-co-acrylic acid) membranes.
- 25) I.S. Tashlykov, A.V. Kasperovich, G.K. Wolf, Surface Coatings and Technology 158-159 (2002) p. 498-502, Elastomer surface modification by means of SAID of metal-based layers.
- 26) M. Ohring, Academic Press (2002), Materials Science of Thin Films 2nd Edition.
- 27) J. Musil, J. Lestina, J. Vlcek, T. Tolg, Journal of Vacuum Science Technology A Mar/Apr (2001) p. 420-424, Pulsed dc magnetron discharge for high-rate sputtering of thin films.
- 28) L. Yeping, F. Yue-E, F. Rong, X. Jinyun, Radiation Physics and Chemistry 60 (2001) p. 637-642, Study of plasma-polymerization deposition of C₂H₂/CO₂/H₂ onto ethylene-co-propylene rubber membranes.
- 29) N. Vahdat, V.D. Sullivan, Journal of Applied Polymer Science, Vol. 79, (2001) p. 1265-1272, Estimation of Permeation Rate of Chemicals Through Elastomeric Materials.
- 30) C. Guizard, B. Boutevin, F. Guida, A. Ratsimihety, P. Amblard, J.-C. Lasserre, S. Naiglin, Separation and Purification Technology 22-23 (2001) p. 23-30, VOC vapour transport properties of new membranes based on cross-linked fluorinated elastomers.

- 31) F. Sanchetter, A. Billard, Surface and Coatings Technology 142-144 (2001) p. 218-224, Main features of magnetron sputtered aluminum-transition metal alloy coatings.
- 32) B. Szikora, Vacuum 61 (2001) p. 397-401, Bohm criterion in magnetron plasma.
- 33) M. Ouddane, Y. Rancourt, Journal of Applied Polymer Science, Vol. 79 (2000), Sorption and Diffusion of a Brake Fluid in EPDM Elastomers.
- 34) H. Kupfer, G. K. Wolf, Nuclear Instruments and Methods in Physics Research B 166-167 (2000) p. 722-731, Plasma and ion beam assisted metallization of polymers and their application.
- 35) H. Aguilar, R. G. Kander, Society of Automotive Engineers, Inc. (2002), Number 2000-01-1099, Fuel Permeation Study on Various Seal Materials.
- 36) P. Siemroth, T. Schulke, Surface and Coatings Technology 133-134 (2000) p. 106-113, Copper metallization in microelectronics using filtered vacuum arc deposition – principles and technological development.
- 37) C. Hanson, CRC Press LLC (2000), Hansen Solubility Parameters, A User's Guide.
- 38) M. Heller, J. Legare, S. Wang, S. Fukuhara, Journal of Vacuum Science Technology A 17(4), Jul/Aug (1999), p. 2219-2124, Thermal stability and sealing performance of perfluoroelastomer seals as a function of crosslinking chemistry.
- 39) N. Nancheva, P. Docheva, M. Misheva, Materials Letters 39 (1999) p. 81-85, Defects in Cu and Cu-O films produced by reactive magnetron sputtering.
- 40) E. Kusano, K. Fukushima, T. Saitoh, S. Saiki, N. Kikuchi, H. Nanto, A. Kinbara, Surface and Coatings Technology 120-121 (1999) p. 189-193, Effects of Ar pressure on ion flux energy distribution and ion fraction in r.f.-plasma-assisted magnetron sputtering.
- 41) T. M. Minea, J. Bretagne, G. Gousset, L. Magne, D. Pagnon, M. Touzeau, Surface and Coatings Technology 116-119 (1999) p. 558-563, PIC-MCC simulation of a r.f. planar magnetron discharge and comparison with experiment.
- 42) I.S. Tashlykov, V.I. Kasperovich, M.G. Shadrukhin, A.V. Kasperovich, G.K. Wolf, W. Wesch, Surface Coatings and Technology 116-119 (1999) p. 848-

852, Elastomer treatment by arc metal deposition assisted with self-ion irradiation.

- 43) Y. Yampolskii, S. Shishatskii, A. Alentiev, K. Loza, Journal of Membrane Science 148 (1998) p. 59-69, Correlations with and prediction of activation energies of gas permeation and diffusion in glassy polymers.
- 44) Z. Radzimski, W. Posadowski, S. Rosnagel, S. Shingubara, Journal of Vacuum Science Technology B, May/June (1998) p. 1102-1106, Directional copper deposition using dc magnetron self-sputtering.
- 45) Siddaramaiah, S. Roopa, U. Premakumar, Polymer Vol. 39 No. 17 (1998) p. 3925-3931, Sorption and diffusion of aromatic penetrants into natural rubber blends.
- 46) C. C. Pereira, A. C. Habert, R. Nobrega, C. P. Borges, Journal of Membrane Science 138 (1998) p. 227-235, New insights in the removal of diluted volatile organic compounds from dilute aqueous solution by pervaporation process.
- 47) E. Lugscheider, S. Barwulf, C. Barimani, M. Riester, H. Hilgers, Surface and Coatings Technology 108-109 (1998) p. 398-402, Magnetron-sputtered hard material coatings on thermoplastic polymers for clean room applications.
- 48) P. J. Kelly, R. D. Arnell, Surface and Coatings Technology 98 (1998) p. 1370-1376, The determination of the current-voltage characteristics of a closed-field unbalanced magnetron sputtering system.
- 49) J. Musil, Vacuum, Volume 50, number 3-4 (1998) p. 363-372, Low-pressure magnetron sputtering.
- 50) R. C. Dorf, CRC Press LLC (1998), The Engineering Handbook.
- 51) T. M. Aminabhavi, S. F. Harlapur, Chemical Engineering and Processing 36 (1997) p. 363-370, Sorption and diffusion of organic liquids into engineering fluoroelastomer membranes in the temperature interval 30-60°C.
- 52) G. V. Zee, J. D. Graauw, Journal of Applied Polymer Science, Vol. 66 (1997) p. 347-353, Determination of the Diffusivity in Elastomer Solutions by Batch Sorption Studies from a Dilute Liquid Phase.
- 53) M.L. Johnson, D.M. Manos, T. Provost, Journal of Vacuum Science Technology A 15(3), May/Jun (1997), p. 763-767, Gas permeation leakage through reusable seals.

- 54) J. Schulte, G. Sobe, Surface and Coatings Technology 97 (1997) p. 510-515, Investigation of the mechanisms of magnetron sputtering of aluminum with mixtures of argon and nitrogen in the partially reactive mode.
- 55) C. Charrier, P. Jacquot, E. Denisse, J. P. Millet, H. Mazille, Surface and Coatings Technology 90 (1997) p. 29-34, Aluminum and Ti/Al multiplayer PVD coatings for enhanced corrosion resistance.
- 56) M. Knights, Plastics Technology (1997) p. 32-34, Exotic Coextrusions Produce Low Permeation Fuel Lines for Cars.
- 57) N. G. McCrum, C. P. Buckley, C. B. Bucknall, Oxford Science Publications (1997), Principles of Polymer Engineering 2nd Edition.
- 58) J. Musil, A. Rajskey, A. J. Bell, J. Matous, Journal of Vacuum Science Technology A Jul/Aug (1996) p. 2187-2191, High-rate magnetron sputtering.
- 59) G. Unnikrishnan, S. Thomas, S. Varghese, Polymer Vol. 37 No. 13 (1996) p. 2687-2693, Sorption and diffusion of aromatic hydrocarbons through filled natural rubber.
- 60) Z. N. Farhat, Y. Ding, D. O. Northwood, A. T. Alpas, Materials Science and Engineering A206 (1996) p. 302-313, Effect of grain size on friction and wear of nanocrystalline aluminum.
- 61) A. T. Mohammadi, T. Matsuura, S. Sourirajan, Gas Separation and Purification Vol. 9, No. 3, (1995) p. 181-187, Gas separation by silicone-coated dry asymmetric aromatic polyamide membranes.
- 62) M. Misina, J. Musil, Surface and Coatings Technology 74-75 (1995) p. 450-454, Plasma diagnostics of low pressure microwave-enhanced d.c. sputtering discharge.
- 63) D. Muller, Y. R. Cho, E. Fromm, Surface and Coatings Technology 74-75 (1995) p. 849-856, Adhesion strength of ductile aluminium and brittle TiN coatings on steel, aluminum and copper, measured by fracture mechanics tests.
- 64) J. F. Friedrich, L. Wigan, W. Unger, A. Lippitz, J. Erdmann, H.-V. Gorsler, D. Prescher, H. Wittrich, Surface and Coatings Technology 74-75 (1995) p. 910-918, Barrier properties of plasma and chemically fluorinated polypropylene and polyethyleneterephthalate.

- 65) Annual Book of ASTM Standards (1995), Standard Test for Rubber Property – Vapor Transmission of Volatile Liquids.
- 66) J. R. Fried, Prentice Hall PTR (1995), Polymer Science and Technology.
- 67) H. Hahn, R. S. Averback, Journal of Applied Physics 67 (1990) p. 1113-1115, The production of nanocrystalline powders by magnetron sputtering.
- 68) A. N. Pargellis, Journal of Vacuum Science Technology A Nov/Dec (1987) p. 3412-3416, Distribution of copper deposited inside holes by sputtering.
- 69) S. Swann, Journal of Vacuum Science Technology A Jul/Aug (1987) p. 1750-1754, Spatial distribution of sputtered atoms from magnetron source.
- 70) L. T. Ball, I. S. Falconer, D. R. McKenzie, J. M. Szmelt, Journal of Applied Physics 59 (1986) p. 720-724, An interferometric investigation of the thermalization of copper atoms in a magnetron sputtering discharge.
- 71) L. Laurenson, N. T. M. Dennis, Journal of Vacuum Science Technology A May/Jun (1985), Permeability of common elastomers for gases over a range of temperatures.

APPENDIX A: SUPPORTING DATA

Swell in ASTM Test Fuel C

Table 25: Nitrile Swell Data

Nitrile Butadiene Rubber - Aluminum Swell in ASTM Test Fuel C				Nitrile Butadiene Rubber - Copper Swell in ASTM Test Fuel C			
NBR: NOT COATED				NBR: NOT COATED			
Test Number	Starting Weight	Final Weight	Percent Swell	Test Number	Starting Weight	Final Weight	Percent Swell
16	5.1428	5.7747	12.3%	16	5.1428	5.7747	12.3%
17	5.1017	5.7628	13.0%	17	5.1017	5.7628	13.0%
Average	5.1223	5.7688	12.6%	Average	5.12225	5.76875	12.6%
NBR: ALUMINUM - 10 mTorr				NBR: COPPER - 10 mTorr			
Test Number	Starting Weight	Final Weight	Percent Swell	Test Number	Starting Weight	Final Weight	Percent Swell
14	5.0697	5.7741	13.9%	10	5.1107	5.7421	12.4%
18	5.0697	5.7027	12.5%	10	5.0498	5.5708	10.3%
Average	5.0697	5.7384	13.2%	Average	5.0803	5.6565	11.3%
NBR: ALUMINUM - 20 mTorr				NBR: COPPER - 20 mTorr			
Test Number	Starting Weight	Final Weight	Percent Swell	Test Number	Starting Weight	Final Weight	Percent Swell
15	5.1098	5.7034	11.6%	10	5.0949	5.7553	13.0%
19	5.1098	5.7882	13.3%	10	5.1038	5.6297	10.3%
Average	5.1098	5.7458	12.4%	Average	5.0994	5.6925	11.6%
NBR: ALUMINUM - 30 mTorr				NBR: COPPER - 30 mTorr			
Test Number	Starting Weight	Final Weight	Percent Swell	Test Number	Starting Weight	Final Weight	Percent Swell
20	5.0765	5.6961	12.2%	10	5.0975	5.7525	12.8%
21	5.0854	5.7653	13.4%	10	5.1264	5.6898	11.0%
Average	5.0810	5.7307	12.8%	Average	5.1120	5.7212	11.9%
NBR: Average Values							
No Coating	Al Average	Cu Average					
12.6%	12.8%	11.6%					

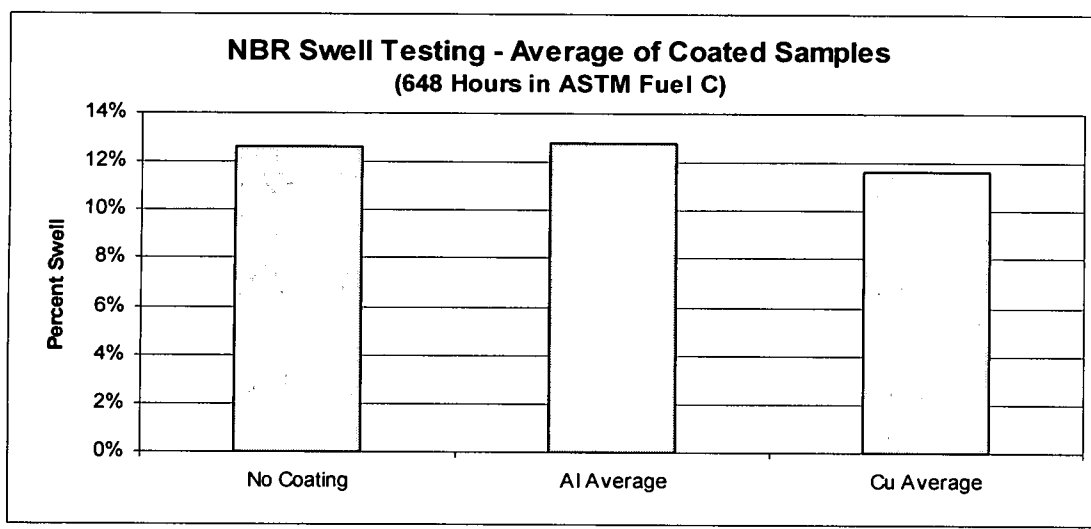
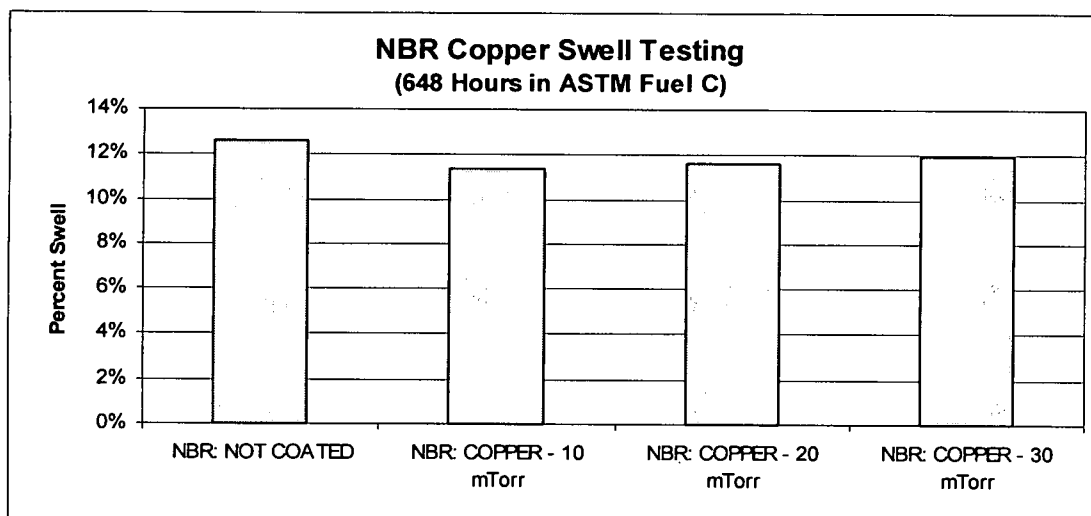
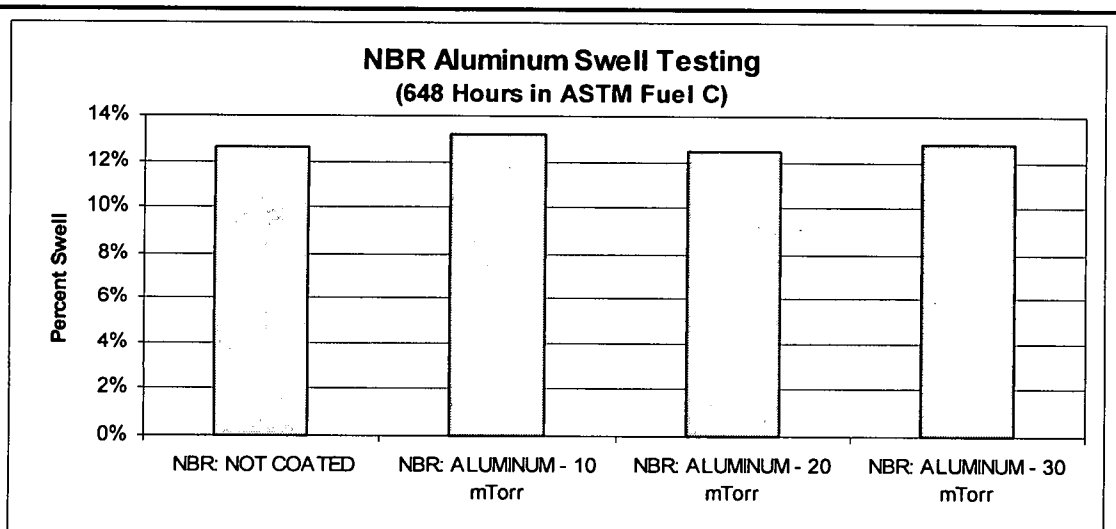


Illustration 94: Nitrile Swell Diagrams

Table 26: Fluorosilicone Swell Data

Fluorosilicone Rubber - Aluminum Swell in ASTM Test Fuel C				Fluorosilicone Rubber - Copper Swell in ASTM Test Fuel C			
FVMQ: NOT COATED				FVMQ: NOT COATED			
Test Number	Starting Weight	Final Weight	Percent Swell	Test Number	Starting Weight	Final Weight	Percent Swell
1	6.5805	6.8637	4.3%	1	6.5805	6.8637	4.3%
2	6.5873	6.8892	4.6%	2	6.5873	6.8892	4.6%
Average	6.5839	6.8765	4.4%	Average	6.5839	6.87645	4.4%
FVMQ: ALUMINUM - 10 mTorr				FVMQ: COPPER - 10 mTorr			
Test Number	Starting Weight	Final Weight	Percent Swell	Test Number	Starting Weight	Final Weight	Percent Swell
22	6.5914	6.8983	4.7%	27	6.6151	6.9009	4.3%
23	6.6543	6.9063	3.8%	36	6.6526	6.9184	4.0%
Average	6.6229	6.9023	4.2%	Average	6.6339	6.9097	4.2%
FVMQ: ALUMINUM - 20 mTorr				FVMQ: COPPER - 20 mTorr			
Test Number	Starting Weight	Final Weight	Percent Swell	Test Number	Starting Weight	Final Weight	Percent Swell
12	6.6268	6.7601	2.0%	28	6.5509	6.8256	4.2%
24	6.6268	6.8940	4.0%	37	6.6632	6.9265	4.0%
Average	6.6268	6.8271	3.0%	Average	6.6071	6.8761	4.1%
FVMQ: ALUMINUM - 30 mTorr				FVMQ: COPPER - 30 mTorr			
Test Number	Starting Weight	Final Weight	Percent Swell	Test Number	Starting Weight	Final Weight	Percent Swell
13	6.5789	6.8223	3.7%	29	6.5897	6.8459	3.9%
25	6.5789	6.8313	3.8%	38	6.6252	6.8842	3.9%
Average	6.5789	6.8268	3.8%	Average	6.6075	6.8651	3.9%
FVMQ: Average Values							
No Coating	Al Average	Cu Average					
4.4%	3.7%	4.0%					

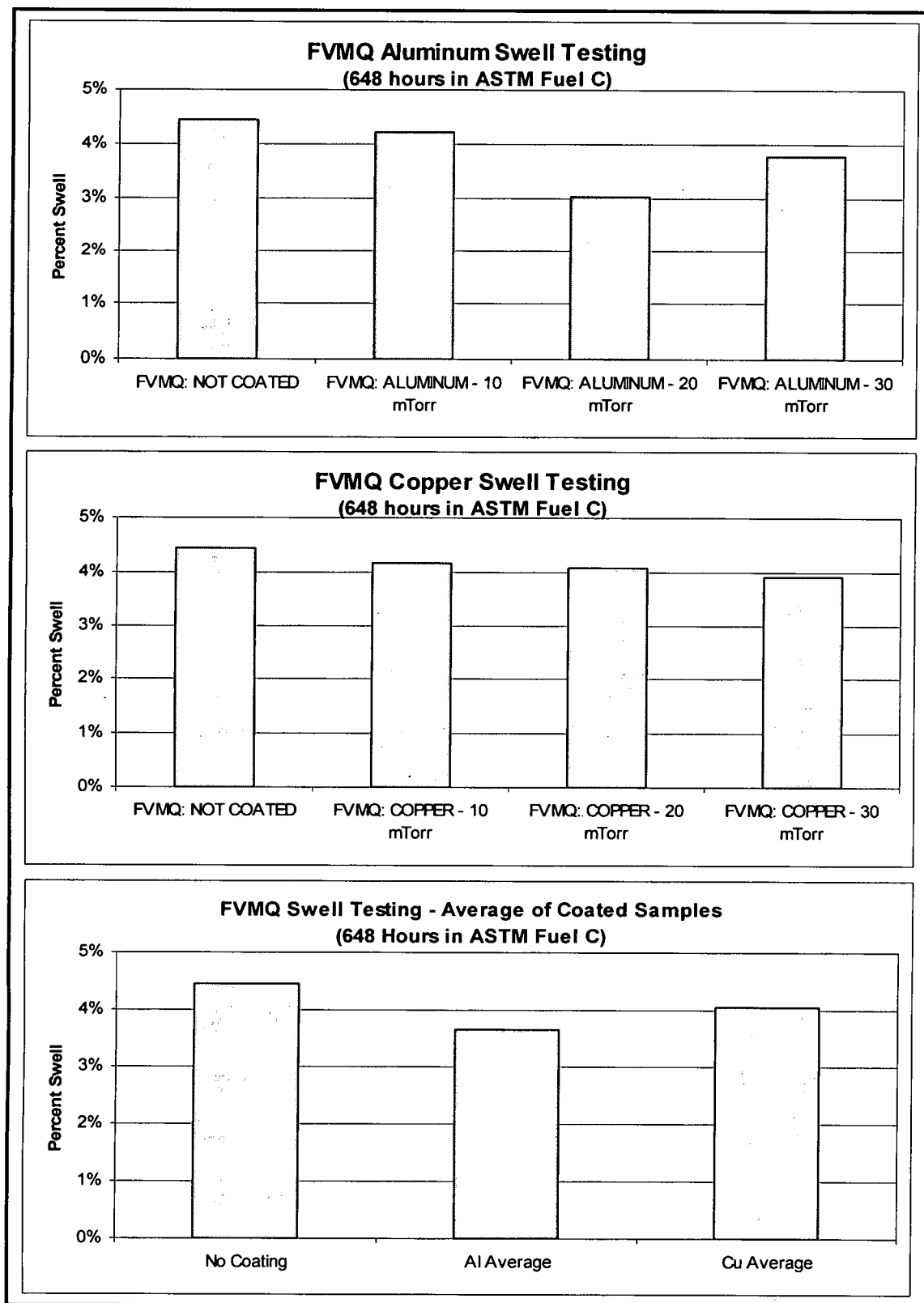


Illustration 95: Fluorosilicone Swell Diagrams

Table 27: Fluorocarbon Swell Data

Fluorocarbon Rubber - Aluminum Swell in ASTM Test Fuel C				Fluorocarbon Rubber - Copper Swell in ASTM Test Fuel C			
FKM: NOT COATED				FKM: NOT COATED			
Test Number	Starting Weight	Final Weight	Percent Swell	Test Number	Starting Weight	Final Weight	Percent Swell
3	8.4242	8.5190	1.1%	3	8.4242	8.519	1.1%
4	8.3931	8.4914	1.2%	4	8.3931	8.4914	1.2%
Average	8.4086	8.5052	1.1%	Average	8.40865	8.5052	1.1%
FKM: ALUMINUM - 10 mTorr				FKM: COPPER - 10 mTorr			
Test Number	Starting Weight	Final Weight	Percent Swell	Test Number	Starting Weight	Final Weight	Percent Swell
5	8.3010	8.3935	1.1%	33	8.6948	8.7566	0.7%
6	8.4245	8.5175	1.1%	42	8.6898	8.8035	1.3%
Average	8.3627	8.4555	1.1%	Average	8.6923	8.7801	1.0%
FKM: ALUMINUM - 20 mTorr				FKM: COPPER - 20 mTorr			
Test Number	Starting Weight	Final Weight	Percent Swell	Test Number	Starting Weight	Final Weight	Percent Swell
9	8.5814	8.6741	1.1%	34	8.7600	8.8775	1.3%
10	8.3781	8.4721	1.1%	43	8.6921	8.8087	1.3%
Average	8.4798	8.5731	1.1%	Average	8.7261	8.8431	1.3%
FKM: ALUMINUM - 30 mTorr				FKM: COPPER - 30 mTorr			
Test Number	Starting Weight	Final Weight	Percent Swell	Test Number	Starting Weight	Final Weight	Percent Swell
11	8.4781	8.5714	1.1%	35	8.4979	8.6166	1.4%
Average	8.4781	8.5714	1.1%	44	8.5313	8.6446	1.3%
FKM: Average Values				Average	8.5146	8.6306	1.4%
No Coating	Al Average	Cu Average					
1.1%	1.1%	1.2%					

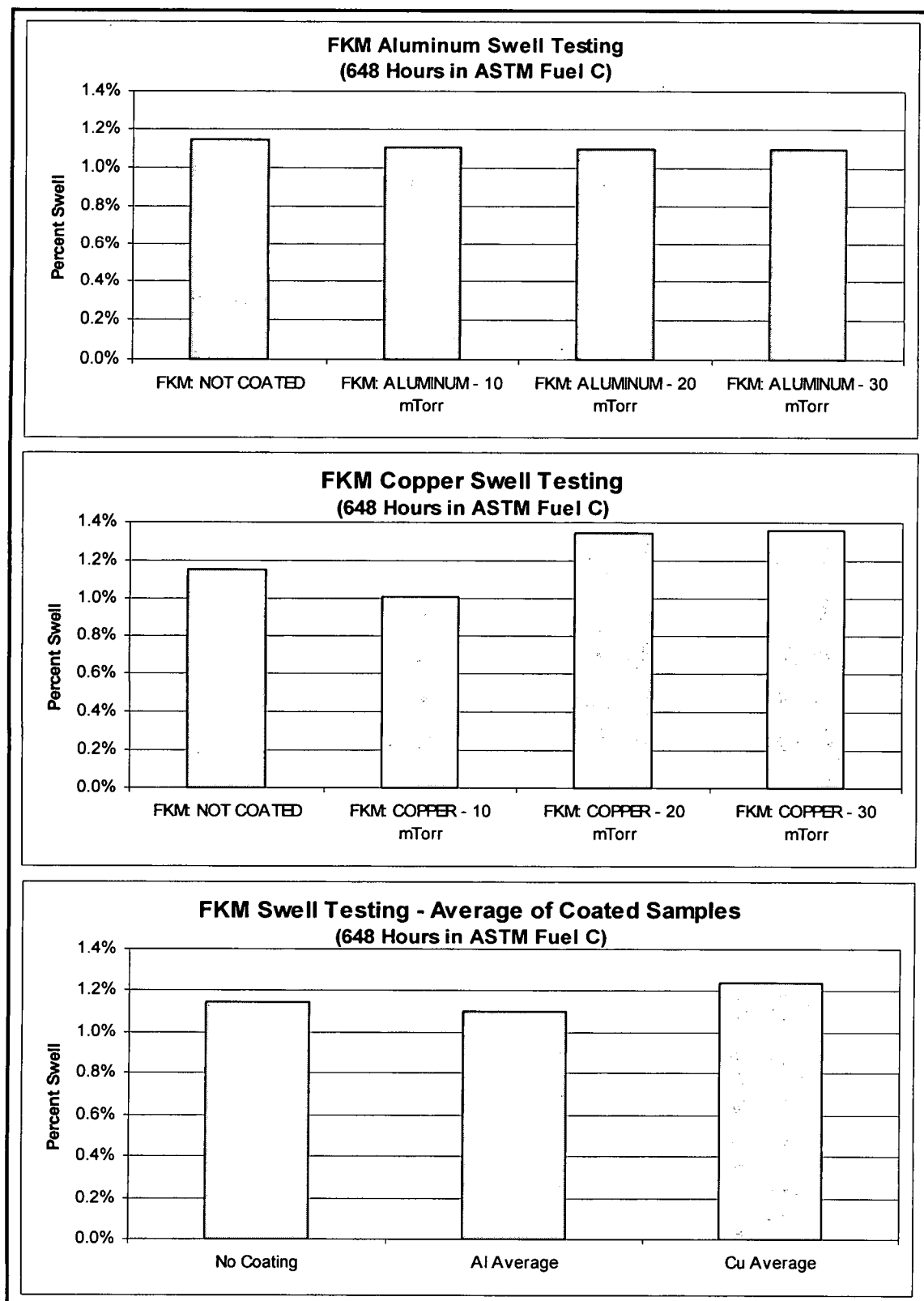


Illustration 96: Fluorocarbon Swell Diagrams

Weight Change Due to Permeation

Table 28: Aluminum Coated Nitrile Weight Change Data

NITRILE BUTADIENE RUBBER - ALUMINUM - ASTM Fuel C Permeation						
TEST NO.	NBR: NOT COATED					
16	Permeation Time (hrs)	24.00	192.00	333.75	525.00	673.00
	Weight Loss (mg)	0.44	5.60	8.39	10.55	11.53
17	Permeation Time (hrs)	24.00	192.00	333.75	525.00	673.00
	Weight Loss (mg)	0.38	5.72	8.73	11.14	12.24
Average	Permeation Time (hrs)	24.00	192.00	336.00	528.00	648.00
	Weight Loss (mg)	0.41	5.66	8.59	10.87	11.73
TEST NO.	NBR: Al - 10 mTorr					
14	Permeation Time (hrs)	24.00	167.50	360.75	502.50	693.75
	Weight Loss (mg)	0.13	2.91	5.49	6.82	8.10
18	Permeation Time (hrs)	24.00	192.00	333.25	525.00	668.00
	Weight Loss (mg)	0.44	5.83	8.63	10.80	11.79
Average	Permeation Time (hrs)	24	192.00	336.00	528.00	648.00
	Weight Loss (mg)	0.28	4.57	6.95	8.92	9.74
TEST NO.	NBR: Al - 20 mTorr					
15	Permeation Time (hrs)	24.00	167.50	360.75	502.50	693.75
	Weight Loss (mg)	0.12	2.80	5.29	6.57	7.79
19	Permeation Time (hrs)	24.00	192.00	333.25	525.00	668.00
	Weight Loss (mg)	0.41	5.80	8.75	11.15	12.28
Average	Permeation Time (hrs)	24	192.00	336.00	528.00	648.00
	Weight Loss (mg)	0.26	4.50	6.92	8.97	9.83
TEST NO.	NBR: Al - 30 m Torr					
20	Permeation Time (hrs)	24.00	192.00	333.25	525.00	668.00
	Weight Loss (mg)	0.40	5.48	8.17	10.20	11.10
21	Permeation Time (hrs)	24.00	192.00	333.25	525.00	668.00
	Weight Loss (mg)	0.44	5.95	9.02	11.52	12.70
Average	Permeation Time (hrs)	24	192.00	336.00	528.00	648.00
	Weight Loss (mg)	0.42	5.72	8.64	10.89	11.77
AVERAGE WEIGHT CHANGES						
	NBR: Al Average					
Average	Permeation Time (hrs)	24	192.00	336.00	528.00	648.00
	Weight Loss (mg)	0.32	4.93	7.50	9.59	10.45

Table 29: Copper Coated Nitrile Weight Change Data

NITRILE BUTADIENE RUBBER - COPPER - ASTM Fuel C Permeation						
TEST NO.	NBR: NOT COATED					
16	Permeation Time (hrs)	24.00	192.00	333.75	525.00	673.00
	Weight Loss (mg)	0.44	5.60	8.39	10.55	11.53
17	Permeation Time (hrs)	24.00	192.00	333.75	525.00	673.00
	Weight Loss (mg)	0.38	5.72	8.73	11.14	12.24
Average	Permeation Time (hrs)	24.00	192.00	336.00	528.00	648.00
	Weight Loss (mg)	0.41	5.66	8.59	10.87	11.73
TEST NO.	NBR: Cu - 10 mTorr					
30	Permeation Time (hrs)	23.75	192.25	359.25	502.75	671.75
	Weight Loss (mg)	0.01	1.99	3.47	4.47	5.38
39	Permeation Time (hrs)	23.00	167.75	335.00	502.25	718.25
	Weight Loss (mg)	0.39	5.13	8.57	10.49	11.83
Average	Permeation Time (hrs)	24	192.00	336.00	528.00	648.00
	Weight Loss (mg)	0.22	3.88	5.94	7.66	8.36
TEST NO.	NBR: Cu - 20 mTorr					
31	Permeation Time (hrs)	23.75	192.25	359.25	502.75	671.75
	Weight Loss (mg)	0.05	2.80	4.81	6.12	7.28
40	Permeation Time (hrs)	23.00	167.75	335.00	502.25	718.25
	Weight Loss (mg)	0.37	5.09	8.53	10.44	11.76
Average	Permeation Time (hrs)	24	192.00	336.00	528.00	648.00
	Weight Loss (mg)	0.23	4.26	6.56	8.48	9.26
TEST NO.	NBR: Cu - 30 mTorr					
32	Permeation Time (hrs)	23.75	192.25	359.25	502.75	671.75
	Weight Loss (mg)	0.02	2.16	3.82	4.92	5.94
41	Permeation Time (hrs)	23.00	167.75	335.00	502.25	718.25
	Weight Loss (mg)	0.35	5.04	8.66	10.77	12.26
Average	Permeation Time (hrs)	24	192.00	336.00	528.00	648.00
	Weight Loss (mg)	0.20	3.93	6.15	8.04	8.83
AVERAGE WEIGHT CHANGES						
	NBR: Cu Average					
Average	Permeation Time (hrs)	24	192.00	336.00	528.00	648.00
	Weight Loss (mg)	0.22	4.02	6.21	8.06	8.82

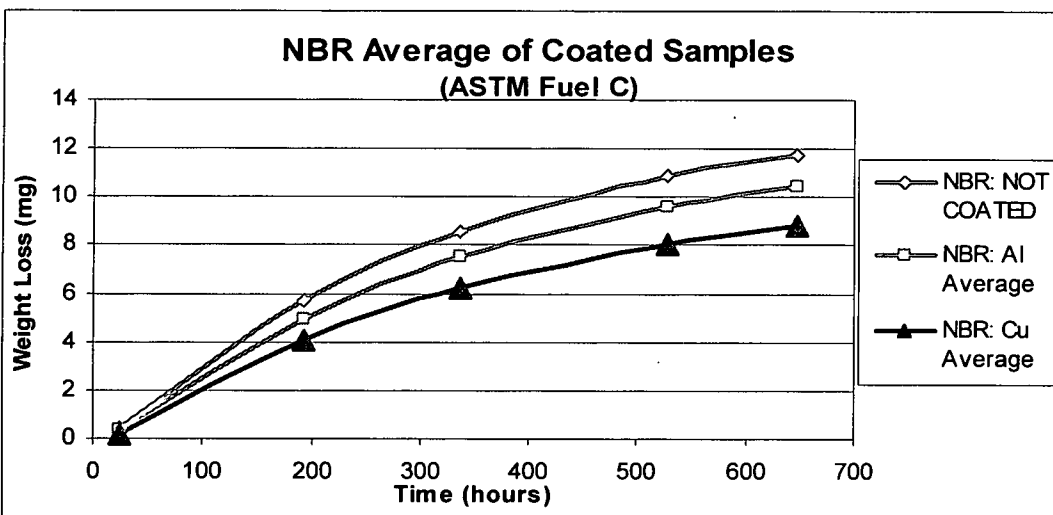
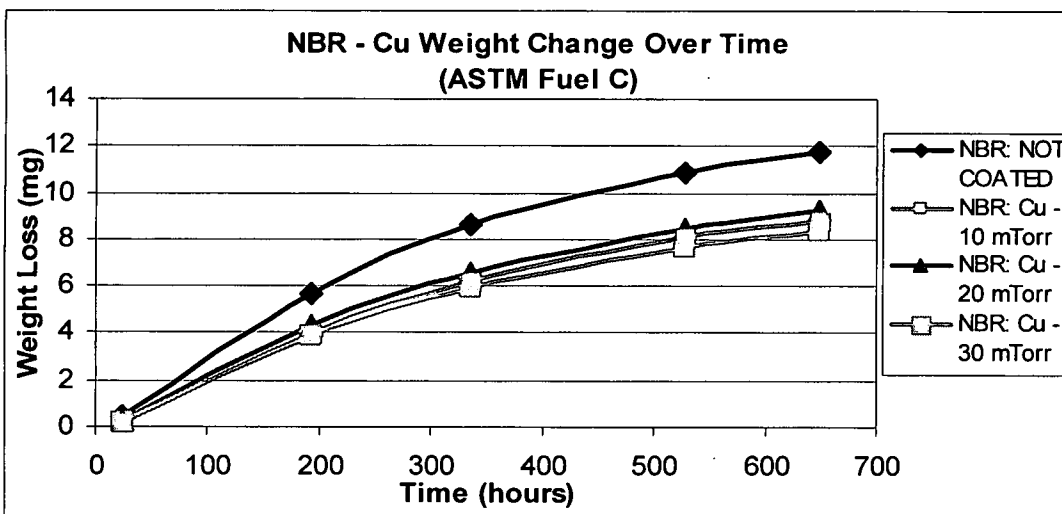
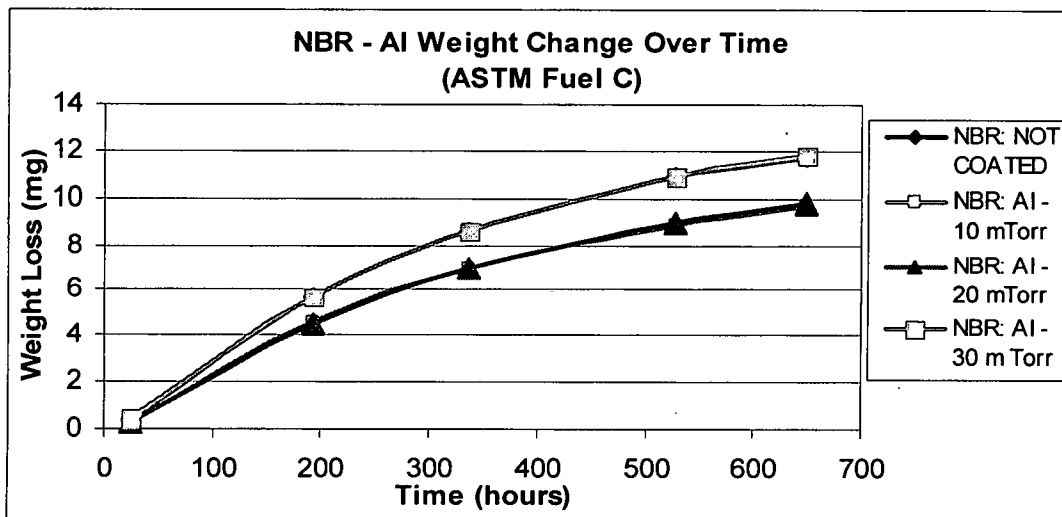


Illustration 97: Nitrile Weight Change Charts

Table 30: Aluminum Coated Fluorosilicone Weight Change Data

FLUOROSILICONE RUBBER - ALUMINUM - ASTM Fuel C Permeation						
TEST NO.	FVMQ: NOT COATED					
1	Permeation Time (hrs)	24.50	168.17	376.75	501.33	669.58
	Weight Loss (mg)	0.37	3.41	7.45	9.59	
2	Permeation Time (hrs)	24.50	168.17	376.75	501.33	669.58
	Weight Loss (mg)	0.37	3.37	7.35	9.45	
Average	Permeation Time (hrs)	24.00	192.00	336.00	528.00	648.00
	Weight Loss (mg)	0.37	3.81	6.40	8.92	9.80
TEST NO.	FVMQ: Al - 10 mTorr					
22	Permeation Time (hrs)	24.00	192.00	333.25	525.00	668.00
	Weight Loss (mg)	0.39	3.97	6.83	10.32	12.63
23	Permeation Time (hrs)	147.00	171.00	361.00	506.50	650.00
	Weight Loss (mg)	3.18	3.69	7.15	10.02	12.07
Average	Permeation Time (hrs)	24	192.00	336.00	528.00	648.00
	Weight Loss (mg)	0.39	4.04	6.79	10.38	12.18
TEST NO.	FVMQ: Al - 20mTorr					
12	Permeation Time (hrs)	24.00	167.50	360.75	502.50	693.75
	Weight Loss (mg)	0.32	2.97	6.20	8.26	10.57
24	Permeation Time (hrs)	24.00	192.00	333.25	525.00	668.00
	Weight Loss (mg)	3.10	3.61	7.06	9.97	12.11
Average	Permeation Time (hrs)	24	192.00	336.00	528.00	648.00
	Weight Loss (mg)	1.71	3.51	6.47	9.30	10.92
TEST NO.	FVMQ: Al - 30mTorr					
25	Permeation Time (hrs)	147.00	171.00	361.00	506.50	650.00
	Weight Loss (mg)	3.09	3.60	7.01	9.80	11.79
26	Permeation Time (hrs)	147.00	171.00	361.00	506.50	650.00
	Weight Loss (mg)	4.48	5.10	8.28	9.92	10.80
Average	Permeation Time (hrs)	24	192.00	336.00	528.00	648.00
	Weight Loss (mg)	0.46	4.81	7.26	10.12	11.28
AVERAGE WEIGHT CHANGES						
	FVMQ: Al Average					
Average	Permeation Time (hrs)	24	192.00	336.00	528.00	648.00
	Weight Loss (mg)	0.85	4.12	6.84	9.93	11.46

Table 31: Copper Coated Fluorosilicone Weight Change Data

FLUOROSILICONE RUBBER - COPPER - ASTM Fuel C Permeation						
TEST NO.	FVMQ: NOT COATED					
1	Permeation Time (hrs)	24.50	168.17	376.75	501.33	669.58
	Weight Loss (mg)	0.37	3.41	7.45	9.59	
2	Permeation Time (hrs)	24.50	168.17	376.75	501.33	669.58
	Weight Loss (mg)	0.37	3.37	7.35	9.45	
Average	Permeation Time (hrs)	24.00	192.00	336.00	528.00	648.00
	Weight Loss (mg)	0.37	3.81	6.40	8.92	9.80
TEST NO.	FVMQ: Cu - 10 mTorr					
27	Permeation Time (hrs)	23.75	192.25	359.25	502.75	671.75
	Weight Loss (mg)	0.27	3.16	5.66	7.57	9.50
36	Permeation Time (hrs)	23.00	167.75	335.00	502.25	718.25
	Weight Loss (mg)	0.37	3.55	6.96	9.97	12.95
Average	Permeation Time (hrs)	24	192.00	336.00	528.00	648.00
	Weight Loss (mg)	0.34	3.61	6.16	9.12	10.65
TEST NO.	FVMQ: Cu - 20mTorr					
28	Permeation Time (hrs)	23.75	192.25	359.25	502.75	671.75
	Weight Loss (mg)	0.28	3.18	5.25	7.53	9.42
37	Permeation Time (hrs)	23.00	167.75	335.00	502.25	718.25
	Weight Loss (mg)	0.37	3.55	6.95	9.93	12.84
Average	Permeation Time (hrs)	24	192.00	336.00	528.00	648.00
	Weight Loss (mg)	0.34	3.62	5.95	9.10	10.58
TEST NO.	FVMQ: Cu - 30mTorr					
29	Permeation Time (hrs)	23.75	192.25	359.25	502.75	671.75
	Weight Loss (mg)	0.26	3.01	5.36	7.12	8.86
38	Permeation Time (hrs)	23.00	167.75	335.00	502.25	718.25
	Weight Loss (mg)	0.37	3.53	6.93	9.92	12.89
Average	Permeation Time (hrs)	24	192.00	336.00	528.00	648.00
	Weight Loss (mg)	0.33	3.52	6.00	8.86	10.31
AVERAGE WEIGHT CHANGES						
	FVMQ: Cu Average					
Average	Permeation Time (hrs)	24	192.00	336.00	528.00	648.00
	Weight Loss (mg)	0.33	3.58	6.04	9.03	10.51

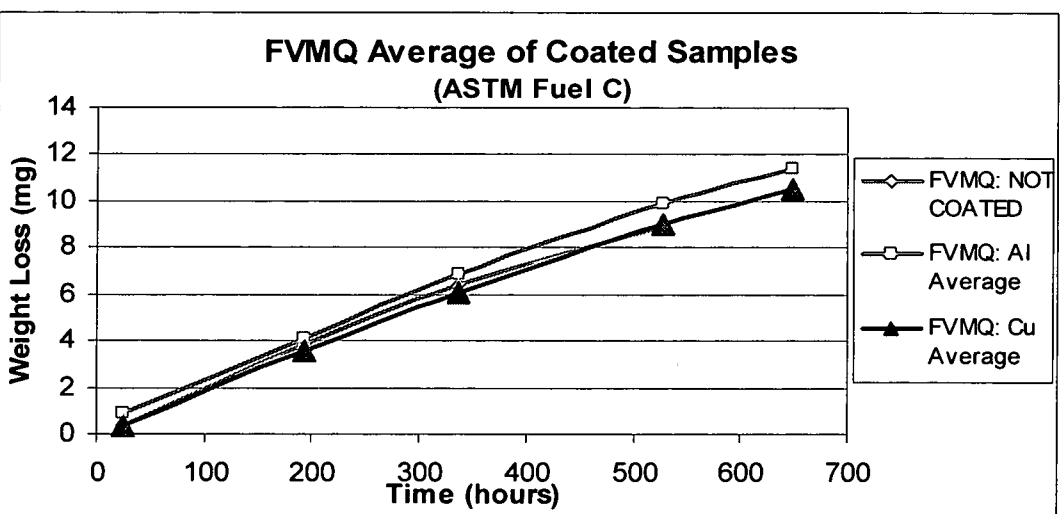
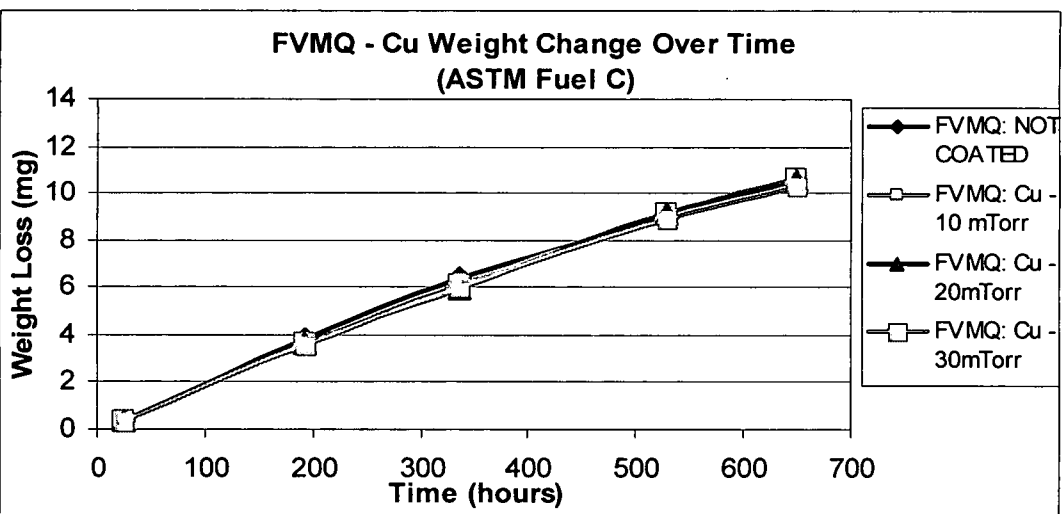
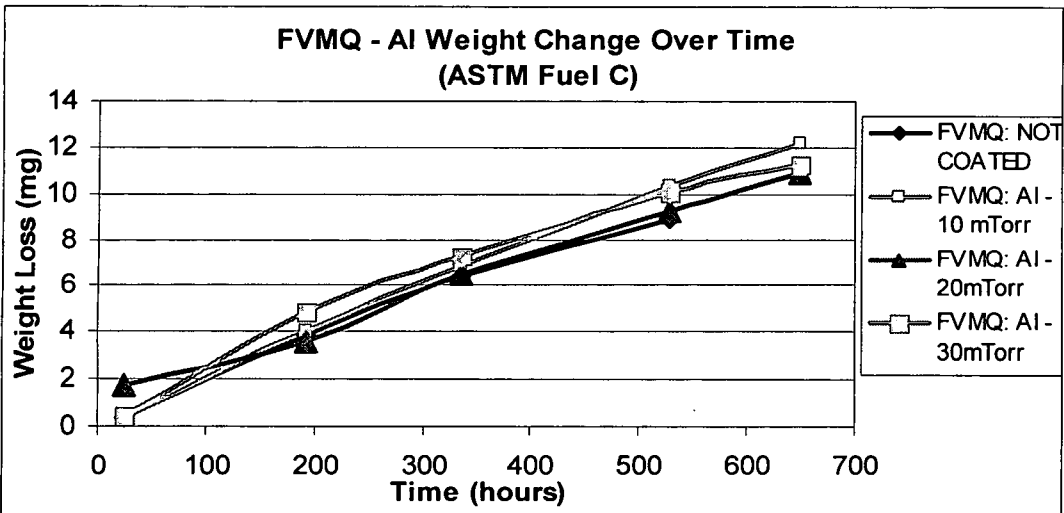


Illustration 98: Fluorosilicone Weight Change Charts

Table 32: Aluminum Coated Fluorocarbon Swell Data

FLUOROCARBON RUBBER - ALUMINUM - ASTM Fuel C Permeation						
TEST NO.	FKM: NOT COATED					
3	Permeation Time (hrs)	24.50	168.17	376.75	501.33	669.58
	Weight Loss (mg)	-0.0021	-0.0045	-0.0044	-0.0035	-0.0060
4	Permeation Time (hrs)	24.50	168.17	376.75	501.33	669.58
	Weight Loss (mg)	-0.0019	-0.0050	-0.0047	-0.0038	-0.0065
Average	Permeation Time (hrs)	24.00	192.00	336.00	528.00	648.00
	Weight Loss (mg)	-0.0020	-0.0050	-0.0049	-0.0038	-0.0058
TEST NO.	FKM: Al - 10 mTorr					
5	Permeation Time (hrs)	24.50	168.17	376.75	501.33	669.58
	Weight Loss (mg)	-0.0072	-0.0031	-0.0031	-0.0024	-0.0047
6	Permeation Time (hrs)	24.50	168.17	376.75	501.33	669.58
	Weight Loss (mg)	-0.0081	-0.0028	-0.0026	-0.0015	-0.0034
Average	Permeation Time (hrs)	24	192.00	336.00	528.00	648.00
	Weight Loss (mg)	-0.0076	-0.0026	-0.0028	-0.0020	-0.0036
TEST NO.	FKM: Al - 20mTorr					
9	Permeation Time (hrs)	24.50	168.17	376.75	501.33	669.58
	Weight Loss (mg)	-0.0062	-0.0031	-0.0023	-0.0019	-0.0047
10	Permeation Time (hrs)	24.50	168.17	376.75	501.33	669.58
	Weight Loss (mg)	-0.0076	-0.0030	-0.0018	-0.0015	-0.0042
Average	Permeation Time (hrs)	24	192.00	336.00	528.00	648.00
	Weight Loss (mg)	-0.0069	-0.0027	-0.0021	-0.0019	-0.0040
TEST NO.	FKM: Al - 30mTorr					
11	Permeation Time (hrs)	24.50	168.17	376.75	501.33	669.58
	Weight Loss (mg)	-0.0062	-0.0030	-0.0020	-0.0020	-0.0045
	Permeation Time (hrs)					
	Weight Loss (mg)					
Average	Permeation Time (hrs)	24	192.00	336.00	528.00	648.00
	Weight Loss (mg)	-0.0062	-0.0026	-0.0020	-0.0019	-0.0039
AVERAGE WEIGHT CHANGES						
	FKM: Al Average					
Average	Permeation Time (hrs)	24	192.00	336.00	528.00	648.00
	Weight Loss (mg)	-0.01	0.00	0.00	0.00	0.00

Table 33: Copper Coated Fluorocarbon Swell Data

FLUOROCARBON RUBBER - COPPER - ASTM Fuel C Permeation						
TEST NO.	FKM: NOT COATED					
3	Permeation Time (hrs)	24.50	168.17	376.75	501.33	669.58
	Weight Loss (mg)	-0.0021	-0.0045	-0.0044	-0.0035	-0.0060
4	Permeation Time (hrs)	24.50	168.17	376.75	501.33	669.58
	Weight Loss (mg)	-0.0019	-0.0050	-0.0047	-0.0038	-0.0065
Average	Permeation Time (hrs)	24.00	192.00	336.00	528.00	648.00
	Weight Loss (mg)	-0.0020	-0.0050	-0.0049	-0.0038	-0.0058
TEST NO.	FKM: Cu - 10 mTorr					
33	Permeation Time (hrs)	23.75	192.25	359.25	502.75	671.75
	Weight Loss (mg)	-0.0010	-0.0011	-0.0014	-0.0033	-0.0032
42	Permeation Time (hrs)	23.00	167.75	335.00	502.25	718.25
	Weight Loss (mg)	-0.0012	0.0021	0.0005	0.0002	-0.0021
Average	Permeation Time (hrs)	24	192.00	336.00	528.00	648.00
	Weight Loss (mg)	-0.0011	0.0005	-0.0004	-0.0017	-0.0022
TEST NO.	FKM: Cu - 20mTorr					
34	Permeation Time (hrs)	23.00	167.75	335.00	502.25	718.25
	Weight Loss (mg)	-0.0009	0.0015	0.0010	0.0009	-0.0022
43	Permeation Time (hrs)	23.00	167.75	335.00	502.25	718.25
	Weight Loss (mg)	0.0158	0.0191	0.0175	0.0172	0.0147
Average	Permeation Time (hrs)	24	192.00	336.00	528.00	648.00
	Weight Loss (mg)	0.0075	0.0104	0.0092	0.0089	0.0074
TEST NO.	FKM: Cu - 30mTorr					
35	Permeation Time (hrs)	23.00	167.75	335.00	502.25	718.25
	Weight Loss (mg)	-0.0007	0.0015	0.0009	0.0006	-0.0020
44	Permeation Time (hrs)	23.00	167.75	335.00	502.25	718.25
	Weight Loss (mg)	-0.0007	0.0019	0.0003	0.0005	-0.0022
Average	Permeation Time (hrs)	24	192.00	336.00	528.00	648.00
	Weight Loss (mg)	-0.0007	0.0017	0.0006	0.0004	-0.0010
AVERAGE WEIGHT CHANGES						
	FKM: Cu Average					
Average	Permeation Time (hrs)	24	192.00	336.00	528.00	648.00
	Weight Loss (mg)	0.00	0.00	0.00	0.00	0.00

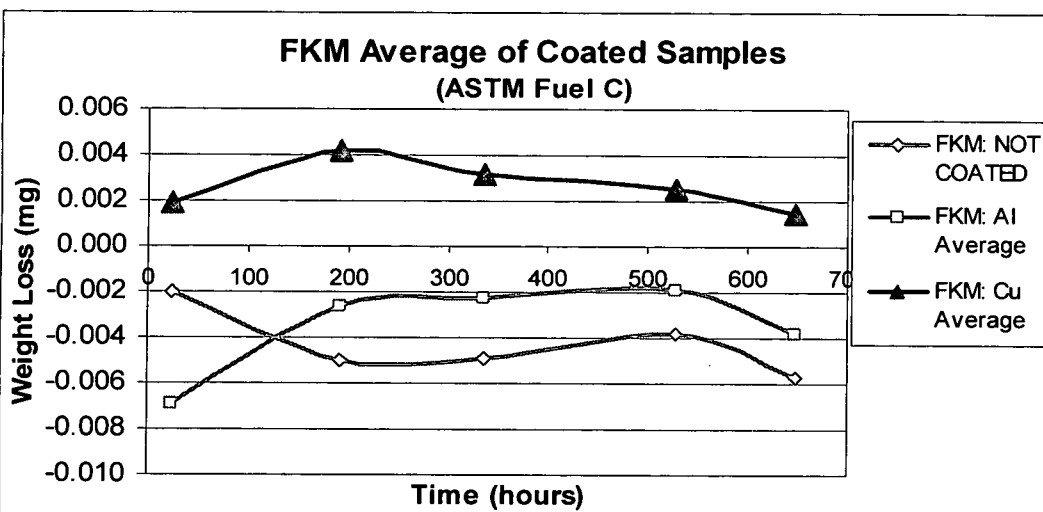
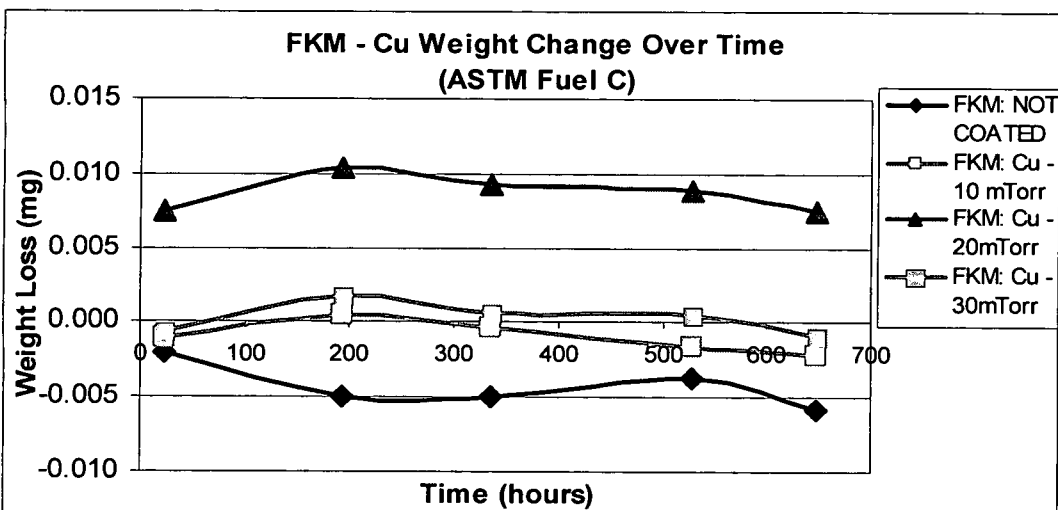
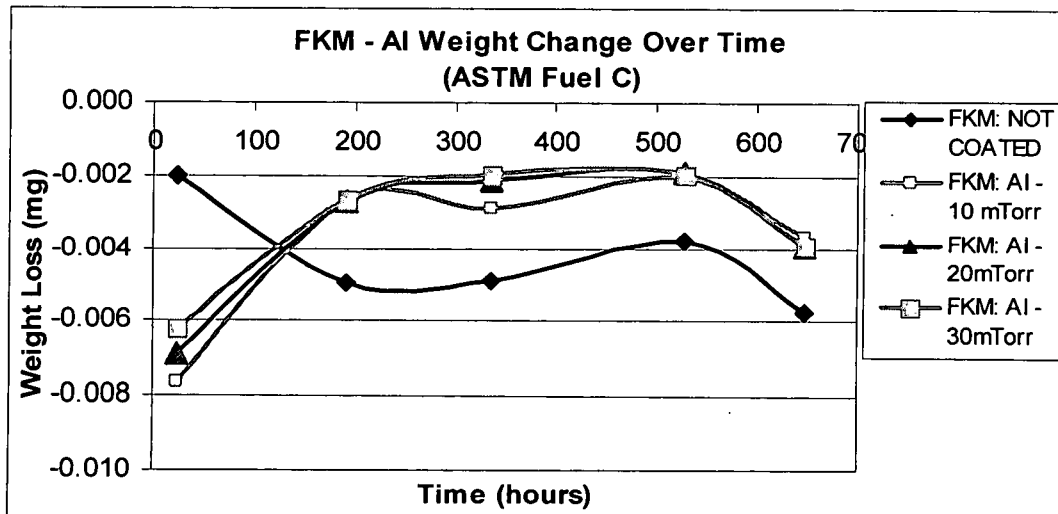


Illustration 99: Fluorocarbon Weight Change Charts

Permeation from Start of Test

Table 34: Aluminum Coated Nitrile Permeation Data

NITRILE BUTADIENE RUBBER - ALUMINUM - ASTM Fuel C Permeation						
TEST NO.	NBR: NOT COATED					
16	Permeation Time (hrs)	24.00	192.00	333.75	525.00	673.00
	Perm. Rate (mg/(m*s ²))	2.54	4.00	3.44	2.75	2.35
17	Permeation Time (hrs)	24.00	192.00	333.75	525.00	673.00
	Perm. Rate (mg/(m*s ²))	2.14	4.08	3.58	2.91	2.49
Average	Permeation Time (hrs)	24.00	192.00	336.00	528.00	648.00
	Perm. Rate (mg/(m*s ²))	2.34	4.04	3.50	2.82	2.49
TEST NO.	NBR: Al - 10 mTorr					
14	Permeation Time (hrs)	24.00	167.50	360.75	502.50	693.75
	Perm. Rate (mg/(m*s ²))	0.71	2.38	2.09	1.86	1.60
18	Permeation Time (hrs)	24.00	192.00	333.25	525.00	668.00
	Perm. Rate (mg/(m*s ²))	2.50	4.16	3.55	2.82	2.43
Average	Permeation Time (hrs)	24	192.00	336.00	528.00	648.00
	Perm. Rate (mg/(m*s ²))	1.61	3.32	2.85	2.32	2.08
TEST NO.	NBR: Al - 20mTorr					
15	Permeation Time (hrs)	24.00	167.50	360.75	502.50	693.75
	Perm. Rate (mg/(m*s ²))	0.70	2.29	2.01	1.79	1.54
19	Permeation Time (hrs)	24.00	192.00	333.25	525.00	668.00
	Perm. Rate (mg/(m*s ²))	2.33	4.14	3.60	2.91	2.19
Average	Permeation Time (hrs)	24	192.00	336.00	528.00	648.00
	Perm. Rate (mg/(m*s ²))	1.51	3.27	2.84	2.33	1.96
TEST NO.	NBR: Al - 30mTorr					
20	Permeation Time (hrs)	24.00	192.00	333.25	525.00	668.00
	Perm. Rate (mg/(m*s ²))	2.31	3.91	3.36	2.66	2.51
21	Permeation Time (hrs)	24.00	192.00	333.25	525.00	668.00
	Perm. Rate (mg/(m*s ²))	2.48	4.25	3.71	3.01	2.49
Average	Permeation Time (hrs)	24	192.00	336.00	528.00	648.00
	Perm. Rate (mg/(m*s ²))	2.40	4.08	3.52	2.83	2.55
PERMEATION CALCULATED FROM START OF TEST						
	NBR: Al Average					
Average	Permeation Time (hrs)	24	192.00	336.00	528.00	648.00
	Perm. Rate (mg/(m*s ²))	1.84	3.56	3.07	2.49	2.19

Table 35: Copper Coated Nitrile Permeation Data

NITRILE BUTADIENE RUBBER - COPPER - ASTM Fuel C Permeation						
TEST NO.	NBR: NOT COATED					
16	Permeation Time (hrs)	24.00	192.00	333.75	525.00	673.00
	Perm. Rate (mg/(m*s ²))	2.54	4.00	3.44	2.75	2.35
17	Permeation Time (hrs)	24.00	192.00	333.75	525.00	673.00
	Perm. Rate (mg/(m*s ²))	2.14	4.08	3.58	2.91	2.49
Average	Permeation Time (hrs)	24.00	192.00	336.00	528.00	648.00
	Perm. Rate (mg/(m*s ²))	2.34	4.04	3.50	2.82	2.49
TEST NO.	NBR: Cu - 10 mTorr					
30	Permeation Time (hrs)	23.75	192.25	359.25	502.75	671.75
	Perm. Rate (mg/(m*s ²))	0.07	1.42	1.32	1.22	1.10
39	Permeation Time (hrs)	23.00	167.75	335.00	502.25	718.25
	Perm. Rate (mg/(m*s ²))	2.30	4.19	3.51	2.86	2.26
Average	Permeation Time (hrs)	24	192.00	336.00	528.00	648.00
	Perm. Rate (mg/(m*s ²))	1.19	2.83	2.43	2.00	1.79
TEST NO.	NBR: Cu - 20mTorr					
31	Permeation Time (hrs)	23.75	192.25	359.25	502.75	671.75
	Perm. Rate (mg/(m*s ²))	0.30	2.00	1.84	1.67	1.49
40	Permeation Time (hrs)	23.00	167.75	335.00	502.25	718.25
	Perm. Rate (mg/(m*s ²))	2.20	4.16	3.49	2.85	2.24
Average	Permeation Time (hrs)	24	192.00	336.00	528.00	648.00
	Perm. Rate (mg/(m*s ²))	1.26	3.11	2.69	2.21	1.98
TEST NO.	NBR: Cu - 30mTorr					
32	Permeation Time (hrs)	23.75	192.25	359.25	502.75	671.75
	Perm. Rate (mg/(m*s ²))	0.09	1.54	1.46	1.34	1.21
41	Permeation Time (hrs)	23.00	167.75	335.00	502.25	718.25
	Perm. Rate (mg/(m*s ²))	2.06	4.12	3.54	2.94	2.34
Average	Permeation Time (hrs)	24	192.00	336.00	528.00	648.00
	Perm. Rate (mg/(m*s ²))	1.09	2.87	2.52	2.10	1.89
PERMEATION CALCULATED FROM START OF TEST						
	NBR: Cu Average					
Average	Permeation Time (hrs)	24	192.00	336.00	528.00	648.00
	Perm. Rate (mg/(m*s ²))	1.18	2.94	2.55	2.10	1.88

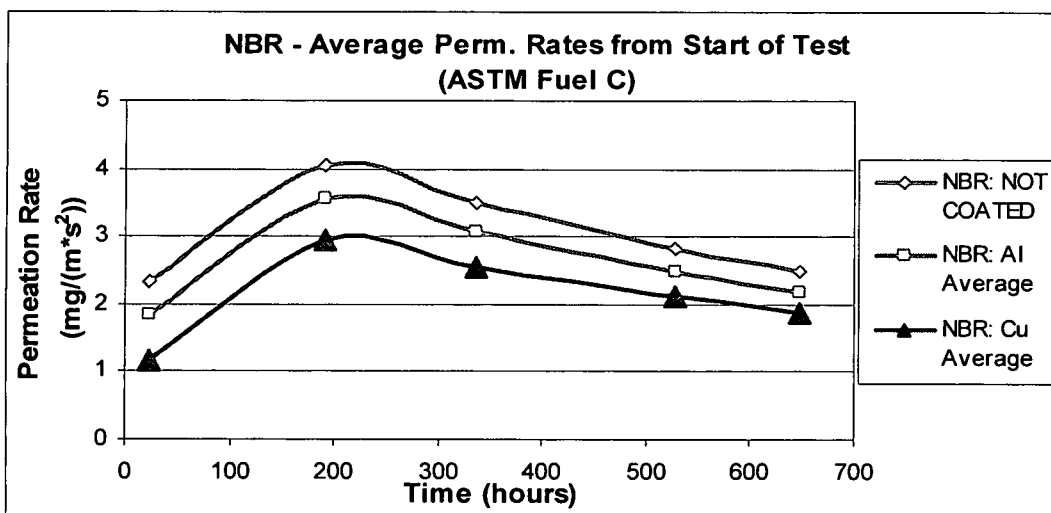
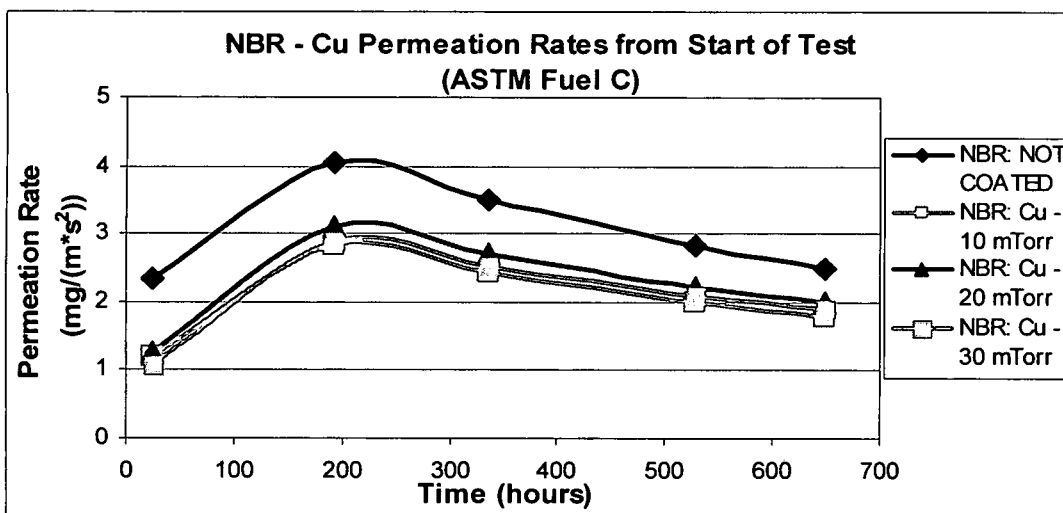
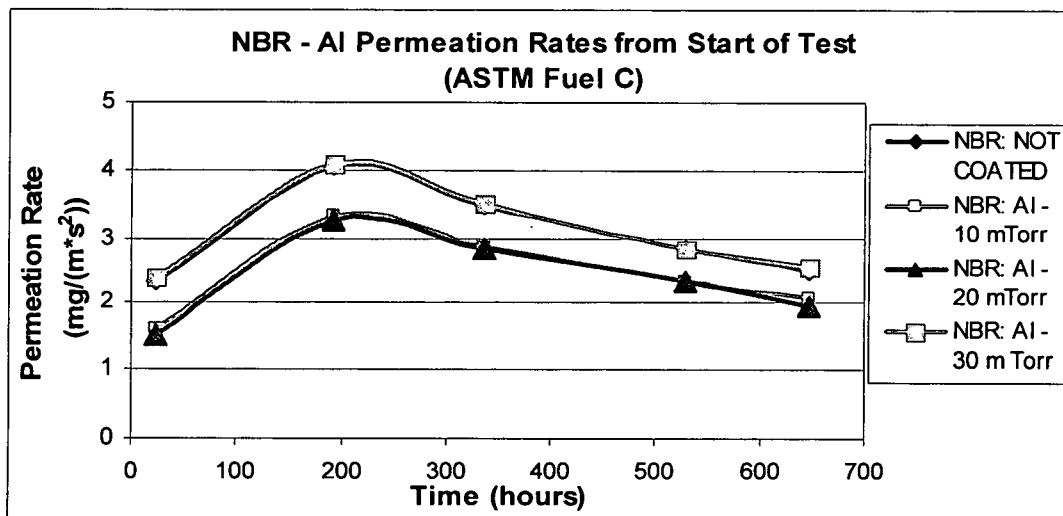


Illustration 100: Nitrile Permeation Charts

Table 36: Aluminum Coated Fluorosilicone Permeation Data

FLUOROSILICONE RUBBER - ALUMINUM - ASTM Fuel C Permeation						
TEST NO.	FVMQ: NOT COATED					
1	Permeation Time (hrs)	24.50	168.17	376.75	501.33	669.58
	Perm. Rate (mg/(m*s ²))	2.08	2.78	2.71	2.62	0.00
2	Permeation Time (hrs)	24.50	168.17	376.75	501.33	669.58
	Perm. Rate (mg/(m*s ²))	2.07	2.75	2.67	2.58	0.00
Average	Permeation Time (hrs)	24.00	192.00	336.00	528.00	648.00
	Perm. Rate (mg/(m*s ²))	2.08	2.80	2.69	2.38	0.43
TEST NO.	FVMQ: Al - 10 mTorr					
22	Permeation Time (hrs)	24.00	192.00	333.25	525.00	668.00
	Perm. Rate (mg/(m*s ²))	2.21	2.83	2.81	2.69	0.00
23	Permeation Time (hrs)	147.00	171.00	361.00	506.50	650.00
	Perm. Rate (mg/(m*s ²))	2.96	2.96	2.71	2.71	2.55
Average	Permeation Time (hrs)	24	192.00	336.00	528.00	648.00
	Perm. Rate (mg/(m*s ²))	2.21	2.89	2.78	2.68	1.50
TEST NO.	FVMQ: Al - 20mTorr					
12	Permeation Time (hrs)	24.00	167.50	360.75	502.50	693.75
	Perm. Rate (mg/(m*s ²))	1.85	2.43	2.36	2.25	2.09
24	Permeation Time (hrs)	24.00	192.00	333.25	525.00	668.00
	Perm. Rate (mg/(m*s ²))	2.89	2.89	2.68	2.70	2.55
Average	Permeation Time (hrs)	24	192.00	336.00	528.00	648.00
	Perm. Rate (mg/(m*s ²))	2.37	2.64	2.97	2.63	2.39
TEST NO.	FVMQ: Al - 30mTorr					
25	Permeation Time (hrs)	147.00	171.00	361.00	506.50	650.00
	Perm. Rate (mg/(m*s ²))	2.89	2.89	2.66	2.65	2.49
26	Permeation Time (hrs)	147.00	171.00	361.00	506.50	650.00
	Perm. Rate (mg/(m*s ²))	4.18	4.09	3.14	2.69	2.28
Average	Permeation Time (hrs)	24	192.00	336.00	528.00	648.00
	Perm. Rate (mg/(m*s ²))	2.29	3.44	2.97	2.63	2.39
PERMEATION CALCULATED FROM START OF TEST						
	FVMQ: Al Average					
Average	Permeation Time (hrs)	24	192.00	336.00	528.00	648.00
	Perm. Rate (mg/(m*s ²))	2.29	2.99	2.91	2.65	2.09

Table 37: Copper Coated Fluorosilicone Permeation Data

FLUOROSILICONE RUBBER - COPPER - ASTM Fuel C Permeation						
TEST NO.	FVMQ: NOT COATED					
1	Permeation Time (hrs)	24.50	168.17	376.75	501.33	669.58
	Perm. Rate (mg/(m*s ²))	2.08	2.78	2.71	2.62	0.00
2	Permeation Time (hrs)	24.50	168.17	376.75	501.33	669.58
	Perm. Rate (mg/(m*s ²))	2.07	2.75	2.67	2.58	0.00
Average	Permeation Time (hrs)	24.00	192.00	336.00	528.00	648.00
	Perm. Rate (mg/(m*s ²))	2.08	2.80	2.69	2.38	0.43
TEST NO.	FVMQ: Cu - 10 mTorr					
27	Permeation Time (hrs)	23.75	192.25	359.25	502.75	671.75
	Perm. Rate (mg/(m*s ²))	1.57	2.25	2.16	2.06	1.94
36	Permeation Time (hrs)	23.00	167.75	335.00	502.25	718.25
	Perm. Rate (mg/(m*s ²))	2.23	2.90	2.85	2.72	2.47
Average	Permeation Time (hrs)	24	192.00	336.00	528.00	648.00
	Perm. Rate (mg/(m*s ²))	1.90	2.60	2.52	2.37	2.26
TEST NO.	FVMQ: Cu - 20mTorr					
28	Permeation Time (hrs)	23.75	192.25	359.25	502.75	671.75
	Perm. Rate (mg/(m*s ²))	1.62	2.26	2.00	2.05	1.92
37	Permeation Time (hrs)	23.00	167.75	335.00	502.25	718.25
	Perm. Rate (mg/(m*s ²))	2.23	2.90	2.84	2.71	2.45
Average	Permeation Time (hrs)	24	192.00	336.00	528.00	648.00
	Perm. Rate (mg/(m*s ²))	1.93	2.60	2.44	2.37	2.25
TEST NO.	FVMQ: Cu - 30mTorr					
29	Permeation Time (hrs)	23.75	192.25	359.25	502.75	671.75
	Perm. Rate (mg/(m*s ²))	1.51	2.15	2.05	1.94	1.81
38	Permeation Time (hrs)	23.00	167.75	335.00	502.25	718.25
	Perm. Rate (mg/(m*s ²))	2.18	2.88	2.83	2.71	2.46
Average	Permeation Time (hrs)	24	192.00	336.00	528.00	648.00
	Perm. Rate (mg/(m*s ²))	1.85	2.54	2.45	2.31	2.19
PERMEATION CALCULATED FROM START OF TEST						
	FVMQ: Cu Average					
Average	Permeation Time (hrs)	24	192.00	336.00	528.00	648.00
	Perm. Rate (mg/(m*s ²))	1.89	2.58	2.47	2.35	2.23

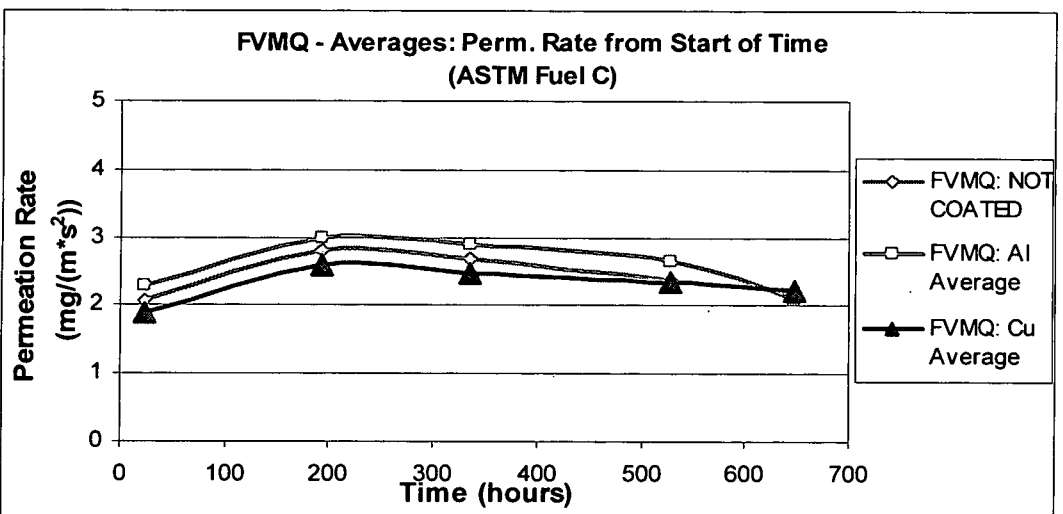
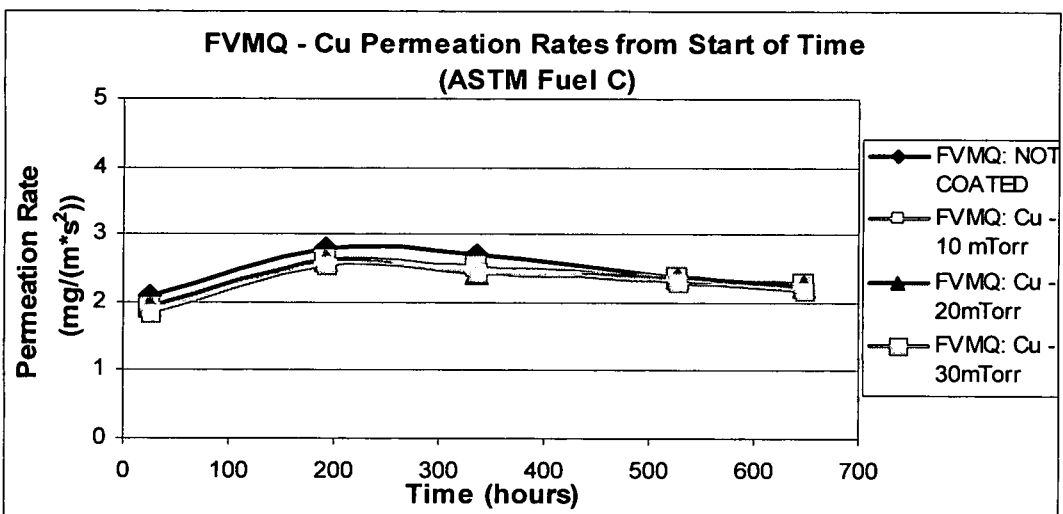
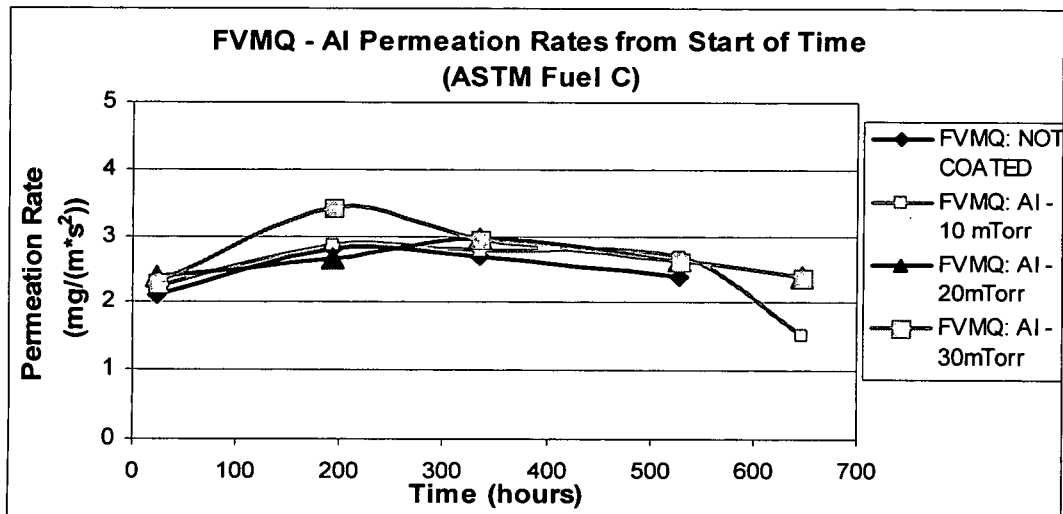


Illustration 101: Fluorosilicone Permeation Charts

Table 38: Aluminum Coated Fluorocarbon Permeation Data

FLUOROCARBON RUBBER - ALUMINUM - ASTM Fuel C Permeation						
TEST NO.	FKM: NOT COATED					
3	Permeation Time (hrs)	24.50	168.17	376.75	501.33	669.58
	Perm. Rate (mg/(m*s ²))	-0.0117	-0.0037	-0.0016	-0.0010	-0.0012
4	Permeation Time (hrs)	24.50	168.17	376.75	501.33	669.58
	Perm. Rate (mg/(m*s ²))	-0.0106	-0.0041	-0.0017	-0.0010	-0.0013
Average	Permeation Time (hrs)	24.00	192.00	336.00	528.00	648.00
	Perm. Rate (mg/(m*s ²))	-0.0112	-0.0032	-0.0018	-0.0009	-0.0012
TEST NO.	FKM: Al - 10 mTorr					
5	Permeation Time (hrs)	24.50	168.17	376.75	501.33	669.58
	Perm. Rate (mg/(m*s ²))	-0.0400	0.0039	0.0016	0.0014	0.0005
6	Permeation Time (hrs)	24.50	168.17	376.75	501.33	669.58
	Perm. Rate (mg/(m*s ²))	-0.0454	0.0051	0.0001	0.0012	-0.0015
Average	Permeation Time (hrs)	24	192.00	336.00	528.00	648.00
	Perm. Rate (mg/(m*s ²))	-0.0427	0.0076	0.0034	0.0015	0.0000
TEST NO.	FKM: Al - 20mTorr					
9	Permeation Time (hrs)	24.50	168.17	376.75	501.33	669.58
	Perm. Rate (mg/(m*s ²))	-0.0347	0.0030	0.0005	0.0004	-0.0023
10	Permeation Time (hrs)	24.50	168.17	376.75	501.33	669.58
	Perm. Rate (mg/(m*s ²))	-0.0427	0.0044	0.0008	0.0003	-0.0022
Average	Permeation Time (hrs)	24	192.00	336.00	528.00	648.00
	Perm. Rate (mg/(m*s ²))	-0.0387	0.0076	0.0076	0.0076	0.0076
TEST NO.	FKM: Al - 30mTorr					
11	Permeation Time (hrs)	24.50	168.17	376.75	501.33	669.58
	Perm. Rate (mg/(m*s ²))	-0.0347	0.0031	0.0016	0.0012	0.0004
	Permeation Time (hrs)					
	Perm. Rate (mg/(m*s ²))					
Average	Permeation Time (hrs)	24	192.00	336.00	528.00	648.00
	Perm. Rate (mg/(m*s ²))	-0.0347	0.0057	0.0036	0.0013	0.0006
PERMEATION CALCULATED FROM START OF TEST						
	FKM: Al Average					
Average	Permeation Time (hrs)	24	192.00	336.00	528.00	648.00
	Perm. Rate (mg/(m*s ²))	-0.04	0.01	0.00	0.00	0.00

Table 39: Copper Coated Fluorocarbon Permeation Data

FLUOROCARBON RUBBER - COPPER - ASTM Fuel C Permeation						
TEST NO.	FKM: NOT COATED					
3	Permeation Time (hrs)	24.50	168.17	376.75	501.33	669.58
	Perm. Rate (mg/(m*s ²))	-0.0117	-0.0037	-0.0016	-0.0010	-0.0012
4	Permeation Time (hrs)	24.50	168.17	376.75	501.33	669.58
	Perm. Rate (mg/(m*s ²))	-0.0106	-0.0041	-0.0017	-0.0010	-0.0013
Average	Permeation Time (hrs)	24.00	192.00	336.00	528.00	648.00
	Perm. Rate (mg/(m*s ²))	-0.0112	-0.0032	-0.0018	-0.0009	-0.0012
TEST NO.	FKM: Cu - 10 mTorr					
33	Permeation Time (hrs)	23.75	192.25	359.25	502.75	671.75
	Perm. Rate (mg/(m*s ²))	-0.0058	-0.0008	-0.0005	-0.0009	-0.0007
42	Permeation Time (hrs)	23.00	167.75	335.00	502.25	718.25
	Perm. Rate (mg/(m*s ²))	-0.0071	0.0017	0.0002	0.0001	-0.0004
Average	Permeation Time (hrs)	24	192.00	336.00	528.00	648.00
	Perm. Rate (mg/(m*s ²))	-0.0064	0.0007	-0.0001	-0.0004	-0.0004
TEST NO.	FKM: Cu - 20mTorr					
34	Permeation Time (hrs)	23.00	167.75	335.00	502.25	718.25
	Perm. Rate (mg/(m*s ²))	-0.0054	0.0012	0.0004	0.0002	-0.0004
43	Permeation Time (hrs)	23.00	167.75	335.00	502.25	718.25
	Perm. Rate (mg/(m*s ²))	0.0941	0.0156	0.0072	0.0047	0.0028
Average	Permeation Time (hrs)	24	192.00	336.00	528.00	648.00
	Perm. Rate (mg/(m*s ²))	0.0441	0.0056	0.0038	0.0022	0.0014
TEST NO.	FKM: Cu - 30mTorr					
35	Permeation Time (hrs)	23.00	167.75	335.00	502.25	718.25
	Perm. Rate (mg/(m*s ²))	-0.0042	0.0012	0.0004	0.0002	-0.0004
44	Permeation Time (hrs)	23.00	167.75	335.00	502.25	718.25
	Perm. Rate (mg/(m*s ²))	-0.0042	0.0016	0.0001	0.0001	-0.0004
Average	Permeation Time (hrs)	24	192.00	336.00	528.00	648.00
	Perm. Rate (mg/(m*s ²))	-0.0041	0.0016	0.0002	0.0002	-0.0001
PERMEATION CALCULATED FROM START OF TEST						
	FKM: Cu Average					
Average	Permeation Time (hrs)	24	192.00	336.00	528.00	648.00
	Perm. Rate (mg/(m*s ²))	0.01	0.00	0.00	0.00	0.00

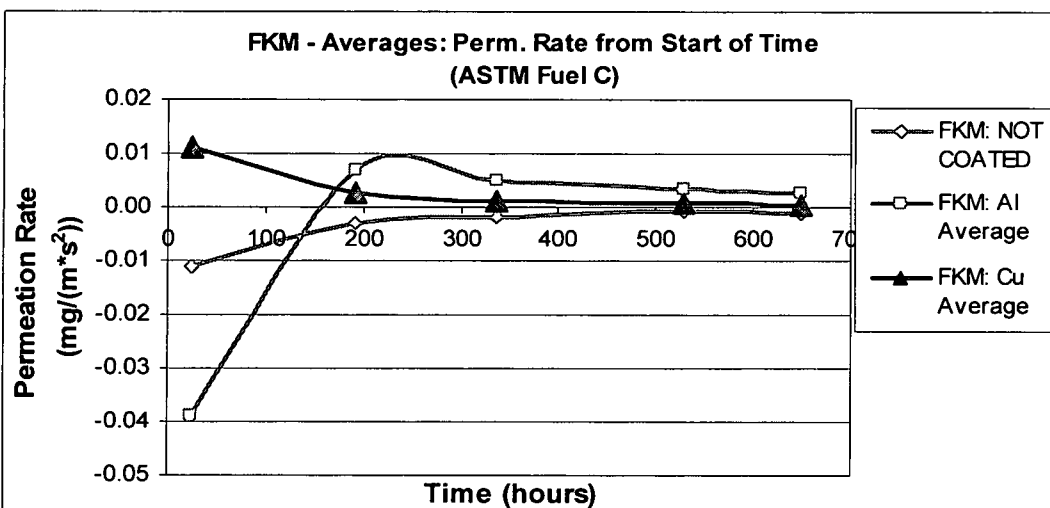
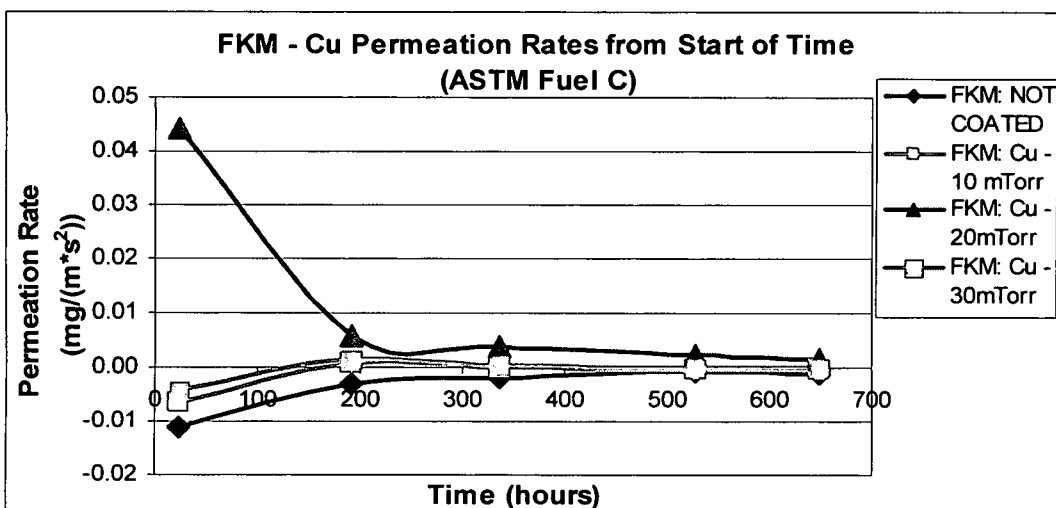
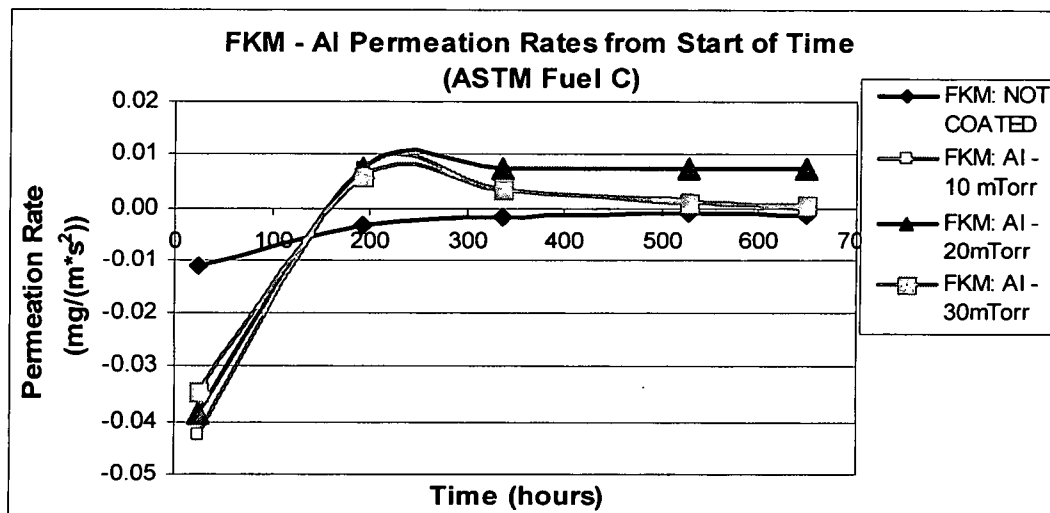


Illustration 102: Fluorocarbon Permeation Charts

Permeation Between Data Points

Table 40: Aluminum Coated NBR Permeation Data (Between Points)

NITRILE BUTADIENE RUBBER - ALUMINUM - ASTM Fuel C Permeation						
TEST NO.	NBR: NOT COATED					
16	Permeation Time (hrs)	24.00	192.00	333.75	525.00	673.00
	Perm. Rate (mg/(m*s ²))	2.54	4.21	2.69	1.55	0.91
17	Permeation Time (hrs)	24.00	192.00	333.75	525.00	673.00
	Perm. Rate (mg/(m*s ²))	2.14	4.36	2.90	1.73	1.03
Average	Permeation Time (hrs)	24.00	192.00	336.00	528.00	648.00
	Perm. Rate (mg/(m*s ²))	2.34	4.29	2.77	1.63	1.09
TEST NO.	NBR: Al - 10 mTorr					
14	Permeation Time (hrs)	24.00	167.50	360.75	502.50	693.75
	Perm. Rate (mg/(m*s ²))	0.71	2.66	1.83	1.28	0.91
18	Permeation Time (hrs)	24.00	192.00	333.25	525.00	668.00
	Perm. Rate (mg/(m*s ²))	2.50	4.40	2.71	1.55	0.95
Average	Permeation Time (hrs)	24	192.00	336.00	528.00	648.00
	Perm. Rate (mg/(m*s ²))	1.61	3.57	2.34	1.38	1.02
TEST NO.	NBR: Al - 20mTorr					
15	Permeation Time (hrs)	24.00	167.50	360.75	502.50	693.75
	Perm. Rate (mg/(m*s ²))	0.70	2.56	1.77	1.23	0.87
19	Permeation Time (hrs)	24.00	192.00	333.25	525.00	668.00
	Perm. Rate (mg/(m*s ²))	2.33	4.40	2.86	1.71	1.08
Average	Permeation Time (hrs)	24.00	192.00	336.00	528.00	648.00
	Perm. Rate (mg/(m*s ²))	1.52	3.52	2.38	1.44	1.06
TEST NO.	NBR: Al - 30mTorr					
20	Permeation Time (hrs)	24.00	192.00	333.25	525.00	668.00
	Perm. Rate (mg/(m*s ²))	2.31	4.14	2.61	1.45	0.86
21	Permeation Time (hrs)	24.00	192.00	333.25	525.00	668.00
	Perm. Rate (mg/(m*s ²))	2.48	4.50	2.97	1.79	1.13
Average	Permeation Time (hrs)	24.00	192.00	336.00	528.00	648.00
	Perm. Rate (mg/(m*s ²))	2.40	4.32	2.76	1.61	1.09
PERMEATION CALCULATED BETWEEN DATA POINTS						
	NBR: Al Average					
Average	Permeation Time (hrs)	24	192.00	336.00	528.00	648.00
	Perm. Rate (mg/(m*s ²))	1.84	3.80	2.49	1.48	1.05

Table 41: Copper Coated NBR Permeation Data (Between Points)

NITRILE BUTADIENE RUBBER - COPPER - ASTM Fuel C Permeation						
TEST NO.	NBR: NOT COATED					
16	Permeation Time (hrs)	24.00	192.00	333.75	525.00	673.00
	Perm. Rate (mg/(m*s ²))	2.54	4.21	2.69	1.55	0.91
17	Permeation Time (hrs)	24.00	192.00	333.75	525.00	673.00
	Perm. Rate (mg/(m*s ²))	2.14	4.36	2.90	1.73	1.03
Average	Permeation Time (hrs)	24.00	192.00	336.00	528.00	648.00
	Perm. Rate (mg/(m*s ²))	2.34	4.29	2.77	1.63	1.09
TEST NO.	NBR: Cu - 10 mTorr					
30	Permeation Time (hrs)	23.75	192.25	359.25	502.75	671.75
	Perm. Rate (mg/(m*s ²))	0.07	1.61	1.22	0.95	0.74
39	Permeation Time (hrs)	23.00	167.75	335.00	502.25	718.25
	Perm. Rate (mg/(m*s ²))	2.30	4.19	3.51	2.86	2.26
Average	Permeation Time (hrs)	24	192.00	336.00	528.00	648.00
	Perm. Rate (mg/(m*s ²))	1.19	2.93	2.40	1.86	1.61
TEST NO.	NBR: Cu - 20mTorr					
31	Permeation Time (hrs)	23.75	192.25	359.25	502.75	671.75
	Perm. Rate (mg/(m*s ²))	0.30	2.23	1.65	1.25	0.94
40	Permeation Time (hrs)	23.00	167.75	335.00	502.25	718.25
	Perm. Rate (mg/(m*s ²))	2.20	4.16	3.49	2.85	2.24
Average	Permeation Time (hrs)	24.00	192.00	336.00	528.00	648.00
	Perm. Rate (mg/(m*s ²))	1.26	3.23	2.63	1.99	1.71
TEST NO.	NBR: Cu - 30mTorr					
32	Permeation Time (hrs)	23.75	192.25	359.25	502.75	671.75
	Perm. Rate (mg/(m*s ²))	0.09	1.75	1.36	1.05	0.82
41	Permeation Time (hrs)	23.00	167.75	335.00	502.25	718.25
	Perm. Rate (mg/(m*s ²))	2.06	4.12	3.54	2.94	2.34
Average	Permeation Time (hrs)	24.00	192.00	336.00	528.00	648.00
	Perm. Rate (mg/(m*s ²))	1.09	2.97	2.50	1.95	1.70
PERMEATION CALCULATED BETWEEN DATA POINTS						
	NBR: Cu Average					
Average	Permeation Time (hrs)	24	192.00	336.00	528.00	648.00
	Perm. Rate (mg/(m*s ²))	1.18	3.04	2.51	1.93	1.68

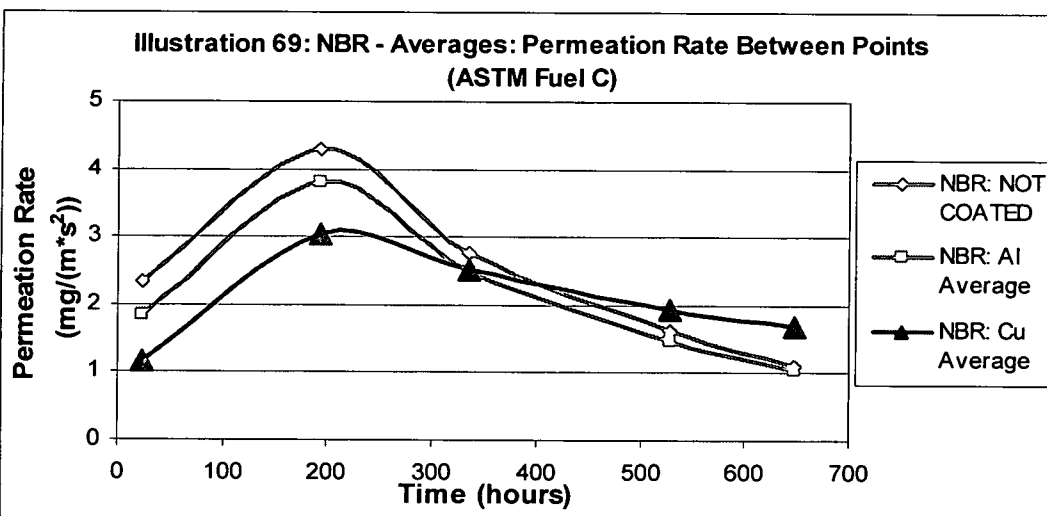
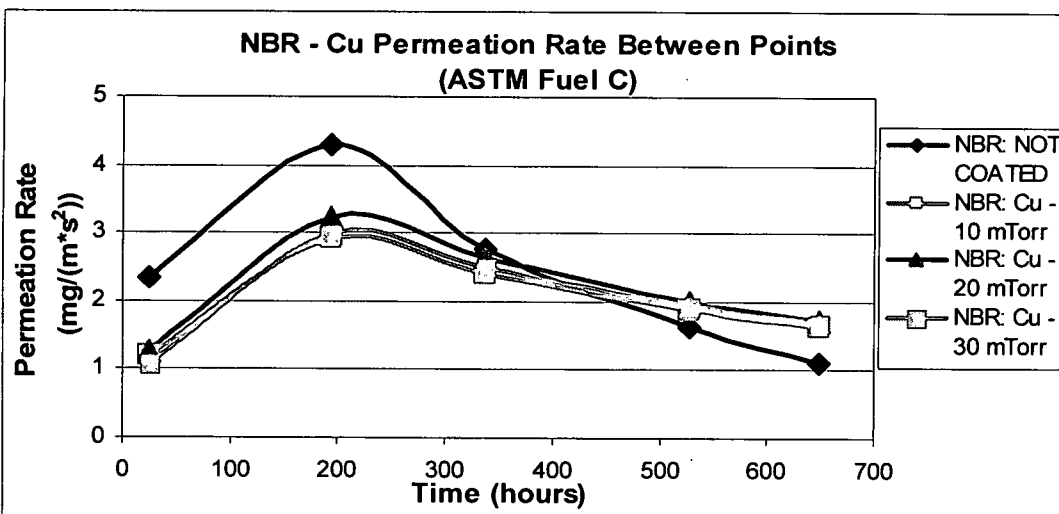
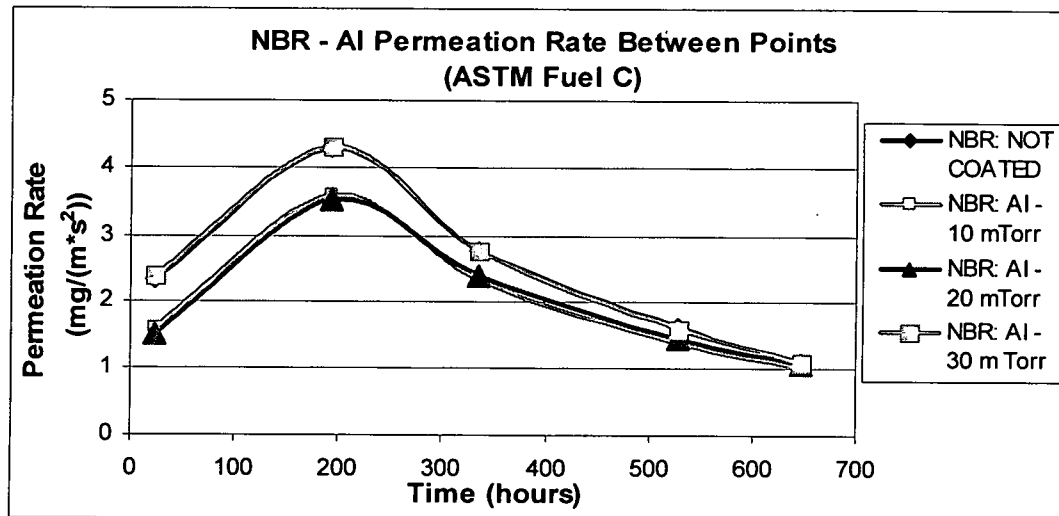


Illustration 103: Nitrile Permeation Charts (Between Points)

Table 42: Aluminum Coated FVMQ Permeation Data (Between Points)

FLUOROSILICONE RUBBER - ALUMINUM - ASTM Fuel C Permeation						
TEST NO.	FVMQ: NOT COATED					
1	Permeation Time (hrs)	24.50	168.17	376.75	501.33	669.58
	Perm. Rate (mg/(m*s ²))	2.08	2.90	2.65	2.36	
2	Permeation Time (hrs)	24.50	168.17	376.75	501.33	669.58
	Perm. Rate (mg/(m*s ²))	2.07	2.86	2.61	2.31	
Average	Permeation Time (hrs)	24.00	192.00	336.00	528.00	648.00
	Perm. Rate (mg/(m*s ²))	2.08	2.92	2.70	2.11	1.74
TEST NO.	FVMQ: Al - 10 mTorr					
22	Permeation Time (hrs)	24.00	192.00	333.25	525.00	668.00
	Perm. Rate (mg/(m*s ²))	2.21	2.92	2.78	2.49	2.21
23	Permeation Time (hrs)	147.00	171.00	361.00	506.50	650.00
	Perm. Rate (mg/(m*s ²))	2.96	2.94	2.50	2.70	1.96
Average	Permeation Time (hrs)	24.00	192.00	336.00	528.00	648.00
	Perm. Rate (mg/(m*s ²))	2.21	2.91	2.64	2.57	2.11
TEST NO.	FVMQ: Al - 20mTorr					
12	Permeation Time (hrs)	24.00	167.50	360.75	502.50	693.75
	Perm. Rate (mg/(m*s ²))	1.85	2.43	2.29	1.99	1.65
24	Permeation Time (hrs)	24.00	192.00	333.25	525.00	668.00
	Perm. Rate (mg/(m*s ²))	2.33	4.40	2.86	1.71	1.08
Average	Permeation Time (hrs)	24.00	192.00	336.00	528.00	648.00
	Perm. Rate (mg/(m*s ²))	2.09	3.43	2.58	1.82	1.45
TEST NO.	FVMQ: Al - 30mTorr					
25	Permeation Time (hrs)	147.00	171.00	361.00	506.50	650.00
	Perm. Rate (mg/(m*s ²))	2.89	2.89	2.46	2.62	1.91
26	Permeation Time (hrs)	147.00	171.00	361.00	506.50	650.00
	Perm. Rate (mg/(m*s ²))	4.18	3.55	2.29	1.55	0.83
Average	Permeation Time (hrs)	24.00	192.00	336.00	528.00	648.00
	Perm. Rate (mg/(m*s ²))	2.15	2.40	2.17	1.82	1.45
PERMEATION CALCULATED BETWEEN DATA POINTS						
	FVMQ: Al Average					
Average	Permeation Time (hrs)	24	192.00	336.00	528.00	648.00
	Perm. Rate (mg/(m*s ²))	2.15	2.91	2.47	2.07	1.67

Table 43: Copper Coated FVMQ Permeation Data (Between Points)

FLUOROSILICONE RUBBER - COPPER - ASTM Fuel C Permeation						
TEST NO.	FVMQ: NOT COATED					
1	Permeation Time (hrs)	24.50	168.17	376.75	501.33	669.58
	Perm. Rate (mg/(m*s ²))	2.08	2.90	2.65	2.36	
2	Permeation Time (hrs)	24.50	168.17	376.75	501.33	669.58
	Perm. Rate (mg/(m*s ²))	2.07	2.86	2.61	2.31	
Average	Permeation Time (hrs)	24.00	192.00	336.00	528.00	648.00
	Perm. Rate (mg/(m*s ²))	2.08	2.92	2.70	2.11	1.74
TEST NO.	FVMQ: Cu - 10 mTorr					
27	Permeation Time (hrs)	23.75	192.25	359.25	502.75	671.75
	Perm. Rate (mg/(m*s ²))	1.57	2.35	2.05	1.82	1.57
36	Permeation Time (hrs)	23.00	167.75	335.00	502.25	718.25
	Perm. Rate (mg/(m*s ²))	2.23	2.90	2.85	2.72	2.47
Average	Permeation Time (hrs)	24	192.00	336.00	528.00	648.00
	Perm. Rate (mg/(m*s ²))	1.90	2.64	2.48	2.24	2.08
TEST NO.	FVMQ: Cu - 20mTorr					
28	Permeation Time (hrs)	23.75	192.25	359.25	502.75	671.75
	Perm. Rate (mg/(m*s ²))	1.62	2.35	1.70	2.18	1.53
37	Permeation Time (hrs)	23.00	167.75	335.00	502.25	718.25
	Perm. Rate (mg/(m*s ²))	2.23	2.90	2.84	2.71	2.45
Average	Permeation Time (hrs)	24	192.00	336.00	528.00	648.00
	Perm. Rate (mg/(m*s ²))	1.93	2.65	2.29	2.44	2.12
TEST NO.	FVMQ: Cu - 30mTorr					
29	Permeation Time (hrs)	23.75	192.25	359.25	502.75	671.75
	Perm. Rate (mg/(m*s ²))	0.09	1.75	1.36	1.05	0.82
38	Permeation Time (hrs)	23.00	167.75	335.00	502.25	718.25
	Perm. Rate (mg/(m*s ²))	2.18	2.88	2.83	2.71	2.46
Average	Permeation Time (hrs)	24.00	192.00	336.00	528.00	648.00
	Perm. Rate (mg/(m*s ²))	1.14	2.33	2.14	1.85	1.70
PERMEATION CALCULATED BETWEEN DATA POINTS						
	FVMQ: Cu Average					
Average	Permeation Time (hrs)	24	192.00	336.00	528.00	648.00
	Perm. Rate (mg/(m*s ²))	1.66	2.54	2.30	2.18	1.97

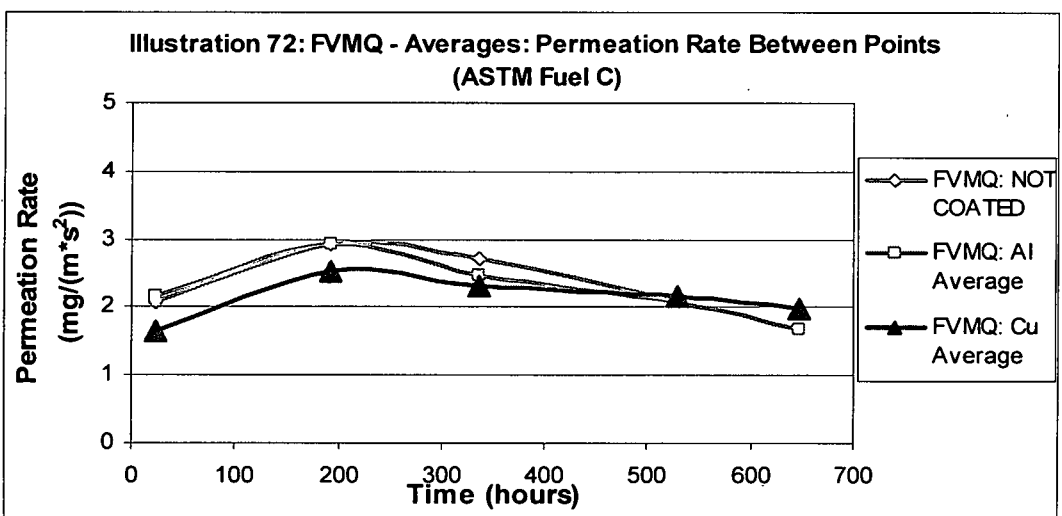
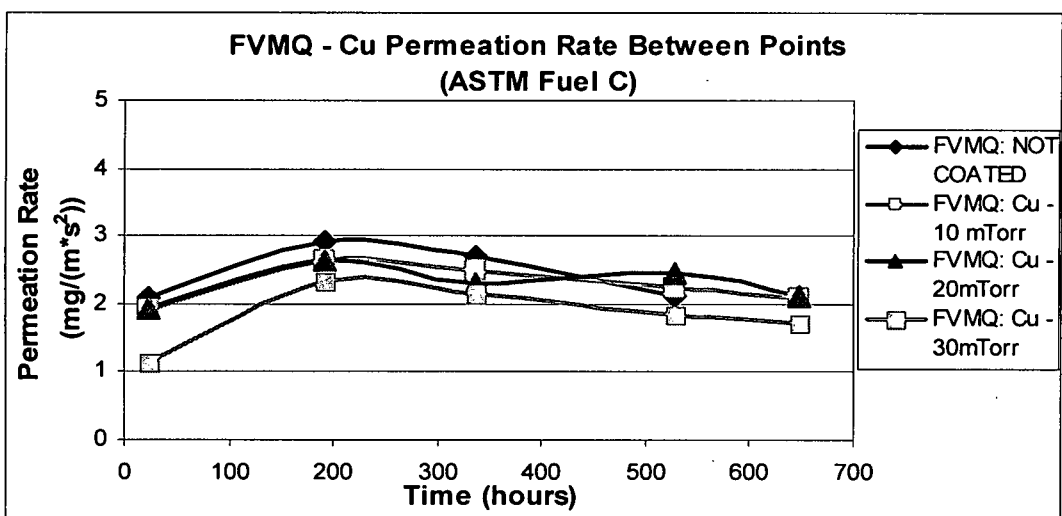
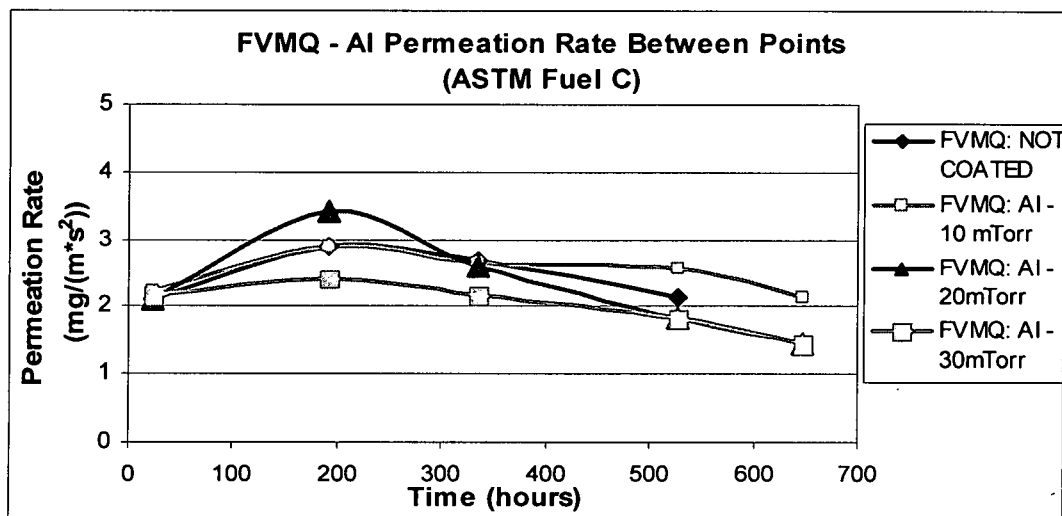


Illustration 104: Fluorosilicone Permeation Charts (Between Points)

Table 44: Aluminum Coated FKM Permeation Data (Between Points)

FLUOROCARBON RUBBER - ALUMINUM - ASTM Fuel C Permeation						
TEST NO.	FKM: NOT COATED					
3	Permeation Time (hrs)	24.50	168.17	376.75	501.33	669.58
	Perm. Rate (mg/(m*s ²))	-0.0117	-0.0023	0.0001	0.0010	-0.0020
4	Permeation Time (hrs)	24.50	168.17	376.75	501.33	669.58
	Perm. Rate (mg/(m*s ²))	-0.0106	-0.0030	0.0002	0.0010	-0.0022
Average	Permeation Time (hrs)	24.00	192.00	336.00	528.00	648.00
	Perm. Rate (mg/(m*s ²))	-0.0112	-0.0018	-0.0001	0.0008	-0.0015
TEST NO.	FKM: Al - 10 mTorr					
5	Permeation Time (hrs)	24.50	168.17	376.75	501.33	669.58
	Perm. Rate (mg/(m*s ²))	-0.0400	0.0039	0.0000	0.0008	-0.0019
6	Permeation Time (hrs)	24.50	168.17	376.75	501.33	669.58
	Perm. Rate (mg/(m*s ²))	-0.0454	0.0051	0.0001	0.0012	-0.0015
Average	Permeation Time (hrs)	24.00	192.00	336.00	528.00	648.00
	Perm. Rate (mg/(m*s ²))	-0.0427	0.0075	0.0026	0.0012	-0.0010
TEST NO.	FKM: Al - 20mTorr					
9	Permeation Time (hrs)	24.50	168.17	376.75	501.33	669.58
	Perm. Rate (mg/(m*s ²))	-0.0347	0.0030	0.0005	0.0004	-0.0023
10	Permeation Time (hrs)	24.50	168.17	376.75	501.33	669.58
	Perm. Rate (mg/(m*s ²))	-0.0427	0.0044	0.0008	0.0003	-0.0022
Average	Permeation Time (hrs)	24.00	192.00	336.00	528.00	648.00
	Perm. Rate (mg/(m*s ²))	-0.0387	0.0065	0.0030	0.0004	-0.0017
TEST NO.	FKM: Al - 30mTorr					
11	Permeation Time (hrs)	24.50	168.17	376.75	501.33	669.58
	Perm. Rate (mg/(m*s ²))	-0.0347	0.0031	0.0007	0.0000	-0.0020
	Permeation Time (hrs)					
	Perm. Rate (mg/(m*s ²))					
Average	Permeation Time (hrs)	24.00	192.00	336.00	528.00	648.00
	Perm. Rate (mg/(m*s ²))	-0.0347	0.0066	0.0032	0.0002	-0.0016
PERMEATION CALCULATED BETWEEN DATA POINTS						
	FKM: Al Average					
Average	Permeation Time (hrs)	24	192.00	336.00	528.00	648.00
	Perm. Rate (mg/(m*s ²))	-0.04	0.01	0.00	0.00	0.00

Table 45: Copper Coated FKM Permeation Data (Between Points)

FLUOROCARBON RUBBER - COPPER - ASTM Fuel C Permeation						
TEST NO.	FKM: NOT COATED					
3	Permeation Time (hrs)	24.50	168.17	376.75	501.33	669.58
	Perm. Rate (mg/(m*s ²))	-0.0117	-0.0023	0.0001	0.0010	-0.0020
4	Permeation Time (hrs)	24.50	168.17	376.75	501.33	669.58
	Perm. Rate (mg/(m*s ²))	-0.0106	-0.0030	0.0002	0.0010	-0.0022
Average	Permeation Time (hrs)	24.00	192.00	336.00	528.00	648.00
	Perm. Rate (mg/(m*s ²))	-0.0112	-0.0018	-0.0001	0.0008	-0.0015
TEST NO.	FKM: Cu - 10 mTorr					
33	Permeation Time (hrs)	23.75	192.25	359.25	502.75	671.75
	Perm. Rate (mg/(m*s ²))	-0.0058	-0.0001	-0.0002	-0.0018	0.0001
42	Permeation Time (hrs)	23.00	167.75	335.00	502.25	718.25
	Perm. Rate (mg/(m*s ²))	-0.0071	0.0017	0.0002	0.0001	-0.0004
Average	Permeation Time (hrs)	24	192.00	336.00	528.00	648.00
	Perm. Rate (mg/(m*s ²))	-0.0064	0.0010	0.0001	-0.0008	-0.0002
TEST NO.	FKM: Cu - 20mTorr					
34	Permeation Time (hrs)	23.00	167.75	335.00	502.25	718.25
	Perm. Rate (mg/(m*s ²))	-0.0054	0.0012	0.0004	0.0002	-0.0004
43	Permeation Time (hrs)	23.00	167.75	335.00	502.25	718.25
	Perm. Rate (mg/(m*s ²))	0.0941	0.0156	0.0072	0.0047	0.0028
Average	Permeation Time (hrs)	24	192.00	336.00	528.00	648.00
	Perm. Rate (mg/(m*s ²))	0.0441	0.0056	0.0038	0.0022	0.0014
TEST NO.	FKM: Cu - 30mTorr					
35	Permeation Time (hrs)	23.00	167.75	335.00	502.25	718.25
	Perm. Rate (mg/(m*s ²))	-0.0042	0.0012	0.0004	0.0002	-0.0004
44	Permeation Time (hrs)	23.00	167.75	335.00	502.25	718.25
	Perm. Rate (mg/(m*s ²))	-0.0042	0.0016	0.0001	0.0001	-0.0004
Average	Permeation Time (hrs)	24	192.00	336.00	528.00	648.00
	Perm. Rate (mg/(m*s ²))	-0.0041	0.0016	0.0002	0.0002	-0.0001
PERMEATION CALCULATED BETWEEN DATA POINTS						
	FKM: Cu Average					
Average	Permeation Time (hrs)	24	192.00	336.00	528.00	648.00
	Perm. Rate (mg/(m*s ²))	0.01	0.00	0.00	0.00	0.00

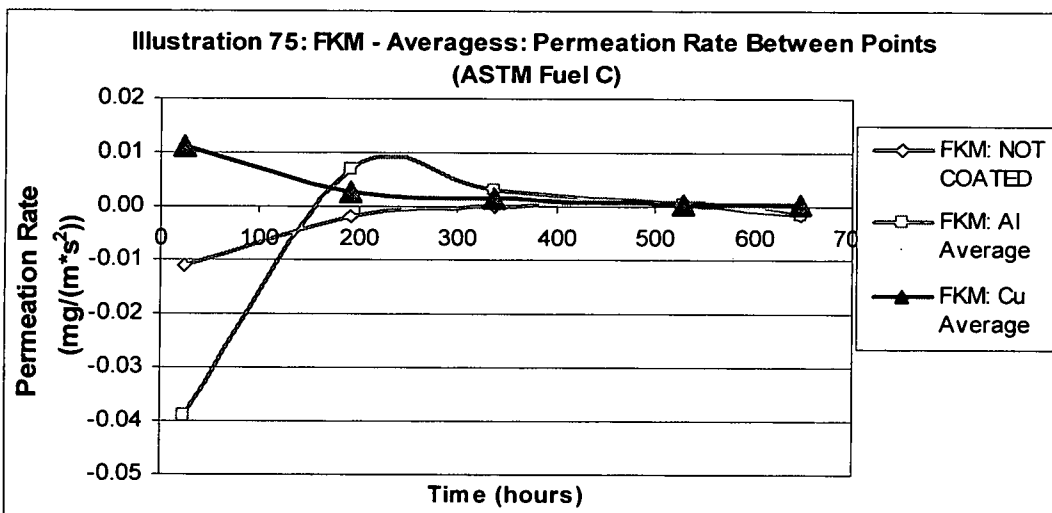
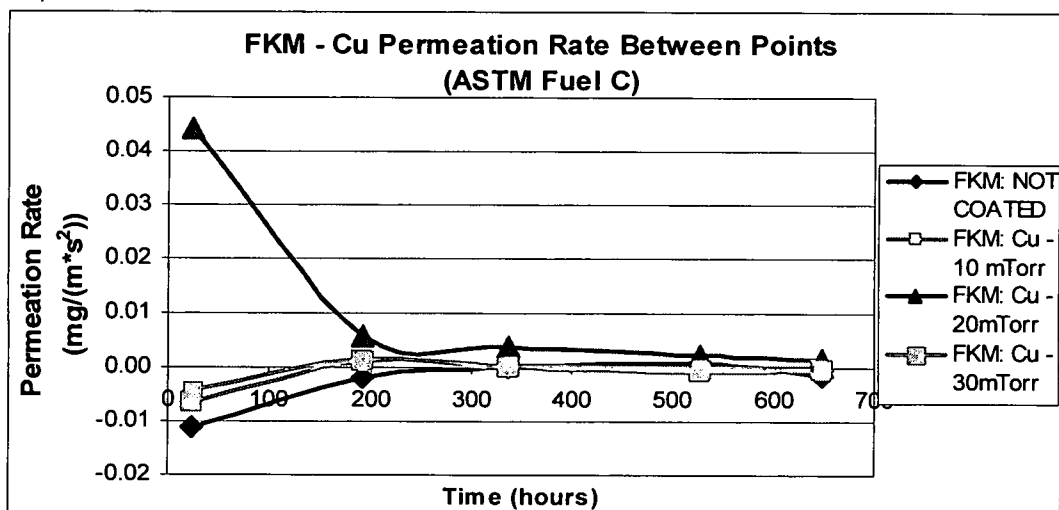
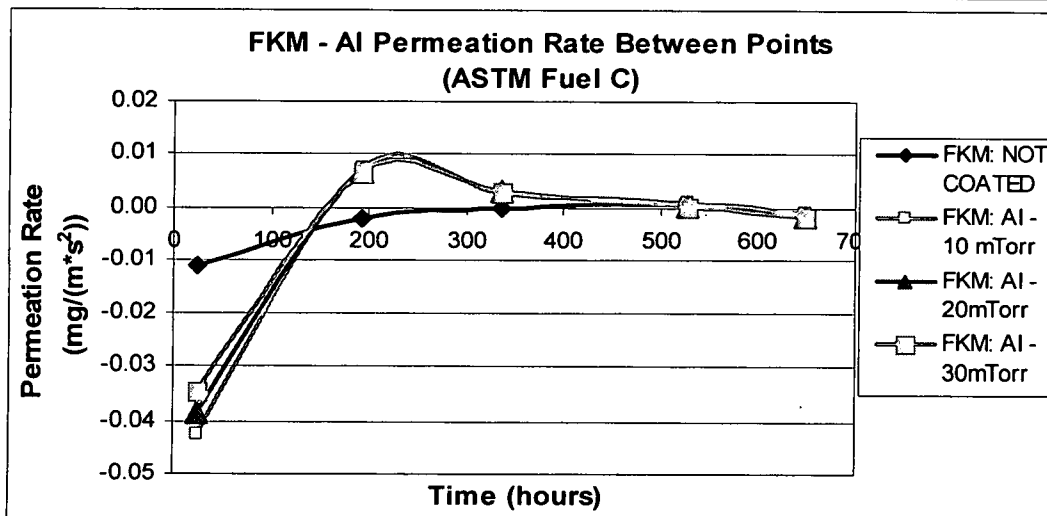


Illustration 105: Fluorocarbon Permeation Charts (Between Points)

Tensile Curves

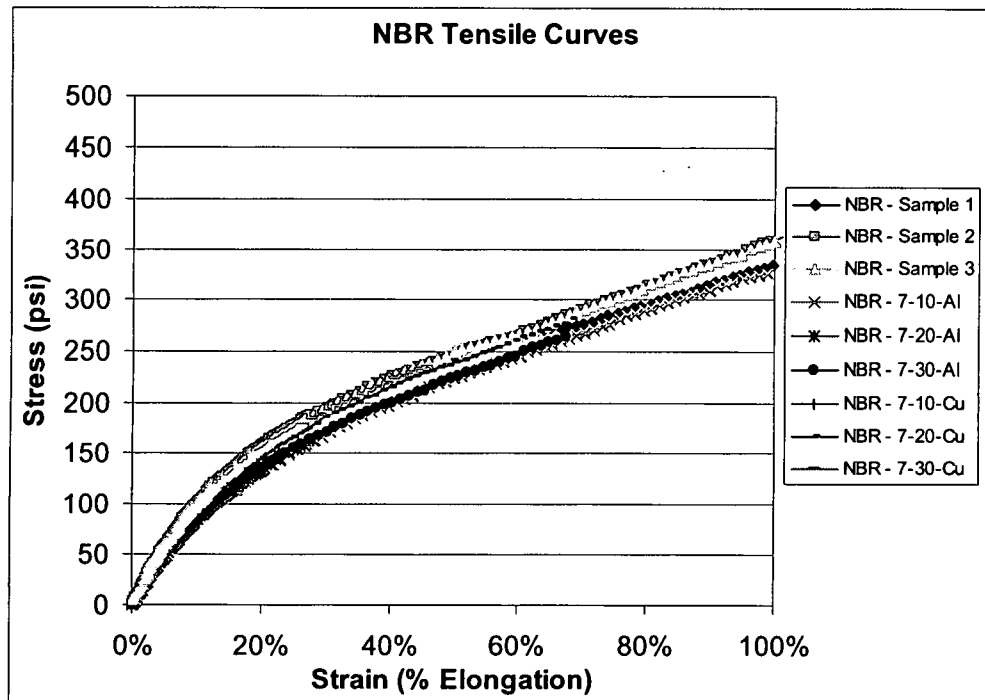


Illustration 106: NBR Tensile Curves (All Samples)

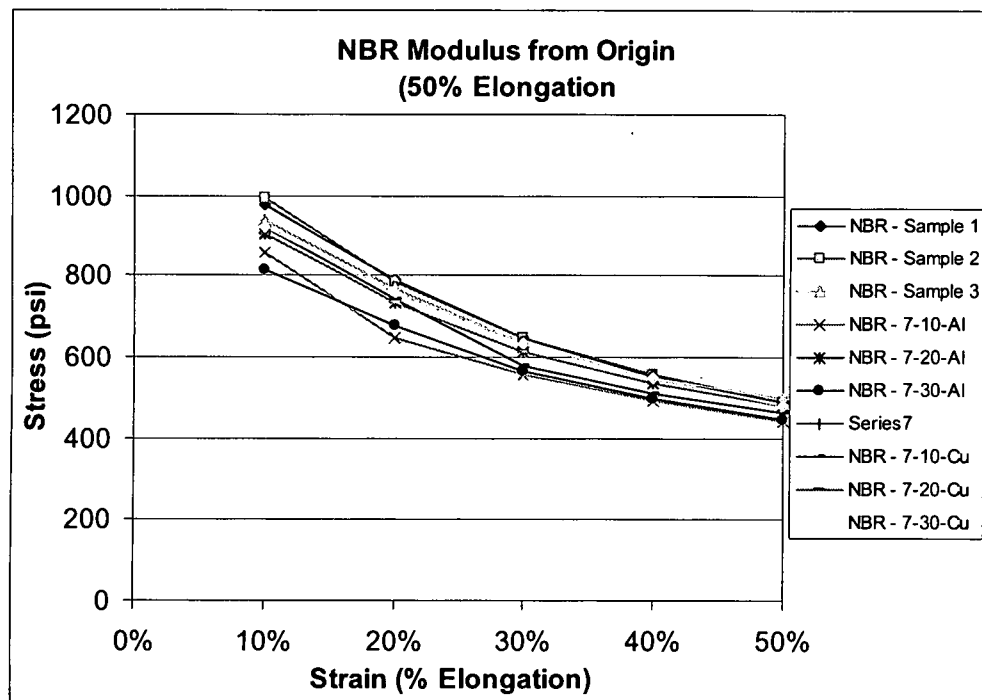


Illustration 107: NBR Modulus Curves (All Samples)

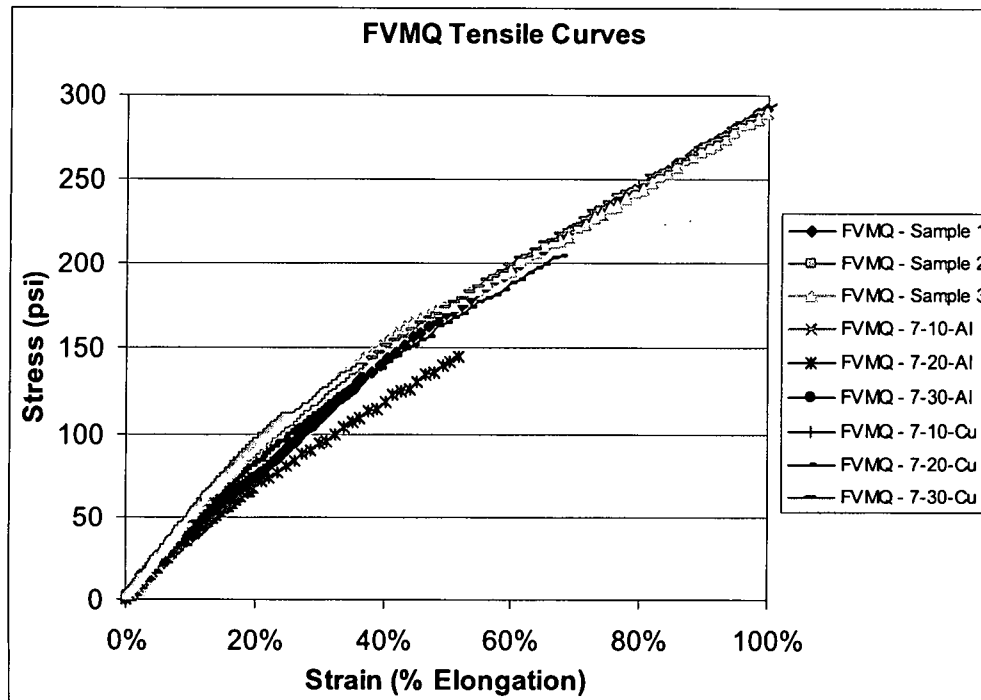


Illustration 108: FVMQ Tensile Curves (All Samples)

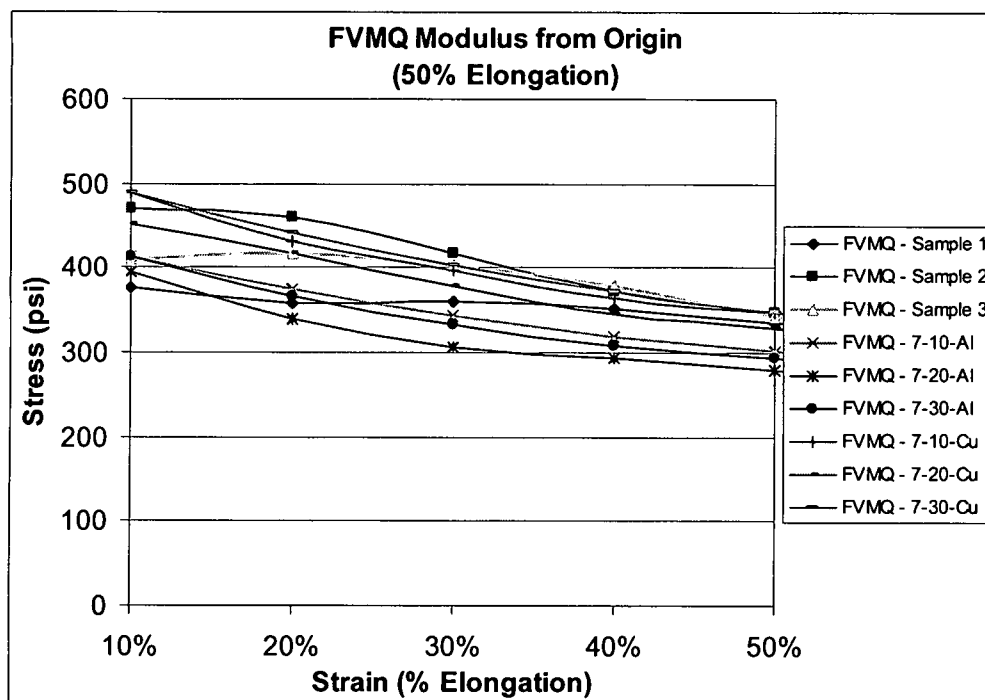


Illustration 109: FVMQ Modulus Curves (All Samples)

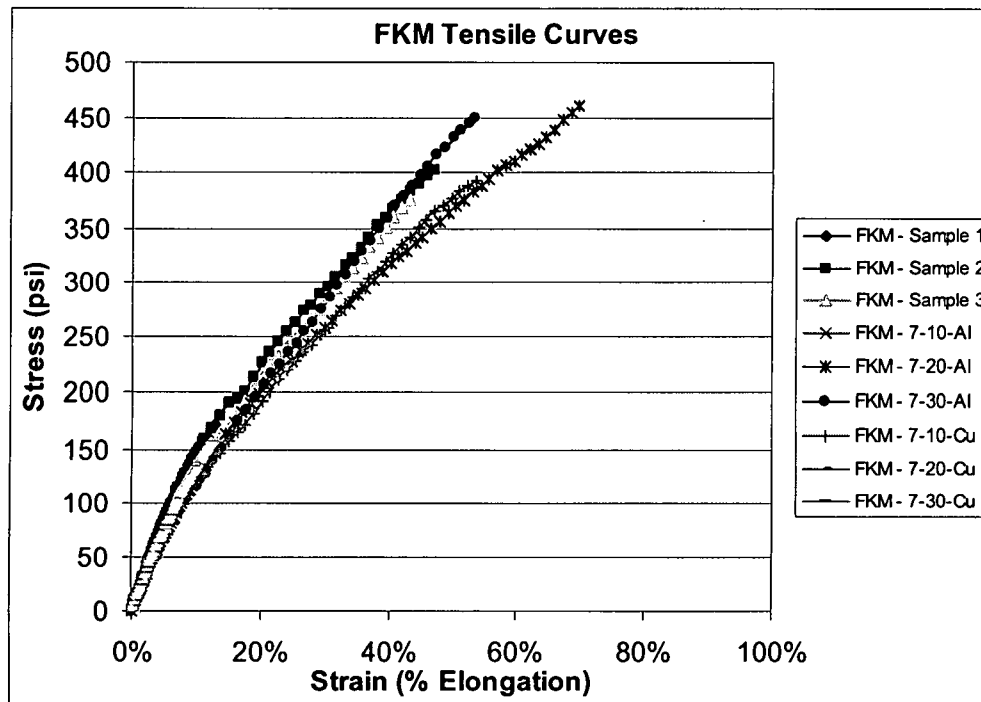


Illustration 110: FKM Tensile Curves (All Samples)

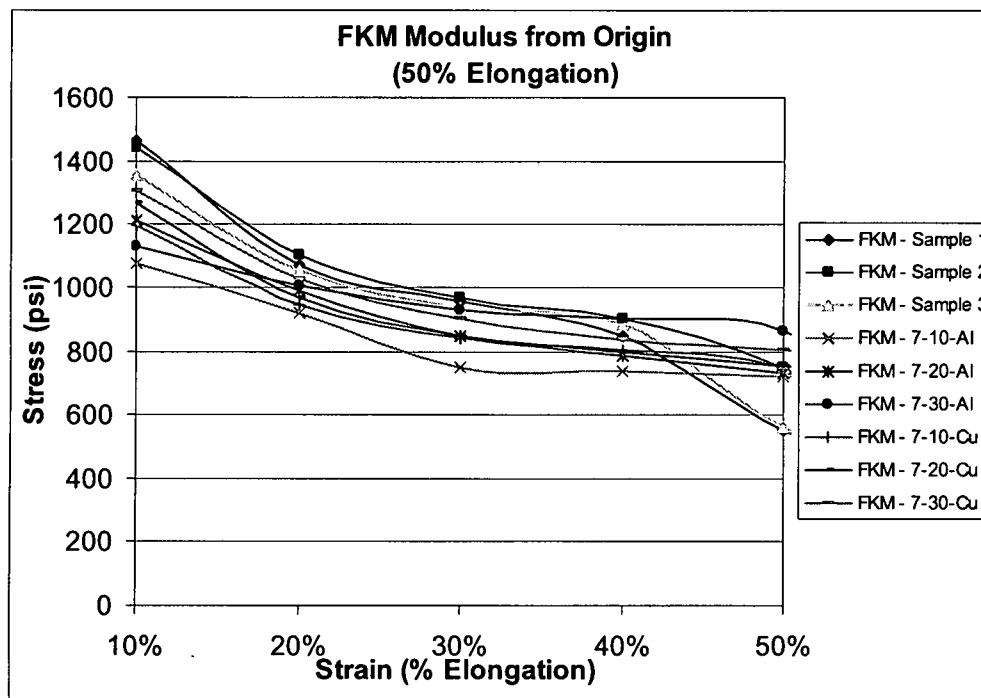


Illustration 111: FKM Modulus Curves (All Samples)

Sample Testing Records

Table 46: Sample Testing Records (Samples 1 through 22)

Test No.	Test Seat	Sample Type	Polymer	Coating	Time (min)	Pressure (mTorr)	Starting Weight (g)	24.50 Hrs	168.17 Hrs	376.75 Hrs	501.33 Hrs	669.58 Hrs
1	1	FVMQ	FVMQ	---	---	---	185.7347	185.3621	182.3224	178.2887	176.1455	
2	2	FVMQ	FVMQ	---	---	---	184.2971	183.9264	180.9239	176.9451	174.8466	
3	3	FKM	FKM	---	---	---	188.1436	188.1457	188.1481	188.148	188.1471	188.1496
4	4	FKM	FKM	---	---	---	186.3181	186.3200	186.3231	186.3228	186.3219	186.3246
DATE TESTED							5/17/2004	5/18/2004	5/24/2004	6/2/2004	6/7/2004	6/14/2004
TIME TESTED							4:50 PM	5:20 PM	5:00 PM	9:35 AM	2:30 PM	2:45 PM

Test No.	Test Seat	Sample Type	Polymer	Coating	Time (min)	Pressure (mTorr)	Starting Weight (g)	24.50 Hrs	168.17 Hrs	376.75 Hrs	501.33 Hrs	669.58 Hrs
5	5	1	FKM	Aluminum	10	10	186.0705	186.0720	186.0751	186.0751	186.0744	186.0767
6	6	1	FKM	Aluminum	10	10	185.6438	185.6455	185.6483	185.6481	185.647	185.6489
7	7	4	FVMQ	Aluminum	10	10	184.2520	183.8915	180.929	176.9771	174.882	
8	8	4	FVMQ	Aluminum	10	10	185.6618	185.3181	182.4831	178.6504	176.5381	
9	9	2	FKM	Aluminum	10	20	186.9658	186.9671	186.9702	186.9694	186.969	186.9718
10	10	2	FKM	Aluminum	10	20	185.8067	185.8083	185.8113	185.8101	185.8098	185.8125
11	11	3	FKM	Aluminum	10	30	187.0809	187.0822	187.0852	187.0842	187.0842	187.0867
DATE TESTED							5/17/2004	5/18/2004	5/24/2004	6/2/2004	6/7/2004	6/14/2004
TIME TESTED							4:50 PM	5:20 PM	5:00 PM	9:35 AM	2:30 PM	2:45 PM

Test No.	Test Seat	Sample Type	Polymer	Coating	Time (min)	Pressure (mTorr)	Starting Weight (g)	24.00 Hrs	167.50 Hrs	360.75 Hrs	502.50 Hrs	693.75 Hrs
12	1	5	FVMQ	Aluminum	10	20	186.5235	186.1992	183.5535	180.3215	178.2648	175.9582
13	2	6	FVMQ	Aluminum	10	30	184.6978	184.3835	181.775	178.6189	176.6404	174.4634
14	7	7	NBR	Aluminum	10	10	185.0046	184.8796	182.0909	179.5098	178.185	176.9082
15	8	8	NBR	Aluminum	10	20	184.1477	184.0256	181.344	178.8542	177.5811	176.3616
DATE TESTED							6/7/2004	6/8/2004	6/14/2004	6/22/2004	6/28/2004	7/6/2004
TIME TESTED							3:15 PM	3:15 PM	2:45 PM	4:00 PM	1:45 PM	1:00 PM

Test No.	Test Seat	Sample Type	Polymer	Coating	Time (min)	Pressure (mTorr)	Starting Weight (g)	24.00 Hrs	192.00 Hrs	333.75 Hrs	525.00 Hrs	673.00 Hrs
16	3	NBR	NBR	---	---	---	184.5820	184.1378	178.9802	176.1933	174.0318	173.0525
17	4	NBR	NBR	---	---	---	186.3183	185.9432	180.5965	177.5928	175.1824	174.0747
DATE TESTED							6/14/2004	6/15/2004	6/22/2004	6/28/2004	7/6/2004	7/12/2004
TIME TESTED							4:00 PM	4:00 PM	4:00 PM	1:45 PM	1:00 PM	5:00 PM

Test No.	Test Seat	Sample Type	Polymer	Coating	Time (min)	Pressure (mTorr)	Starting Weight (g)	24.00 Hrs	192.00 Hrs	333.25 Hrs	525.00 Hrs	668.00 Hrs
18	5	7	NBR	Aluminum	10	10	185.6252	185.1865	179.7933	176.9999	174.8290	173.8332
19	6	8	NBR	Aluminum	10	20	186.9175	186.5102	181.1141	178.1627	175.7670	174.6381
20	9	9	NBR	Aluminum	10	30	183.2572	182.8526	177.7787	175.0868	173.0540	172.1526
21	10	9	NBR	Aluminum	10	30	187.5247	187.0897	181.571	178.5057	176.0027	174.826
22	11	4	FVMQ	Aluminum	10	10	187.0189	186.6319	183.0508	180.1892	176.6998	174.3921
DATE TESTED							6/14/2004	6/15/2004	6/22/2004	6/28/2004	7/6/2004	7/12/2004
TIME TESTED							4:00 PM	4:00 PM	4:00 PM	1:45 PM	1:00 PM	5:00 PM

Table 47: Sample Testing Records (Samples 23 through 55)

Test No.	Test Seat	Sample Type	Polymer	Coating	Time (min)	Pressure (mTorr)	Starting Weight (g)	147.00 Hrs	171.00 Hrs	361.00 Hrs	506.50 Hrs	650.00 Hrs
23	1	4	FVMQ	Aluminum	10	10	185.4280	182.2528	181.7381	178.2768	175.4064	173.3546
24	2	5	FVMQ	Aluminum	10	20	185.8528	182.7529	182.242	178.7941	175.8788	173.7455
25	7	6	FVMQ	Aluminum	10	30	184.4430	181.3481	180.8412	177.4336	174.6473	172.6512
26	8	6	FVMQ	Aluminum	10	30	183.1020	178.6182	177.9972	174.8218	173.1779	172.3061
DATE TESTED							7/6/2004	7/12/2004	7/13/2004	7/20/2004	7/27/2004	8/2/2004
TIME TESTED							2:00 PM	5:00 PM	5:00 PM	5:30 PM	4:30 PM	4:00 PM

Test No.	Test Seat	Sample Type	Polymer	Coating	Time (min)	Pressure (mTorr)	Starting Weight (g)	23.75 Hrs	192.25 Hrs	359.25 Hrs	502.75 Hrs	671.75 Hrs
27	3	13	FVMQ	Copper	7	10	186.8257	186.5535	183.6653	181.1646	179.2575	177.3267
28	4	14	FVMQ	Copper	7	20	186.4111	186.1304	183.235	181.1646	178.8783	176.9932
29	5	15	FVMQ	Copper	7	30	185.1671	184.9047	182.1533	179.8025	178.0442	176.3091
30	6	16	NBR	Copper	7	10	182.8178	182.8063	180.8258	179.3447	178.3503	177.4422
31	9	17	NBR	Copper	7	20	185.6953	185.6425	182.895	180.8828	179.5743	178.4154
32	10	18	NBR	Copper	7	30	184.3258	184.3100	182.1625	180.5063	179.4020	178.3885
33	11	10	FKM	Copper	7	10	187.2185	187.2195	187.2196	187.2199	187.2218	187.2217
DATE TESTED							7/12/2004	7/13/2004	7/20/2004	7/27/2004	8/2/2004	8/9/2004
TIME TESTED							5:15 PM	5:00 PM	5:30 PM	4:30 PM	4:00 PM	5:00 PM

Test No.	Test Seat	Sample Type	Polymer	Coating	Time (min)	Pressure (mTorr)	Starting Weight (g)	23.00 Hrs	167.75 Hrs	335.00 Hrs	502.25 Hrs	718.25 Hrs
34	1	11	FKM	Copper	7	20	188.0092	188.0101	188.0077	188.0082	188.0083	188.0114
35	2	12	FKM	Copper	7	30	187.3691	187.3698	187.3676	187.3682	187.3685	187.3711
36	3	13	FVMQ	Copper	7	10	185.5303	185.1564	181.9793	178.5664	175.5598	172.5759
37	4	14	FVMQ	Copper	7	20	185.1574	184.7833	181.61	178.209	175.2295	172.3158
38	5	15	FVMQ	Copper	7	30	185.7034	185.338	182.1775	178.7767	175.7822	172.8098
39	6	16	NBR	Copper	7	10	184.2808	183.8954	179.1539	175.7123	173.7879	172.4555
40	7	17	NBR	Copper	7	20	184.0249	183.6565	178.9341	175.494	173.5832	172.2678
41	8	18	NBR	Copper	7	30	185.6496	185.3031	180.6056	176.9867	174.8812	173.389
42	9	10	FKM	Copper	7	10	187.9277	187.9289	187.9256	187.9272	187.9275	187.9298
43	10	11	FKM	Copper	7	20	188.1115	188.0957	188.0924	188.094	188.0943	188.0968
44	11	12	FKM	Copper	7	30	186.4714	186.4721	186.4695	186.4711	186.4709	186.4736
DATE TESTED							8/9/2004	8/10/2004	8/16/2004	8/23/2004	8/30/2004	9/8/2004
TIME TESTED							5:45 PM	4:45 PM	5:30 PM	4:45 PM	4:00 PM	4:00 PM

Test No.	Test Seat	Sample Type	Polymer	Coating	Time (min)	Pressure (mTorr)	Starting Weight (g)	49.50 Hrs	170.25 Hrs	435.50 Hrs	603.50 Hrs
45	1	Toluene	FVMQ				187.2950	185.9462	182.4194	174.6752	170.09
46	2	Toluene	NBR				185.0949	176.6847	162.7192	162.0917	162.0064
47	3	Toluene	FVMQ	Copper	7	10	188.0748	186.7074	183.1814	175.4583	170.9045
48	4	Toluene	FVMQ	Copper	7	20	186.4499	185.1167	181.6063	173.8937	169.3687
49	5	Toluene	NBR	Copper	7	10	186.0490	178.5388	163.5322	162.8309	162.7447
50	6	Toluene	NBR	Copper	7	20	183.4950	176.3869	163.2719	162.6595	162.5761
51	7	Isooctane	FVMQ				183.7254	183.6478	183.3205	182.5973	182.1842
52	8	Isooctane	NBR				182.7274	182.7288	182.7234	182.7227	182.7168
53	9	Isooctane	FVMQ	Copper	7	30	181.8309	181.7500	181.4102	180.6678	180.2406
54	10	Isooctane	NBR	Copper	7	10	181.4715	181.4140	181.4089	181.4079	181.4035
55	11	Isooctane	NBR	Copper	7	20	179.5551	179.6567	179.5513	179.5507	179.5458
DATE TESTED							9/13/2004	9/15/2004	9/20/2004	10/1/2004	11/8/2004
TIME TESTED							11:30 AM	1:00 PM	1:45 PM	3:00 PM	3:00 PM

APPENDIX B: SUPPLEMENTARY INFORMATION

Magnetron Sputtering

Magnetron sputtering is the most widely used variant of DC sputtering.

DC sputtering is a physical vapor deposition process, meaning that the depositing atoms are liberated from the surface of the target material by physical means, rather than chemical processes or due to thermal effects. In the basic process of DC sputtering, atoms can be ejected or sputtered from solid materials at room temperature by bombardment of the target with energetic, positively charged ions. These sputtered atoms can then traverse a reduced pressure ambient and deposit on the substrate that is to be coated. The impinging atoms are generated in a gas plasma in the deposition chamber. The term plasma was first coined by Irving Langmuir in 1929 to describe ionized gases in high current vacuum tubes [26]. A plasma is a quasineutral gas, composed of weakly ionized gases consisting of electrons, ions, neutral atoms and molecular species. The plasma exhibits a collective behavior in the presence of applied electromagnetic fields.

For a gas to undergo gaseous breakdown and become a plasma, first a stray electron near the cathode carrying an initial current is accelerated towards the anode by the applied electric field. This electron collides with a neutral gas

atom and converts it to a positively charged ion and liberating another electron. This yields a cascade effect, whereby the electric field drives the ions in the opposite direction of the electrons, whereby the ions collide with the cathodic target, ejecting particles from the surface of the target and secondary electrons. For this breakdown to occur, the distance between the anode and cathode must be sufficient to allow electrons to gain the requisite energy for the ionization cascade. The Townsend equation relates the current required for the plasma to develop in relation to the distance between the electrodes. The Townsend equation is as follows [26].

$$i = i_0 \frac{e^{\alpha d}}{[1 - \gamma_e e^{(\alpha d - 1)}]} \quad (1)$$

Where: i = discharge current

i_0 = initial current

α = Townsend ionization coefficient: the probability per unit length of ionization occurring during an electron-gas atom collision

γ_e = Townsend secondary-electron emission: the number of secondary electrons emitted at the cathode per ion incident

For an electron of charge q traveling a distance (λ), the probability of reaching the ionization potential (V_i) is $e^{(-V_i/qe\lambda)}$. As such, the Townsend ionization coefficient can be calculated as follows.

$$\alpha = \frac{1}{\lambda} e^{-\frac{V_i}{q\varepsilon\lambda}} \quad (2)$$

Where: λ = the distance the electron is traveling

q = electron charge

v_i = ionization potential

ε = breakdown field

λ = mean free path (intercollision distance)

The probability of atoms colliding is related to the concentration of the gas N (number of atoms/cm³) and the collision cross-section (σc) of the particles.

This relationship can be expressed by the following equation.

$$1/\lambda = N\sigma c. \quad (3)$$

From this we can infer that $\lambda = P^{-1}$, as the pressure is a measurement of the gas density [26]. As such, it can be expected that α will be a function of the system pressure. Breakdown will occur when the denominator of equation 1 goes to 0, as the current at this condition will be infinite. From this and the equations above, the critical breakdown field ($\varepsilon = \varepsilon_B$) and voltage ($V_B = d\varepsilon_B$) can be expressed by Paschen's Law.

$$V_B = \frac{APd}{\ln(Pd) + B'} \quad (4)$$

Where: P_d = system pressure

A, B = constants for the given system.

At low system pressures (P_d), there are few electron-ion collisions and the secondary electron yield is too low to sustain ionization. At high pressures, the collisions are too frequent and the electrons do not acquire sufficient energy to ionize the gas atoms. There is a region in between these extremes where the plasma discharge is self-sustaining, typically a few hundred to few thousand volts [26]. Magnetron sputtering has the advantage of displacing the Paschen values to lower system pressures relative to simple discharge and as such has one to two orders of magnitude higher current draw for the same voltage. This yields higher deposition rates in magnetron sputtering at lower pressures.

Since magnetron sputtering occurs at lower pressures (typically a few millitorr), the sputtered atoms fly-off in ballistic fashion to impinge on the substrate to be coated. This is accomplished, as the sputtered atoms avoid gas phase collisions and scattering. In magnetron sputtering, the sputtering gas plasma is magnetically confined such that secondary electrons emitted from the target are trapped in small spaces and yield higher local ionization. This leads to higher ion bombardment upon the target and a subsequently increased sputter rate [69]. In practical application, the inclusion of one powerful central magnet and a ring of additional magnets, which ring the back of the target. These magnets create fields on the front face of the target, which confines the electron

motion. Ionization of the working gas is most intense in this area, leading to the most intense plasma there.

Because the gas pressure is low in magnetron sputtering, the sputtered atoms are not scattered by the background gas. As such, this is a line of site process, with high compressive stresses. In addition, since low pressures are required, it is possible to produce plasmas from ionized coating materials, which are self-sputtering, meaning that no inert gas is required [49]. Upon bombardment of incoming ions onto the target material, the ions may reflect back, stick, absorb, scatter, eject or sputter atoms, or get buried in subsurface layers (ion implantation). The energy of the impinging atoms is critical in defining the nature of their interaction with the target surface, by changing the probability of surface sticking and re-sputtering [26]. At low impact energies, the condensation and chemisorption can both occur readily. As the impact energy increases, the sticking probability decreases. At higher impact energies, sputtering occurs readily. Increasing beyond this level, the energy is too high and ion implantation occurs.

Permeation Cup Design

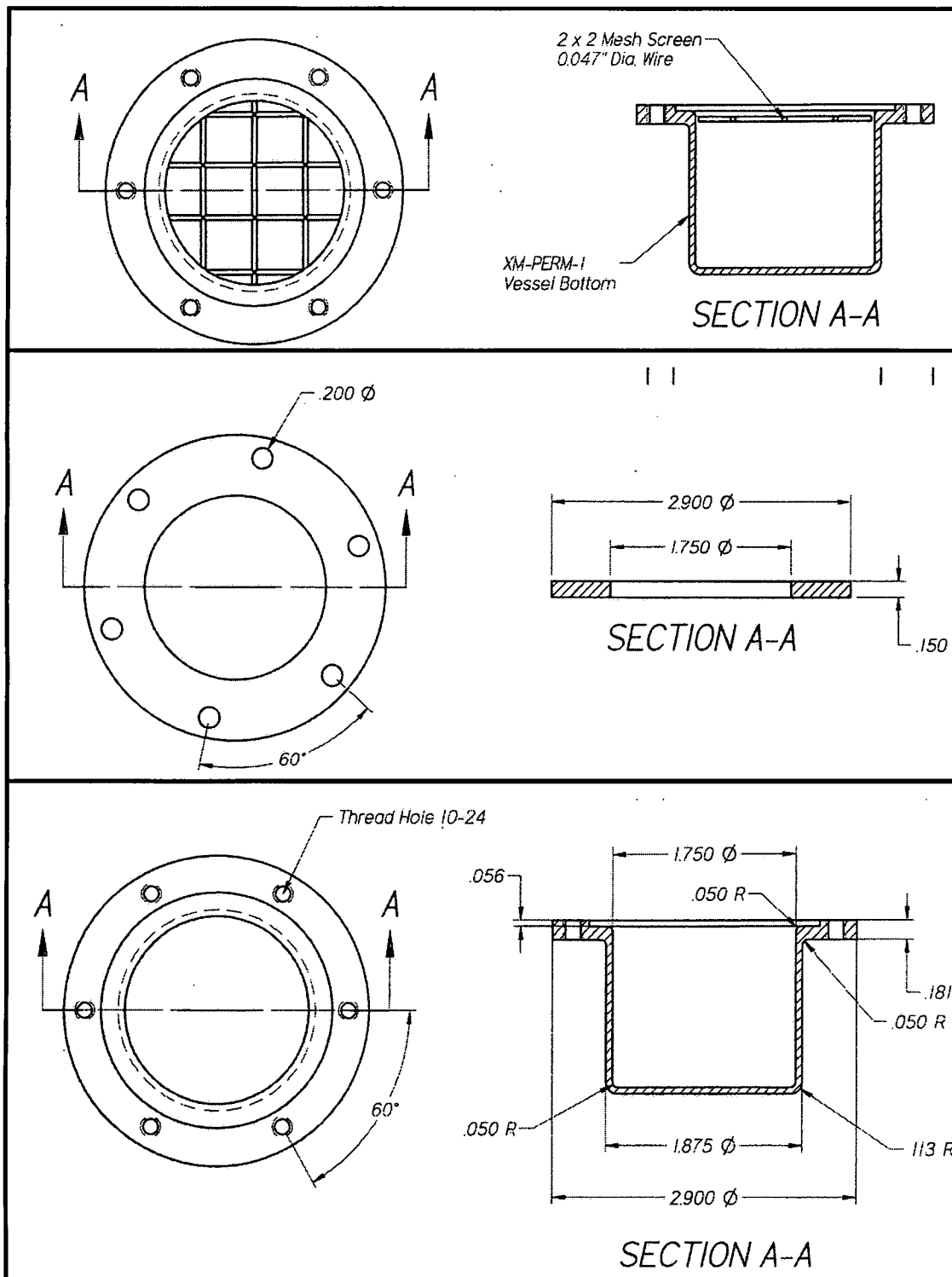


Illustration 112: Permeation Cup Design

C++ Code for Cubic Spline to Normalize Permeation Curves

```
//-----
```

```
#include <vcl.h>
#include <math.h>
#pragma hdrstop
#include <fstream.h>
#include <cstring.h>
#include <iostream.h>
```

```
#include "Unit1.h"
```

```
//-----
```

```
#pragma package(smart_init)
#pragma resource "*.dfm"
```

```
double In[1000];
double Out[1000];
double T[100][100];
double Y[100][100];
double H[100][100];
double B[100][100];
double P[100][100];
double U[100][100];
double V[100][100];
double Z[100][100];
double X[100][100];
double D[100][100];
double Q[100][100];
double Total[100];
double Av[100];
double J[100];
double Sum[100];
double Avg[100];
int q;
int b;
```

```

TForm1 *Form1;
//-----
__fastcall TForm1::TForm1(TComponent* Owner)
    : TForm(Owner)
{
}
//-----

void __fastcall TForm1::Button1Click(TObject *Sender)
{
    int k = StrToInt(Num->Text);           // determine number of data points

    int s = StrToInt(Spacing->Text);       // determine space between data points

    int z = Input->Text.Length();          // determine the length of the input file name

    int Cu = StrToInt(Curves->Text);

    char v[80];                           // String of input file name

    for (int i=0; i<z; i++)                // set v to the input file name
        v[i] = Input->Text[i+1];
    v[z] = '\0';

    ifstream g(v);                         // extract the given input values

    for (int m=0; m<Cu; m++)
    {
        for (int i=0; i<k; i++)
        {
            g >> T[m][i];    // Input "x" Values
        }
        for (int i=0; i<k; i++)
        {
            g >> Y[m][i];    // Input "y" Values
        }
    }
}

```

```

for (int m=0; m<Cu; m++)
{
    for (int i=0; i<(k-1); i++)                // Determine Z-values (this is the
                                                // solution vector (X[i]) for the square
                                                // matrix of A,B,C,D values for
                                                // the cubic spline.
    {
        H[m][i] = (T[m][i+1] - T[m][i]);
        P[m][i] = H[m][i];
        B[m][i] = (Y[m][i+1] - Y[m][i])/H[m][i];
    }

    U[m][1] = 2*(H[m][0] + H[m][1]);
    V[m][1] = 6*(B[m][1] - B[m][0]);

    for (int i=2; i<(k-1); i++)
    {
        U[m][i] = 2*(H[m][i] + H[m][i-1]) - (H[m][i-1]*H[m][i-1])/U[m][i-1];
        V[m][i] = 6*(B[m][i] - B[m][i-1]) - (H[m][i-1]*V[m][i-1])/U[m][i-1];
    }

    Z[m][k] = 0;

    for (int i=(k-2); i>0; i--)
    {
        Z[m][i] = (V[m][i]-H[m][i]*Z[m][i+1])/U[m][i];
    }

    Z[m][0] = 0;

    Total[m] = (T[m][k-1]-T[m][0])/s;                // Determine number of increments
                                                        // of input size.

    int w = 0;
    int c = 0;

    while(c<1)                                        // Determine total number of
    {                                                  // X-nodes.
        if (w < T[m][0])
        {

```

```

        c=0;
        int z = w+s;
        w = z;
    }
    else
        c=1;
}

X[m][0] = w;

for (int i=0; i<Total[m]; i++)                // Determine X-node locations
{
    X[m][i] = X[m][0] + s*i;
}

for(int j=0; j<Total[m]; j++)                // Determine which increment of
{                                              // spacing to use for determination
    q = 0;                                    // of y-values
    for(int i=1; i<k; i++)
    {
        if (X[m][j] < T[m][i])
        {
            q=(i-1);
            i=k;
        }
        else
        {
            q = q;
        }
    }
}

double l = T[m][q+1]-T[m][q];    // Detmine y-values for a given x
double tmp = (Z[m][q]/2) + (X[m][j]-T[m][q])*(Z[m][q+1]-Z[m][q])/(6*l);
tmp = -(l/6)*(Z[m][q+1]+2*Z[m][q])+(Y[m][q+1]-Y[m][q])/l+(X[m][j]-T[m][q])*tmp;
D[m][j] = Y[m][q] + (X[m][j]-T[m][q])*tmp;
}
}

```

for (int i=0; i<Cu; i++)	// Determine starting x-point for
{	// the cubic spline. This is the
if (Av[0]<X[i][0])	// lowest X-value for which there
{	// is a value for each curve.
Av[0]=X[i][0];	
b=i;	
}	
else	
Av[0]=Av[0];	
}	
 for (int m=0; m<Cu; m++)	// Determine starting X-point
{	// locations for each of the curves
for (int i=0; i<Total[m]; i++)	// This is because not all curves
{	// necessarily start at the
if (X[m][i]<Av[0])	// minimum value.
{	
J[m]=i+1;	
X[m][i]=X[m][i];	
}	
else	
X[m][i]=X[m][i];	
}	
}	
 for (int i=1; i<Total[b]; i++)	// Determine the average
{	// Y-values at each point
Av[i]=X[b][i];	
}	
 for (int m=0; m<Cu; m++)	// Sum the y-values for each
{	// X-point location.
for (int i=0; i<Total[b]; i++)	
{	
int po = i + J[m];	
Sum[i] = D[m][po]+Sum[i];	

```

    }
}

for (int i=0; i<Total[b]; i++)
{
    Avg[i] = Sum[i]/Cu;
}

// Determine the Average for
// the Y-value at each X point.

int zo = Output->Text.Length();

char vo[80];
// Output file name

for (int i=0; i<zo; i++)
    vo[i] = Output->Text[i+1];
vo[zo] = '\0';

ofstream h(vo);
// Output File generation

for (int m=0; m<Cu; m++)
{
    // Output the input X-points
    h << "Input_X ";
    for (int i=0; i<k; i++)
    {
        h << T[m][i] << " ";
    }
    h << "\nInput_Y ";
    // Output the input Y-points
    for (int i=0; i<k; i++)
    {
        h << Y[m][i] << " ";
    }
    h << "\n";
}

h << "XPoints ";
// Output the average spline
for (int i=0; i<Total[b]; i++)
{
    // X-points
    h << Av[i] << " ";
}

```

```

    }

    h << "\nAverage ";           // Output the average spline
    for (int i=0; i<Total[b]; i++) // Y-points
    {
        h << Avg[i] << " ";
    }

}
//-----

```

Permeation Chamber Pictures

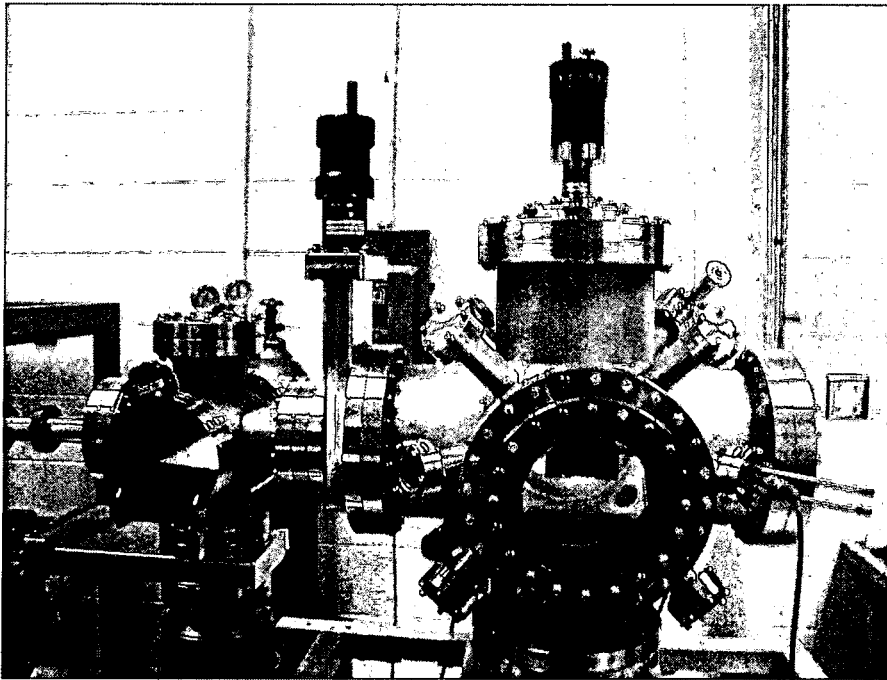


Illustration 113: Deposition Chamber

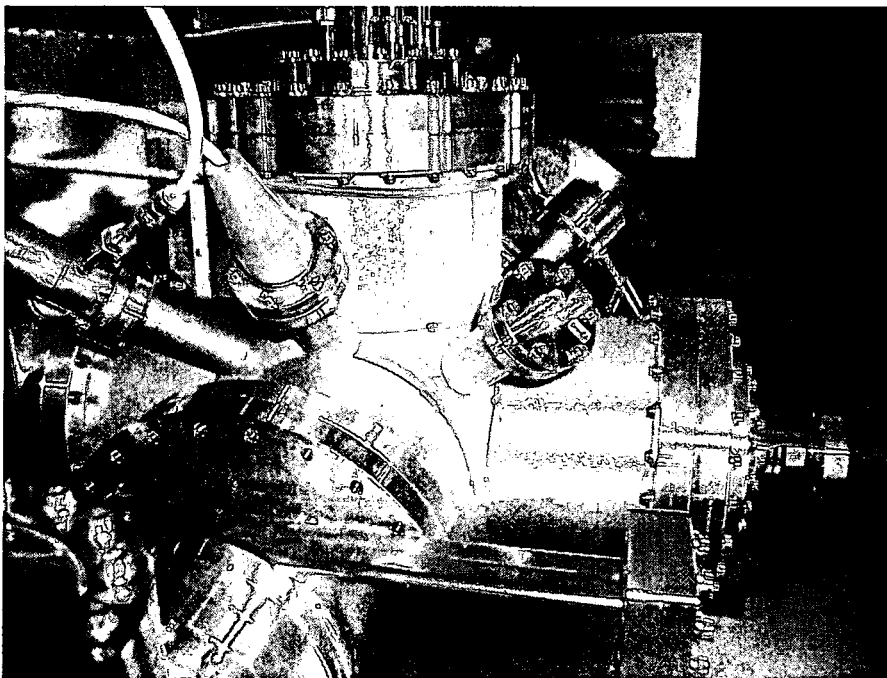


Illustration 114: Main Chamber

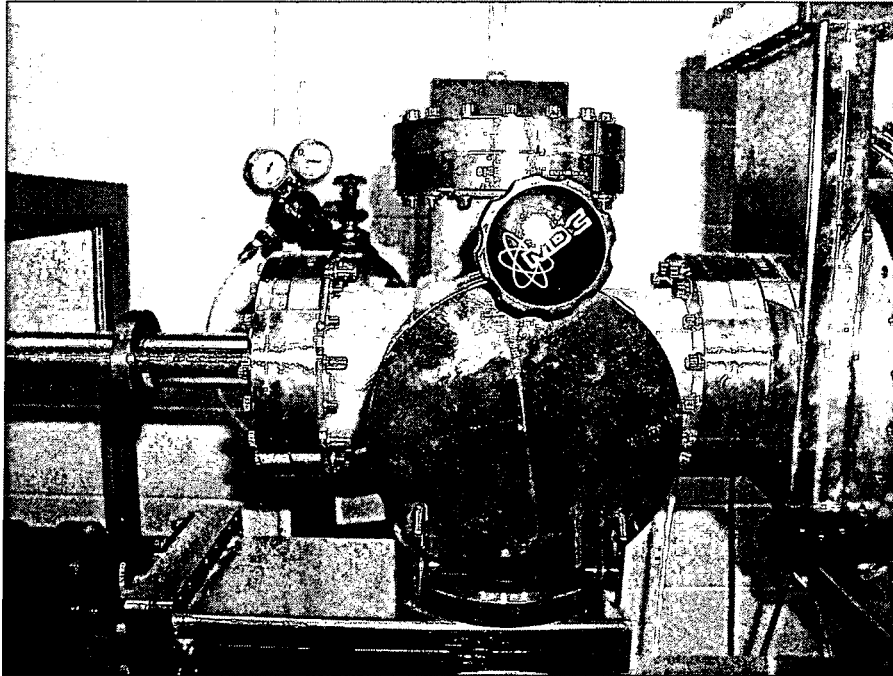


Illustration 115: Secondary Chamber

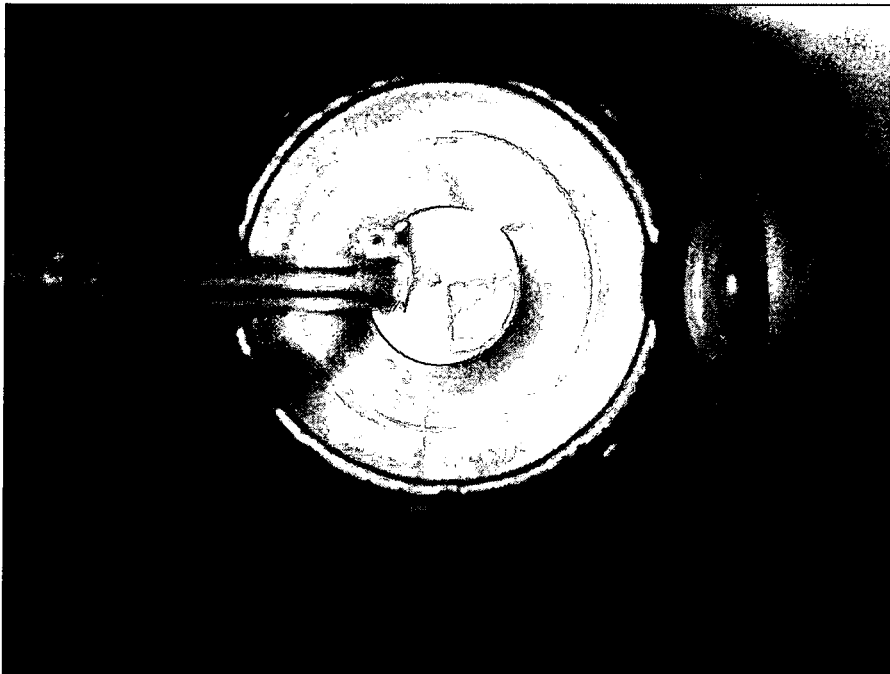


Illustration 116: Interior End View – Sample Shutter Closed

Deposition Pictures

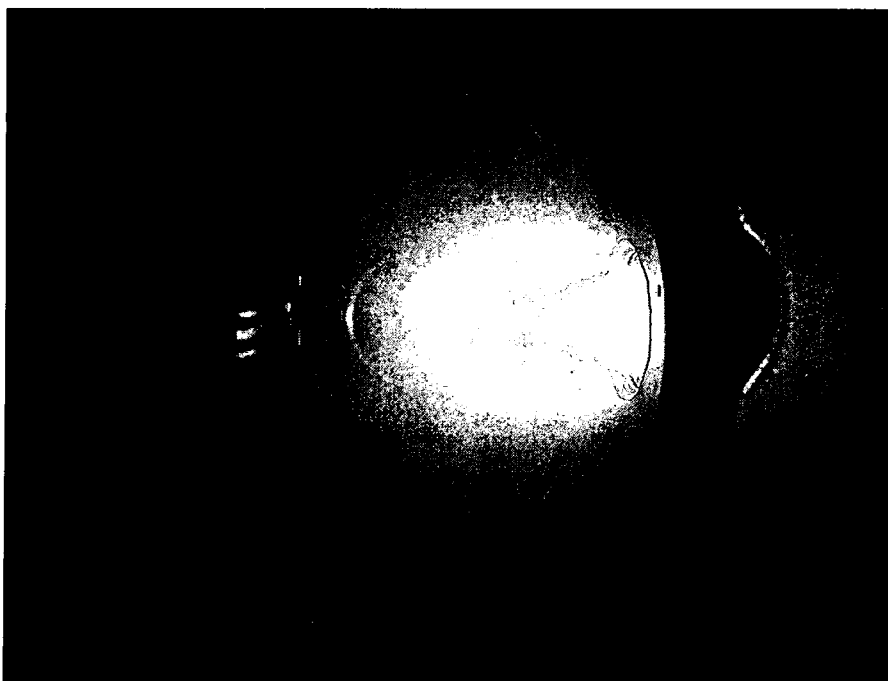


Illustration 117: 10 mTorr Copper Deposition – Side View

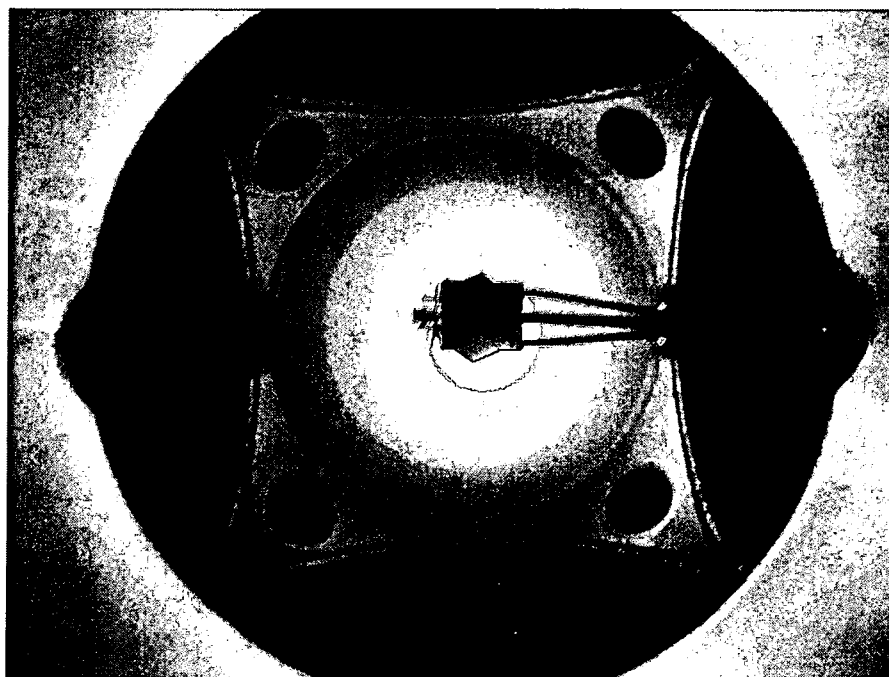


Illustration 118: 10 mTorr Copper Deposition – Rear View

Sample Pictures

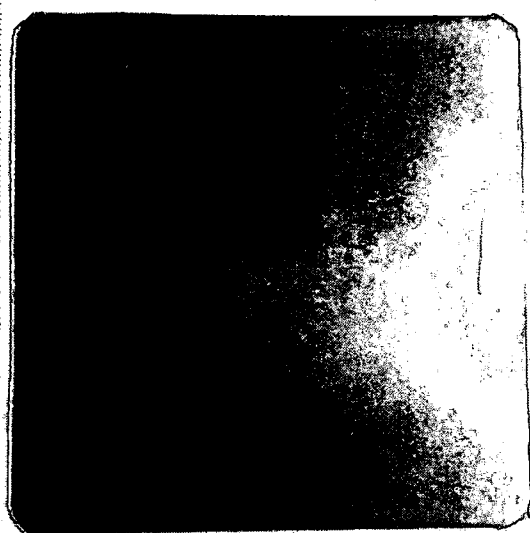


Illustration 119: NBR Uncoated

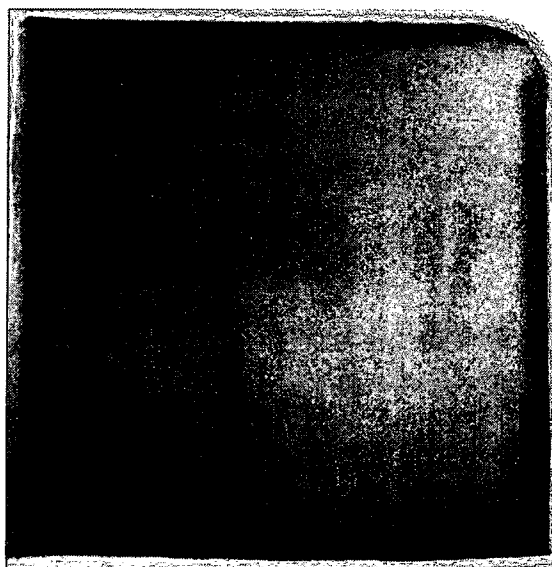


Illustration 120: NBR-Al 10 mTorr

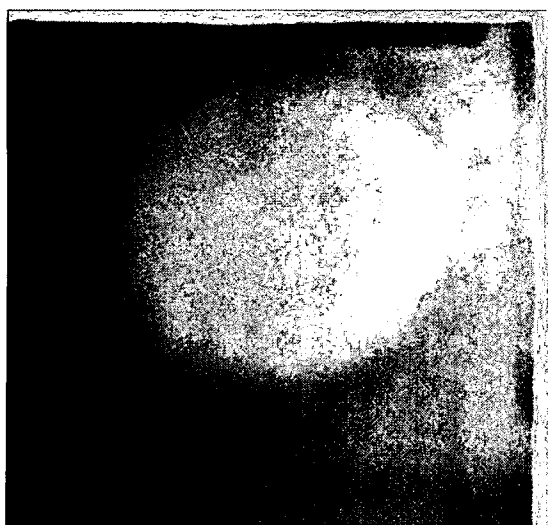


Illustration 121: NBR-Al 20 mTorr

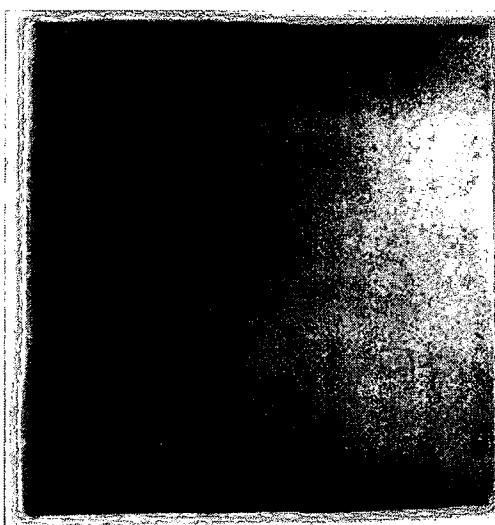


Illustration 122: NBR-Al 30 mTorr

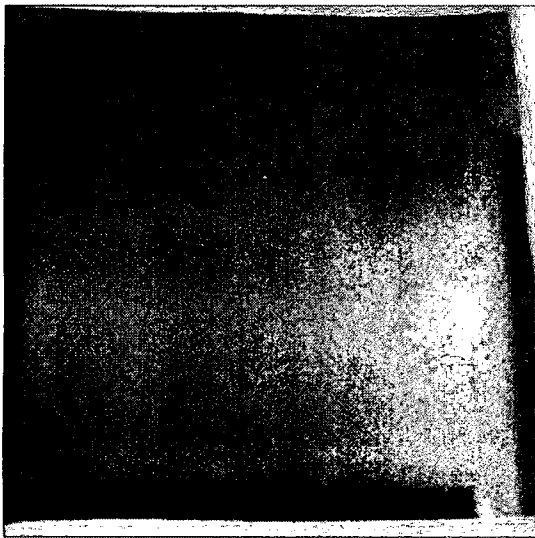


Illustration 123: NBR-Cu 10 mTorr

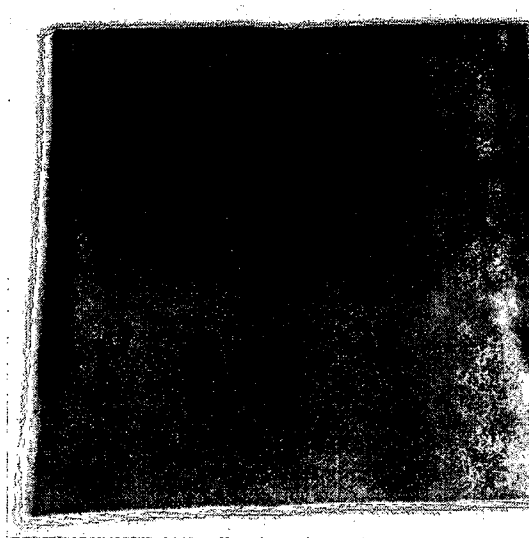


Illustration 124: NBR-Cu 20 mTorr

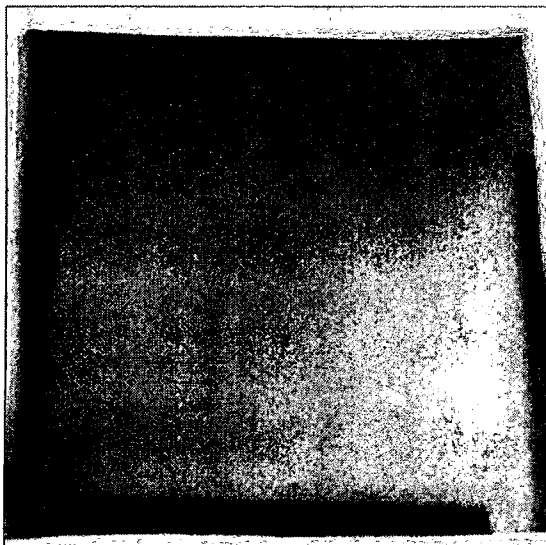


Illustration 125: NBR-Cu 30 mTorr

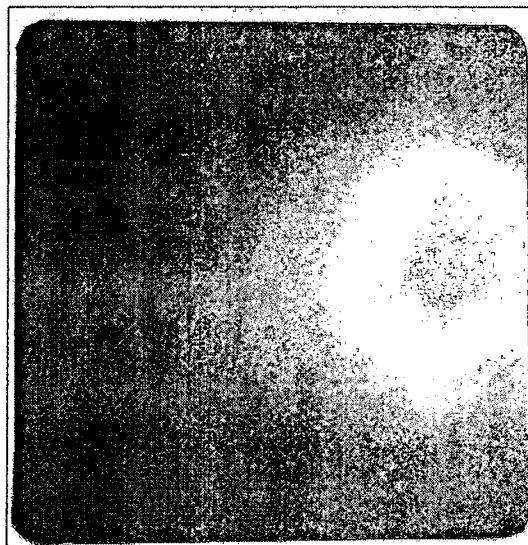


Illustration 126: FVMQ Uncoated

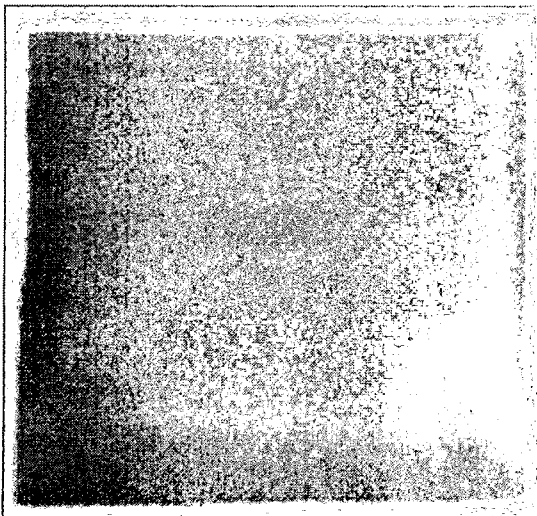


Illustration 127: FVMQ – Al 10 mTorr

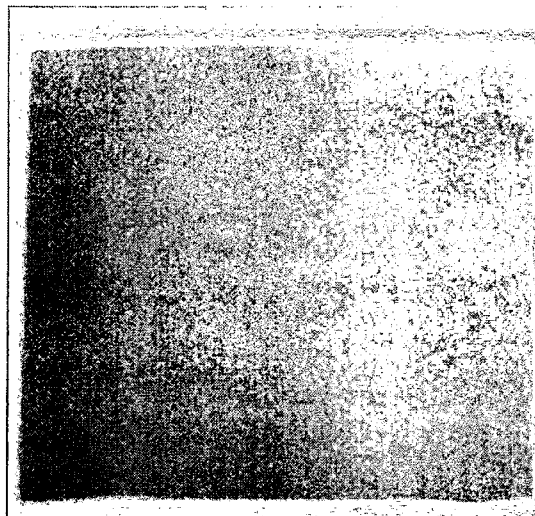


Illustration 128: FVMQ – Al 20 mTorr

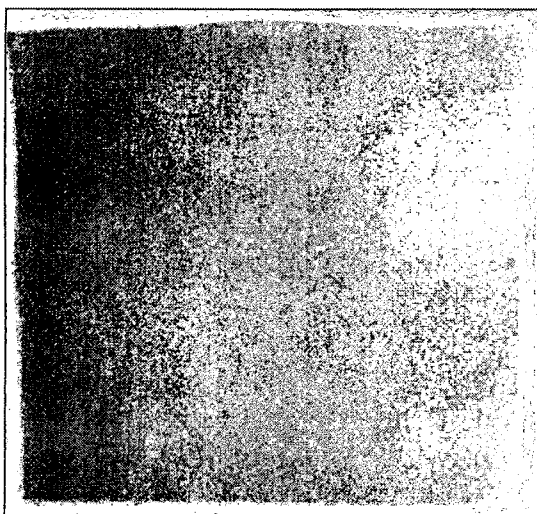


Illustration 129: FVMQ – Al 30 mTorr

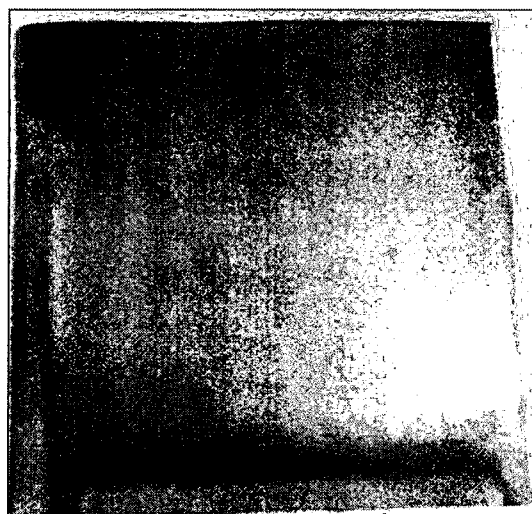


Illustration 130: FVMQ – Cu 10 mTorr



Illustration 131: FVMQ – Cu 20 mTorr

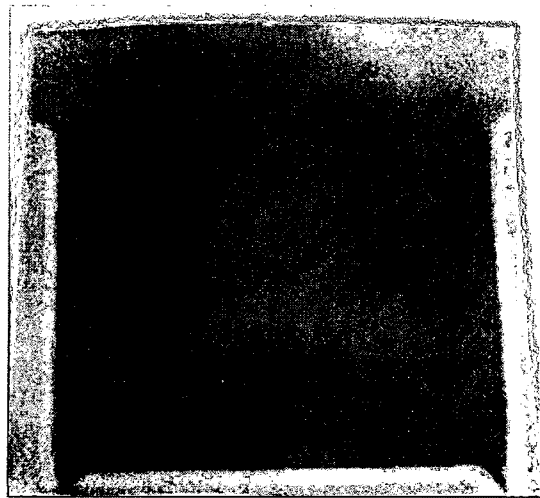


Illustration 132: FVMQ – Cu 30 mTorr

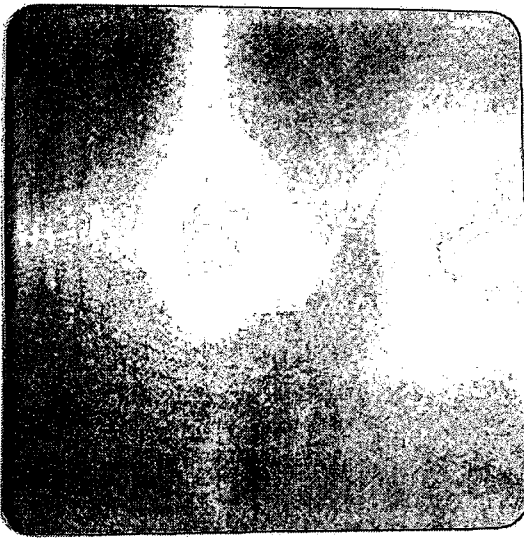


Illustration 133: FKM Uncoated

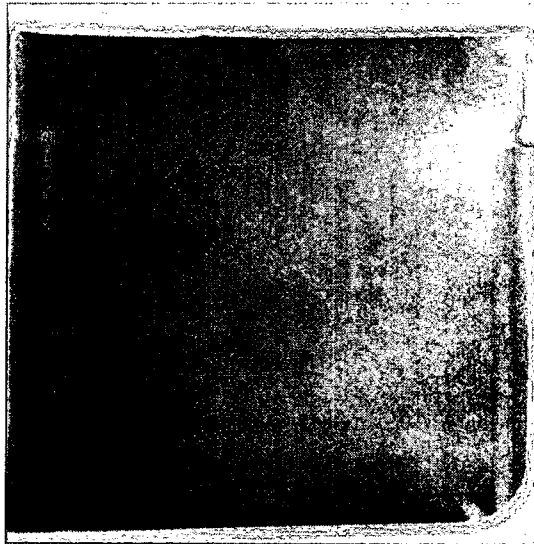


Illustration 134: FKM – Al 10 mTorr

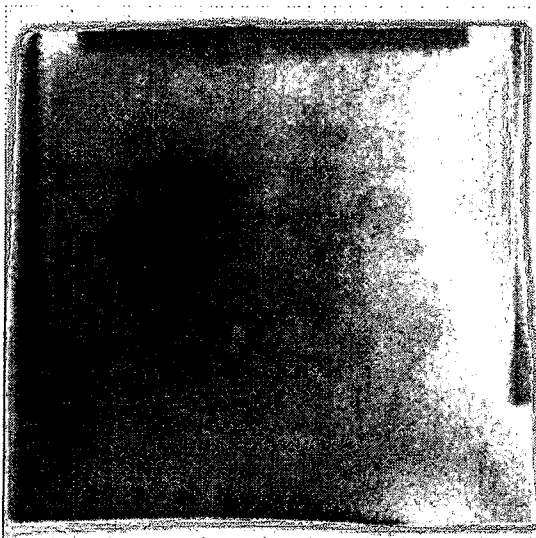


Illustration 135: FKM – Al 20 mTorr

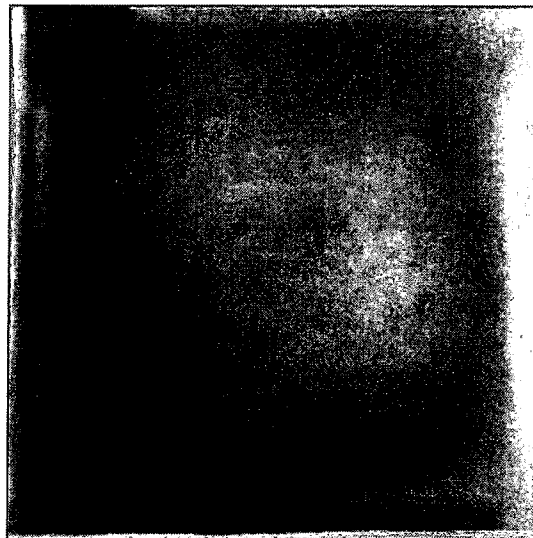


Illustration 136: FKM – Al 30 mTorr

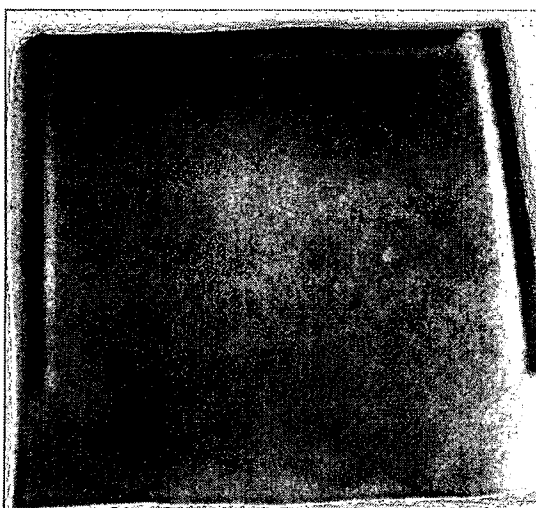


Illustration 137: FKM – Cu 10 mTorr

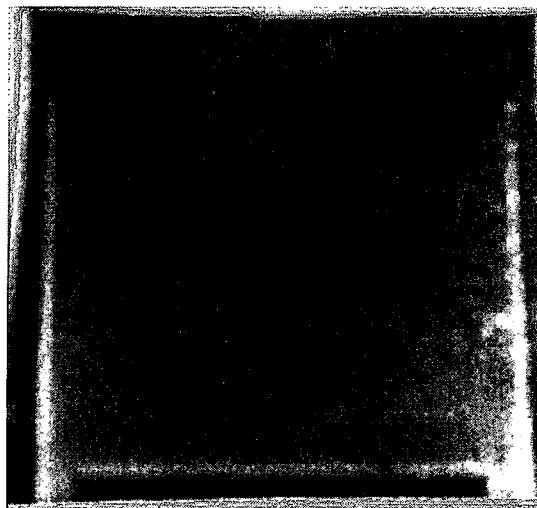


Illustration 138: FKM – Cu 20 mTorr

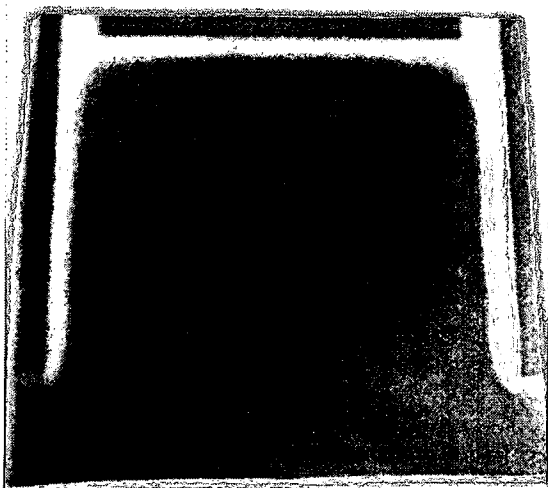


Illustration 139: FKM – Cu 30 mTorr

R702032368

The HF Group

Indiana Plan

T 044479 F 18 00



4/27/2006